Measurement of Double Differential $t\bar{t}$ Production Cross Sections with the CMS Detector

Dissertation

zur Erlangung des Doktorgrades

an der Fakulät für Mathematik, Informatik und Naturwissenschaften

Fachbereich Physik

der Universität Hamburg

vorgelegt von

Ievgen Korol

aus Ukrainka (Ukraine)

Hamburg

2016

Folgende Gutachter empfehlen die Annahme der Dissertation:
PD Dr. Olaf Behnke
Prof. Dr. Peter Schleper

Datum der Disputation: 18. April 2016

Hiermit erklre ich an Eides statt, dass ich die vorliegende Dissertationsschrift selbst verfasst und keine anderen als die angegebenen Quellen und Hilfsmittel benutzt habe.

I hereby declare, on oath, that I have written the present dissertation by my own and have not used other than the acknowledged resources and aids.

Hamburg, den 3 Februar 2016

Abstract

The high energy scale of the pp collisions at the Large Hadron Collider (LHC) at CERN makes this facility to a real factory for the production of $t\bar{t}$ pairs. This enables to study the top-quark properties and its production and decay mechanisms in unprecedent detail. The dileptonic decay channel of the top-quark pair, in which both W bosons, produced from the top-quark decay, decay into a lepton and neutrino, is studied in this analysis. The limitation to one electron and one muon in final state used in this work allows to strongly suppress the possible background processes and leads to a higher signal purity. About 40k events with a top-quark pair have been selected using the $\sqrt{s} = 8$ TeV data recorded with the CMS detector in the year 2012. Exploiting this large sample, double differential top-quark pair production cross sections are measured for the first time. The cross sections are studied as functions of various observables which describe the top and top-pair kinematics.

To obtain the full kinematics of the $t\bar{t}$ final state, which contains two undetected neutrinos, a kinematic reconstruction procedure was developed and exploited in this work. The new procedure makes use of all available constraints and is based on a repeated reconstruction of each event with detector observables smeared according to their resolutions in order to obtain for each event solutions for the kinematic constraint equations. In order to obtain double differential cross sections, the distributions of reconstructed observables are then corrected for detector effects by using a double differential unfolding procedure, which is based on a χ^2 minimization.

The double differential cross sections presented in this work allow to test the Standard Model in detail and investigate previously seen disagreements between measured and predicted single differential cross sections. The results of this work are compared to Standard Model predictions (up to next-to-leading order of the hard interaction description), implemented in various Monte Carlo event generators.

In general, the results agree with the predictions, except for some cases, which are discussed in detail.

Kurzfassung

Die hohe Energieskala der pp Kollisionen am Large Hadron Collider (LHC) am CERN macht diese Beschleunigeranlage zu einer wahren $t\bar{t}$-Paar Produktionsfabrik. Dies erlaubt es die Eigenschaften und Produktions- und Zerfallmechanismen von top-Quarks mit beispielloser Präzision zu erforschen. In dieser Analyse wurden top-Quarkpaare im dileptonischen Zerfallskanal untersucht bei dem beide W-Bosonen aus den top-Quarkzerfällen in ein Lepton und Neutrino zerfallen. Die Beschränkung in dieser Arbeit auf Endzustände mit einem Elektron und einem Muon unterdrückt sehr stark mögliche Untergrundprozesse und führt zu einer hohen Signalreinheit. Etwa 40k Ereignisse mit einem Top-Quark Paar sind aus den Daten, die mit dem CMS Detektor im Jahr 2012 bei einer Schwerpunktsenergie von $\sqrt{s} = 8$ TeV genommen wurden, ausgewählt worden. Diese große Datenmenge ermöglicht es zum ersten Mal doppel-differenzielle Wirkungsquerschnitte der Top-Quark-Paar Produktion zu messen. Die Wirkungsquerschnitte sind als Funktion von verschiedenen Variablen, die die Kinematik des Top-Quarks und des Top-Quarkpaares beschreiben, untersucht worden. Um die volle Kinematik des $t\bar{t}$ Endzustandes mit zwei nicht detektierbaren Neutrinos zu erhalten, wurde ein neues Verfahren der kinematischen Ereignisrekonstruktion im Rahmen dieser Arbeit entwickelt und benutzt. Bei diesem Verfahren werden alle möglichen kinematischen "Constraints" rigoros benutzt und jedes Ereignis mehrfach rekonstruiert mit verschiedenen Detektorobservablen gemäss ihrer Auflösungen, um für jedes Ereignis Lösungen für die kinematischen "Constraints" zu finden. Die beobachteten Verteilungen der Daten als Funktion zweier rekonstruierter kinematischer Variablen wurden dann mit einer zweidimensionalen Entfaltungsmethode, basierend auf einer χ^2-Minimisierung, auf Detektoreffekte korrigiert um so die doppeltdifferenziellen Wirkungsquerschnitte zu erlangen. Die in dieser Arbeit gewonnenen Wirkungsquerschnitte erlauben es das Standardmodell der Teilchenphysik in grosser Detailtiefe zu überprüfen und vorher beobachtete Diskrepanzen zwischen gemessenen und vorhergesagten einfach-differenziellen Wirkungsquerschnitten genauer anzuschauen. Die Resultate dieser Arbeit werden mit Standardmodellvorhersagen (bis hin zur nächstführenden Ordnung der QCD Störungsreihe), repräsentiert durch vier Monte Carlo Ereignisgeneratoren, verglichen.

Im Allgemeinen stimmen die Resultate und Vorhersagen überein, außer in einigen kinematischen Bereichen, was ausführlich untersucht und diskutiert wird.

Contents

Chapter 1

Introduction

Nowadays the heaviest known elementary particle is the top quark which is as heavy as an atom of gold. The search for this particle lasted more than two decades and ended successfully in March 1995 at the Fermi National Accelerator Laboratory, Fermilab, where the discovery of the top quark was announced [1].

The third generation of quarks, which consists of top and bottom quarks, was predicted in 1973 by Kobayashi and Maskawa [2]. However, the huge mass of the top quark was not expected, so it could not be discovered for a long time, while its partner, the bottom quark, was experimentally found already four years after its theoretical prediction [3].

To produce a top quark one needs to concentrate an immense amount of energy into a small region of space. This is done at the accelerator experiments. The most powerful accelerator nowadays is the Large Hadron Collider (LHC), CERN. Delivering proton-proton collisions with a center-of-mass energy of 7 TeV in 2011 and 8 TeV in 2012, it became a real top quark factory. The large number of events with top quarks produced at the LHC gives us a unique possibility to study precisely the properties of the heaviest quark.

The top quarks are dominantly produced together with antitop quark, which is called in the following $t\bar{t}$ production. Top quarks decay before they could hadronize. Each top quark of the pair decays to a W boson and a b-quark almost exclusively. The W boson has several decay channels. In this work only the decay channel, where both W bosons from the two top quarks decay to electron, muon and (anti)neutrinos, is studied. For this purpose the 19 fb^{-1} data sample with 8 TeV center-of-mass energy taken in 2012 was analyzed.

This work represents the first measurement of the normalized double differential (2D) top pair production cross section at the LHC. The double differential $t\bar{t}$ production cross sections provide a stringent test of the Standard Model of Particle Physics, as they allow to study the $t\bar{t}$ production dynamics in unprecedented detail. For the measurement of the double differential production cross sections a new kinematic reconstruction of the $t\bar{t}$ events was implemented, providing an accurate and unbiased determination of the momenta of the top and the antitop-quarks.

This reconstruction was used for single differential cross section measurements [4] which were published recently. In these measurements it was observed that the transverse momentum spectrum of the top quarks is softer than in several Monte Carlo predictions

based on calculations up to Next-to-Leading Order (NLO) QCD. The study of 2D cross sections allows to further investigate the origin of this discrepancy. For this purpose the measurement is done in nine different 2D variable combinations connected to the top kinematics and results are compared to various model predictions. The object selection presented in this work closely follows the strategy of the single differential measurement.

In order to contribute to future measurements with higher statistics during the next runs of the LHC, a part of my work was connected to the studies of irradiated prototype silicon sensors and readout chips for the Phase-I upgrade of the CMS pixel detector.

This thesis is structured the following way. Chapter 2 provides an introduction to the theoretical knowledge behind the measurements performed in this analysis. It gives a brief overview of the Standard Model of particle physics and top quark physics in particular.

Chapter 3 describes the experimental setup used to obtain the data for this analysis. It provides information about the LHC accelerator and the CMS detector, giving a brief introduction to each detector part.

Chapter 4 elucidates the studies performed for the upgrade of the barrel pixel part of the CMS detector. The upgraded detector is planned to be operated starting from 2016.

Simulations of the pp collisions and of the detector response were used to study detector effects for the $t\bar{t}$ double differential cross sections measurements. Additionally, the simulated samples allow a comparison of the results of the measurements to the theoretical models implemented in the simulations. An overview of the simulation models and techniques exploited for the analysis described in this thesis is presented in chapter 5.

The reconstruction of the collision events collected by the CMS detector is described in chapter 6. After selecting objects like leptons, jets and missing transverse energy, which fulfill the event selection criteria described in chapter 7, the $t\bar{t}$ candidate has to be reconstructed out of them. The procedure of the full kinematic reconstruction of the $t\bar{t}$ system in the dileptonic final state is introduced in chapter 8.

Having the fully reconstructed event kinematics, the double differential $t\bar{t}$ production cross sections are determined as described in chapter 9. This section gives an overview of the data unfolding and explains the cross section evaluation. The determination of systematic uncertainties (sources and values) are described in chapter 10. Chapter 11 delivers the cross section results and the comparison to the theory models and the discussion of the presented results.

A summary of the thesis and an outlook are provided in chapter 12.

Chapter 2

The Standard Model of Particle Physics

This chapter provides an introduction to Elementary Particle Physics as described by the Standard Model (SM). First the particles of the SM are presented, then the way they interact is shown. A short introduction to the physics of the top quark is given in the end.

2.1 Introduction

The main question which elementary particle physics addresses is '*What is the matter made of?*' This question was stated many thousands years ago and is still of current interest. First guesses about the structure of matter were made already in ancient Greece by the philosopher-atomist Demokrit, who claimed that everything around us consists of tiny undevidable chunks called *atomos* [5]. But the elementary particle physics (elementary here means unstructured) in a modern sense started with J.J. Thomson's discovery of the *electron* [6] in 1897. The electrons were correctly assumed to be constituents of atoms. A much more detailed picture of the atom structure was obtained after Ernest Rutherford's scattering experiment [7], proving atom cores to be much smaller than the full atoms and showing that an atom consists of a heavy positively charged core, called *nucleus* and very light negatively charged electrons. The nucleus was later proven to be non-elementary, consisting of *protons* and *neutrons*, which were later demonstrated to consist of *quarks*. However, up to date no structure of electrons and quarks was discovered and they are according to our knowledge elementary particles.

Many particles were subsequently discovered during the last sixty years. Now having an idea what the structureless bricks making up matter in the Universe are, particle physics states another important question: '*How do the particles interact?*'.

The Standard Model of particle physics is a theory describing the basic elementary particles and interactions between them. This theory is overall successfully describing many phenomena and agrees with the experimental efforts. However, there is also a number of challenges which the Standard Model is facing. In particular

- gravity is not included,

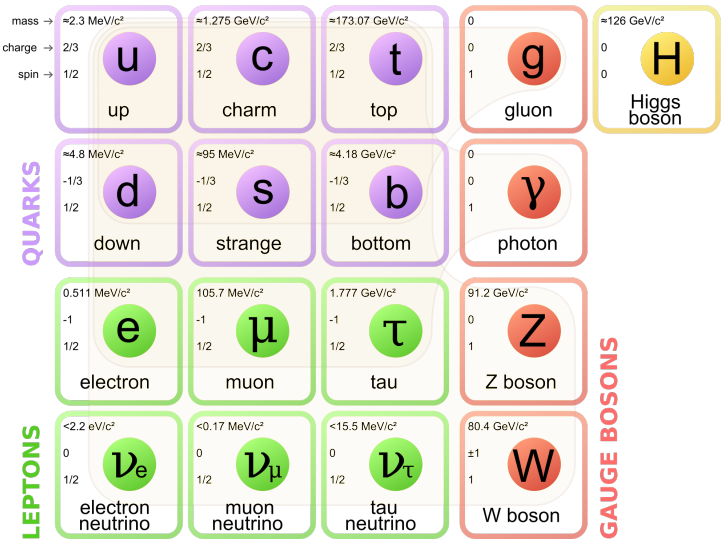

Figure 2.1: The Standard Model of Elementary Particle Physics with three generations of matter fermions, gauge bosons and a Higgs boson. The properties of the particles are also shown in each box. Figure taken from [8]

- dark matter and dark energy do not fit into the model,
- the matter-antimatter asymmetry in the Universe is not explained.

2.2 Elementary Particles

The Standard Model asserts that all the material in the Universe is made up of elementary *fermions* (particles which have half-integer spin – $\frac{n}{2}\hbar$, $n = 1, 3, 5, ...$ and $\hbar$ is a reduced Planck constant) interacting through the fields, carried by *bosons* (particles which have integer spin – $n\hbar$, $n = 0, 1, 2, 3, ...$).

The Fig.2.1 shows all the known elementary constituents of matter and fields.

2.2.1 Leptons

The two bottom rows of fermions in the Fig.2.1 represent the known *leptons* with their masses, charges and spins.

In general, the fermions are described with the Dirac equation [9], which has solutions with positive and also with negative energy states. The latter are treated as *antiparticles*. So every lepton, being a fermion, has an antiparticle. In Fig.2.1 only particles are shown. The electron e^- has an antiparticle, called positron e^+. The antiparticle of the muon – μ^+ – and tauon – τ^+ – don't have any special name. As far as we know, the electron is a stable particle. The muon μ^- and tauon τ^- differ from the electron by their masses and their finite lifetimes. Neutral leptons, neutrinos ν, also have antiparticles, antineutrinos $\bar{\nu}$.

Leptons are grouped into families and each lepton family has a corresponding lepton number: an electron and an electron neutrino have a lepton number l_e, the muon and its neutrino have a lepton number l_μ and the τ with it's neutrino have the lepton number l_τ. Leptons have positive lepton numbers and antileptons – negative ones.

2.2.2 Quarks

The two upper rows in the Fig.2.1 list the known *quarks*, showing their masses, charges and spins.

Quarks are also fermions. However, there is a number of properties which are very different to the leptons. They have a *flavour* (up, down, charm, strange, top and bottom) and a non-integer electric charge ($\frac{2}{3}e$ or $-\frac{1}{3}e$, where e is the electron charge). Quarks also have a charge called *color*.

The systems of bound quarks are called *hadrons*. The examples of such systems are *baryons*, which consist of three quarks, and *mesons*, which consist of a quark and antiquark. The only stable yet known baryon is the proton. All the known mesons are unstable.

The baryons are fermions as they consist of an odd number of quarks which have spins $\frac{1}{2}$. The mesons have integer spins (0 or 1). This means that mesons are bosons.

2.3 Interactions

An interaction is the way the particles effect upon another particles and objects in their environment. The interaction is performed through exchange of mediator bosons.

Nowadays only four basic interactions are known: *strong*, *electromagnetic*, *weak* and *gravity*. Each of them can be characterized by a *strength*[1]. The following table shows the rough order of the interaction strengths, the mediator and the theory, which describes these interactions [10]:

Interaction	**Strength**	**Theory**	**Mediator**
Strong	10	Quantum Chromodynamics	Gluon
Electromagnetic	10^{-2}	Quantum Electrodynamics	Photon
Weak	10^{-13}	Flavordynamics	W and Z Bosons
Gravitation	10^{-42}	Geometrodynamics	Graviton

All the equations and values listed in this work are presented assuming that $\hbar = c = 1$, where c is a speed of light. This is called the *natural units*. More details on every interaction is presented in the following section.

[1] A *strength* [10] of the four basic forces can be determined as the value of each force between two objects with given masses and charges and placed on a distance r between each other. After all, the strength is an ambiguous notion, as the value of the force depends on the nature of the interacting objects and on the distance between them – we can get different orders of strength on different distances and between different objects. The strength should not be understood literally, but just as a measure of order.

2.3.1 Electromagnetic Interaction

The theory behind the electromagnetic interactions – Quantum Electrodynamics (QED) [11] – was developed earlier than the other interactions quantum theories. It describes the interactions between the elementary electrically charged fermions via mediator photons. The electromagnetic interaction is such that the oppositely electrically charged objects attract each other while same sign charges repulse. This interaction is present at any distance, getting weaker proportionally to the distance squared. QED is based on the gauge group $U(1)$. Every electromagnetic phenomena is ultimately reducible to the following elementary process, see Fig. 2.2.

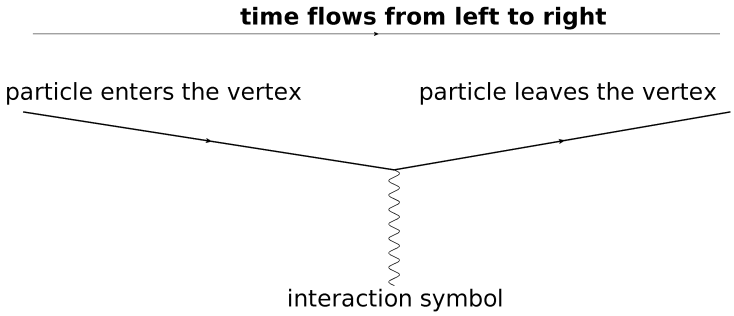

Figure 2.2: Feynman graph of the elementary QED process.

The more complex processes can be described combining two or more of these elementary vertices.

The coupling constant, or the interaction strength of the electromagnetic interaction is given as following:

$$\alpha = \frac{e^2}{4\pi\epsilon_0} \approx \frac{1}{137}, \tag{2.1}$$

where ϵ_0 is the permitivity of vacuum and e is the electron charge.

As the coupling constant is small ($\alpha \ll 1$), it can be used for expansion in perturbative calculations (observable $\sim \sum_{k=0}^{\infty} c_k \cdot \alpha^k$). The naming of the processes, described by each of the terms of the α expansion is Leading Order process (LO, which takes into account the first term with non-zero c_k), Next-to-Leading Order process (NLO, also takes to account the next term, additionally to the LO), Next-to-Next-to-Leading Order process (NNLO), etc.

2.3.2 Strong Interaction

The theory which describes the strong interaction is Quantum Chromodynamics (QCD), which is based on the gauge group $SU(3)$. Only the objects which have a color charge can interact strongly. The color charge (first mentioned in sec. 2.2.2) has three eigenstates: red (r), blue (b) and green (g). As for any other charge, the color charge eigenstates have also anticharges – anticolors. The combination of the color and corresponding anticolor, as well as the combination of all the colors/anticolors results in colorless states.

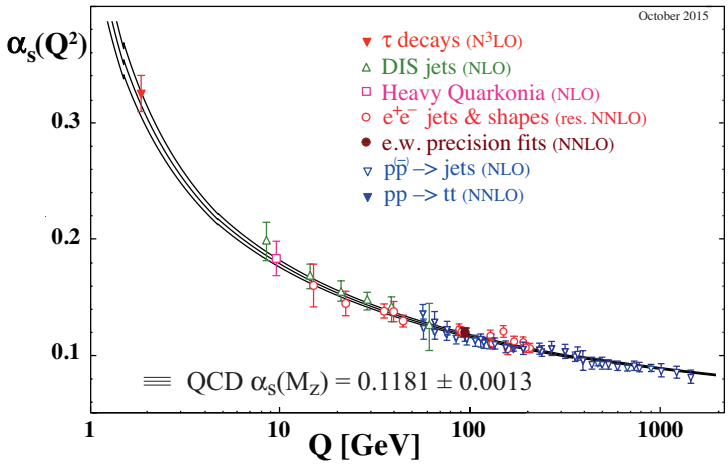

Figure 2.3: Summary of measurements of α_s as a function of the respective energy scale Q. The respective degree of QCD perturbation theory used in the extraction of α_s is indicated in brackets (NLO: next-to-leading order; NNLO: next-to-next-to leading order; res. NNLO: NNLO matched with resummed next-to-leading logs; N3LO: next-to-NNLO). Figure taken from [12].

The mediators of the strong interaction are gluons. These particles are massless and carry two colors – color and anticolor. The strong interaction is the interaction between quarks and gluons via gluons. The color charge is conserved during the interaction.

The coupling constant of the strong interaction, α_s, is depending on the energy scale Q. As shown in the Fig. 2.3, α_s rapidly increases with decreasing Q. This means that at larger distances the strength of the interaction increases a lot. This phenomenon is called *confinement* and this means that the quarks can not exist in an isolated state. The more the quarks separate from each other in terms of distance, the stronger they interact, the harder it becomes to separate them further. Even if enough energy is present to separate quarks more and more from each other, the gluon field will become critically high and produce a quark-antiquark pair out of the vacuum. This process may repeat sequentially. The phenomenon of sequential quark pair production is called *hadronization*.

The confinement constrains the maximum distances on which the interaction in terms of the gluon field is observed before producing a quark-antiquark pair. The limit of the region of strong interaction impact is of the order of the nucleon size $\sim 10^{-15}$ m.

The opposite tendency which can be observed in Fig. 2.3 is that the α_s is getting smaller for higher values of the Q. This means that for the shorter interaction distances, the coupling constant becomes weaker. This phenomenon carries the name *asymptotic freedom* [13]. Under these conditions the quarks can be effectively treated as free particles. The asymptotically free quarks are assumed to be observed in the *quark-gluon plasma* [14] – the state of matter with extremely high density and/or temperature.

2.3.3 Weak Interaction

The strength of the weak interaction is many orders of magnitude smaller than the one for the electromagnetic and strong interaction. This fact explains the name *weak*.

A charge, which is responsible for the weak interaction is the *weak isospin* I_3. All the left-handed[2] leptons and quarks carry the ability to interact weakly. A widely known example of the weak interaction is the process of the β-decay. The lepton number and lepton flavour both conserve in the weak interaction.

There are two kinds of weak interaction: *neutral*, mediated by the Z-bosons, and *charged*, mediated by the $W^{\pm}$. The masses of the mediators are shown in the Fig. 2.1. In the neutral weak interaction there is no electric charge as well as no quark flavour exchange between the interacting particles. In the charged weak interaction, both the electric charge and the quark flavour exchange, are present. In the charged weak interactions the quark flavour can exchange not only within one generation, but also between the generations. This intergeneration flavour exchange is described the following way:

$$\begin{pmatrix} u \\ d \end{pmatrix} \begin{pmatrix} c \\ s \end{pmatrix} \begin{pmatrix} t \\ b \end{pmatrix} \tag{2.2}$$

These are the quark mass eigenstates. The weak quark eigenstates differ from the mass eigenstates. For the former ones, the d, s and b states are replaced with their linear combinations d', s' and b', expressed as follows:

$$\begin{pmatrix} d' \\ s' \\ b' \end{pmatrix} = \begin{pmatrix} V_{ud} & V_{us} & V_{ub} \\ V_{cd} & V_{cs} & V_{cb} \\ V_{td} & V_{ts} & V_{tb} \end{pmatrix} \begin{pmatrix} d \\ s \\ b \end{pmatrix}. \tag{2.3}$$

The matrix V in 2.3 is the Cabibbo-Kobayashi-Maskawa matrix (CKM-matrix) [2], which describes the transition probability between different quark flavours. Experimentally defined, the matrix elements have the following magnitudes [16]:

$$V = \begin{pmatrix} 0.974 & 0.225 & 0.003 \\ 0.225 & 0.973 & 0.041 \\ 0.009 & 0.040 & 0.999 \end{pmatrix}. \tag{2.4}$$

The diagonal elements of the CKM matrix (2.4) are close to 1, being much larger than the off-diagonal elements. Thus, flavour transformations within one generation are preferred.

As the masses of the gauge bosons which mediate the weak interaction are quite large (see Fig. 2.1), the range of the interaction is restricted to a size of $\sim \frac{1}{M_W}$, where M_W is the mass of the $W^{\pm}$ boson, 80.4 GeV.

[2]The *chirality* of the particle defines it's handnessness. The left-handed and right-handed states are different components of the Dirac spinor [15]. The parity transformation change the chirality (from left-handed to right handed and vise versa). For massless particles chirality is the same as helicity – the property of the particle, which describes the coincidence of the spin and motion directions.

2.3.4 Electroweak Unification and Symmetry Breaking

If one compares the neutral weak interactions and the electromagnetic ones, it becomes obvious that they are very similar, differing mainly on the mediator of the interaction. This can be also seen in Fig. 2.4.

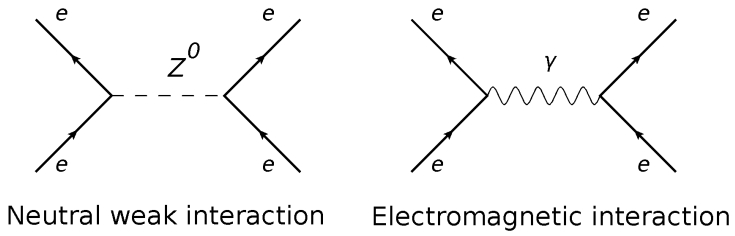

Figure 2.4: e^+e^- scattering in the electromagnetic (right) and neutral weak (left) interactions.

A unification of these two interactions would seem to be a natural idea. It is not that simple as replacing the Z^0 by the photon γ, one should take to account both processes and their interferences.

The theory [17] which describes the unified electroweak interactions is based on the $SU(2) \times U(1)$ symmetry. To make the Lagrangian of the weak interaction symmetric to the $SU(2)$ transformations, three fields are introduced: W^1_μ, W^2_μ and W^3_μ. These fields couple to fermions with the coupling constant g. The fields W^1_μ and W^2_μ couple to the left-handed fermions and the W^3_μ is coupling to the neutrinos. The $W^\pm$ couples to the left-handed fermions, thus it can be represented as a linear combination of W^1_μ and W^2_μ:

$$W^\pm = \frac{1}{\sqrt{2}}(W^1_\mu \mp iW^2_\mu). \tag{2.5}$$

The symmetry $U(1)$ introduces the additional field B_μ which couples to neutrinos. The related coupling constant is g'. To describe the electromagnetic field, the Z_μ and γ_μ fields are introduced:

$$Z_\mu = \frac{1}{\sqrt{g^2 + g'^2}}(gW^3_\mu - g'B_\mu), \tag{2.6}$$

$$\gamma_\mu = \frac{1}{\sqrt{g^2 + g'^2}}(gW^3_\mu + g'B_\mu). \tag{2.7}$$

A free parameter of the Standard Model, which is introduced in this context, is the weak mixing angle θ_W, which is expressed as follows:

$$\cos(\theta_W) = \frac{g}{\sqrt{g^2 + g'^2}}. \tag{2.8}$$

Thus, the fields Z_μ and γ_μ can be expressed via this angle:

$$Z_\mu = W^3_\mu \cos(\theta_W) - B_\mu \sin(\theta_W), \tag{2.9}$$

$$\gamma_\mu = W^3_\mu \cos(\theta_W) + B_\mu \sin(\theta_W). \tag{2.10}$$

So in fact, the photon γ and the Z^0 mix the states of W^3_μ (corresponding to W^0) and B_μ (corresponding to B^0). The mixing angle θ_W has been measured experimentally [16] and corresponds to approximately 30^o.

There is also a charge introduced to describe the electroweak interaction, which is called a *hypercharge* Y and is expressed in the Gell-Mann–Nishijima equation:

$$Y = (2Q - I_3). \tag{2.11}$$

Here Q is an electric charge in units of the electron charge e and I_3 is the weak isospin.

The whole model, however, is based on the assumption that all gauge bosons have to be massless, which is not the case. The known experimental fact is that the $W^\pm$ and Z^0 bosons carry a non-zero mass [16]. The masses appear in this theory due to *spontaneous gauge symmetry breaking*. In another words, the particles remain massless, but a new field appears. The particles couple to this field and obtain masses in this interaction. The symmetry breaking is accompanied with the appearance of three massless particles with zero spin, so-called *Goldstone bosons*. They are eliminated by the *Higgs mechanism* [18], which, however, introduces a massive particle with zero spin - *Higgs boson*. At the time when the Higgs mechanism was introduced, such particle was not yet discovered. A Higgs-like particle was discovered only in 2012 [19,20] and it's properties still need to be checked for the consistency to the theoretical predictions.

2.3.5 Gravity

The fourth interaction which is present in our Universe is gravity. The gravity is not included in the Standard Model, but it has to be mentioned for a consistent picture. The gravity is described by the *general relativity*, which is a classical non-quantum field theory. Up to now it couldn't be combined with the Standard Model. The Standard Model breaks down at the large scale, where gravity starts to play role. Although the extension of the Standard Model is predicting the existence of a gravity gauge boson – a *graviton* with a spin 2 and zero mass – there has been no experimental proof of it's existence to date. The "charge" which reacts to the gravity is the mass of the interacting object.

The gravitation force between the elementary particles is very weak, even though the distances are very small (the gravity strength is proportional to $\sim \frac{1}{r^2}$). The reason for that are very low masses of the interacting particles. Gravity only becomes noticable on large distances when large, electrically uncharged objects with large masses are interacting. For example, the movement of the bodies in outer space (planets, stars, asteroids, etc) are to the large extend governed by gravity.

The influence of gravity is negligible for the processes studied in this thesis, thus it is neglected.

2.4 Top Quark Physics

In this thesis the process of $t\bar{t}$ production in pp collisions is being analyzed. Some more details of the top quark physics should be presented. The top quark has unique properties compared to the other elementary particles: it is the heaviest known elementary particles and its mass is so large that its lifetime is smaller than the typical hadronization time. Thus, the top quark decays faster than it can hadronize, which means that studying the top quark is gaining knowledge about a bare quark. This section describes the production process of the top quark and its decay.

2.4.1 Top Quark Production

The top quark production cross section depends on the center-of-mass energy of the experiment in which it is produced. From Fig. 2.5 one can judge that the LHC with its large center-of-mass energy (design energy of 14 TeV) acts like a top production factory. The top production cross section (σ_{top}) at the LHC scale is almost an order of magnitude larger than for the TEVATRON.

The top quarks may be produced as single top quarks or in pairs.

Single Top Production

Single top quarks can be produced in the weak interaction processes via the Wtb vertex.

There are three production modes of the single top – t-channel, s-channel and tW-channel. These production channels are shown in Fig. 2.6.

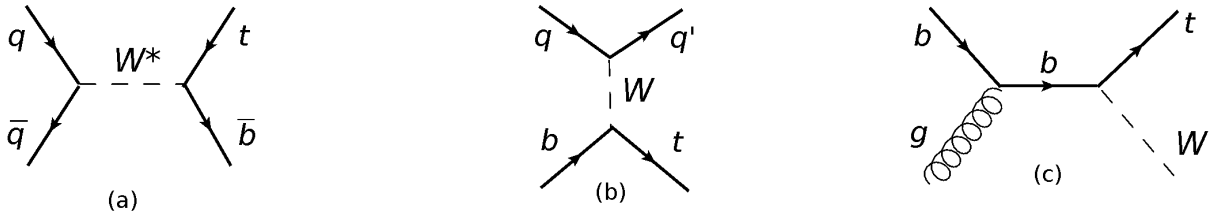

Figure 2.6: Feynman diagrams for the LO single t-quark production. Three different production channels for single top quarks are illustrated: the s-channel (a), the t-channel (b) and the W-associated tW-channel (c).

Single top quark production is interesting for various studies. It is a test of the Standard Model and it is directly sensitive to the CKM matrix element $|V_{tb}|$.

Top Quark Pair Production

The dominant SM $t\bar{t}$ production mechanism at the LHC is the gluon-gluon fusion. In QCD the inclusive production cross section of the $t\bar{t}$ pair from the proton-proton interaction can be factorized as follows [22]:

$$\sigma_{pp\to t\bar{t}}(s, m_t) = \sum_{i,j=q,\bar{q},g} \int dx_i dx_j f_i(x_i, \mu_f^2) f_j(x_j, \mu_f^2) \cdot \hat{\sigma}_{ij\to t\bar{t}}(\hat{s}, m_t, \mu_f, \mu_r, \alpha_s). \quad (2.12)$$

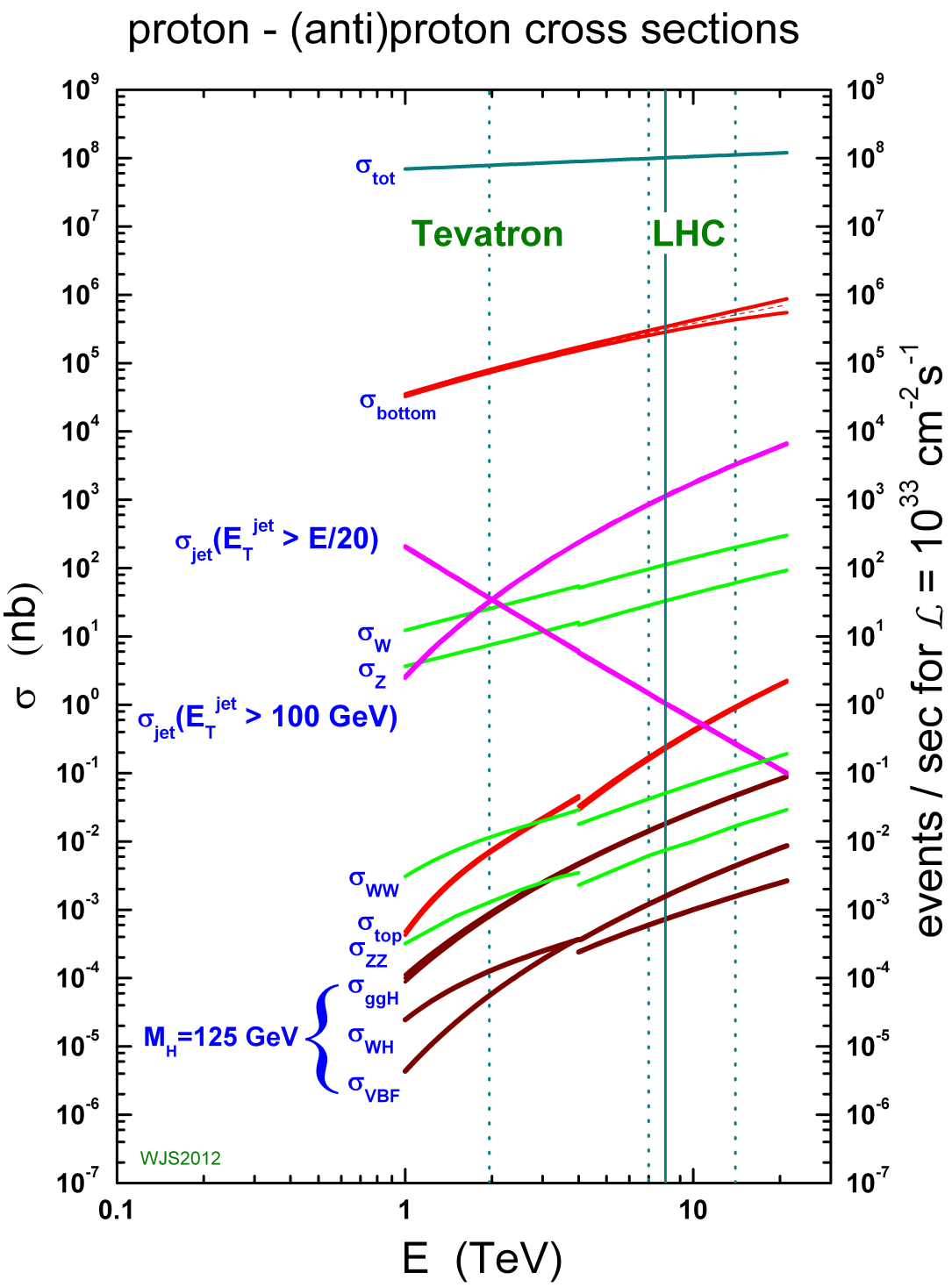

Figure 2.5: Standard Model cross sections in $pp(\bar{p})$ collisions for different SM processes depending on the energies. The turquoise vertical line presents the energy of the Large Hadron Collider running in 2012. The plot is taken from [21].

Here the sum is running over all quarks and gluons contributing to the process, m_t is the mass of the top quark, s is the squared center-of-mass energy for the pp collision, x is the parton momentum fractions with respect to the proton momenta, $\mu_{f,r}$ are the factorization and renormalization scales, $\hat{s} = sx_ix_j$ is the partonic center-of-mass energy, α_s is the strong coupling constant and $f_{i(j)}(x, \mu_f^2)$ is the parton distribution function (PDF).

The formula 2.12 is a convolution of long-distance contributions (proton densities) and short distance contributions (hard scattering cross sections). As the mass of the $t\bar{t}$ pair is high, the α_s turns out to be quite low (see Fig. 2.3), thus the perturbative expansion of the hard scattering cross sections is possible which is of the form $\sigma \sim \sum_k c_k \alpha_s^k(\mu)$, where the smallest k defines the leading order. The PDF, is depending on the parton flavour i, parton momentum fraction x_i and the energy scale of the interaction. A PDF gives a probability that within the interaction of a given scale a parton with a given flavour i and longitudinal momentum fraction x_i will be found in a proton. PDFs can not be expanded in perturbative QCD (pQCD), thus need a parametrization, depending on x. The dependence on the scale Q is described in the DGLAP evolution [23–25]. The scale can be chosen arbitrarily. This scale is called *factorization scale* μ_f.

The proton densities are obtained as a result of fits to experimental data. The PDFs are determined by different groups (for example, MMHT [26] or CTEQ [27]). The backbone of any modern PDFs are inclusive ep scattering cross sections measured in deep inelastic ep scattering (DIS) at HERA over a wide kinematic range of proton momentum fractions x and hard scales Q. An example of PDFs obtained by the HERA experiments H1 and ZEUS from fits to their combined inclusive DIS data are shown in Fig. 2.7.

At the LHC $t\bar{t}$ pairs are dominantly produced in the process of gluon-gluon fusion $gg \to t\bar{t}$ (at 80% of the cases at 8 TeV pp collisions) and to somewhat lesser extent in quark-antiquark annihilation $q\bar{q} \to t\bar{t}$ (at 20% of the cases). These LO production processes are shown in Fig. 2.8. In the NLO production processes there are also partonic sub-processes with $gq(g\bar{q})$ present.

In the leading order picture the proton momentum fractions x_1 and x_2 of the two partons (gg or $q\bar{q}$) producing the $t\bar{t}$ pair can be derived as follows. One can write down the momentum conservation equation:

$$p^t + p^{\bar{t}} = x_1 p_1 + x_2 p_2, \tag{2.13}$$

where $p^t = (p_x^t, p_y^t, p_z^t, E^t)$ and $p^{\bar{t}} = (p_x^{\bar{t}}, p_y^{\bar{t}}, p_z^{\bar{t}}, E^{\bar{t}})$ are the top and antitop momenta respectively, $p_1 = (E_p, 0, 0, -E_p)$ and $p_2 = (E_p, 0, 0, E_p)$ denote the momenta of two protons. Multiplying the eq. 2.13 by p_1 or p_2 and neglecting the m_p^2 terms, one can obtain the following expressions:

$$x_{1(2)} = \frac{E^t + E^{\bar{t}} - (+)p_z^t - (+)p_z^{\bar{t}}}{2E_p}. \tag{2.14}$$

The studies of the $t\bar{t}$ production process provide a very important test of the Standard Model. In particular, the process of $t\bar{t}$ production in the pp collisions at the LHC (sec. 2.4.1, Fig.2.8) is precisely predictable in QCD. Thus, the $t\bar{t}$ production cross section measurement can provide constraints on the PDF and the strong coupling constant α_s.

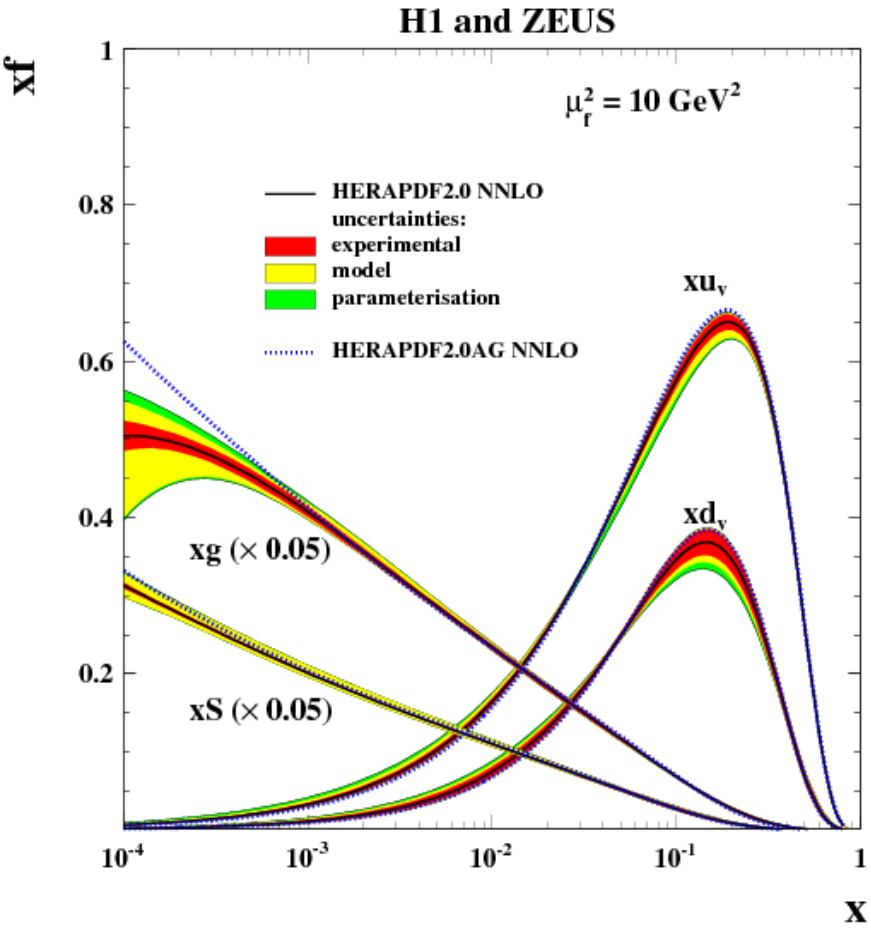

Figure 2.7: PDFs from HERAPDF2.0 [28].

The total $t\bar{t}$ production cross section is accurately calculated up to NNLO, which means that the experimental measurement of this cross sections provide a test of perturbative QCD. On the other hand, the deviation from the QCD predictions may point to some processes beyond the Standard Model. In addition, a measurement of the $t\bar{t}$ production cross sections may deliver information about various top properties, e.g. mass or spin of the t-quark.

2.4.2 Top Quark Pair Decay

The top quark decays before hadronizing almost exclusively to a b-quark and a W-boson, as the value of $|V_{tb}|$ is almost 1 (see eq. 2.4).

The decay modes of the $t\bar{t}$ pairs can be classified according to the decay mode of the W bosons. The decay modes and their branching ratios are presented in Fig. 2.9:

- *Full hadronic channel.* Both W bosons decay into quark-antiquark pairs – $t\bar{t} \rightarrow (W^+ \rightarrow q\bar{q}')b\,(W^- \rightarrow q''\bar{q}''')\bar{b}$. This decay channel has the largest branching ratio[3].

[3]The *branching ratio* of a specific decay of a particular particle/system is the probability of this

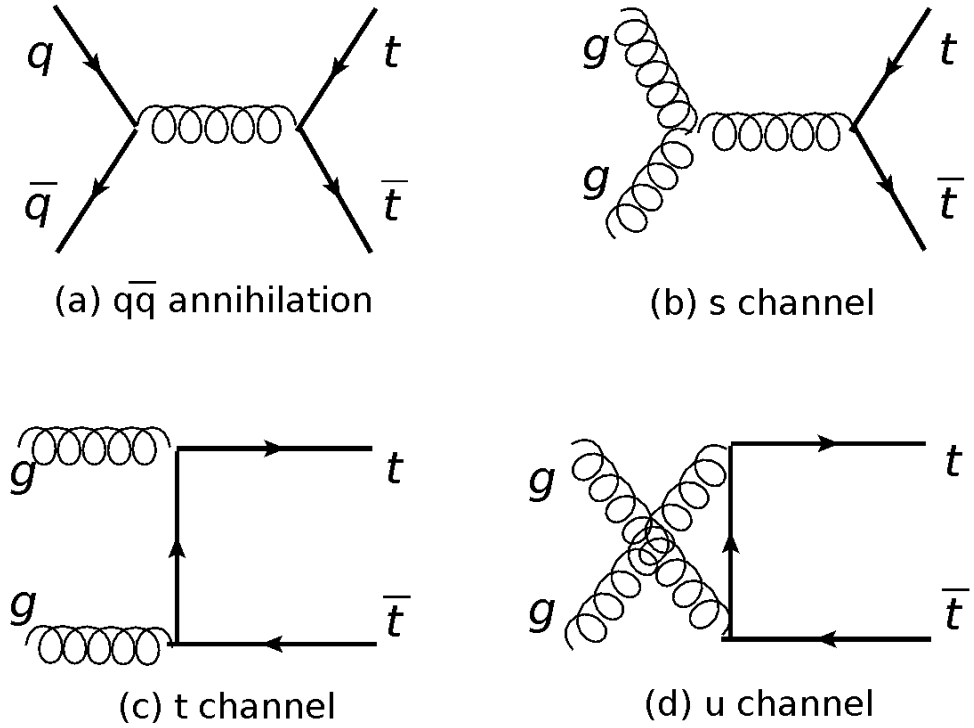

Figure 2.8: Feynman diagrams for the LO $t\bar{t}$ production.

However, this state has a not very pure quality in the LHC environment, as a large number of quark and gluon jets is produced and similar final states are produced in many other non top production processes at the LHC.

- *Semileptonic (lepton+jet) channel.* One W boson decays hadronically, another one - into two leptons: $t\bar{t} \to (W^{\pm} \to q\bar{q}')b\,(W^{\mp} \to l^{\mp}\nu)\bar{b}$. The high momentum lepton, which occurs in this process, is a signature that helps to identify the decay.

- *Dileptonic channel.* Both W bosons decay into leptons – $t\bar{t} \to (W^{+} \to l^{+}\nu_{l^-})b(W^{-} \to l^{-}\bar{\nu}_{l^-})\bar{b}$. This decay channel has the smallest branching ratio, but the two high momentum leptons are a clear signature which helps to distinguish this final state from other processes occurring in the LHC collisions.

This analysis is based on the dileptonic channel. However, only the final states with one electron and one muon of opposite charge is considered. The ones with the decaying into an $e\mu$ final state τ leptons are not taken into account as signal.

particle/system to decay via this decay mode.

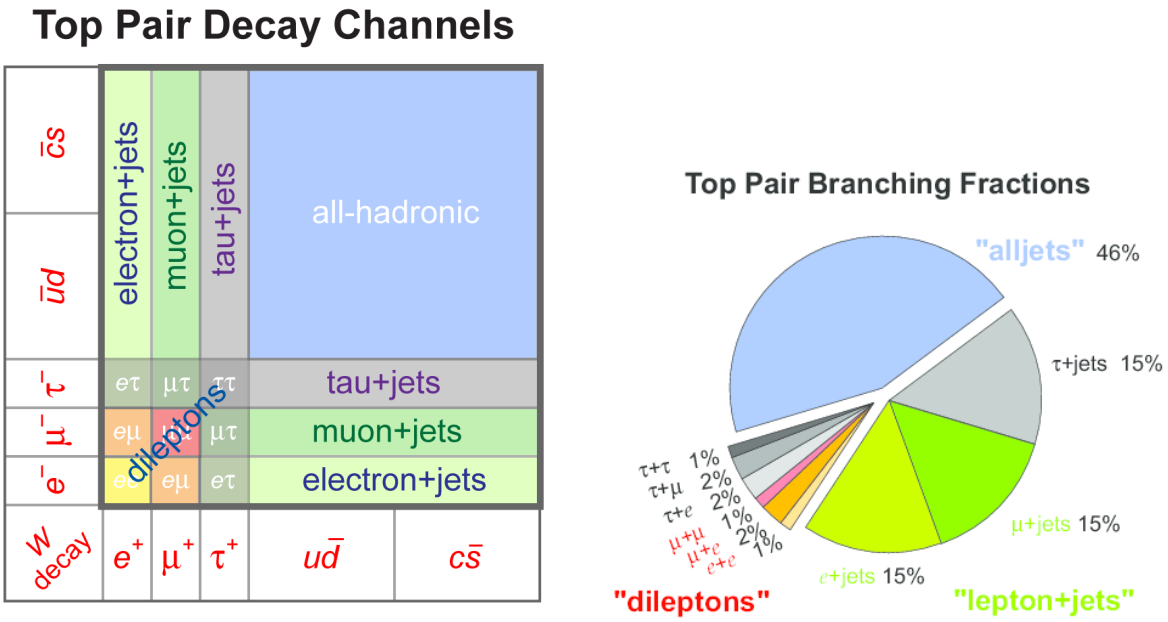

Figure 2.9: $t\bar{t}$ decay channels. On the right the branching ratio of different decay channels are shown. The diagrams are taken from [29].

Chapter 3

Experimental Setup

To test the theories, which describe elementary particle physics, collider experiments are carried out.

This chapter is divided into three parts. The first part is devoted to the description of the Large Hadron Collider. The second part of the chapter is revealing the CMS detector construction and features in more detail how it was used to produce the final results of this work. The third and the last part of this chapter is about the upgrade plans for the CMS detector to operate with higher energies and luminosities.

3.1 Large Hadron Collider

The fastest protons in the world, ever controlled by mankind, are produced in Switzerland at CERN. The machine which operates these protons is called Large Hadron Collider (LHC). The LHC is installed in a ring-shaped tunnel 26.7 km long placed $45 - 170$ m underground. Inside the tunnel there are two rings with vacuum tubes where proton (or lead nuclei) beams are circulating in opposite directions. There are four locations where the beams are crossing and the protons can collide with each other. The designed center-of-mass energy for those collisions is $\sqrt{s} = 14$ TeV, which means 7 TeV per colliding proton.

The protons are guided around the ring by $\sim$8 T superconducting magnets. For optimal usage of the LHC one needs to preaccelerate and preform the proton bunches. For this purpose the LHC is supported by a preacceleration system.

The way of the protons literally starts from a bottle of hydrogen gas. H_2 molecules are entering a duoplasmatron proton source [30] where they are stripped off the electrons. The protons produced by the source have to go through the chain of preaccelerators to satisfy very stringent needs of the LHC, such as the delivery of many high intensity proton bunches (2808 per LHC ring) with small transverse and well defined longitudinal emittances. The following acceleration injector chain is used for the LHC (Fig. 3.1):

- Protons first enter the *Linac2* [32] where they are accelerated up to 50 MeV and sent to the Proton Synchrotron Booster (PSB);
- *PSB* [33] is composed of four synchrotron rings (to avoid charge repulsion) which

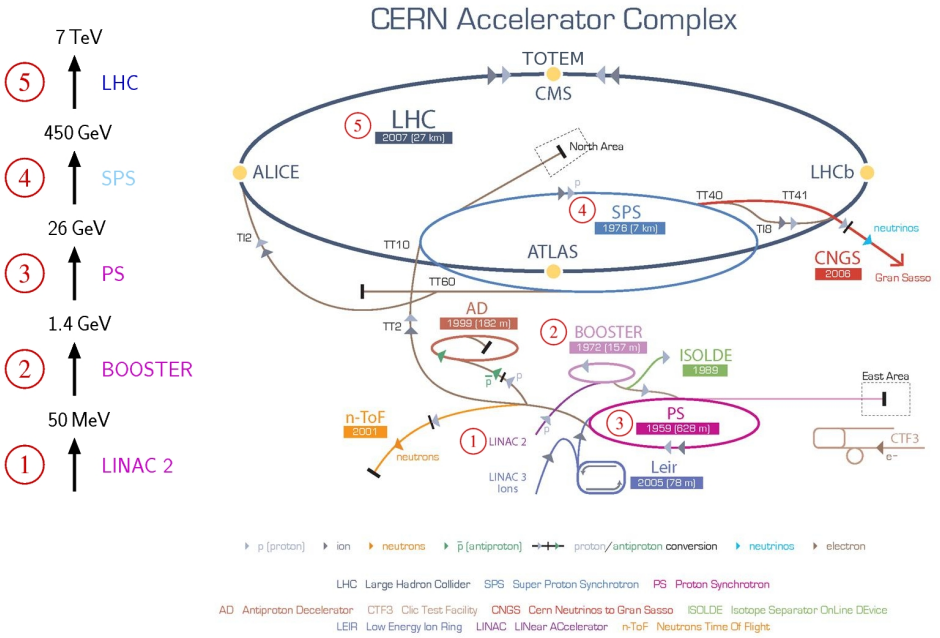

Figure 3.1: The complex of accelerators at CERN. Plot taken from [31].

raise the energy of the particles to 1.4 GeV for injection into the Proton Synchrotron (PS);

– *PS* [33] increases the energy up to 26 GeV and it takes 3.6 s to inject the protons to the Super Proton Synchrotron (SPS);

– *SPS* [33] is the second largest accelerator at CERN which provides 450 GeV protons injected to the LHC.

The most important accelerator characteristic is the number of protons in a coincidence area per time called *instantaneous luminosity* $\mathcal{L}$. The designed value at the LHC is $\mathcal{L} = 10^{34}$ cm^{-2} s^{-1}. The accelerator was providing a peak luminosity $\mathcal{L} = 7.7 \cdot 10^{33}$ cm^{-2} s^{-1} during the run in 2012.

The integral of the instantaneous luminosity over the time is defined as *integrated luminosity* L:

$$L = \int \mathcal{L} dt. \tag{3.1}$$

LHC provided 23.3 fb^{-1} of integrated luminosity for the run in 2012 from which 21.8 fb^{-1} were recorded by the Compact Muon Solinoid (CMS) detector (see Fig.3.2).

The measurements of the collision products are performed with complex particle detectors. There are four of them on the LHC ring, *ALICE*, *LHCb*, *ATLAS* and *CMS*, each located around the point where beams of particles of different directions are brought to collision. These detectors have different construction according to slightly different physics goals.

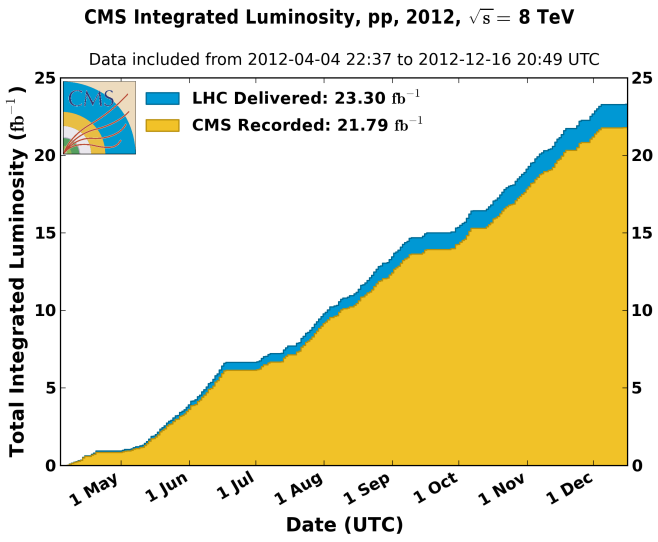

Figure 3.2: Cumulative luminosity versus day delivered (blue) and recorded by the CMS (orange) for proton-proton collisions during stable beam time in 2012. Plot taken from [34].

- ALICE (A Large Ion Collider Experiment) [35] is designed to work with heavy ion collisions. The goal of the ALICE experiment studies is the strongly interacting matter in extremely high density state called *quark-gluon plasma*. This state of matter provides a unique possibility to investigate bare quarks and also to study the early Universe which was so dense $\sim 10^{-12}$ seconds after the Big Bang.
  The ALICE detector weights 10000 tons and is 26 m long, 16 m high and 16 m wide. It lies in a depth of 56 m below the ground on the territory of France.

- LHCb (Large Hadron Collider beauty) [36] is investigating CP violation and heavy flavour physics via rare B hadron decays. As the $b\bar{b}$ pairs are mostly produced in the forward and backward directions, and their production cross section is very high, there was no need to construct a big and expensive 4π detector complex. For this reason the LHCb is a one-side spectrometer corresponding to the forward beam direction. For a better detection of the b-decays the LHCb features a movable tracking system which can go very close to the beam pipe.
  The LHCb detector weights 5600 tons and is 21 m long, 10 m high and 13 m wide. It is located at a depth of 100 m below the ground on the territory of France.

- ATLAS (A Toroidal LHC ApparatuS) [37] is one of the two general purpose detectors at the LHC. It serves to reach many physical goals – from Standard Model examination and Higgs searches to the studies of dark matter, extra dimensions and new physics. These tasks are mainly similar to the ones from the CMS experiment (the second general purpose detector at the LHC ring), but it uses different technical solutions.
  The ATLAS detector is built around the beam pipe such that the collision point is located in its center. It consists of the inner tracking system and calorimeter,

both surrounded by the barrel (2 T) and toroid magnets (0.5 to 1 T). The muon spectrometer is located on the outer layers of the detector.
Having a length of 45 m, a height of 25 m and a width of 25 m ATLAS is the largest particle detector complex at the LHC. However, its mass is rather low (compared to the other LHC general purpose detector, CMS) reaching 7000 tonnes. It is situated in a cavern 100 m under the ground on the territory of Switzerland.

- The CMS (Compact Muon Solenoid) is the second general purpose detector on the LHC. A more detailed description of this apparatus will follow in section 3.2.

3.2 The Compact Muon Solenoid

The analysis presented in this work was performed on the data recorded by the Compact Muon Solenoid (CMS) detector [38] during the 2012 run period in proton-proton collisions with center-of-mass energy $\sqrt{s}$ =8 TeV. This section will describe in more detail the construction and performance of the CMS detector.

Any particle detector is being constructed with respect to the measurements which are planned to be done with it. The main purpose of the CMS detector is the accurate measurement of the trajectories, momenta and energies of all particles produced in high energetic *pp* collision. To cope with this task, the setup of the CMS detector has to contain different parts, which are able to measure all the characteristics of the *pp* collision products.

- Tracking detectors manage the reconstruction of the trajectory of a charged particle.
- The magnet bends charged particles more or less strong depending on their momenta and masses. Thus, the curvature of the trajectory of the particle gives the information about its momentum.
- Calorimeters measure the energy of the particles.
- Muon systems are precisely measuring muons, as they are located in the regions, where nothing, except muons, is expected to appear.

Taken into account the high luminosities (see Sec.3.1) at the LHC, the detectors have to deal with multiple collisions per bunch crossing - pile up. Not to get distorted by a large amount of particles flowing to one sensor unit, the detector must have a fine enough granularity. The designed bunch spacing of 25 ns requires a fast enough readout. Radiation hardness of the materials is very important considering high luminosity and small bunch spacing. In the end the price and feasibility play a crucial role in the detector complex creation.

The positioning, materials, granularity and technologies of the different detector part have to be chosen accounting to the physical goals of the detector and budget limits.

The CMS facility being a general purpose detector was designed to make its parts fulfill as many physical goals as possible. The final onion-like construction of the apparatus is shown in Fig. 3.3. The overall detector size reaches 28.7 m in length and 15.0 m in width.

The total weight of the facility is 14000 tones, which makes CMS the heaviest particle detector at the LHC. The detector is cylindrically symmetric around the beam pipe and also symmetric to the left and right side along the beam direction relative to the collision point. The CMS detector is located in an underground cavern near Cessy, France.

A common coordinate system is used with the CMS experiment. The origin is assumed to be located at the nominal collision point, the x-axis is pointing to the center of the LHC ring and the y-axis is pointing vertically upwards. Thus the z-axis points along the beam axis to make the coordinate system right-handed. As the detector is symmetric around the beam pipe, it may be convenient to use cylindrical or spherical coordinate systems. The azimuthal angle ϕ is measured from the x-axis in the $x-y$ plane in the range $(0, 2\pi)$ and the polar angle θ from the $+z$-axis in the range $(0, \pi)$. The radial coordinate r is the transverse distance from the coordinate origin.

The *pseudorapidity* η is often used instead of the polar angle:

$$\eta = -\ln(\tan\frac{\theta}{2}) = \frac{1}{2}\ln\frac{|\vec{p}| + p_L}{|\vec{p}| - p_L}, \tag{3.2}$$

where $\bar{p}$ is the particle momentum vector and p_L is a longitudinal component. The other variable which can be used instead of η for the massive particles is the *rapidity* y:

$$y = \frac{1}{2}\ln\frac{E + p_L}{E - p_L}, \tag{3.3}$$

where E is the energy of the particle.

The transverse momentum and energy of a particle, denoted as p_T and E_T, are also commonly used in the data analysis. They are defined in the $(x-y)$ plane. Another variable representing the energy imbalance in the transverse plane, is the *missing transverse energy* E_T^{miss}.

3.2.1 Solenoid magnet

The 3.8 T superconducting CMS solenoid, 13 m in length and 6 m in diameter, is shown in Fig. 3.4. The flux is returned through a 10000 ton heavy yoke [38]. A very strong magnet allows not only curving high momentum muons for their better transverse momentum reconstruction, but also keeps soft particles with a small bending radius inside the inner detector layers. This reduces occupancy inside the calorimeters allowing only higher momentum particles to pass through. A solenoid design allows a compact size of the powerful magnet. On the other hand this limits the tracking precision at high pseudorapidities, as in the very forward regions there will be tracks, which are not influenced by a magnetic field [40] and thus their transverse momentum cannot be measured.

3.2.2 Tracking Detector

The inner tracking detector [38, 42] (also called tracker) at CMS is the closest detector component to the beam line and to the collision point having a length of 5.8 m and a diameter of 2.5 m. It is designed for a precise track and secondary vertex measurement. The tracker is positioned inside the solenoid (see Section 3.2.1). The particle momentum

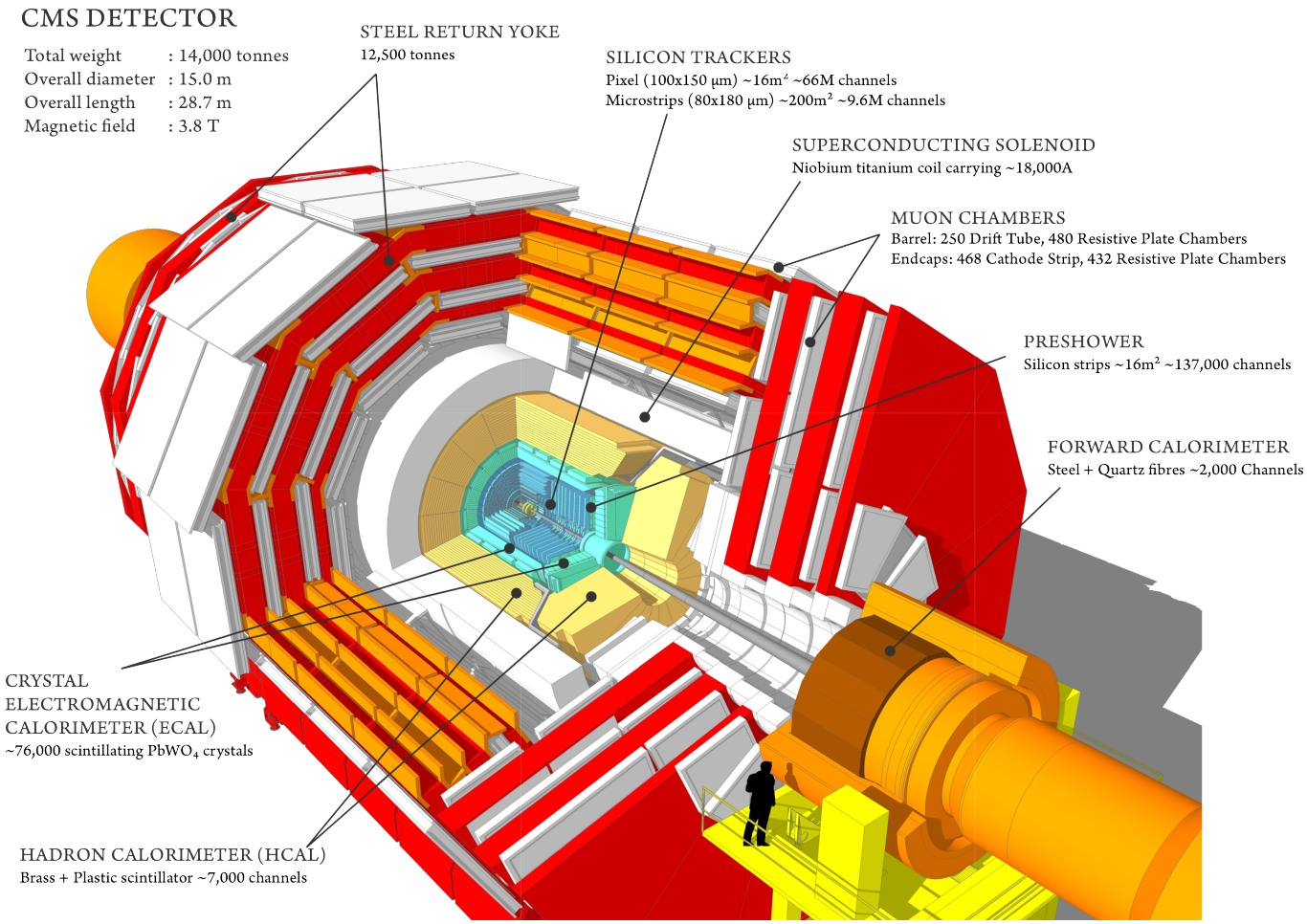

Figure 3.3: Sectional view of the CMS detector with highlighting different components. The LHC beams collide in the center of the machine. The central axis of the detector corresponds to the beam line. Figure taken from [39].

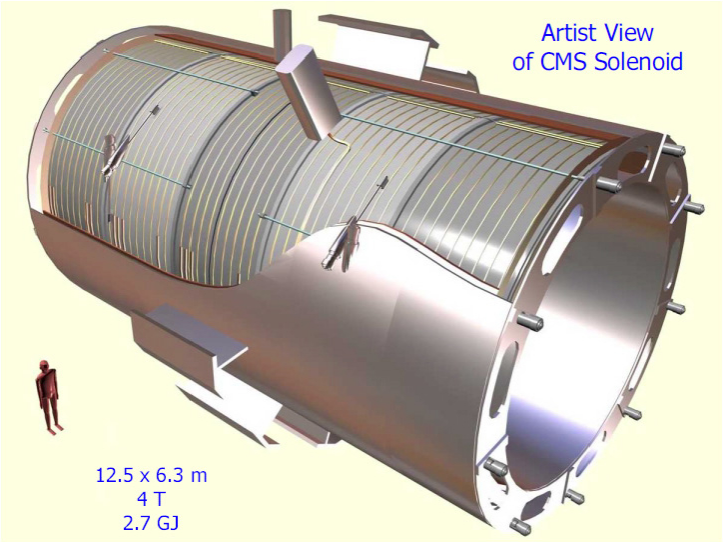

Figure 3.4: A schematic view of the CMS solenoid. Figure taken from [41].

measurement is the best in the areas where the magnetic field is sizable. This corresponds to the central pseudorapidity ranges $|\eta| < 2.5$, thus the most emphasis of the tracker design is on the central areas. The requirements of high granularity, fast readout and radiation hardness lead to a tracker design based entirely on silicon detectors technologies. The tracking detector consists of *pixel* and *strip* silicon modules and its overall structure is displayed in Fig. 3.5.

- The pixel detector is located at the closest distance to the proton-proton collision point. It is composed of three co-axial barrel layers (BPIX) 4.4 cm, 7.3 cm and 10.2 cm far from the beamline and two forward discs (FPIX) on positive and negative z sides at $\pm$34.5 cm and $\pm$46.5 cm. Altogether the detector consists of 66 million pixels each of a size 100×150 μm^2. A hit position resolution of 15-20 μm was reached [43]. As shown in Fig. 3.5, the pixel detector covers the rapidity range $|\eta| < 2.5$.

- A silicon strip detector composed of ten layers follows right after the pixel detector and reaches a distance of 130 cm far from the beamline. It consists of four inner barrel layers or Tracker Inner Barrel (TIB), two inner endcaps each containing 3 discs or Tracker Inner Disk (TID), six outer barrel layers or Tracker Outer Barrel (TOB) and two outer Tracker EndCaps (TEC). Each of the components has a specific design corresponding to it's position. The sensors in TIB and TOB are placed parallel to the beamline, and in TID and TEC they are perpendicular to the beam pipe. Overall the silicon tracker consists of 9.3 million strips.

With overall 200 m^2 of active silicon area CMS tracking detector became the largest silicon tracker ever built.

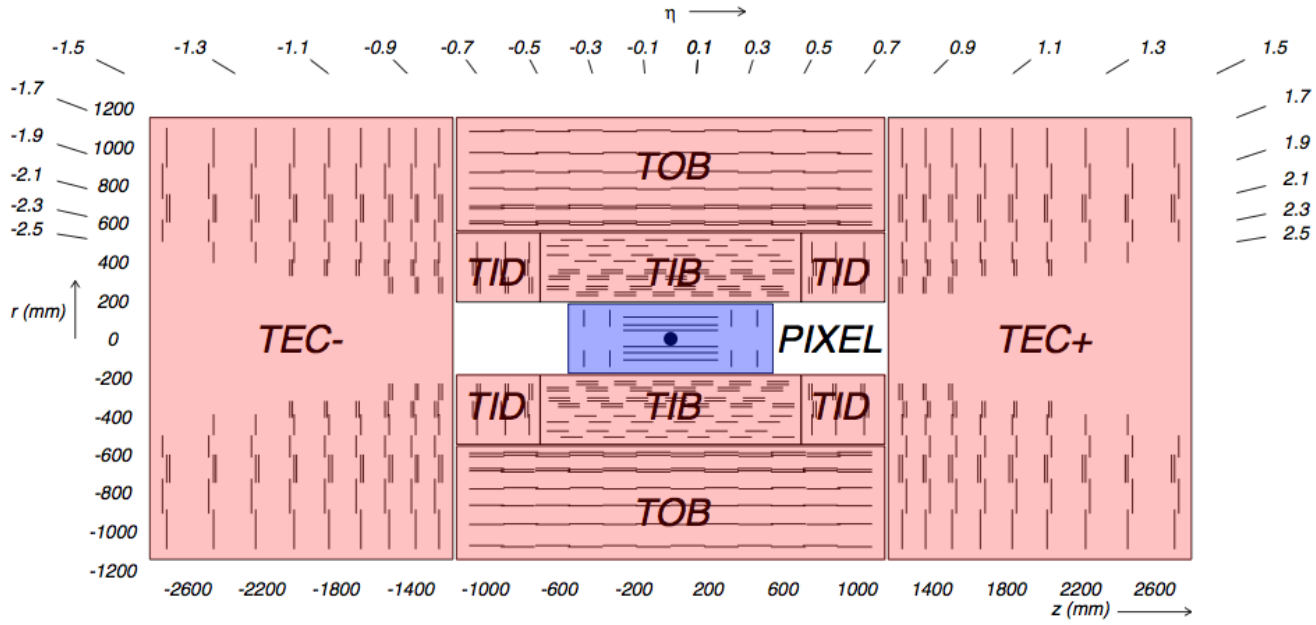

Figure 3.5: CMS tracking detector. The pixel part is marked with blue and the strip part with red. Figure taken from [44].

3.2.3 Electromagnetic Calorimeter

The Electromagnetic Calorimeter (ECAL) [38,45,46] is a detector component which comes next after the tracker on the way of particles from the collision point. The facility is assigned to measure the full electron and photon energies in all directions. A very special lead tungsten ($PbWO_4$) scintillating crystal was made to build up the ECAL. The crystalline is heavier than stainless steel but transparent. Each crystal weights 1.5 kg having a size from 22×22 mm^2 to 26×26 mm^2 with the length of 230 .

The ECAL is a homogeneous detector made up of the *barrel* part (EB) covering the range of $|\eta| < 1.479$ and two *endcaps* (EE) in the range ($1.479 < |\eta| < 3.0$) as shown in Fig. 3.6. For a high precision measurements of low momentum photons a *Preshower* is installed right before the endcaps.

The EB consists of 61200 crystals of lead tungsten joined in modules with 5 crystals in each. It is cylindrically surrounding the beam pipe starting at a distance of $r = 1.29$ m from it. The material is dense and thus reduces the particle's path allowing a smaller overall size of this detector component. Each crystal has a length of 230 mm, corresponding to $25.8X_0$[1]. To avoid the particles traveling through the cracks between the single submodules they are all tilted by 3° with respect to the direction to the nominal collision point. The lead tungsten scintillation decay time[2] is of the order of 25 ns, thus 80% of the light signals are emitted fast enough to fit into the bunch spacing designed for

[1]The radiation length in $PbWO_4$ is $X_0 = 0.86$ cm. It corresponds to the distance which an electron should pass in this specific material to reduce it's energy by a factor of $\frac{1}{e}$ and to $\frac{7}{9}$ of the mean free paths for a pair production by a photon.

[2]The scintillation decay time is the time required for scintillation emission to decrease to e^{-1} of its maximum.

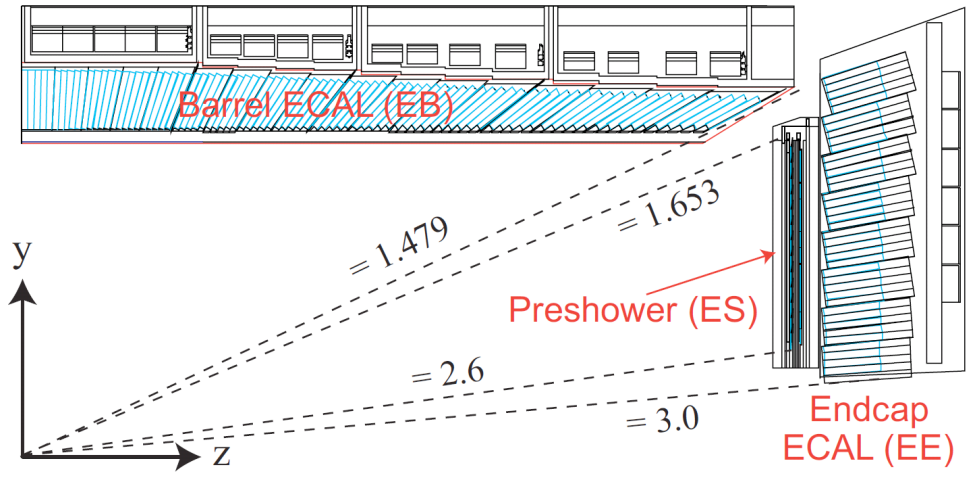

Figure 3.6: CMS electomagnetic calorimeter sketch. Different components and their pseudorapidity ranges are shown. Figure taken from [47].

the LHC. A special avalanche photomultiplier designed to work under the high magnetic fields is glued on the back side of each crystal to detect the scintillated light [48].

A Preshower forms a 20 cm thick disc which contains two layers of lead to form the showering each followed by a layer of silicon strips to detect the particles from the shower. A much finer granularity of the silicon strips (2 mm wide each) compared to the crystals in EB and EE allow a more accurate particle distinction.

The EE consists of two endcaps each being composed of 7324 lead tungsten crystals placed at $z = \pm 3.154$ m. As for the EB the modules at EE are slightly tilted but each crystal is a bit shorter compared to the barrel layer ($24.7X_0$). Vacuum phototriodes [48] were glued to the back side of the scintillating planes.

The energy resolution $\sigma(E)$ of the ECAL detector is given as [38]:

$$(\frac{\sigma}{E})^2 = (\frac{S}{\sqrt{E}})^2 + (\frac{N}{E})^2 + C^2, \tag{3.4}$$

where S is a stochastic term due to measurement fluctuations, N is a noise term due to electronics and pile up noise and C is a constant term due to systematic imperfections and from temperature instabilities. The ECAL energy resolution was primary determined on a test beam using electrons in the energy range from 20 GeV to 240 GeV [49] and the result was the following:

$$(\frac{\sigma}{E})^2 = (\frac{2.8\%}{\sqrt{E}})^2 + (\frac{12\%}{E})^2 + (0.3\%)^2, \tag{3.5}$$

where the variation terms correspond to the ones listed in 3.5 and E is the energy in GeV.

After a measurement of the ECAL characteristics with proton-proton collisions with a centre-of-mass energy $\sqrt{s}$ =7 TeV at the LHC in 2010 and 2011 it was found that for the 60 GeV electrons the energy resolution varies from 1.1% in the barrel to 5% in the forward regions [50].

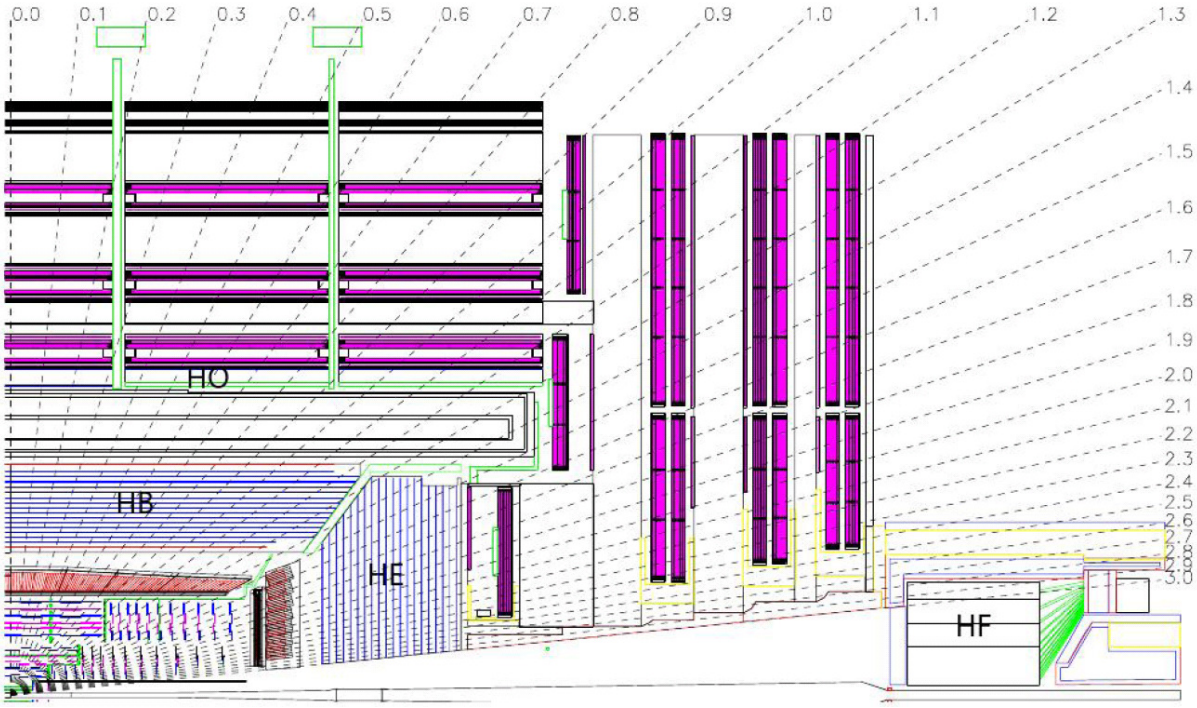

Figure 3.7: CMS hadron calorimeter sketch. Different components and their pseudorapidity ranges are shown. Figure taken from [51].

3.2.4 Hadron Calorimeter

The Hadron Calorimeter (HCAL) [38] at CMS follows the ECAL and aims to capture until full stop all the particles which entered it, except for the muons and the invisible neutrinos. As it is assumed that electrons are absorbed in the ECAL, the HCAL is primarily designed to measure the full energy of hadrons. Due to the hermiticity, the detector should identify all hadron decay products in a hard proton-proton collision. Thus any energy imbalance would point to the existence of non-interacting neutral particles such as neutrinos.

One of the main challenges of the hadronic calorimeter design was to fit it inside the compact solenoid (see sec.3.2.1). The solution was to put one of the parts of the detector component outside the magnet coil. Thus the HCAL consists of the barrel (HB), outer barrel (HO), endcap (HE) and forward (HF) parts. A schematic sketch of the hadron calorimeter is presented in Fig. 3.7.

The HB and HE are sampling calorimeters composed of brass and stainless steel plates (some of them made of Russian Navy brass shell casements in World War II) interleaved with scintillators. The HB covers the pseudorapidity range of $|\eta|$ <1.3. It contains 14 brass and 2 stainless steel absorbers, each from 50.4 mm to 56.6 mm thick. The HE covers more the forward region in pseudorapidity – 1.6< $|\eta|$ <3.0. It is composed of 18 layers of 79 mm thick brass plates. The scintillator plastic tiles are located after each absorber layer. The gaps between tiles are covered with reflective paint to prevent the light emitted inside one scintillator plate traveling outside as this light gives the energy estimate. Optic fibers fitted into specially cut grooves on top of scintillating tiles collect light signals and pass them to the readout boxes with hybrid photodiodes. The signals

collected from successive tiles, one behind the other, are optically added and form so called "towers". The towers are indicating the particle path in the calorimeter.

The HB and HE material thickness provides only $5.82\lambda_I$ [3] in the central region to $10.6\lambda_I$ in the more forward region. The ECAL material overall is equal to $1.1\lambda_I$. This is not enough to stop all the hadron showers[4] so the additional outer calorimeter HO was placed outside the solenoid. Using the solenoid and yoke material itself and adding also some own absorber plates, HO provides additional $11.6\lambda_I$ in the most central regions.

The forward calorimeter part HF starts at $z = \pm 11.6$ m and cover a pseudorapidity range $3.0 < |\eta| < 5.2$. It has a cylindrical shape with the inner radius r =12.5 cm and outer radius r =130.0 cm. The overall length of HF is 165 cm. It consists of absorbing steel grooved plates and quartz light emitting tubes placed in these grooves parallel to the beam pipe. As the HF faces not only hadronic but also the electromagnetic radiation it has to be sensitive to both. Thus half of the quartz tubes spread over the whole length of the HF (165 cm) and the other half (short quartz tubes) starts only at 22 cm from the front side of the HF. The long and the short quartz fibers have different readouts. Electromagnetic showers would start very early not reaching the short quartz tubes.

The energy resolution $\sigma(E)$ of the HCAL has been measured for 20-300 GeV pions. The result is the following [52]:

$$(\frac{\sigma}{E})^2 = \frac{115^2}{E} + 5.5^2, \tag{3.6}$$

where energy is taken in GeV.

3.2.5 Muon Detector

The Muon Detector [38] together with the solenoid are the detectors which were giving the name to the CMS detector. As muons pass through calorimeters materials without significant losses [53], the muon detection systems can be placed on the outer layers of the whole CMS apparatus. The unique signature of a muon in the event can be used for triggering. Muons appear in many processes of physical interest at CMS, like Higgs or heavy resonances decays.

The muon system stations are located outside the solenoid and in-between the return yoke plates. A muon track is fitted to the hits in each station and interpolated to the tracker. That is why the muon system and the central tracking detector have to be aligned with a precision of one sixth of a millimeter.

The muon detector consists of 1400 gaseous chambers of three types: 250 Drift Tubes (DT), located in barrel region of $|\eta|$ <1.2, 540 Cathode Strip Chambers (CSC) as endcaps covering the pseudorapidity of 0.9< $|\eta|$ <2.4 and 610 Resistive Plate Chambers (RPC) placed in both, barrel and endcap regions, and covering the range $|\eta|$ <1.6. A schematic view of the muon detecting system with its components is presented on Fig. 3.8.

The DT measures the muon position with a help of a system of 4 cm wide gas tubes filled with 15% of Argon and 85% of carbon dioxide. Each tube contains a stretched

[3] λ_I is *nuclear interaction length*, or the average length the particle has to travel inside the material before undergoing an inelastic nuclear interaction

[4] To fully contain a 1 TeV hadronic jet a thickness of roughly $11\lambda_I$ is needed.

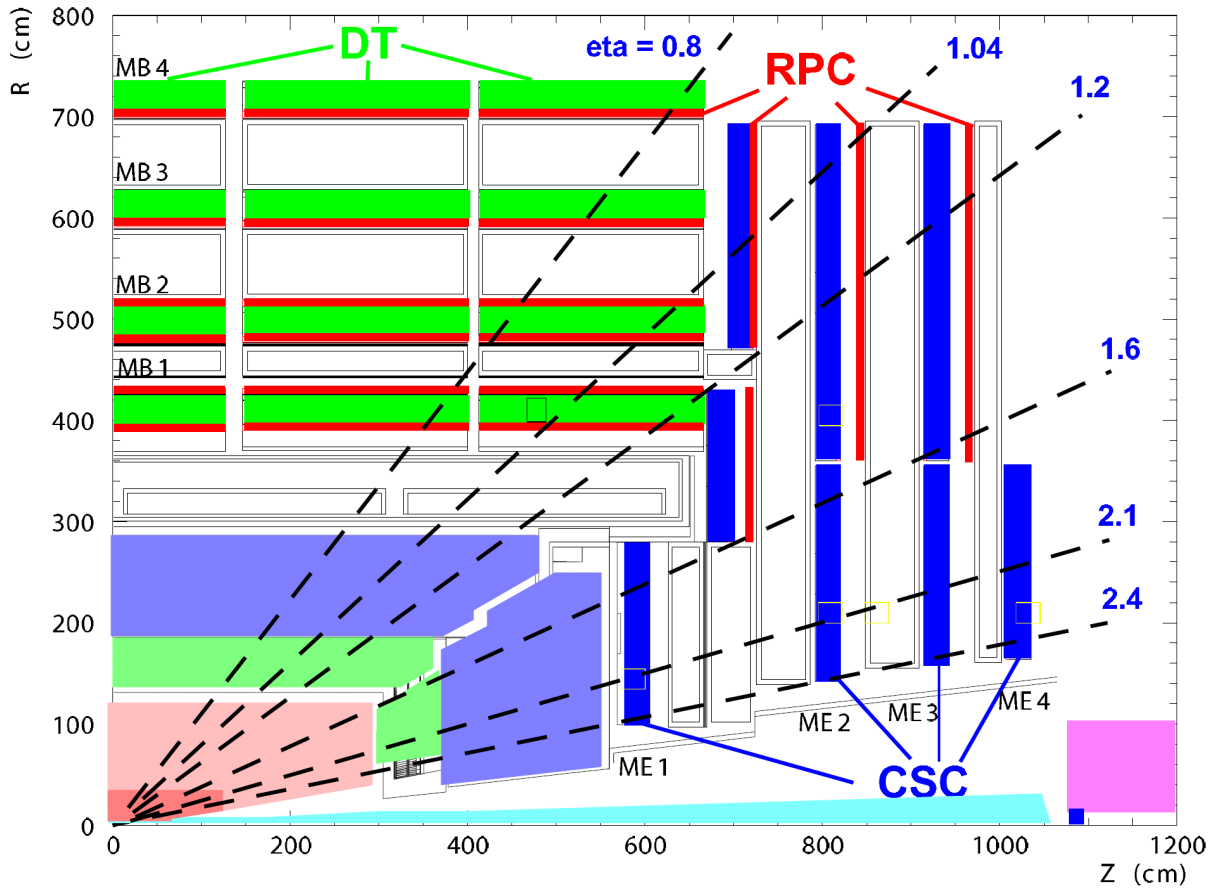

Figure 3.8: CMS muon detection system sketch. Different components and their position are shown. Figure taken from [38].

positively charged wire inside to collect the charge from the gas ionized by the muons. The DT has four layers divided into four stations (together with RPCs) each. The stations are aligned parallel to the beam line and measure the coordinates in (r, ϕ) plane. Three inner stations additionally provide the measurements in the z direction with four additional radial aligned DTs.

The CSCs disks are used in the endcap regions. Each of them is composed of seven copper cathode strip planes with six anode wire planes in-between, located in a gas volume. Wires and planes have perpendicular directions, thus providing two coordinates of the tracks.

The RPCs provide precise timing measurements and can tag from which bunch crossing the particle comes. This is used to trigger (see sec. 3.2.6) the events.

Muon momentum measurements from a combination of measurements in the muon system and the tracker reach relative resolution of 1% – 3% for muon p_T ranging from 20 GeV to 100 GeV.

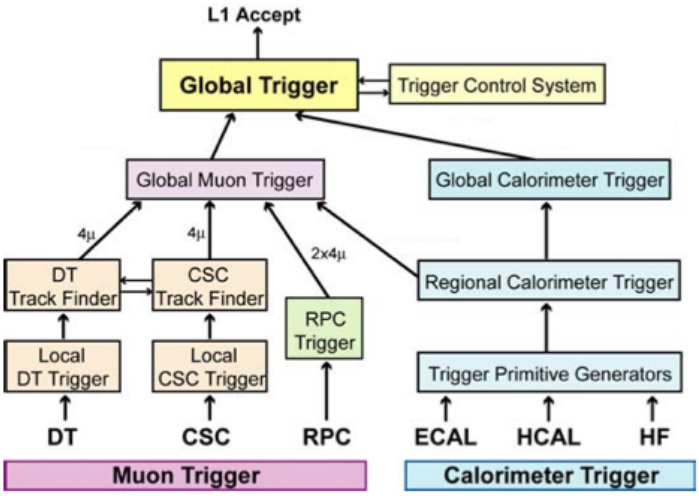

Figure 3.9: CMS Level 1 trigger architecture. The plot is taken from [38].

3.2.6 Triggers

The LHC provides proton-proton collisions every 25 ns, which means that particles from one bunch crossing still travel in the detector at the time when the next collision takes place. There is no way to store the huge amount of information from every collision, but even if it were, a greater part of the events would contain no traces of interesting physics. Most of the collisions are low energetic with no chance to produce heavy resonances or Higgs bosons.

Thus there is a need to filter the collisions and record only those which have interesting outcome products. This task is taken over by a trigger system [38]. Unlike the three-level trigger system commonly used by other collider experiments, CMS has decided to install a first and a high level trigger omitting the second one.

The *Level-1 trigger* (L1) consists of a custom designed programmable electronics, FPGA, ASICs and programmable look-up tables (LUTs). The trigger L1 is designed to reduce the nominal LHC collision rate of 40 MHz to 100 kHz. The data from different detector parts is stored synchronously in a pipeline with a time stamp corresponding to the bunch crossing it appeared from. The information from calorimeters and muon systems is taken to run a primitive and fast algorithms of particles and jets reconstruction. The information is subsequently collected, compared and is accepted if the trigger requirements are fulfilled. A more detailed L1 trigger architecture is shown in Fig. 3.9. The time of the L1 decision is 3.2 μs.

The *High Level Trigger* (HLT) is a software system represented by a filter farm with about a thousand commercial processors. The information from the L1 trigger is passed to the computers where it is processed in parallel. The amount of information and read-out speed define the requirements on the transfer network. Complex modern network switches solved these problems. HLT performs a mini-reconstruction of the objects detected, typically it takes events with leptons, muons and jets with minimum p_T and η requirement, but also some restrictions on global event characteristics, like the missing transverse energy $E^{miss}{}_T$ can be set. An event is written if it is accepted by at least one

HLT. If a trigger has a rather low threshold for some physical interest thus accepting too many events, it is being prescaled. This means that not all of the events that a trigger accepts are written, but only some fraction of them.

The total event rate reduction after L1 and HLT triggers perform is designed to be of a factor 10^6. Despite the trigger filtering the information which has to be recorded at the designed rate reaches 1 MByte per second, which is analysed with a high-performance computer infrastructure [54].

Chapter 4

Upgrade of the Pixel Tracker

The CMS detector as described in chapter 3 was performing during the time period between 2010 and 2012. It provided a center-of-mass energy up to 8 TeV and the bunch spacing was 50 ns. However, the LHC program was planned for at least a decade longer and the plan includes several improvements (see Fig. 4.1).

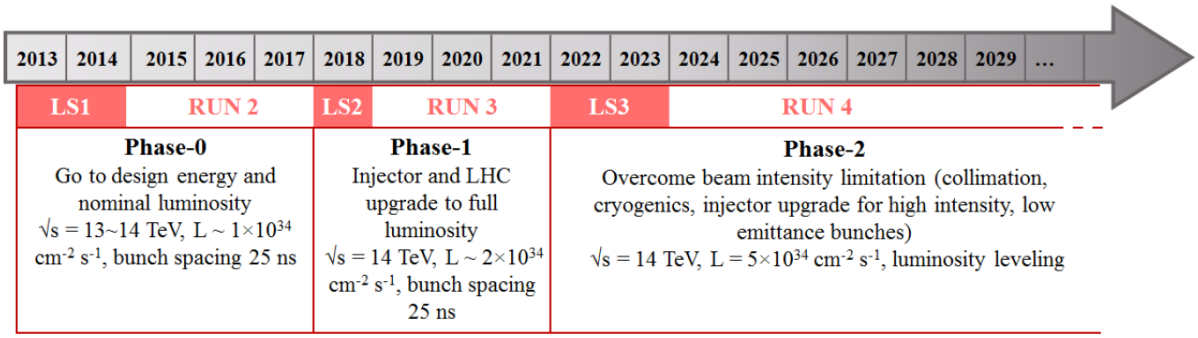

Figure 4.1: LHC upgrade program. The plot is taken from [55].

After the shutdown for two years, from the beginning of 2013 until the beginning of 2015, the LHC center-of-mass energy was increased up to 13 TeV and will be further increased to the designed value of 14 TeV. The next long shutdown is planned in 2018. Until that time it is planned that the peak luminosity will reach $10^{34}\text{cm}^{-2}\text{s}^{-1}$ (comparing to the $7 \cdot 10^{33}\text{cm}^{-2}\text{s}^{-1}$ reached in 2012). The total integrated luminosity which is planned to achieve prior the second long shutdown is 100 fb^{-1} [56]. This LHC phase is called *Phase 0*.

The plan after the second long shutdown (2018) is to increase the brightness of the bunches in the accelerators. This is planned to be done with improving the injectors. In the period after a second long shut down and until 2022 (so-called *Phase 1*) the LHC will reach a peak luminosity of $2 - 3 \cdot 10^{34}\text{cm}^{-2}\text{s}^{-1}$ and deliver about 300 fb^{-1} of data [57].

The third long shutdown in 2022-2023 will be used for the improvements of the LHC accelerating system by exchanging the aged parts by the new and improved ones (focusing magnets, cryogenics system, etc.). After these improvements, the LHC is expected to reach a peak luminosity of $2 - 3 \cdot 10^{34}\text{cm}^{-2}\text{s}^{-1}$. The period of LHC operation after the third long shut down is called *Phase 2* [57].

It is natural that the changes of the accelerator systems have to be reflected also in the detector construction. If the collisions with higher energies and frequencies are provided by the accelerator machine, the detector might be overloaded with information and some of its parts might be damaged by the higher radiation. That is why the CMS is also being upgraded simultaneously with the LHC.

The silicon pixel tracker (see the description in sec. 3.2.2) is the innermost part of the CMS detector mounted around the beam pipe and being the closest detector to the collision point. That means that it receives the highest irradiation dose and operates in a very dense particle environment. After the upgrade in 2015 the conditions for the pixel tracker will get even more severe. That is why it has to be significantly upgraded to perform with the sufficient precision.

This chapter describes the studies performed in frames of the fourth layer barrel pixel detector upgrade for the LHC Phase 1. It is mainly concentrated on the barrel pixel tracker, and specifically on the tests for the planned fourth layer of the latter.

4.1 Plan For the Upgrade of the Barrel Pixel Tracker

This section will give a brief overview of the plan for the whole CMS silicon pixel upgrade in frames of so-called Phase I upgrade. The purpose of this upgrade is to remake and update the present silicon pixel tracker to make it suitable for the high luminosity and energy runs which will start after the year 2018. The replacement of the silicon pixel tracker is planned for the technical stop in 2018.

The main goal for the updated pixel detector is that it should function at higher luminosities with the same or even better performance as the current pixel tracker on the lower luminosities [56]. For these needs new read-out chips (ROCs) have to be designed such that the data losses are minimized. In addition, the readout system as well as all the other detector components have to be radiation hard, as the expected doses which the detector has to meet (especially the first layer, which is the closest to the beam pipe) are much increased.

It was also decided to increase the number of barrel layers of the pixel detector from 3 to 4 (see Fig. 4.2). They were designed as four concentric cylinders with a length of 548.8 mm and radii between 30 mm and 160 mm. This improves the track identification, which is crucial in the environment with a twice higher pile-up, expected for the LHC run after 2018. In addition the innermost layer of the detector is moved closer to the collision point (by 10 mm), while the layers 2 and 3 are almost unchanged in the position. The beam pipe will also be made smaller to allow the closer approach to the interactions.

Each layer will constructed of 22 mm wide facets, in total consisting of 1184 rectangular pixel modules. Each module consists of 16 pixel chips. The total number of pixels will be increased from roughly 48 M to 79 M.

The addition of the fourth layer increases the amount of material which the particles have to go through. This is not the desired feature for the innermost detectors. So the volume of the material, which the detector is made of, has to be decreased. First of all, the readout system itself is planned to be thinner (it is easy to see in the Fig. 4.2, where the new pixel barrels are thinner). Secondly, the electronic boards will be moved out of

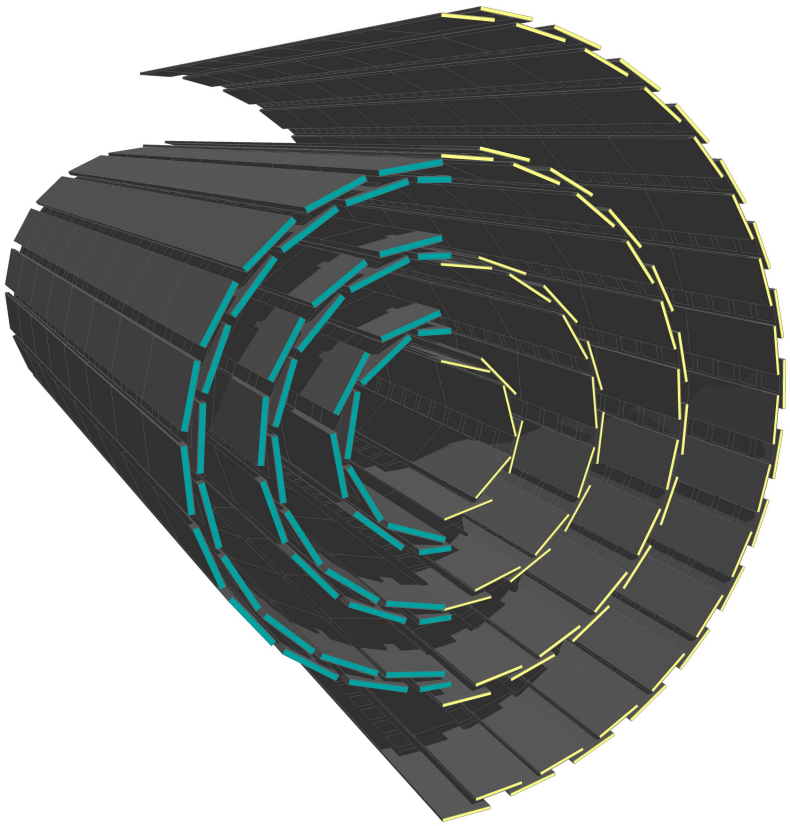

Figure 4.2: The model of the barrel pixel tracker before (on the left) and after the Phase 1 upgrade (on the right). Figure taken from [56].

the detector volume. Additionally, a new CO_2 cooling system [56] with a light-weight mechanical support will save material budget.

The planned improvements will lead to higher efficiencies, lower fake track rates (see sec. 6.1.1, track selection), lower read-out dead time, and extended lifetime of the detector. This results in a better identification of the particles for offline analysis and HLT.

The planned upgraded detector performance was simulated. It was compared to the performance of the non-upgraded tracker. This comparison is shown in Fig. 4.3. These simulations were performed on the simulated $t\bar{t}$ samples. The studies show overall higher efficiencies and lower fake rates for the upgrade detector for a higher pileup scenarios.

4.2 Studies of Irradiated Prototype Modules

The expected performance of the barrel pixel tracker was confirmed in the simulated experiments. However, it is also crucial to test the performance of the device under real conditions.

Prototype single chips were produced for the needs of such tests. These are chips of the design which was meant for the production of the real detector facility, but supplemented with a separate readout system and board to enable an independent operation of such a

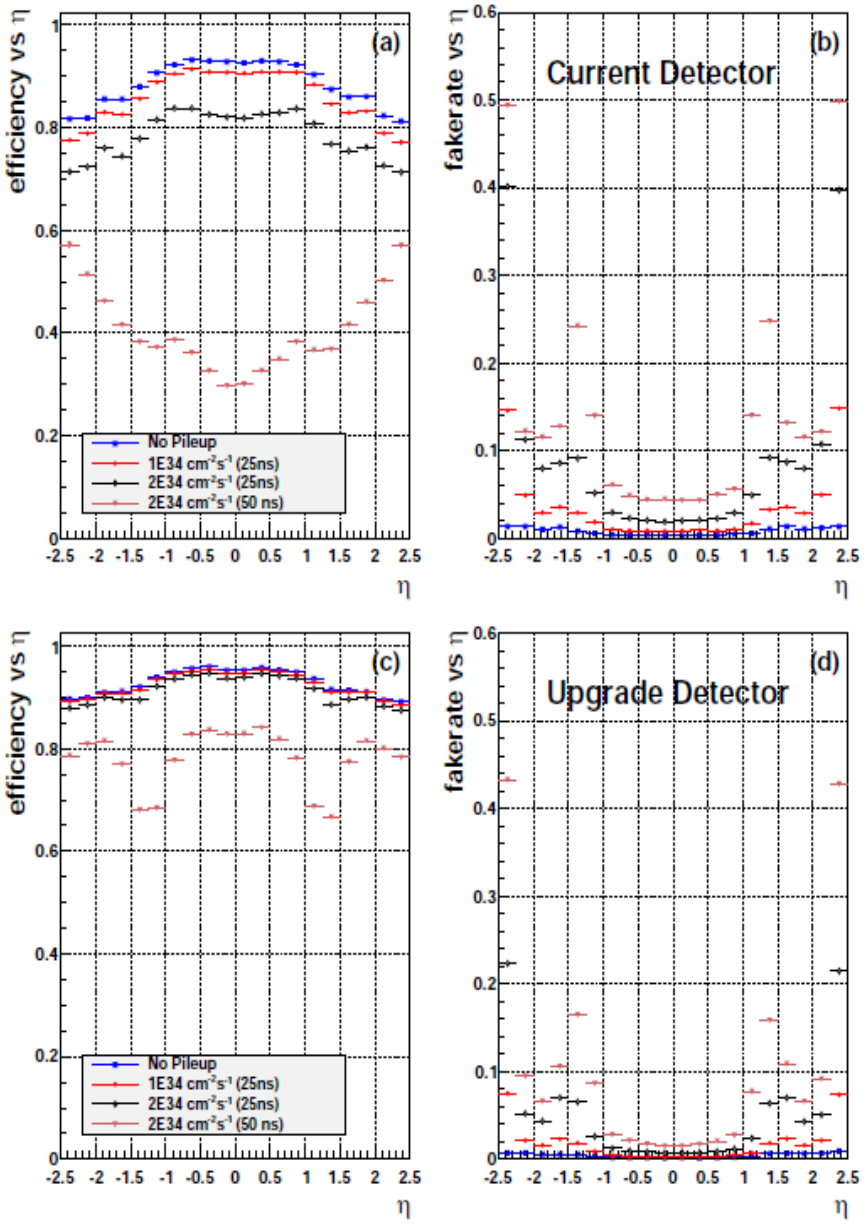

Figure 4.3: Tracking efficiency (a,c) and fake rate (b,d) for the simulated $t\bar{t}$ sample as a function of track pseudorapidity η, for the current detector (a,b) and the upgrade pixel detector (c,d). Results are shown for zero pileup (blue squares), an average pileup of 25 (red dots), an average pileup of 50 (black diamonds), and an average pileup of 100 (brown triangles). The ROC data losses were simulated as expected at each given luminosity. The plot is taken from [56].

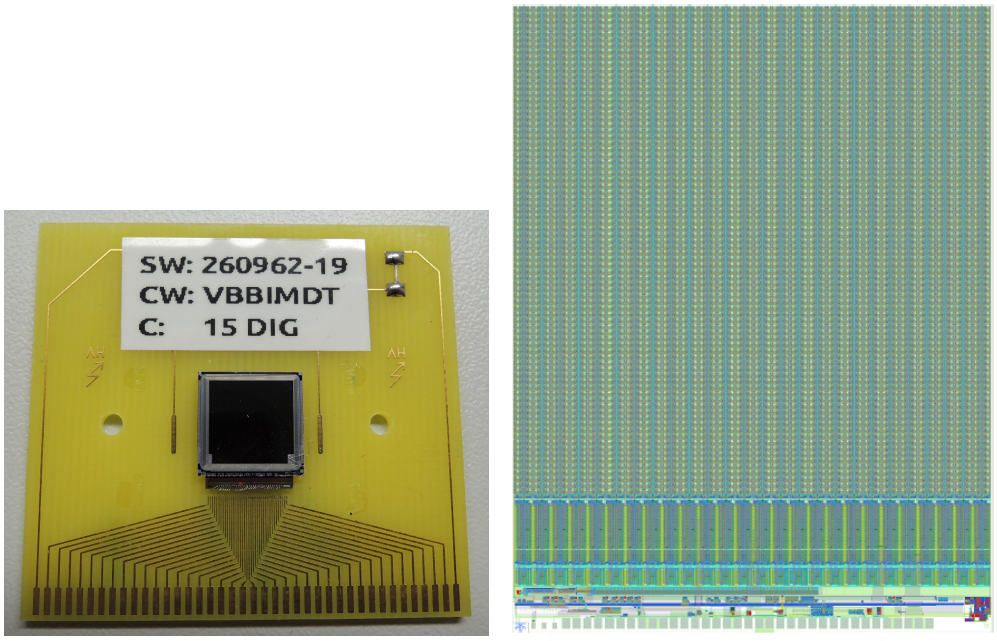

Figure 4.4: The photo of the prototype silicon pixel chip for the Phase I upgrade of the CMS BPIX, layer 4, mounted to the readout panel (on the left) and a magnified readout chip layout print (on the right).

chip.

In this work tests of the prototype chips for the fourth layer barrel pixel (BPIX) detector were performed. The layout of the prototype chip is shown in Fig. 4.4. The chip is a 1/16 part of the modules from which the pixel detector will consist. One prototype chip contains 80 rows and 52 columns of pixels, each of the size 100×150 μm^2. These pixels collect electrons from oxygenated high-resistivity n-type silicon sensors of 285 μm thickness with n+ implants.

Each pixel is bump-bonded to the ROC. The ROCs are fabricated in 250 nm CMOS (Complementary Metal-Oxide-Semiconductor) employing the radiation hard design rules. For the upgrade, the data buffer is increased to be able to work with higher occupancy connected with the higher data flow from the more frequent and dense LHC collisions. Furthermore the measured charges are digitalized and transmitted at 160 MHz. The effect of the internal cross talk is reduced by design optimization and use of the 6 metal layers for the circuit, which allowed to operate at lower thresholds.

One of the important tests was to examine the chips with new design with respect to their radiation hardness. As discussed before the pixel detector will receive the maximum dose of the radiation being the closest detector part to the collision point (see Fig. 4.5). It is expected that the dose absorbed by the layer 1 of BPIX during the full lifetime of the detector will be 100 MRad, or 1 MGy. Layer 2 is expected to absorb 40 MRad (0.4 MGy), layer 3 – 20 MRad (0.2 MGy) and layer 4 – 13 MRad (0.13 MGy).

For the studies of the properties of the irradiated prototype chips for layer 4 of BPIX, the prototype chips were irradiated at the CERN PS [58] with the 23 GeV protons up to fluences of $3.8 \cdot 10^{14}$ p/cm^2. This corresponds to the expected lifetime dose of the layer

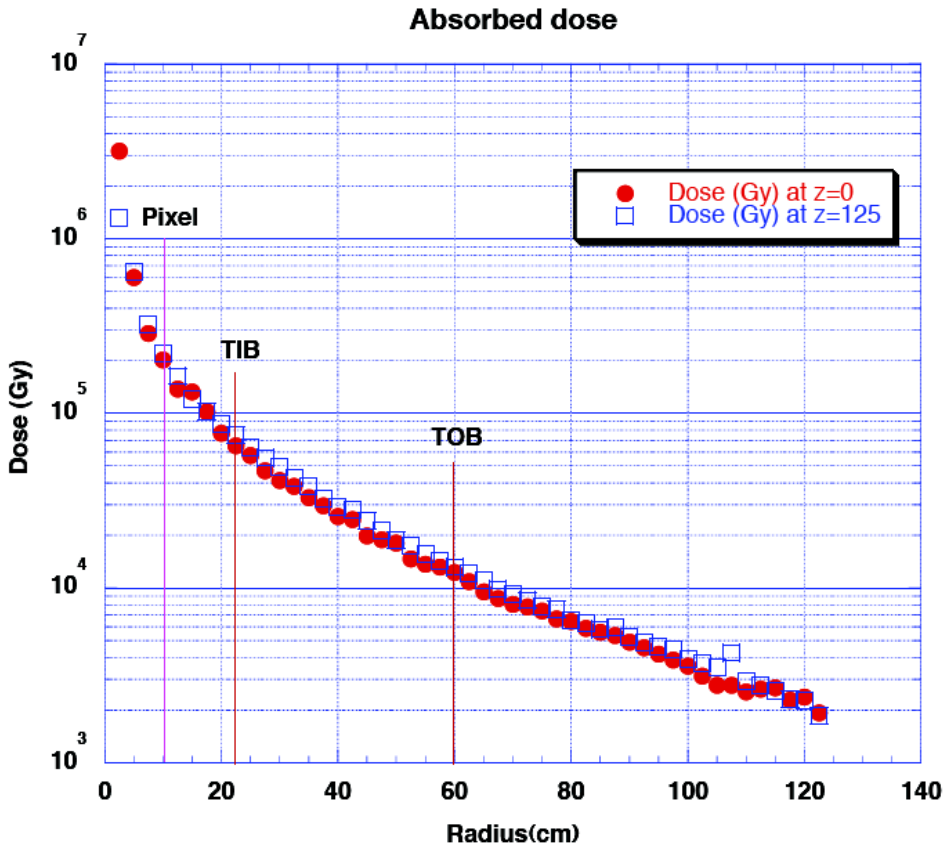

Figure 4.5: The dose in Gy to be absorbed by different tracker parts at different radial distance from the LHC pp beam line for different z coordinate values. The average position of the pixel detector is marked with a red vertical line. The location of different parts of the silicon strip detector are also shown for comparison. The dose is defined for the expected full run time of the LHC until 2018, which corresponds to an integrated luminosity of 500 fb^{-1}. The plot is taken from [56].

4 of the BPIX (approximately 16 MRad).

The prototype chips were irradiated such that the silicon sensor side was facing the beam. The readout chips on the back side received a dose up to 130 kGy. The tests in the laboratory at DESY [59] showed the full functionality of the irradiated ROCs.

4.2.1 DESY Beam Test

To test the functionality of the prototype silicon pixel chip, one needs to deliver some particles with relatively high energy and let the chip register them. For this purpose so called "beam tests" are performed. For the studies described in this thesis, the DESY beam test facility was exploited.

The DESY beam test facility makes use of the electron-positron synchrotron DESY II [60, 61], which provides electron and positron beams with up to 1000 particles per cm^2 at energies of up to 6 GeV. However, these are not the particles which are directed to

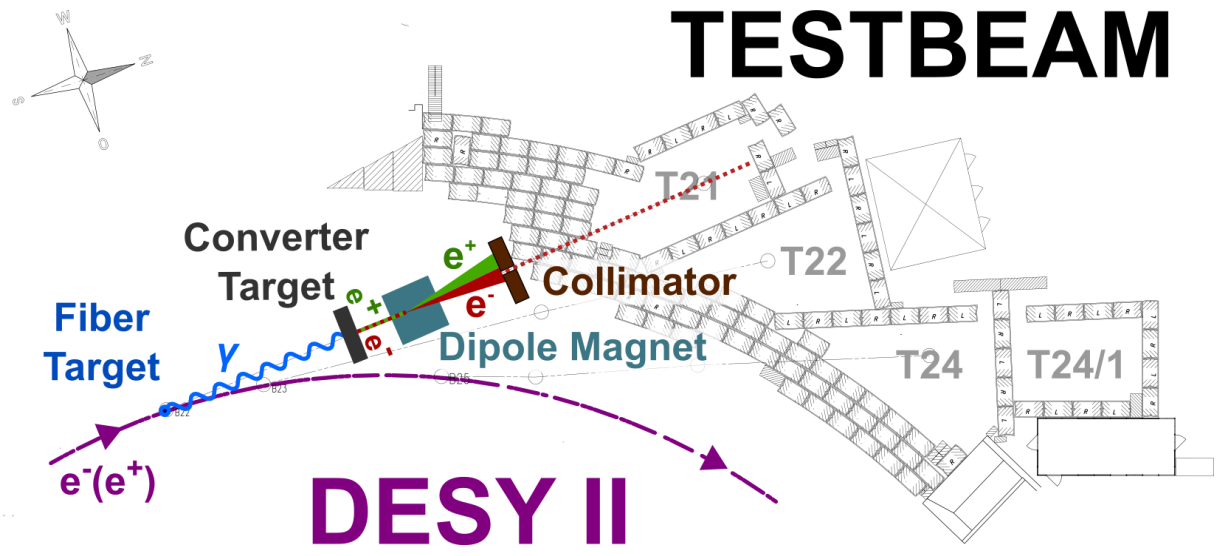

Figure 4.6: Schematic layout of the test beam facility at DESY. The plot is taken from [62].

the beam test areas. The circulating DESY II beam hits the 25μm thick carbon fiber and emits bremsstrahlung. The resulting photons are afterwards converted to electron-positron pairs on the converter, which is actually a copper plane. The resulting beam is passed to a dipole magnet for separating the particles with the required momentum. Afterwards the beam is collimated and brought to the area where it can be exploited for the experimental needs. The scheme of the facility which delivers the beam for the tests is shown in Fig. 4.6.

4.2.2 EUDET Telescope and Experimental Setup

For the beam test studies described in the following a telescope of the EUDET/AIDA-family [63] (see Fig. 4.7) was exploited. It consists of two arms each equipped with three sensor planes kept at a stable temperature by a cooling system. Each sensor plate can be moved along the beam axis to meet some particular experimental requirements.

The telescope serves as a device which measures the particle path with a very good precision so that it is assumed to be known. The EUDET telescope is equipped with silicon pixels. The telescope sensors have a track position resolution of 4.3 μm and they are made with a minimum of material (their thickness is only 50 μm), so that the precision doesn't drop even on the lowest energy border of the test beam ($\sim$ 1 GeV), when the contribution of the interaction of the particles with matter becomes sizable.

The installed Mimosa (Minimum Ionizing MOS Active Pixel Sensor) sensors (with a size of 21×11 mm^2 with squared pixels with a size of 18.4 μm) developed for the EUDET telescope make use of the MAPS (Monolitic Active Pixel Sensors) technology [64, 65].

The prototype silicon pixel chip for the BPIX upgrade was placed in between two arms of the telescope. In the beam test campaign the tested device (in case of these studies it's the prototype chip) is called a Device-Under-Test (DUT). The DUT and it's board are placed in a special frame which allows tilting and turning (see Fig. 4.8). This enables studies of the detector behavior with inclined particle tracks producing multi-pixel

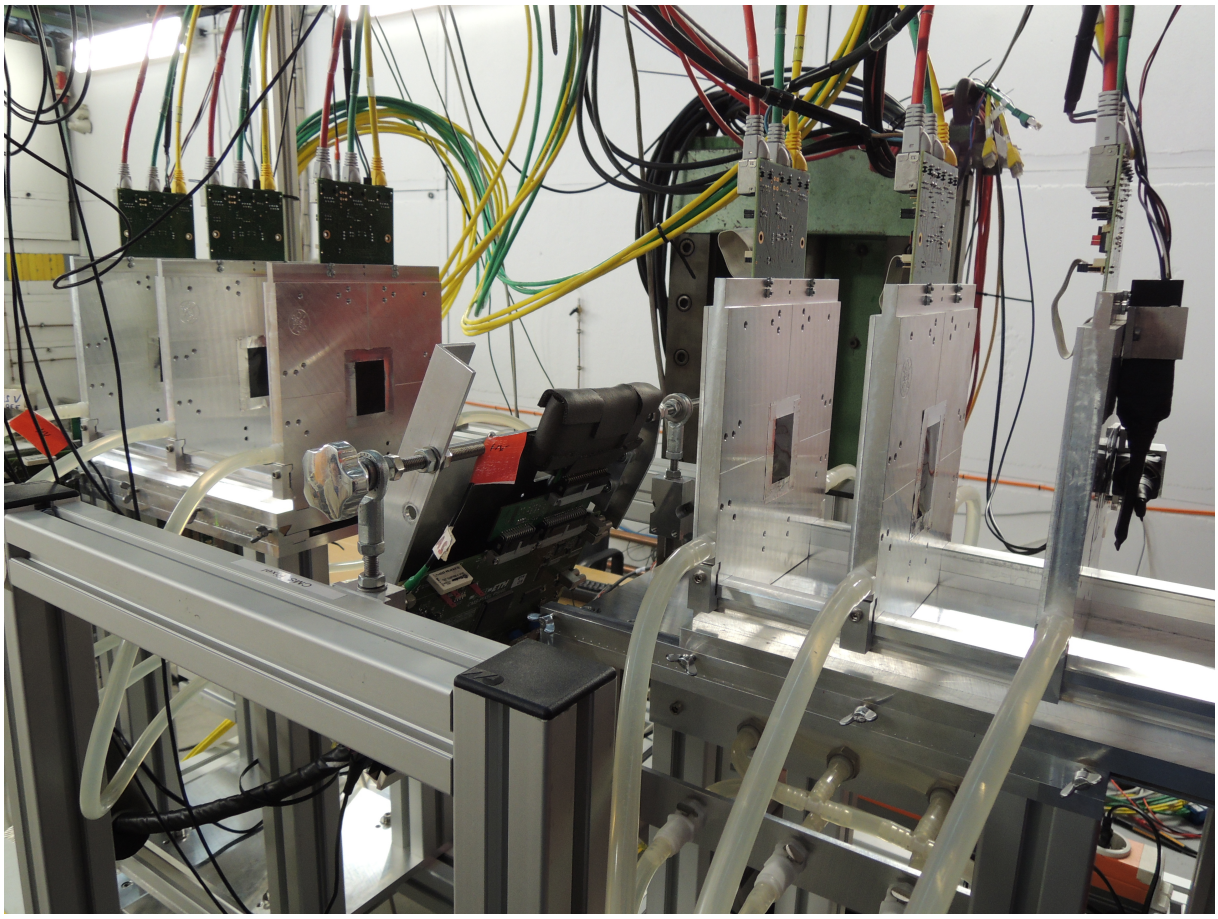

Figure 4.7: Photo of the EUDET telescope present at the beam test line 21 at DESY. The device under test is installed in between the two groups consisting of three telescope plates each. The electron/positron beam impinges perpendicularly onto the EUDET telescope planes coming in from the right side of this photo.

clusters.

There is a second CMS prototype chip placed downstream at the end of the beam telescope. It had to serve as a reference for the measurement of the DUT efficiency, as it has the same time of the working cycle as the DUT (25 ns). The Mimosa has a much longer cycle (115 μs) and it can't be used as a reference for the DUT.

On the front before and right after the telescope two crossed scintillators are located. They serve as a trigger. If their signals coincide, the particle has passed all the way through the telescope. The typical duration of one run when the telescope, DUT and reference chip were registering the test beam particles, was from 10 to 30 minutes having several hundred thousand trigger signals.

4.2.3 Data Taking

The data from the telescope was passed to the computer through network cables (see Fig. 4.7) and from the CMS prototype chips – through USB cables. These are the signals

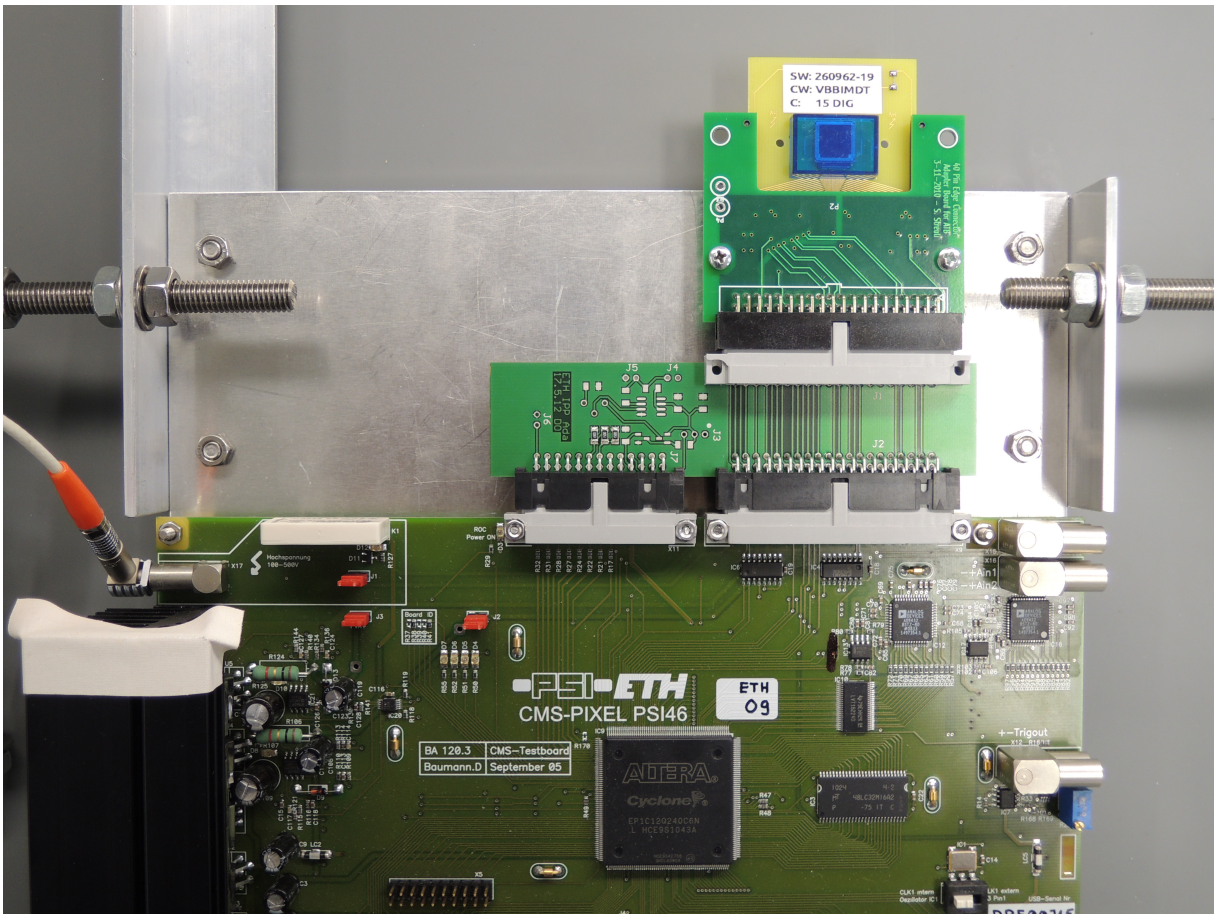

Figure 4.8: Photo of the DUT (prototype silicon pixel chip for the BPIX 4^{th} layer upgrade) and it's board in the metal frame mounted between two arms of the EUDET telescope at the DESY beam test area.

which inform about the particles hitting the detector plane. Afterwards the received data had to be preanalysed.

To gain accurate knowledge of the geometry of the setup, alignment procedure was done with the Millipede algorithm [66].

The neighboring fired pixels on the pixel detector are grouped into clusters and the centers of the clusters are the hits. The tracks were reconstructed from the hits using the general broken lines algorithm [67]. It takes into account the multiple scattering in the detector planes.

To define the telescope resolution, first the particle track was reconstructed using the hits in the first and third telescope planes. Then the second plane was used to determine the difference between the reconstructed particle track position and the actual hit in the second telescope plane.

This basic information from the telescope and from the prototype chips is used for the further analysis.

4.2.4 Analyzing the Prototype Chip Properties

Several crucial properties which are important for the future BPIX detector operation were measured during the DESY test beam campaign.

Charge Collection

The external bias voltage is needed to collect all the charge which was released due to the particle crossing the silicon bulk of the detector. If the bias voltage is not high enough, not all the charge is collected. The voltage at which the full charge starts to be collected is called *depletion voltage*. The negative bias voltage is applied on the *p*-implant side. A schematic path of the ionizing particle through the silicon sensor and of the resulting charge collection is shown in 4.9.

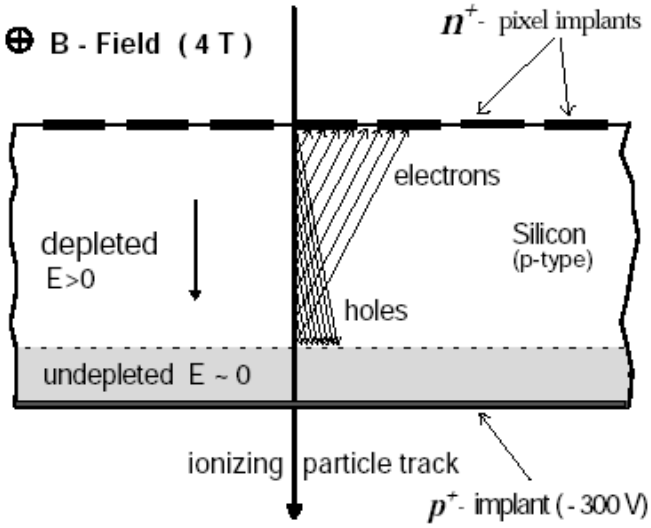

Figure 4.9: The sketch of the charge collection from the ionizing particle crossing the silicon sensor. The figure is taken from [68].

After the irradiation damages in the silicon material are introduced. These damages may trap the ionized charge which is traveling through the silicon bulk to the place where it is read off. That is why a higher voltage is needed so that the particles overcome the traps. However, there is a practical power dissipation related with the ohmic heating and on the bias voltage supply. If the depletion voltage is higher than the voltage allowed by these limitations, the full depletion conditions for the sensors can never be reached. That is why it is necessary to test if the full depletion region can be reached and if so, then at which bias voltage.

To study this problem, the external bias voltage was varied from the very low values up to few hundred volts. The collected charge was measured for each value of supplied bias voltage.

Fig. 4.10 shows the collected pixel cluster charge normalized to the maximum charge collected and tracking efficiency, which was defined as the number of tracks which were

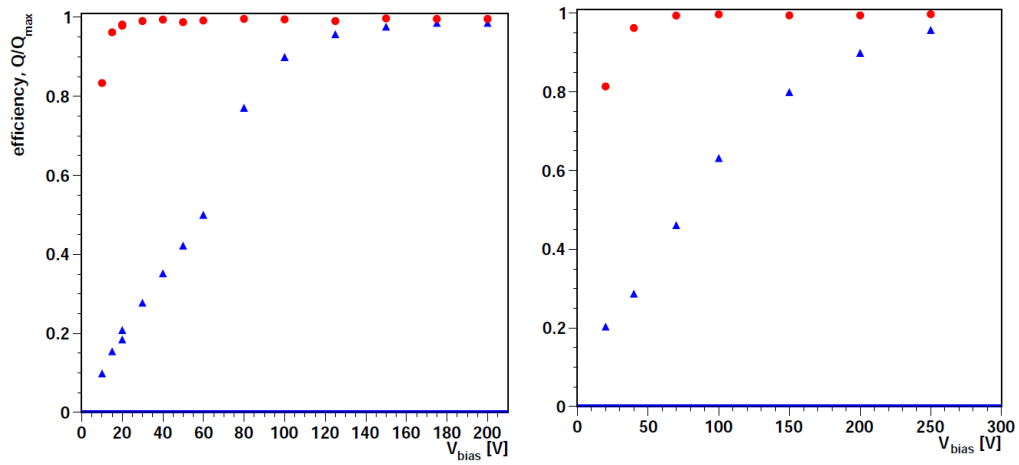

Figure 4.10: Charge collection efficiency, normalized to the maximum cluster charge (triangles) and tracking efficiency (circles) of the prototype silicon sensor for the CMS pixel tracker irradiated with $0.9 \cdot 10^{14}$ p/cm^2 (left) and $3.8 \cdot 10^{14}$ p/cm^2 (right) as function of the applied bias voltage.

registered in telescope, reference and DUT chips over the number of tracks registered in telescope and reference chip. These quantities are shown for two chips which were irradiated with doses of $0.9 \cdot 10^{14}$ p/cm^2 and $3.8 \cdot 10^{14}$ p/cm^2.

For the prototype chip which was irradiated with $0.9 \cdot 10^{14}$ p/cm^2, the collected charge drops quickly for bias voltages below -110 V. Only about one third of the charge is collected with a bias voltage lower than -30 V. However, the tracking efficiency still remains higher than 90%. This means, that the detector is fully efficient in terms of tracking with only one third of the charge collected.

For the chip with higher dose of $3.8 \cdot 10^{14}$ p/cm^2 full depletion is reached only with -250 V. The full tracking efficiency is reached at -70 V, where around half of the charge was collected.

Additionally, the absolute pixel cluster charge distribution for the chip irradiated with a dose of $3.8 \cdot 10^{14}$ p/cm^2 was measured with the -250 V bias voltage supplied (see Fig. 4.11). It has an expected Landau shape, peaking at 18 ke. Before the irradiation a similar test was performed for this chip and Landau peak was at 22 ke then. This means that there is a charge loss due to trapping in the silicon bulk after the irradiation.

Position Resolution

The accuracy of the measurement of the position where the particle hit the silicon detector is primarily limited by the size of the silicon pixels. However there is the way to improve the resolution using the charge sharing technique. If the charge from one particle will be collected in more than one pixel, the position of the particle will be defined as the weighted average position of these pixels (the weighting is done corresponding to the amount of charge collected by each pixel). The charge sharing may happen either due to the inclined particle tracks with respect to the silicon sensor plane or because of the Lorentz drift in the magnetic field.

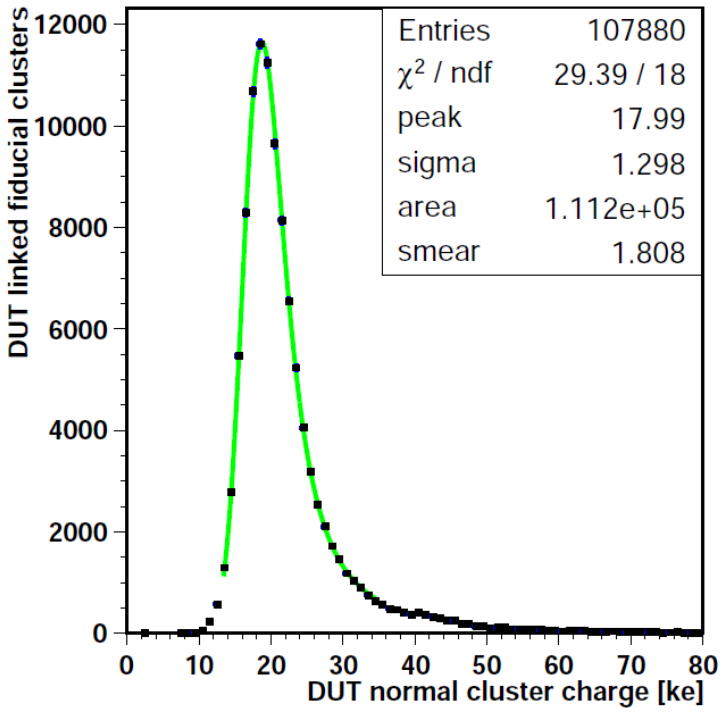

Figure 4.11: Cluster charge distribution measured in the electron beam for a 285 μm thick pixel sensor irradiated with $3.8 \cdot 10^{14}$ p/cm^2 at a bias voltage of -250 V (plateau region).

The particles from the DESY test beam were flying only in one direction. For the resolution improvement, the silicon chips were tilted by a certain angle with respect to the particle path to make the particles cross more than one pixel. This aims at obtaining an optimal charge sharing.

As discussed before, the irradiation introduces defects in the silicon which trap the charge carriers. This may influence the charge sharing and thus the position resolution of the detector. It is also necessary to have the full charge collection to correctly measure the particle position. Thus, the optimal bias voltage has to be delivered.

The resolution at the beam test was defined as the difference between the position of the particle hit defined by the DUT chip and the position of the track defined in the telescope and extrapolated to the DUT. The telescope resolution (around 4.3 μm at 5 GeV beam energy and 150 mm spacing between the telescope plane) is being quadratically subtracted.

To define the optimal tilt angle in the direction of the pixel rows of prototype chip, the DUT was tilted several times at different angles and the pixel row resolution[1] was measured. Fig. 4.12 shows the result of these studies for the prototype chip irradiated with a dose of $3.8 \cdot 10^{14}$ p/cm^2. As expected, first the resolution is getting better with increasing the tilt angle because the particle starts to pass through multiple pixels on it's way and the charge is shared between those pixels. After a certain optimal tilt angle, however,

[1]The *row resolution* of the silicon pixel chip is the resolution of the coordinate in the pixel row direction. This is the direction which an object would have if it would move from one row to the other staying inside one column.

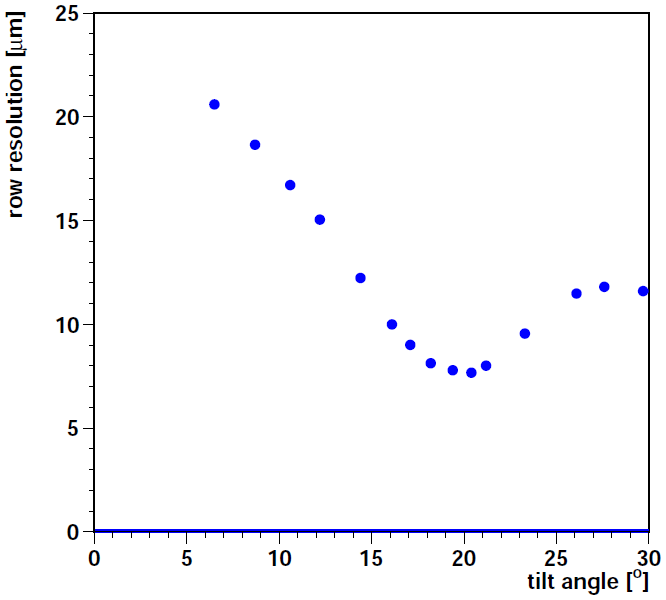

Figure 4.12: Resolution as a function of the tilt angle for a prototype silicon pixel module irradiated with $3.8 \cdot 10^{14}$ p/cm^2. The bias voltage was set to -200 V and the threshold to 1.8 ke.

the resolution starts to get worse again. This is explained with a fact that the particle ionizes too many pixels initiating a very low charge in some of them. This charge doesn't overcome the threshold[2] level of a pixel and is lost. The plot shows that the minimum resolution is reached at the angle of around 20^o. Geometrically, the optimal charge sharing is expected at 19.3^o tilt angle for 100 μm pixels and 285 μm sensor thickness. The higher angle which is practically measured may be explained by the trapping of deep charges. This means that the charges created in a silicon sensor by an ionizing particle trap on the defects starting from some depth of the sensor. Effectively it results in the reduction of the sensitive thickness of the sensor, thus the tilt angle for an optimal charge sharing increases.

For each point in Fig. 4.12 the resolution in pixel row direction was determined as illustrated in Fig. 4.13 using the width of the fitted gaussian. The plot shown is derived with the DUT tilted at 19^o.

The position resolution in the row direction was also measured for different bias voltages supplied. The result is presented in Fig. 4.14. It shows that reducing the bias voltage below 150 V leads to a resolution degradation.

4.2.5 Summary

The prototype chips for the layer 4 of silicon pixel tracker for the CMS Phase 1 upgrade were operating after absorbing doses in order of and much higher than expected to be absorbed during the detector operation time. The damage effects caused by irradiation are observed. However, the chips are fully operable and produce reasonable results. The

[2] A threshold on the charge collected is set on every pixel to avoid noise collection

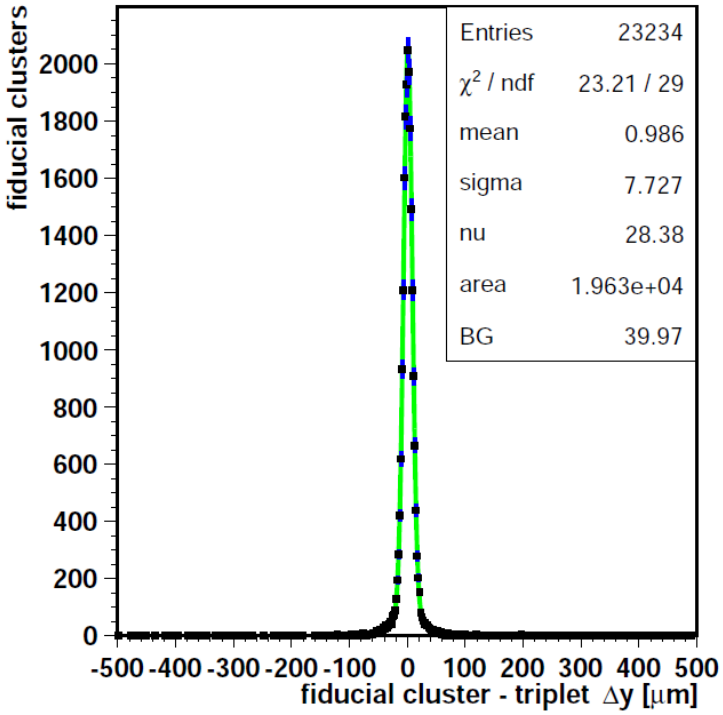

Figure 4.13: Residual between DUT cluster position and telescope track in the direction of the 100 μm pixel size at a bias voltage of -320 V. The sensor was tilted by an angle of 19^o to the beam direction. The charge threshold was set to 1.8 ke. The fluence is $3.8 \cdot 10^{14}$ p/cm^2.

resolution only slightly degrades – the irradiated prototype has the resolution of 6.4 μm in row direction, while before the irradiation this value was 5.5 μm. The full depletion after is reached at 150 V after the irradiation.

In summary the tests of the prototype chips indicate that these types of chips meet the demands for operation after Phase I upgrade.

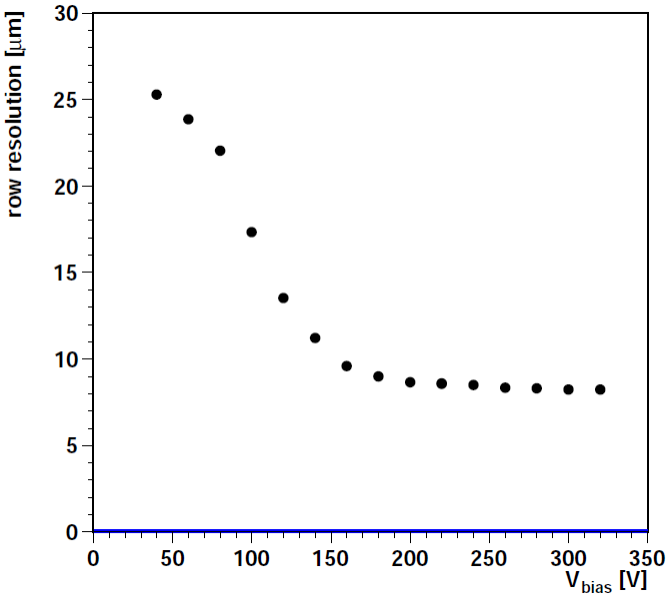

Figure 4.14: Resolution as a function of the applied bias voltage without subtracting the telescope contribution, for a prototype silicon pixel module irradiated with $3.8 \cdot 10^{14}$ p/cm^2.

Chapter 5

Monte Carlo Simulation

To analyze the data from a large particle physics experiment, the modeling of the events and of the detector plays an essential role. The processes of pp interaction and particle production are usually too complicated to be described in every aspect analytically. The same applies to the interactions within the detector volume. However, these tasks can be solved with the help of Monte Carlo (MC) simulation programs. These programs can be used to predict the signal and background processes event yields and to simulate the detector response including efficiency and smearing effects.

In this analysis it is needed to simulate the whole process $pp \to t\bar{t} \to \bar{l}\nu b l\bar{\nu}\bar{b}$, including the subsequent reaction steps (see Fig. 5.1). First the hard scattering has to be simulated to describe the collision and production of partons. Then parton showering tools have to be applied to describe the electromagnetic and QCD radiation of the initial and the final step particles. In the end of the process all the radiation finishes with forming the hadrons. There is also a possibility of interaction with the proton remnants. This interaction is described with the underlying event process.

There exists a number of general-purpose Monte Carlo (GPMC) generators (HERWIG [69], Pythia 6 [70], SHERPA [71]), which provide a full simulation of high-energy collisions. They consist of several components, which describe the process on all the interaction scales, starting from the perturbative QCD on the very small distances up to the QCD-inspired models on the distance scales of hadron formation and decay.

To finalize the analysis modeling, after simulating the particle production and decay processes, it is necessary to "push" the products of this simulation through a model detector. The model detector simulates the interaction of particles with the detector materials and the detector response including noise. Such a detector model can be also used to predict the performance of future facilities.

This chapter gives a brief overview of the processes which were simulated for this analysis and tools used for the simulation.

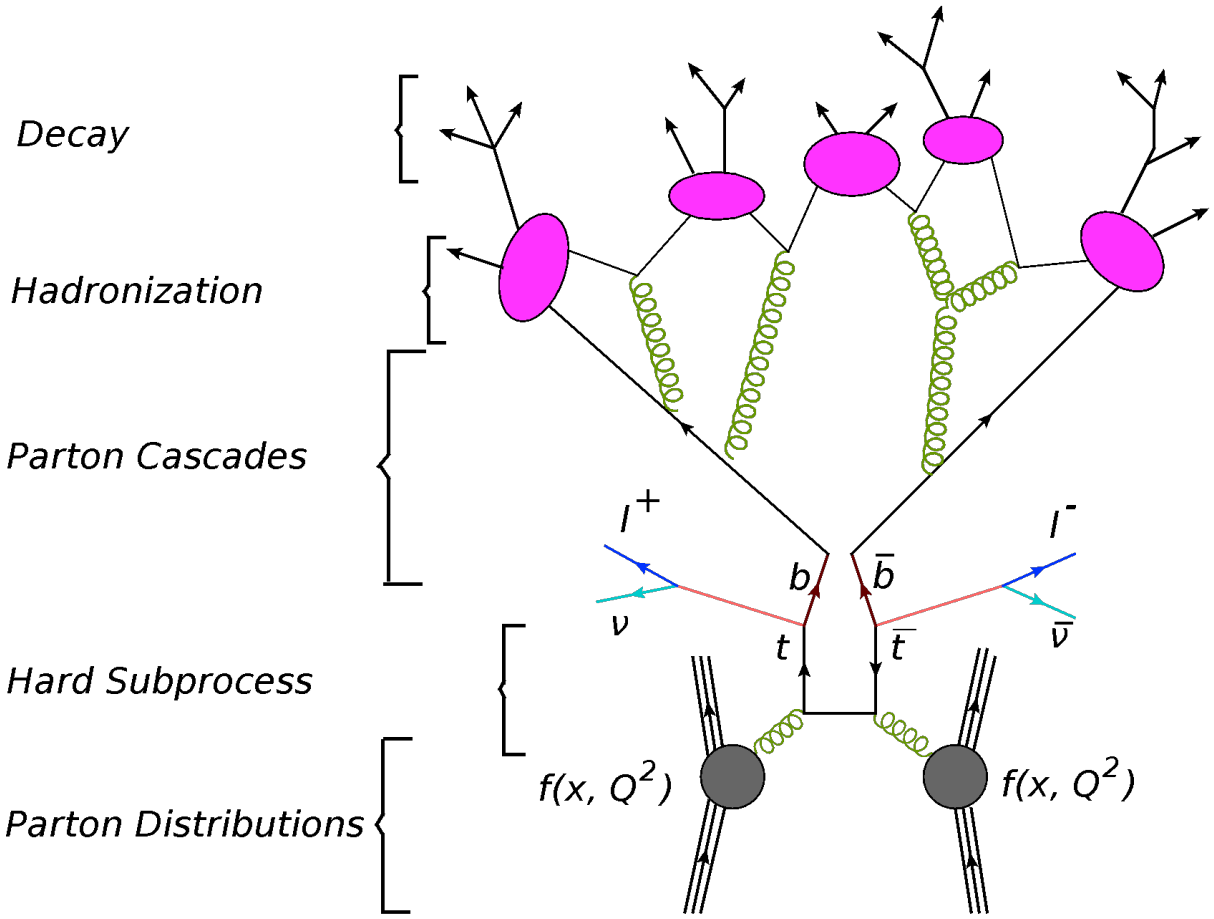

Figure 5.1: $pp \to t\bar{t}X$ collision sketch showing all the subprocesses.

5.1 Different Monte Carlo Models and Generators

5.1.1 Hard Scattering Models

The *hard scattering* describes the interaction of partons which emerge out of the proton (in the case of this analysis – two gluons or a quark-antiquark pair) and take part in the production process which is being studied. The initial momenta of partons are to be chosen according to the used PDFs (see sec. 2.4.1).

The $t\bar{t}$ pair production is taking place in the high energy regime, so that $\alpha_s \ll 1$ (see sec. 2.3.2). This allows to perturbatively calculate the process in different orders of α_s: the higher the order used for the calculations, the more precise the calculation should be. The calculation to different orders of α_s corresponds to specific processes as represented by Feynman diagrams in Fig.5.2. However, there are many subtleties with calculating higher orders, that is why the MC generators are usually limited to LO or NLO calculations.

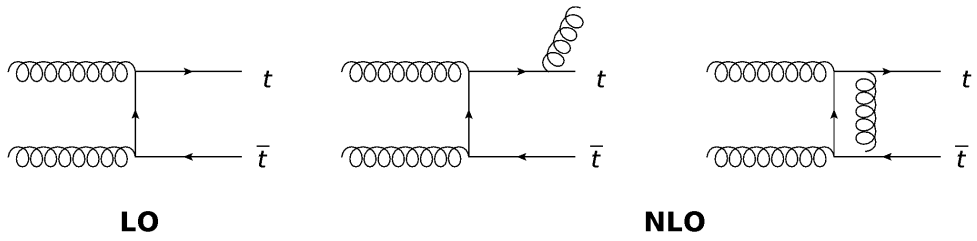

Figure 5.2: Examples of $t\bar{t}$ production diagrams showing leading order and next-to-leading order processes.

5.1.2 Parton Showering

The hard scattering models are usually restricted to a fixed order of perturbation theory. This is not sufficient to describe the whole picture of the event. That is why special *parton showering* techniques were developed to simulate higher order effects. It describes the radiation of the colored objects from initial and final state partons, following the momentum transfer from the higher interaction scales down to the lowest scales of confinement (hadronization) – to the order of 1 GeV.

- **The final state radiation** is described by sequential splitting of the colored objects with energy decreasing after each splitting. This process is repeated until some evolution criterion is reached. Such criteria may be connected with the energy fraction of a radiated object or with the opening angle between the parent and emitted colored object.

- **The initial state radiation** is produced in the similar way to the final state radiation, but inverting the process such that the colored objects out of the shower collapse back to the initial partons out of the protons.

If the parton shower is simply added to the hard scattering, the same process can be modeled twice. Some radiation may be already taken to account in the hard interaction but it is still produced in the parton showering. The problem is treated by employing matching mechanisms [72].

5.1.3 Hadronization Models

In context of the MC generators, the *hadronization* is the process by which a set of colored objects (after showering) is transformed into color-singlet particles, hadrons, which can further decay into other hadrons. This transition is non-perturbative with the scale Q_{had} (with $\alpha_s \sim 1$), which is identical to the shower energy limit. Thus, full QCD calculations are not possible. The hadronization scale may be defined slightly different in different generators.

There are two models which are the basis for the MC generator hadronization:

- **String model**. The basics for this model were taken from the string model of elementary particle physics [73]. The main feature being exploited is the *linear*

confinement, the potential of the color dipole between the color and anticolor is growing linearly with the separation of the color charges up to distances of about a femtometer.

One of the most popular generator string models is the *Lund model* [74]. The linear color potential between the quarks is expressed as $V(r) = \kappa r$, which can be described as a string with tension $\kappa \sim 1\,\mathrm{GeV}/fm \sim 0.2\,\mathrm{GeV}^2$. The Coulomb interaction is neglected. The physical picture of this potential is a colored tube between quark and antiquark. As the quarks start to separate in space, the string grows and finally breaks via the process of a new quark-antiquark pair creation, $q\bar{q} \to q\bar{q}' + q'\bar{q}$. The illustration of this process is shown in Fig. 5.3. In the mechanism described above,

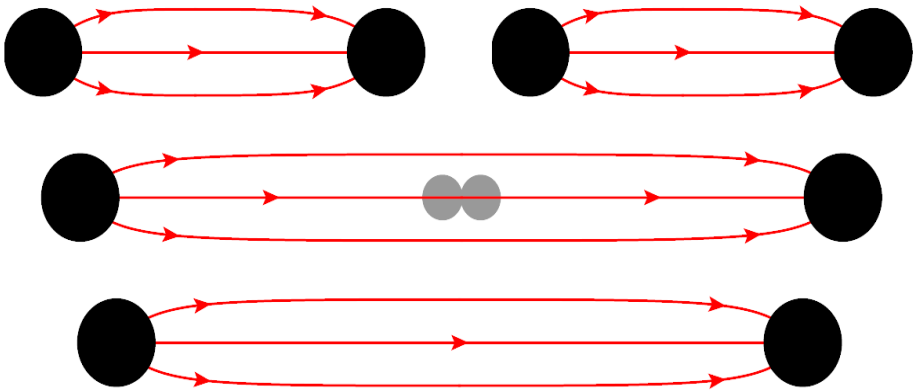

Figure 5.3: Illustration of string breaking by quark pair-creation in the string field. Black spots are the quarks and the red strips are the field illustration.

mesons are produced if after the string breaking states with two quarks are formed. Baryons can be also produced, but in the process where the string breaking produces a pair of diquarks. The hadronization stops after reaching the point when there is not enough energy to create another hadron.

- **Cluster model**. This hadronization model is based on the *preconfinement* [75], or the observation that the color-singlet parton subsystems, called *clusters*, occur with universal mass distribution depending only on the scale Q_0 at which they were formed, and not on the starting scale of the showering. The other key idea of the model is that the gluons are forced to split into a quark-antiquark pair at the end of the parton shower. The clusters formed by the gluon splitting are then forced

to decay into on-shell hadrons. The cluster hadronization in comparison to string hadronization is represented in Fig. 5.4.

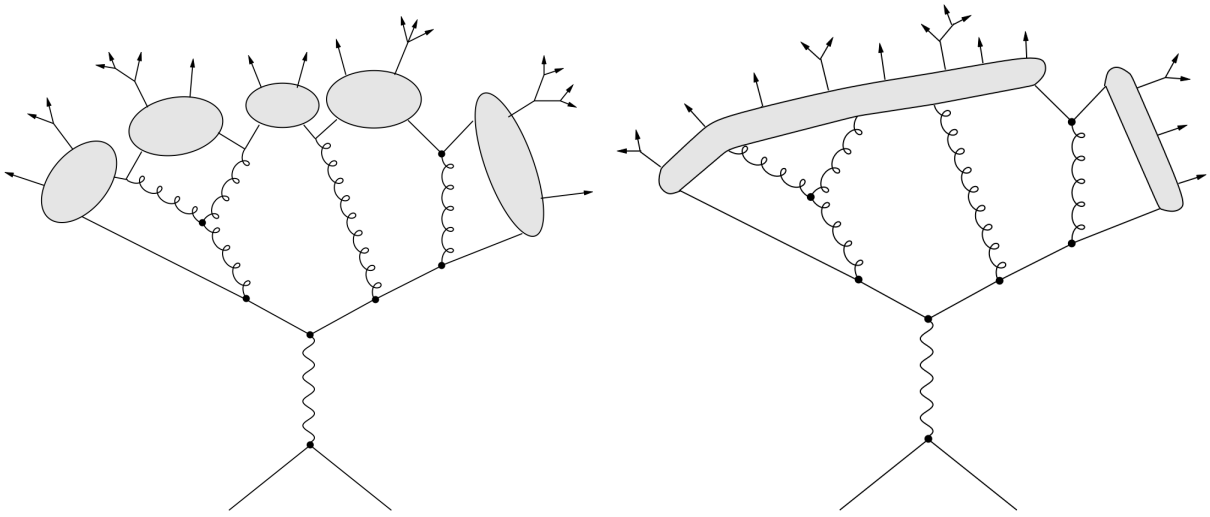

Figure 5.4: Illustration of cluster (left) and string (right) hadronization model. The figure is taken from [76].

5.1.4 Hadron Decay

The hadrons formed after hadronization, are so-called primary hadrons. They can be unstable and they decay into secondary hadrons until the set of stable particles[1] is formed.

One would expect, that all the needed information for the decay would be present in the Particle Data Group (PDG) listings [16]. However, this information is often not complete and requires multiple choices to be made. The more hadrons are included into the simulation, the more choices one has to make.

The individual properties of each generator are:

- which hadrons to include into simulation;
- which decay modes to allow;

In general, the simulation of hadron decays is based on a combination of experimentally measured properties and theoretical assumptions, which might also differ from generator to generator.

5.1.5 Underlying Event

The *underlying event* (UE), is, in terms of the MC generators, the activity beyond the hard process, like multiple parton-parton interactions (MPI) between the beam particles

[1] A typical definition of stable particles in hadron colliders is that their lifetime, $c\tau$, is greater than 10 mm. This includes the weakly decaying strange baryons.

and the hadronization of beam-beam remnants (BBR) [77]. The BBR include hadrons from the partons which do not exchange any appreciable p_T in the collision. The MPI may sometimes give a rise to two or more back-to-back jets (if there were more hard parton-parton interactions in one proton-proton collision). This case is, however, very rare. The main impact is coming from the soft MPI. They may affect, for example, the missing E_T distribution or increase the activity in the forward direction (break-up of the beam remnants).

The UE models are usually tuned to the experimental conditions and on experimental data. The model derived on the CMS data collected at $\sqrt{s} = 0.9\,TeV$ and $\sqrt{s} = 8\,TeV$ is called the $Z2*$ tune [78].

5.1.6 Monte Carlo Generators

After describing the main principles behind the MC simulation of the events for the experiments in the field of elementary particle physics, the list of the generators used for this analysis will be given in the following:

Pythia 6

Pythia [70] is a general-purpose event generator. It models pp, γp and e^+e^- collisions. Pythia includes more than 200 hardcoded hard subprocesses, which include the Standard Model reactions but also some exotic beyond Standard Model processes [72]. The matrix elements of the hard parton scattering are calculated in Pythia in LO QCD accuracy. For the parton showering, the parton emissions are ordered by the transverse momentum of the radiating parton, $Q^2 = p_T(part.)$. For the hadronization, the Lund string model is used. Particle decays are included in Pythia, using specific decay tables containing all relevant decay branching ratios. The $Z2*$ tune for the UE simulation is conventionally (for the CMS experiment) used in Pythia for the UE simulation for this analysis.

Herwig 6

Herwig [69] is a general-purpose LO matrix element plus parton shower generator like Pythia. It can model hadron-hadron, lepton-lepton and hadron-lepton collisions. Herwig is able to produce a fairly large variety of Standard Model QCD, electroweak processes and elementary subprocesses beyond the standard model. The parton showering is ordered by the scale $Q^2 \sim 1 - \cos\theta$, where θ is the angle between the parent and emitted partons. The cluster model is used for the hadronization in Herwig. The model for the UE used here by Herwig was originally derived by ATLAS and is called AUET2 [79].

MadGraph

MadGraph [80] is another general-purpose generator. It can be used to generate the hadron-hadron pp and $p\bar{p}$, as well as the other types of collisions. It gives the LO matrix elements for hard processes with up to 8 particles in the final state.

MadGraph is a pure matrix element generator. It does not include hadronization and provides only leptons, quarks and gluons as outgoing hard particles. The outcome is

afterwards interfaced to some general-purpose generator to generate further steps (parton showering, hadronization).

The problem of double counting of objects in showering, while interfacing MadGraph to the general-purpose generator, is solved with the help of the MLM scheme [81]. In this scheme the showered partons are generated in a restricted phase space with a minimal cone separation between each other. These partons are clustered into jets using the cone algorithms. If the original parton is included in more than one jet, the event is rejected.

For this analysis the PDF CTEQ6L1 set [27] is used in MadGraph to describe the proton structure.

Powheg

The Powheg (Positive Weight Hardest Emission Generator) event generator [82] provides the modeling of the hard interaction with NLO accuracy. The Powheg method doesnot have parton showering included. Thus, it has to be also interfaced with Pythia or Herwig for a full event description. For the description of proton structure, the CT10 [83] PDFs are used.

MC@NLO

The MC@NLO [84] is also an event generator which generates the hard emission with NLO precision. For the showering it has to be interfaced with general-purpose generators, as it is also done for Powheg.

MC@NLO is designed for hadron collisions with production of top quark pairs, Higgs boson, vector boson (single or in pairs), single top, lepton pairs and associated $H + W/Z$.

The MC@NLO generator provides some events with negative weights. However, the fraction of these events is very small [84].

The CTEQ6M [27] PDF sets were exploited in MC@NLO for this analysis.

5.2 Detector simulation

After the bare event with all the particles is simulated, it can be "pushed through" a detector simulation. That means that all of the particles will interact with the materials and electromagnetic fields of the model of a real detector. This allows the estimation of detector efficiencies and smearing of observables such as particles energies, prediction of the performance and comparison of the theoretical models encoded in the event generators to the experimental measurements. The simulation of the detector is performed by means of the Geant simulation toolkit.

Geant 4

Geant4 (GEometry ANd Tracking) [85] is a toolkit designed for an accurate simulation of the passage of particles through matter. The tool includes all the aspects of the simulation, like the geometry of the system, the materials involved, fundamental particles of interest, tracking of particles through materials and electromagnetic fields, the physics processes

governing the particle interactions, the response of sensitive detector components, the storage of events and tracks, the vizualization of detector and particle trajectories and the analysis of the data on different levels of details.

Geant can handle the particle interactions on a very wide energy scale. It also includes a large amount of known particle interaction models.

For the needs of the CMS experiment Geant4 is used for the detector simulation. An example of the display of a fully simulated CMS $t\bar{t}$ event in the $e\mu$ decay channel is shown in Fig. 5.5.

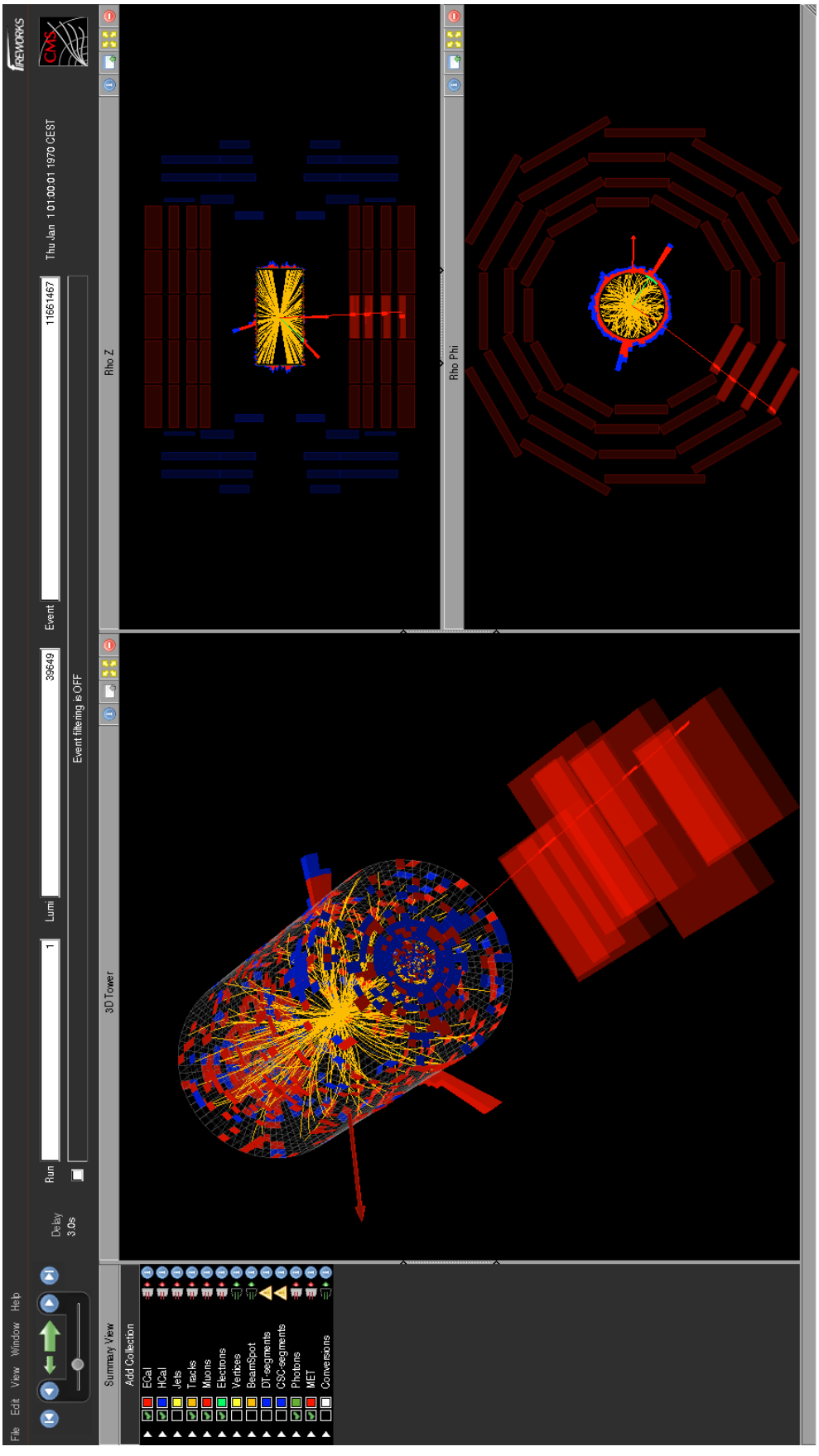

Figure 5.5: Display of a simulated $t\bar{t}$ event in the CMS detector model, produced with the CMS event display.

Chapter 6

Event Reconstruction

The reconstruction procedure is interpreting the detector data as a set of physical objects.

In general, for this analysis each object of the $t\bar{t}$ dileptonic final state was reconstructed using the *Particle Flow* (PF) algorithm [86]. It is an iterative process which reconstructs the particles and jets exploiting the information from all parts of the detector. After an object is reconstructed in one iteration, all the detector signals assigned to it are blinded for the further iterations.

The reconstruction with the PF algorithm following [86] starts with muons as they are the most unambiguous particles to identify. After blinding the muon signals in the detector, the charged hadrons are reconstructed. The next step is the electron reconstruction and afterwards all the remaining signals are assigned to neutral hadrons and photons. After all particles are reconstructed and identified, the missing transverse energy (E_T^{miss}) is constructed using all available information. A complete overview of the PF algorithm can be found in [87].

Different algorithms and methods are used to reconstruct different objects and some of them (relevant for this analysis – leptons, jets and missing transverse energy, responsible for neutrinos) are discussed in this chapter.

6.1 Track and Vertex Reconstruction

Tracks[1] and vertices[2] are the essential objects used for all the particles reconstruction. However they are not the primary detector output and they have to be reconstructed.

6.1.1 Track Reconstruction

The track reconstruction uses the information from the inner tracking detectors. The neighboring pixels and strips which produce signals are grouped to clusters. The position of a cluster defines a hit which is an estimate of the point where a particle crossed the

[1] A *track* is a set of information about the charged particles trajectory and momentum.

[2] A *vertex* is an estimate of a point in space where the particles arise from. It can be either related to the collision point or to the place where some secondary interaction or decay happened.

detector material. A particle trajectory can be tracked by fitting the corresponding sequence of hits. The curvature of the trajectory within the known magnetic field gives the transverse momentum estimate of a particle.

The track reconstruction procedure consists of four main steps as following [88]:

- **Seed generation**: all the possible combinations of three points (3 hits in the first layers of the pixel tracker or two hits from the first tracker layers and the beam spot center[3]) are used to determine a helical trajectory assuming a quasi-uniform magnetic field. Every resulted track is required to have some minimum p_T and maximum beam spot impact parameter[4] to be accepted as an initial track candidate or seed.

- **Track finding**: extrapolates the seeding candidates along the expected flight paths to the consecutive tracking detector layers searching for further hits and reestimating the track parameters respectively. On each consecutive layer all hits from a 3 sigma region around the seed trajectory are tried out and fitted with a Kalman filter [89]. The smallest χ^2 hit is finally taken and the trajectory extrapolation to the next layer is continued until the end of tracker is reached. In case no hit is found on some layer a ghost hit is assumed. The track is not accepted if it contains more than one ghost hit.

- **Track fitting**: after finding the hits in all the tracker layers with the track finding, a track candidate is refitted using the Kalman filter. This procedure is performed releasing the constraints set on the seeding stage.

- **Track selection**: reduces the rate of fake tracks[5] by setting physical and quality constraints on the object produced at the previous step. The requirements are based on a good χ^2 of the fit and a reasonable value of the impact parameter with respect to the beam spot.

The tracking procedure is repeated in several iterations. The first iteration has the hardest requirements - high p_T of the tracks and the smallest impact parameters (such objects are usually easier to reconstruct). After reconstructing the tracks in the first iteration, their hits are removed and the second iteration starts with a bit softer requirements on the seed tracks. In total, six iterations are performed.

6.1.2 Primary Vertex Reconstruction

The primary vertex reconstruction aims to measure the location of all proton-proton collision points in the event (see Fig. 6.1).
The primary vertex reconstruction procedure has three phases described as follows [88]:

[3]The *beam spot* center is defined as an average value of the $p\bar{p}$ interaction points over many events.

[4]An *impact parameter* d_{xy} of the track is a minimum distance of the track to a certain vertex or beam spot in the transverse $x - y$ plane.

[5]A *fake track* is a track produced by the fit but actually there was no real charged particle which produced this track.

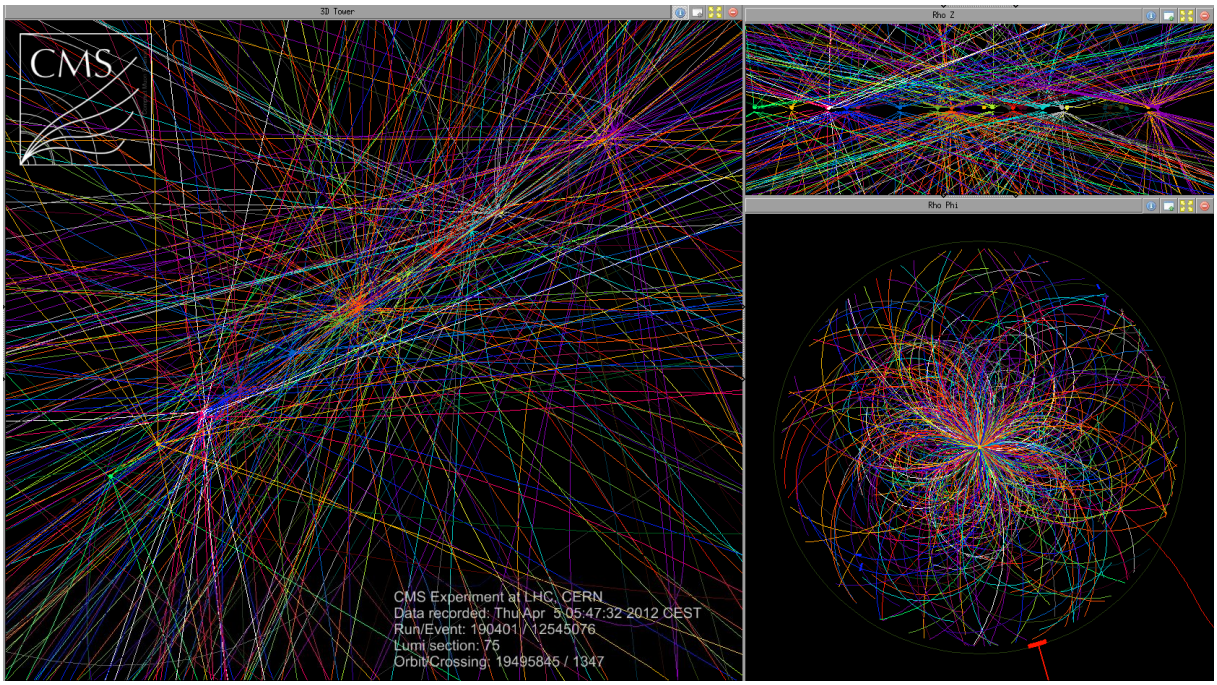

Figure 6.1: Magnified view of the event showing 29 distinct vertices reconstructed corresponding to 29 distinct collisions within a single crossing of the LHC beams. The figure is taken from [90].

- **Track selection**: the tracks for the primary vertex reconstruction are chosen with certain requirements such as to be consistent with being produced in the primary interaction region (the significance of the beam spot impact parameter – its value over its uncertainty – has to be maximum 5), having hits in at least two pixel layers and at least five pixel and strip layers associated with the track and having a χ^2 per degree of freedom for the track fit of not higher than 20.

- **Track clustering**: the main task of the clustering algorithm is to separate the groups of tracks emerging from different primary vertices, not splitting the tracks from one vertex to two, but also not merging the tracks from different vertices to one. The tracks are clustered according to their z-coordinate at the point of closest approach to the beam spot center.
  The algorithm used for the clustering in the CMS 2012 data is the *deterministic annealing* described in detail in [91].

- **Fitting the position of the vertex**: each clustered group of tracks forms a vertex candidate. Only the candidates with at least two tracks are taken and are fitted using an *adaptive vertex fitter* [92]. The output of the fit is the vertex position, its uncertainty and a χ^2. The probability of each track to arise from the reconstructed vertex is determined.

The information on all primary vertices in the event is useful not only for other objects reconstruction but also for separating the signal vertex (with a hard interaction) from

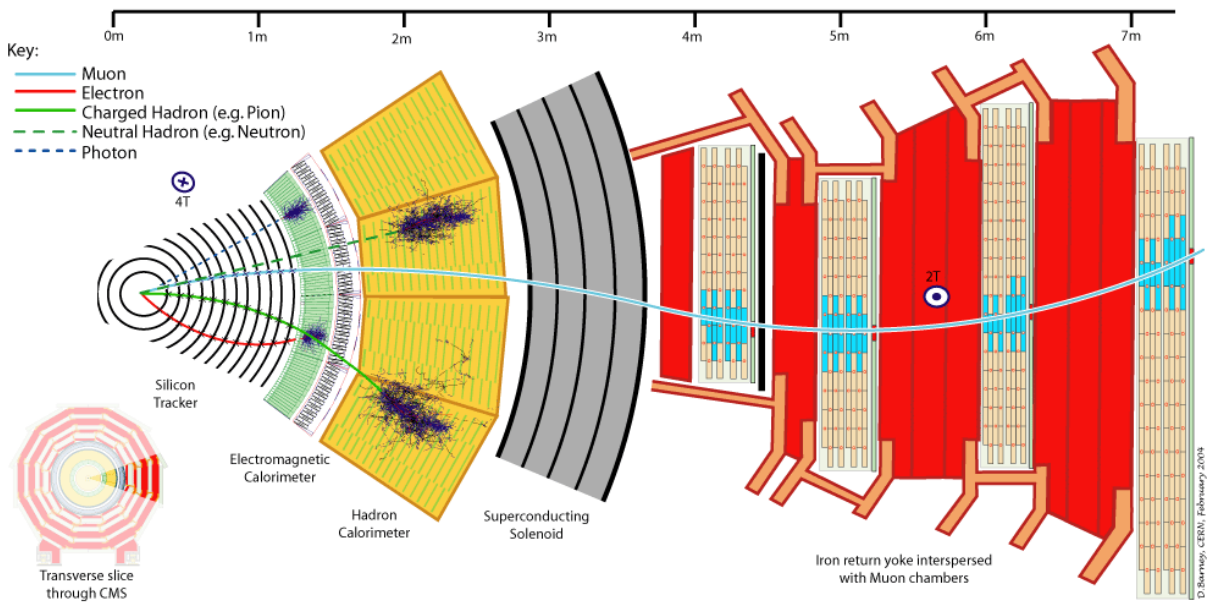

Figure 6.2: Track reconstruction using different sub-detector information in combination in the Particle Flow algorithm. The different charged particles are shown as curved lines: muon (blue), electron (red) and charged hadron (green). Neutral particles are shown with the dashed straight lines. The plot taken from [93].

the others with no useful physics information. On average 20 primary vertices can be reconstructed in one event, corresponding to 20 pp interactions. This is called *pileup*. To choose the proper primary vertex for a collision where a $t\bar{t}$ pair is produced special selection has to be applied (see sec. 7.3).

6.2 Objects Reconstruction

The reconstruction of muons, electrons, jets and missing transverse energy (which are needed for the $t\bar{t}$ dileptonic final state reconstruction) is presented in this section.

6.2.1 Muon Reconstruction

As discussed in section 3.2, the CMS experiment has a well established setup for the muon reconstruction. Muons are the only particles expected to be detected in the muon sub-detector system, thus their identification is unambiguous. Fig. 6.2 shows a muon path in the detector compared to other particles. One can get three types of muons out of the reconstruction:

- **Standalone**: muon tracks are reconstructed using the information from the muon system only. The track reconstruction algorithm [94] is similar to the one used in the tracking system.

- **Tracker**: the tracks, reconstructed in the tracking detector only as described in sec. 6.1.1, are assigned as muons in case they match at least one hit in the muon sub-detector [94].

- **Global**: the muons are reconstructed using the combined fit of tracks from the muon system and from the inner tracker. Here the standalone and tracker muons are fitted together. The details are given in [94].

6.2.2 Electrons reconstruction

The electrons are reconstructed by combining tracks from the tracker with clusters from the ECAL. The electron seeds are created making use of two complementary algorithms as following [95]: *tracker driven seeding* and *ECAL driven seeding*. The former is performed for the tracks with $p_T < 5$ GeV, matching them to the ECAL superclusters[6]. The ECAL driven seeding is performed for the tracks with $p_T \geq 5$ GeV fitting the ECAL superclusters to the tracker tracks. All the seeds are fitted with a Gaussian Sum Fitter (GSM) [96] using the hypothesis that each track is an electron and assuming specific energy losses.

On the next reconstruction step the fitted seeding tracks are preselected. The tracker seeds are preselected by a multivariate analysis (MVA) as described in [97]. For the ECAL seeds restrictions on the GSM matching in η and ϕ are applied [98].

The collection of the tracks formed after this selection is assigned to electrons.

6.2.3 Jet Reconstruction

A quark or a gluon as a colorful object can not exist singly due to the confinement property (see sec. 2.2.2). A quark thus starts to hadronize and form a group of particles (primarily only hadrons) flowing in a similar direction. These sprays of particles are called jets. Special algorithms are developed to find and reconstruct jets.

Jet Finder Algorithms

The idea which lies behind any algorithm of jet finding and reconstruction is the merging of objects which are measured nearby in the detector. Generally a jet can be reconstructed using two strategies [99]:

- *Sequential clustering*: the particles are sequentially recombined according to some distance criterion.

- *Cone algorithms*: a jet is defined as a cone around some direction of dominant energy flow, or seed. Each or some of the particles are tried in a role of the dominant direction seeds. The next step is to define a trial cone around the seed and accept all the particles which enter this cone. The sum of the four-momenta of all objects inside the jet cone is calculated. This jet candidate is assumed to be a new seed. This iterative process continues until stable seeds are found.

[6] A *supercluster* is a group of one or more associated clusters of energy deposits in the ECAL. The transverse energy E_T of the supercluster has to be not lower than 4 GeV.

Although the cone algorithms are fast and simplistic they are not collinear and infrared safe[7] by default.

The sequential clustering algorithms are both infrared and collinear safe. They do not rely on a stable cone. The procedure of constructing a jet starts with defining two distances – d_{ij} (the distance between two objects, particles or pseudojets, i and j in the detector) and d_{iB} (the distance between the object i and the beam direction). These two distances are compared:

- $d_{ij} < d_{iB}$: the objects i and j are combined together to a pseudojet which enters the algorithm again as a single object;
- $d_{ij} > d_{iB}$: the object i is taken as a final jet.

The different sequential clustering algorithms differ at the level of the distance definition. In general the distances are defined as follows [100]:

$$d_{ij} = min(k_{Ti}^{2p}, k_{Tj}^{2p}) \frac{\Delta_{ij}^2}{R^2}, \tag{6.1}$$

$$d_{iB} = k_{Ti}^{2p}, \tag{6.2}$$

$$\Delta_{ij}^2 = (y_i - y_j)^2 + (\phi_i - \phi_j)^2. \tag{6.3}$$

Here the k_{Ti}, y_i and ϕ_i are the transverse momentum, rapidity and azimuth angle of an object i. The R is a cone radius parameter and p is the parameter which varies the power of the energetic term in comparison to the geometrical scale Δ_{ij}. There are three different sequential clustering algorithms depending on the p value:

- $p = 1$ defines the k_T algorithm, where the energetic and spatial term are of the same power;
- $p = 0$ defines the Cambridge/Aachen algorithm, where the energetic term in eq.6.1 is removed thus the spatial part plays the only role;
- $p = -1$ defines the anti-k_T algorithm.

The jets for this analyses were constructed using the anti-k_T sequential clustering algorithm. Being infrared and collinear safe, this algorithm reconstructs circular-shaped jets.

Jet Energy Calibration

The reconstructed jet energy should be corrected for the non-linear and non-uniform responses of the calorimeter. For this a factorized jet calibration method is used [101]. The calibration is performed sequentially in several steps:

[7] *Infrared* and *collinear safety* is the property that if one modifies an event by a collinear splitting or the addition of a soft emission, the set of hard jets that are found in the event should remain unchanged.

- The *Offset correction* removes extra energy due to electronics noise and pileup. It is applied on the reconstructed level of the experimental and simulated data.

- The *Monte Carlo calibration* corrects the energy of the reconstructed jets such that it is equal to the average energy of the generated particle jets. This correction is performed in bins of the jets p_T and η. This correction is applied only on the simulated data.

- The *Relative jet energy correction* ensures a flat response as a function of η. It is applied only on the reconstructed experimental data.

- The *Absolute jet energy correction* balances the p_T response to be linear. It is calibrated on a sample of well reconstructed Z^0 bosons decaying into two jets. This correction is applied only on the reconstructed experimental data.

The first calibration step deals with the additional energy in the jet which does not occur from a hard process but rather from the detector noise or pileup. Obviously this correction produces a factor always smaller than 1, thus the jet energy reduces on this step. The MC corrections aim to make the jet response flat as a function of $|\eta|$ and p_T. The correction on the geometrical position dependence corrects all the energies as if they were measured in the most efficient barrel region using a sample of dijet data events. The p_T dependence correction makes use of $(\gamma^*/Z \to ll)$ events to exploit a good lepton energy and momentum resolutions. Finally residual corrections (relative and absolute energy corrections) are applied on data to correct for some minor disagreement with the simulation.

In general all the correction factors in the kinematic region of interest for this analysis are smaller than 5%.

b-Jets identification

The task of the b-jet identification is to distinguish a b-quark jet from light flavour-, c- and gluon-jets. In particular, the long life time of the beauty hadrons (in the order of 10^{-12} s) is exploited which allows them to travel far enough from the primary interaction point ($c\tau \sim 500\,\mu$m) before decaying. The point in space, which corresponds to the place of the beauty hadron decay can be reconstructed with the trends precisely measured in the silicone pixel detector as a *secondary vertex*. The jet flavour identification algorithm combines information on identified secondary vertex and track impact parameter to the primary vertex (see Fig. 6.3).

The algorithm used for this analysis is called *Combined Secondary Vertex* (CSV) [103]. It defines a likelihood-based discriminator to distinguish b-jets, c-jets and light jets.

The minimum thresholds for the algorithm are defined as three *working points*, loose (L), medium (M) and tight (T), as following [103]:

– CSVL sets the threshold on the actual discriminator value as ≥ 0.244, which has a b-tagging efficiency $\sim 80\%$ and a misidentification probability of light quark jets close to 10%;

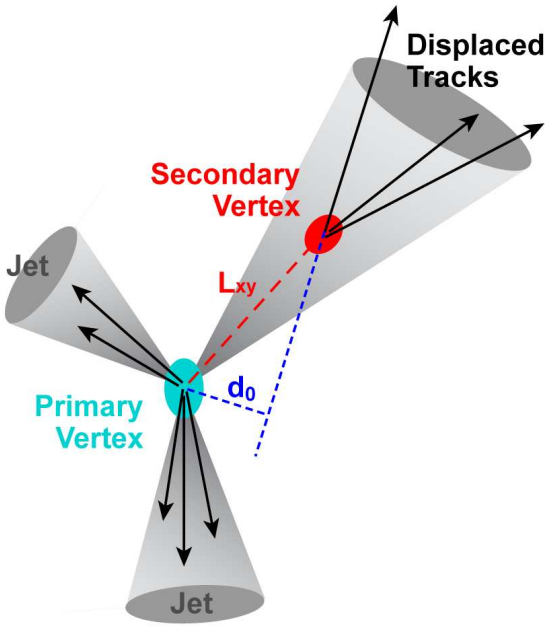

Figure 6.3: A sketch of the event with a reconstructed secondary vertex. A light blue circle is the primary vertex and a red circle is the secondary vertex. The impact parameter of a track is marked with a blue dashed line and a symbol d_0. The sketch is taken from [102].

– CSVM sets a harsher threshold on the discriminator value of ≥ 0.679, which lowers the misidentification probability to $\sim 1\%$, but also reduces the b-tagging efficiency down to 65%;

– CSVT has the hardest threshold on the discriminator value of ≥ 0.898. This lowers the misidentification probability by another factor of 10 (0.1%) and reduces the b-tagging efficiency down to 50%;

In general the efficiency of the CSV algorithm was estimated in data and simulated QCD events [103]. The resulting curve is presented in the Fig. 6.4.

6.2.4 Missing Transverse Energy

The colliding protons in the LHC have no transverse momentum component. Thus from momentum conservation one expects to have a zero sum of the transverse momenta of the objects arising from the collisions. This can be expressed the following way:

$$\sum_{detected\ objects} \vec{p}_T + \sum_{undetected\ objects} \vec{p}_T = 0. \tag{6.4}$$

The sum of the undetected objects transverse momentum is the missing transverse energy E_T^{miss}. It can be expressed from eq. 6.4 as the opposite vectorial sum of the transverse momenta over all reconstructed objects [87]:

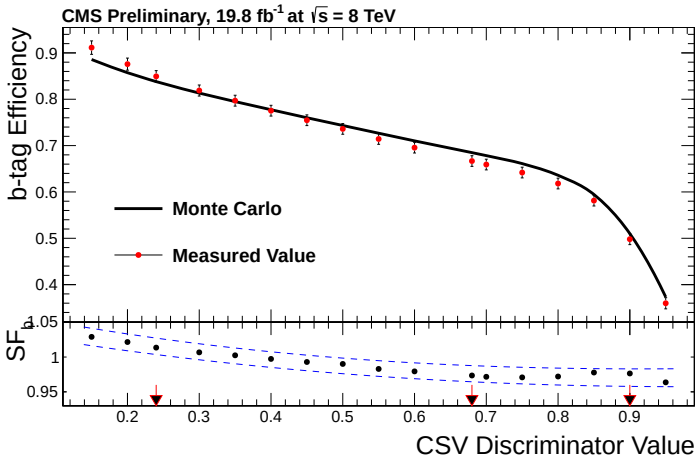

Figure 6.4: The b-jet tagging efficiency as a function of the discriminator threshold for the CSV algorithm. The three CSV working points are marked with the red arrows on the x-axis. The upper panel shows the efficiency measured in data and predicted from the simulation. The lower panel shows the ratio between data and simulation efficiencies, where the blue line represents the combined statistical and systematical uncertainty. The plot is taken from [103].

$$\vec{E}_T^{miss} = -\sum_{detected\ objects} \vec{p}_T. \tag{6.5}$$

The missing transverse energy reconstruction is sensitive to the pileup objects. To correct for the pileup effects a special Boosted Decision Tree (BDT) was trained [104].

An additional *recoil correction* [105] was applied. This was done with the help of a Multi Variate Analysis (MVA) and the resulting missing transverse energy is called *MVA* E_T^{miss}. The MVA E_T^{miss} exhibits a better resolution compared to the missing transverse energy calculated only from the PF (eq.(6.5)).

Chapter 7

Event Selection

This work is aiming at reconstructing the $t\bar{t}$ pair in the dilepton $e\mu$ decay channel, or $t\bar{t} \rightarrow W^+ b\, W^- \bar{b} \rightarrow e^+(\mu^+)\nu b\, \mu^-(e^-)\bar{\nu}\bar{b}$, thus looking for events in the detector with electron and muon of different electrical charge and two jets. The neutrino can not be measured directly but their presence is reflected by a non-zero transverse missing energy E_T^{miss}. The low branching ratio of the $e\mu$ decay channel ($BR \simeq 2.4\%$) is compensated by an excellent lepton identification and reconstruction, which reduces the fraction of background events to large extent.

The reconstructed objects in each event (which corresponds to one bunch crossing) have to fulfill certain criteria to be accepted for this analysis. These criteria are chosen taking to account the physical result this analysis is aiming for and the technical features of the CMS detector parts.

The imperfect correspondence of the simulation model to the real data has to be additionally corrected. The differences in efficiencies of certain procedures in data and simulation are corrected by applying *Scale Factors*, $SF = \frac{\epsilon_{data}}{\epsilon_{MC}}$, on the MC distributions. Here ϵ_{data} is the efficiency determined in the experimental data and ϵ_{MC} is the efficiency from simulation.

This chapter gives an overview of the $t\bar{t}$ event selection. The procedures are based on the CMS Top-Quark-Physics-Analysis group recommendations [106]. The full chain of the event selection is described. The resulting event yields are represented in control distributions, showing the data, simulated signal and backgrounds.

7.1 Background Sources

Not all of the events which have two identified leptons and two jets in the final state are signal events originating from the $t\bar{t}$ system decaying in the dileptonic channel. Events may arise from different processes, called *background* for the specific measurement. In this analysis the background rates are estimated from the simulation. The following background processes are relevant for this analysis:

- $t\bar{t}$ →other. This background source includes the other $t\bar{t}$ decay modes (see sec. 2.4.2) and it is dominated by the dileptonic channel via τ leptons as it has the same final state but with extra neutrinos;

- single top production, which was simulated using POWHEG + PYTHIA. A top is produced in association with a W boson, which can be mistreated as a W boson from the top decay;
- Drell-Yan processes, $Z/\gamma^* \to \tau\tau$ and $Z/\gamma^* \to ee/\mu\mu$, which are generated utilizing PYTHIA. Since they also has a dileptonic final state signature, they can be misidentified as $t\bar{t}$ signal. However, only same flavour leptons are produced in Drell-Yan processes. Therefore, the fraction of these background events in the $e\mu$ final state is small;
- WW, WZ, ZZ diboson production, simulated using PYTHIA. These events can also have a dileptonic final state and may be picked as a $t\bar{t}$ candidate;
- associated $t\bar{t}$ + $W/Z/\gamma$ production, simulated with MADGRAPH + PYTHIA. The reason why this process can be misidentified as a $t\bar{t}$ production is similar to the previous case;
- associated W + $jets$ production, generated using MADGRAPH + PYTHIA;
- QCD multijet processes, generated with PYTHIA.

For the latter two processes, one expects only one ore none hard leptons in the final state. However, the production rates are high and occasionally one or two leptons, which originate from hadron decays or from hadrons misidentified as leptons, can be picked up.

For all the mentioned above background sources with one (zero) top produced, the events can only be misidentified as $t\bar{t}$ signal if there are also at least one (two) jets present in the final state which can be misidentified as b-jet candidates. This requirement suppresses the background processes further.

The simulated background samples were normalized to the data integrated luminosity of 19.7 fb^{-1} and scaled to the total cross sections predicted by higher order calculations [107].

Whereas all the other background yields are only simulated, the estimated total rate of the background caused by Drell-Yan production is partially data driven [108]. The normalization factor for the simulated Drell-Yan events is determined from the comparison of the reconstructed and the simulated Z-peak in the clean decays $Z \to ee/\mu\mu$.

The selection, which will be introduced in this section, is aiming to distinguish the $t\bar{t}$ events from the background processes exploiting physical features of each process.

7.2 Good Runs

For the work presented in this thesis the following CMS data samples were used:

Samples	Events	Run Range
/MuEG/Run2012A-22Jan2013-v1/AOD	2.5M	190456 - 193621
/MuEG/Run2012B-22Jan2013-v1/AOD	15M	193834 - 196531
/MuEG/Run2012C-22Jan2013-v1/AOD	21M	198022 - 203742
/MuEG/Run2012D-22Jan2013-v1/AOD	22M	203777 - 208686

Only the good runs from the LHC certified good run list [109] are selected for the analysis out of these data sets.

7.3 $t\bar{t}$ Event Selection and Correction

The analysis follows closely a previous measurement selection strategy described in [110]. The various selection criteria and related scale factors are summarized as follows:

- **Trigger selection**: The events have to be accepted by the HLT (see section 3.2.6) dilepton triggers, which require the presence of two leptons, electron and muon, with minimum transverse momentum of 17 GeV and 8 GeV, respectively.

  As the triggers may perform with different efficiencies for the data and for MC, scale factor corrections were applied for the latter. As all the data taken with the detector is selected by at least one trigger, there is no "reference" data before the trigger selection. That is why the efficiency of the particular trigger can be determined only relative to another "monitor" trigger. A monitor trigger should be as independent from the tested trigger as possible. The efficiencies were determined from a different data sample triggered by the monitor trigger as a ratio between the number of events which were selected simultaneously by the tested and monitor trigger over the number of events selected by the monitor trigger only. The E_T^{miss}-based trigger was used as a monitor trigger in this work [110]. The scale factors connected to the trigger selection were applied on the MC double differentially in bins of the two leptons pseudorapidities.

- **Beam scrapping**: Accept only events with maximum 10 reconstructed tracks, or more than 10 in case at least quarter of them has high reconstruction quality.

- **Calorimeter noise removal**: Event with anomalous calorimeter noise are removed [111]. This noise is caused by the instrumentation issues with Hybrid Photo Diodes and Readout BoXes. The best HCAL specific algorithm to detect noise are based on analysing the shapes of detected pulses.

- **Vertex requirement**: Events with at least one "good" primary vertex are selected. This means that the number of associated tracks should be larger than 4 and a vertex should be positioned centrally in the detector [1]. Only the "hardest vertex" (with the highest sum of the p_T^2 of the assigned tracks) is taken for the analysis.
  The weight correction depending on the event primary vertex multiplicity is applied event-by-event on the MC to make it match the data distribution. This is called a *pileup correction*. For estimation of the correction value the distribution of the measured luminosity in each bunch crossing [112] multiplied by the total pp inelastic cross section σ_{pp} [113] is taken. The Fig. 7.1 shows how the agreement between the experimental and simulated data improves after this reweighting is applied.

[1] Only the events with a vertex position $|z| < 24$ cm and $|\rho| = |\sqrt{x^2 + y^2}| < 2$ cm are accepted. All the coordinates are given with respect to the CMS coordinate system (see sec.3.2)

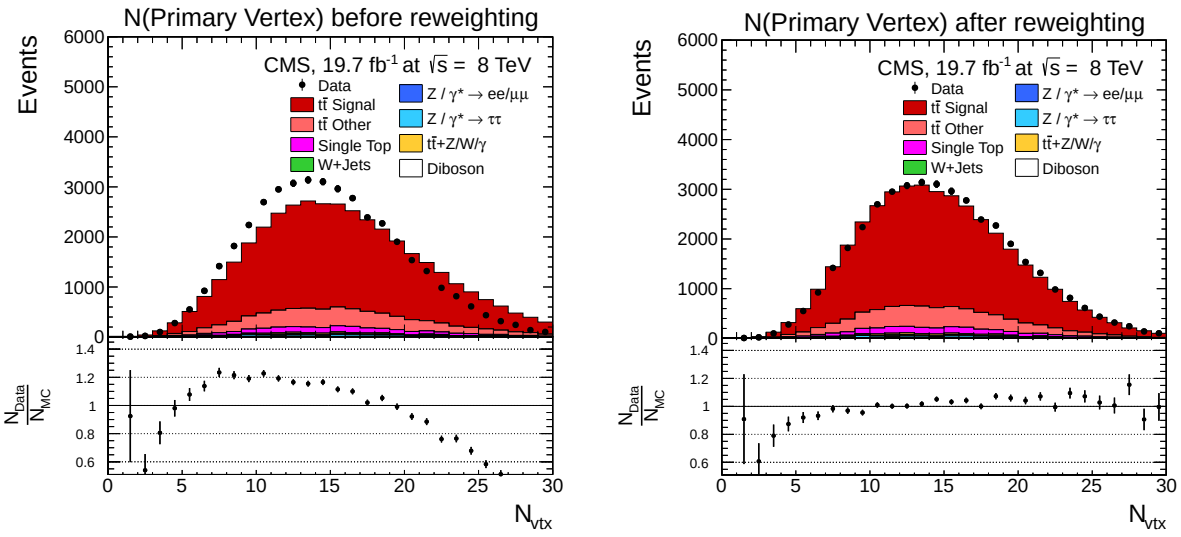

Figure 7.1: The vertex multiplicity control distribution before (left) and after (right) the vertex correction reweighing after the full event selection. The experimental data points (black dots) are shown as well as the simulated distributions (colored histograms) of signal and different backgrounds. The error bars of the data points correspond to the statistical uncertainties. The bottom plot shows the ratio of the event yields in data and MC (sum of all contributions) with error bars representing the statistical uncertainties of the data and MC.

– **Lepton isolation**: All the leptons in the event have to be isolated with $I_{rel} \leq 0.15$ in a cone of $\Delta R = \sqrt{\Delta\eta^2 + \Delta\phi^2} = 0.3$ around the lepton track, where I_{rel} is the relative isolation defined as:

$$I_{rel} = \frac{\sum E_{Tracker} + \sum E_{ECAL} + \sum E_{HCAL}}{p_T(l)}. \tag{7.1}$$

Here $E_{Tracker}$, E_{ECAL} and E_{HCAL} are the energy deposits in the tracking detector, ECAL and HCAL respectively, excluding the energy deposit of the lepton.

As it is shown in the Fig. 7.2, the lepton isolation requirement cuts mainly on the QCD background.

The efficiencies of the lepton isolation were determined using a **tag and probe** method [114]. The corresponding scale factors are applied on the simulation reconstructed level in bins of p_T and η of lepton separately for electrons and for muons.

To correct for pileup the $\delta\beta$ correction was applied for muon and electron isolation [115, 116].

– **Lepton pair selection**: An event has to contain at least two opposite signed leptons (electron-muon pair) with $p_T > 20$ GeV and $|\eta| < 2.4$. The invariant mass of the system of the leading p_T electron and muon has to be more than 20 GeV,

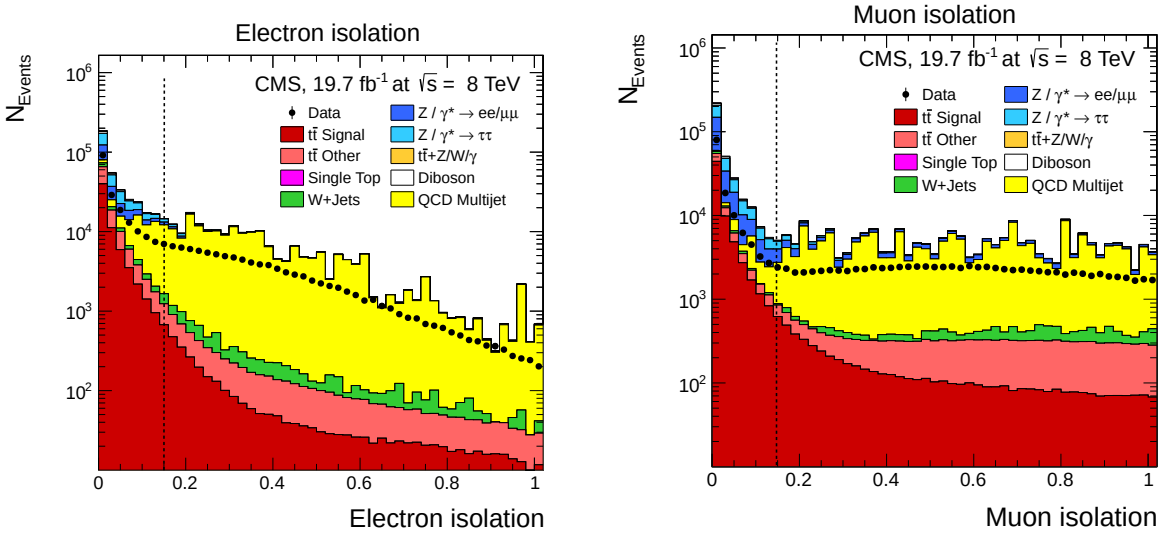

Figure 7.2: Electron (left) and muon (right) relative isolation (I_{rel}) (7.1) after the trigger selection. The vertical dashed lines show the isolation cut value. Other details as in Fig. 7.1.

otherwise the event is rejected. In the following analysis steps only the leading p_T leptons are considered.

– **Jets selection**: Events which contain at least two jets with $p_T > 30$ GeV and $|\eta| \leq 2.4$ are accepted. It is natural to expect that events with less than two jets will be dominated by Drell-Yan background as the leading order Drell-Yan process does not contain jets in the final state. This is also reflected by the jet multiplicity distribution (Fig. 7.3).

– *b*-**jets selection**: An event has to contain at least one jet, tagged as originating from a *b*-quark with *b*-tagging probability according to the CSVL cut criterion (sec. 6.2.3). The multiplicity of the *b*-tagged jets is presented in Fig. 7.4 which shows that cutting the events with no *b*-tagged jets should remove a sizable background fraction. Indeed, Fig. 7.5 presenting the dilepton mass before and after the *b*-jets selection shows this background reduction.

The scale factors corresponding to the *b*-tagging procedure are measured by the BTV group [103] for *b*, *c* and light jets. These scale factors were applied on the MC, separately for the *b*-jets, *c*-jets and light jets, improving much the agreement between data and simulation. This effect can be seen in the Fig. 7.6, which presents the CSV discriminator distribution before and after the *b*-tagging SF reweighing. The data-to-MC ratio plots are getting closer to one with applying the SFs.

The applied selection criteria dramatically reduce the fraction of background events, while retaining a large fraction of the signal.

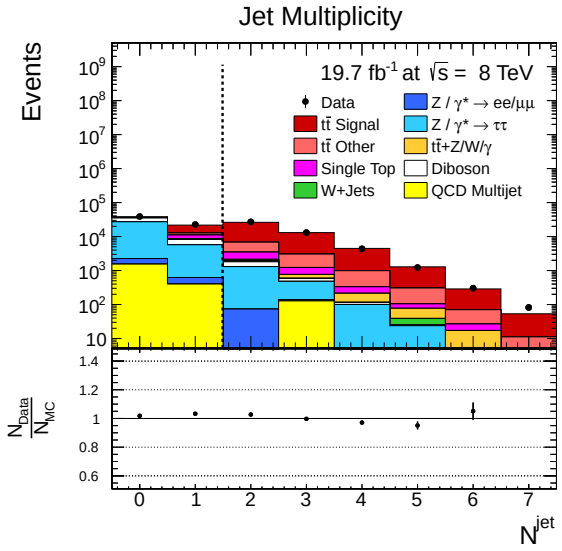

Figure 7.3: Control distribution of the jet multiplicity after the trigger and lepton selection. The vertical dashed line shows cut value on the jet multiplicity. Other details as in Fig. 7.1.

7.4 Control Distributions

The results of the selection described above can be illustrated by control distributions of the objects which are reconstructed for the $t\bar{t}$ final state definition.

The Fig. 7.7 shows the lepton η and p_T. An overall reasonable agreement between the data and simulation shapes is observed in all η and p_T regions.

The kinematics of the reconstructed and selected jets is presented in the Fig. 7.9 which shows the control distributions for the jets η, p_T and the jet multiplicity in the events. The simulation describes better the central rapidity ranges. For jet multiplicities smaller than 5 the MC describes the jet multiplicity distribution of the data well.

The multiplicity for the b-tagged jets is presented in Fig. 7.8 which shows a good agreement for multiplicities smaller than 4.

The control distributions are signal dominated which shows a good performance of the criteria for the $t\bar{t}$ final state selection.

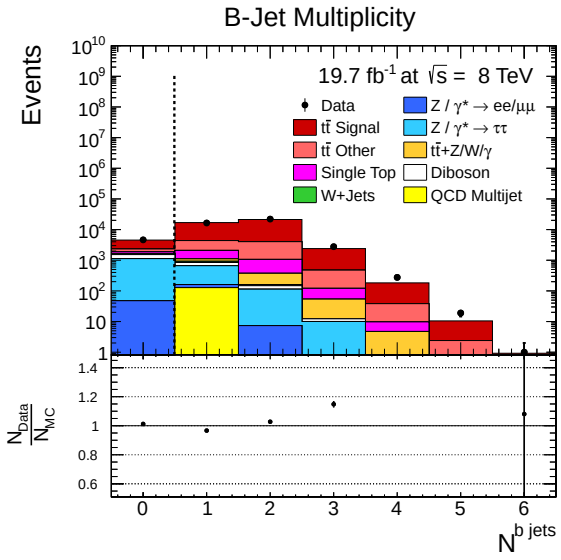

Figure 7.4: Control distribution of the b-jet multiplicity after the trigger and lepton selection. The vertical dashed line shows the cut value on the b-jet multiplicity. Other details as in Fig. 7.1.

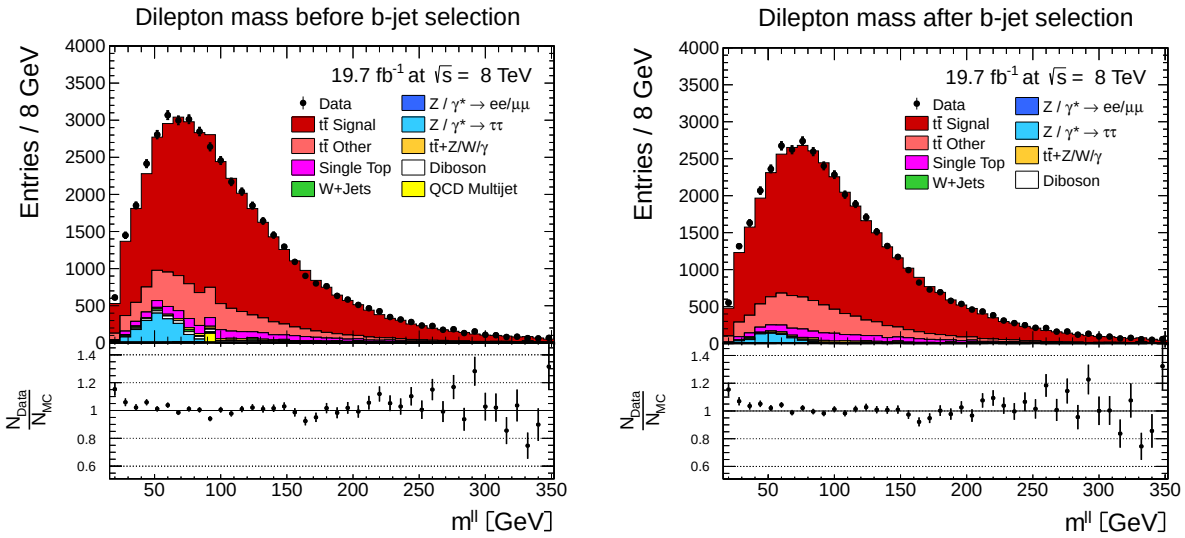

Figure 7.5: Control distribution of the dilepton mass in events after the trigger, lepton and jet selection (left) and after applying in addition the b-jet selection (right). Other details as in Fig. 7.1.

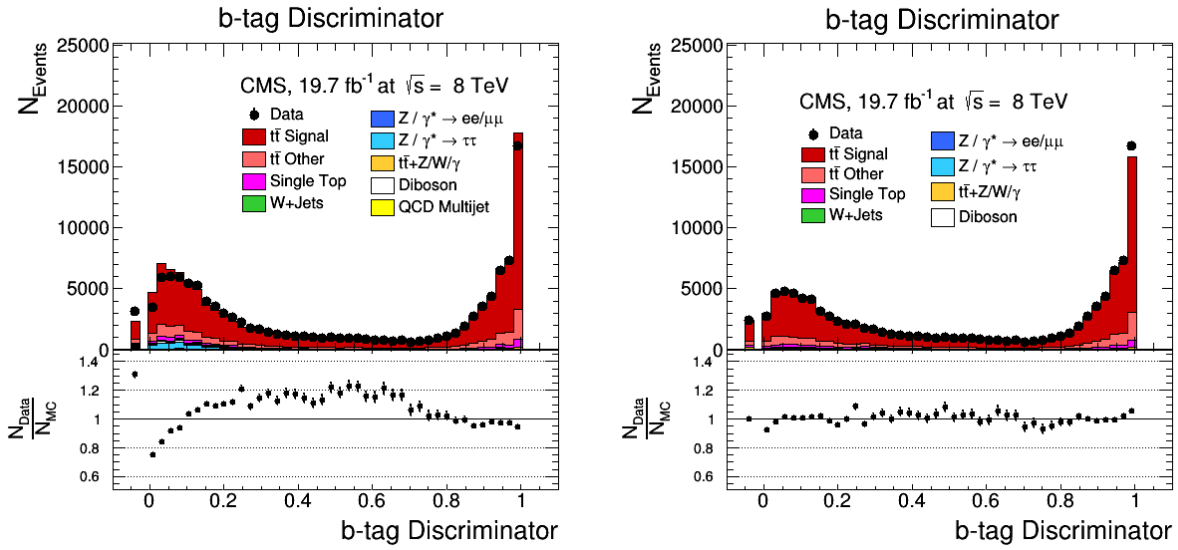

Figure 7.6: Control distribution of the b-tag discriminator in events not applying the b-tag scale factors (left) and after applying the b-tag scale factors (right). Other details as in Fig. 7.1.

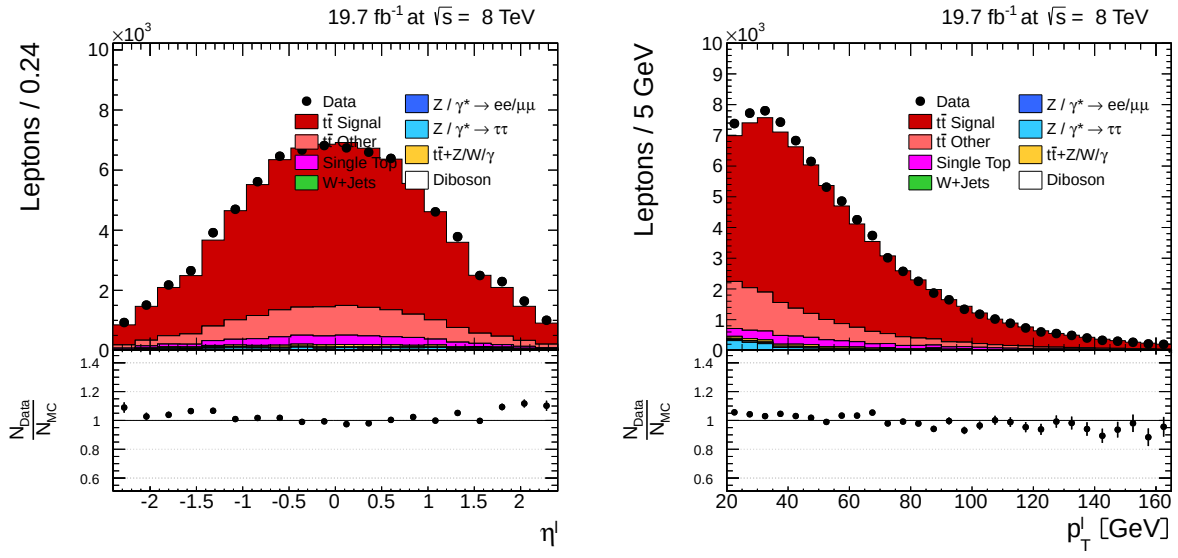

Figure 7.7: Control distribution of lepton η (left) and lepton p_T (right) in events after the whole event selection described in sec. 7.3. Other details as in Fig. 7.1.

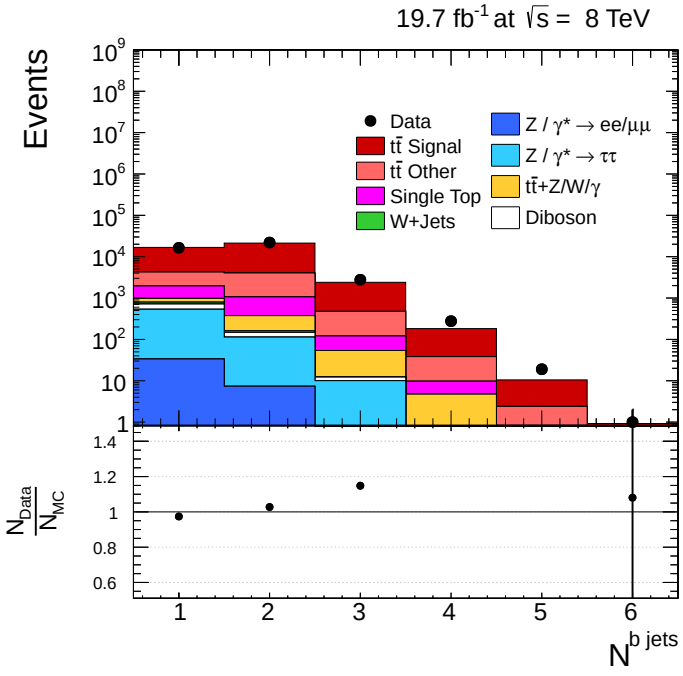

Figure 7.8: Control distribution the b-tagged jets multiplicities in events after the whole event selection described in sec. 7.3. Other details as in Fig. 7.1.

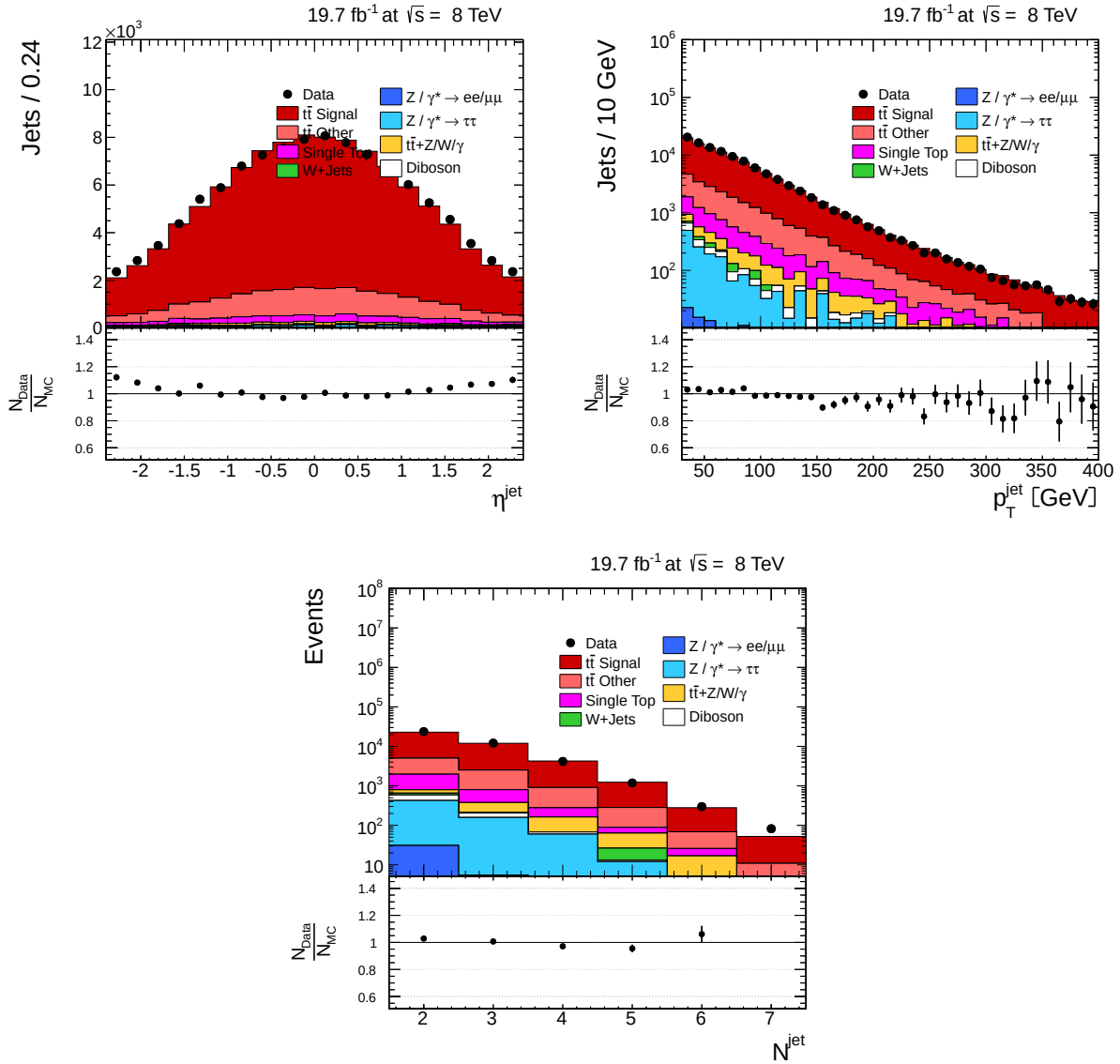

Figure 7.9: Control distribution the jet η (top left) and jet p_T (top right) for all selected jets and the jet multiplicity in events after the whole event selection described in sec. 7.3. Other details as in Fig. 7.1.

Chapter 8

Reconstruction of the top-pair Kinematics

The two neutrinos are not detected, thus additional information and assumptions are needed to determine the full final state kinematics of the $t\bar{t}$ system reconstructed in the dilepton decay channel. This section describes the method used for the full reconstruction. The analytical solution of the kinematic equations (sec. 8.1) as well as a performance test of the method (sec. 8.2 – 8.3) are discussed.

8.1 Analytical Solution of Kinematic Equations

The presence of two undetected neutrinos introduces six unknowns (three momentum components of each neutrino) for the $t\bar{t}$ system in the dilepton final state. The following constraints are being used:

- *t and $\bar{t}$ masses* (m_t and $m_{\bar{t}}$) are assumed to be equal and constrained to the same value of 172.5 GeV [16];

- The whole missing transverse energy E_T^{miss} of the event is assumed to arise entirely from the two neutrinos from the $t\bar{t}$ decay;

- *The $W^{\pm}$ masses* ($m_{W^{\pm}}$) are assumed to be known. As $W^{\pm}$ are resonances with a very small lifetime, their masses are distributed according to a Breit-Wigner function. For this reconstruction, the $W^{\pm}$ masses are set to values randomly taken from the generator Breit-Wigner $W^{\pm}$ mass spectrum.

These assumptions lead to a system of six equations which describe the conservation of energies and momenta:

$$E_{T_x}^{miss} = p_{\nu_x} + p_{\bar{\nu}_x} \tag{8.1}$$
$$E_{T_y}^{miss} = p_{\nu_y} + p_{\bar{\nu}_y} \tag{8.2}$$
$$m_{W^+}^2 = (E_{l^+} + E_\nu)^2 - (p_{l_x^+} + p_{\nu_x})^2 - (p_{l_y^+} + p_{\nu_y})^2 - (p_{l_z^+} + p_{\nu_z})^2 \tag{8.3}$$
$$m_{W^-}^2 = (E_{l^-} + E_{\bar{\nu}})^2 - (p_{l_x^-} + p_{\bar{\nu}_x})^2 - (p_{l_y^-} + p_{\bar{\nu}_y})^2 - (p_{l_z^-} + p_{\bar{\nu}_z})^2 \tag{8.4}$$
$$\begin{aligned} m_t^2 = {} & (E_b + E_{l^+} + E_\nu)^2 - (p_{b_x} + p_{l_x^+} + p_{\nu_x})^2 \\ & - (p_{b_y} + p_{l_y^+} + p_{\nu_y})^2 - (p_{b_z} + p_{l_z^+} + p_{\nu_z})^2 \end{aligned} \tag{8.5}$$
$$\begin{aligned} m_{\bar{t}}^2 = {} & (E_{\bar{b}} + E_{l^-} + E_{\bar{\nu}})^2 - (p_{\bar{b}_x} + p_{l_x^-} + p_{\bar{\nu}_x})^2 \\ & - (p_{\bar{b}_y} + p_{l_y^-} + p_{\bar{\nu}_y})^2 - (p_{\bar{b}_z} + p_{l_z^-} + p_{\bar{\nu}_z})^2 \end{aligned} \tag{8.6}$$

Here the $E_{l^\pm}$ and $p_{l^\pm_{x,y,z}}$ correspond to the lepton(antilepton) energy and momentum components respectively; $E_{b/\bar{b}}$ and $p_{b/\bar{b}_{x,y,z}}$ are the $b/\bar{b}$-jet energy and momentum components respectively; the $E_{T_{x,y}}^{miss}$ are the two components of the missing transverse energy; the $p_{\nu/\bar{\nu}_{x,y,z}}$ are the neutrino (antineutrino) momenta components. The neutrino energies $E_{\nu/\bar{\nu}}$ are determined from their momenta:

$$E_{\nu/\bar{\nu}}^2 = p_{\nu/\bar{\nu}_x}^2 + p_{\nu/\bar{\nu}_y}^2 + p_{\nu/\bar{\nu}_z}^2 \tag{8.7}$$

The quantities $E_{l^\pm}$, $p_{l^\pm_{x,y,z}}$, $E_{b/\bar{b}}$, $p_{b/\bar{b}_{x,y,z}}$ and $E_{T_{x,y}}^{miss}$ are reconstructed from the detector (as described in chapter 6) and $p_{\nu/\bar{\nu}_{x,y,z}}$ are the unknowns.

An analytical solution of the system of equations (8.1–8.6) was proposed in [117]. After a number of transformations the system is reduced to a fourth order polynomial equation for the neutrino momentum component p_{ν_x}:

$$0 = h_0 p_{\nu_x}^4 + h_1 p_{\nu_x}^3 + h_2 p_{\nu_x}^2 + h_3 p_{\nu_x} + h_4, \tag{8.8}$$

where the coefficients $h_0 - h_4$ [117,118] depend on the missing transverse energy E_T^{miss} and four-momenta of the leptons, antileptons, b- and $\bar{b}$-jets.

There can be up to four solutions for equation 8.8. This equation (in case if the coefficients h are such that the equation can not be simplified to the third, second or first order) can not have analytically three or one real solutions as proven in [117], thus, it is expected to get either two or four solutions. However, due to the limited computing accuracy, there may be cases when two solutions are indistinguishable and treated as one. This phenomenon can create three out of four or one out of two solutions.

The distribution of the number of solutions for the generated MadGraph + Pythia $t\bar{t}$ signal sample is shown in Fig. 8.1. Two (four) solutions per event are expected in approx. 80% (20%) of the cases. The cases, when there are one or three solutions found, have a rate of about 0.1%.

8.2 Ambiguity and Detector Effects Treatment

There are several problems arising during the $t\bar{t}$ dilepton final state kinematics reconstruction:

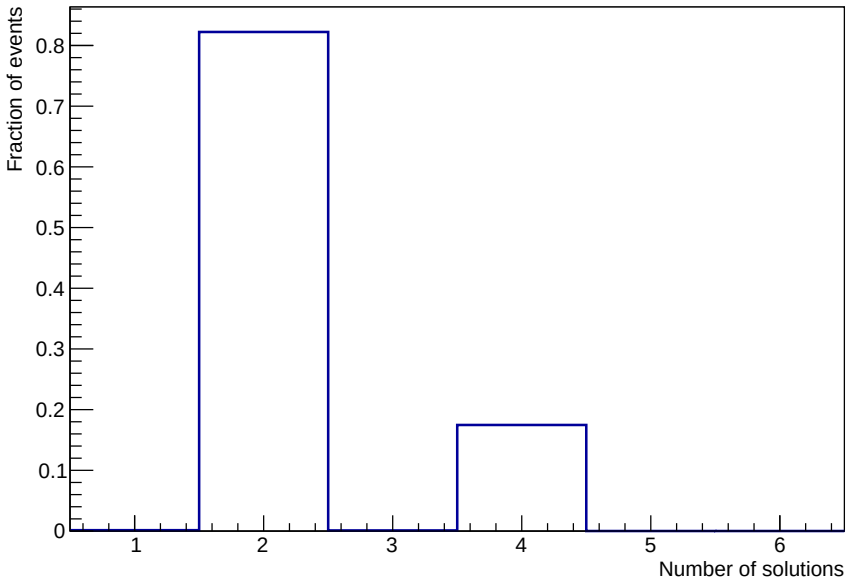

Figure 8.1: Number of solutions of the equation 8.8. The distribution is normalized to unity. The information used for this plot is taken from the generated MadGraph + Pythia $t\bar{t}$ signal for this analysis.

- *Fluctuations of measurement.* There might be no real solutions of the equation 8.8 found for a combination of leptons, jets and missing transverse energy arising from the $t\bar{t}$ system due to reconstruction effects, e.g. detector resolution, jet overlapping, badly reconstructed missing transverse energy, etc. Due to these effects, the kinematics of the reconstructed jets and leptons may be estimated with distortions. Thus, the input parameters of the equations 8.8 will be distorted, which will result in the impossibility to find a real (physical) solution of the equations.

- *Multiple solutions of the kinematic equations.* As discussed in section 8.1 the equation 8.8 has up to four mathematical solutions while only one of them corresponds to the correct kinematics of the neutrino.

- *Multiple combinations of leptons and jets.* An event with a $t\bar{t}$ decaying to a dilepton final state has at least two leptons and two b-jets. However there is a priori no information if a b-jet originates from the t or the $\bar{t}$. For this reason each b-jet candidate is being paired to one of the leptons, and then to another to form a t or $\bar{t}$ candidate. Thus an event with two leptons and two b-jets has two possible $t\bar{t}$ candidates. In case of further jets in the event, the number of $t\bar{t}$ candidates can be up to $N_{jet}!$, where N_{jet} is the jet multiplicity.

8.2.1 Fluctuations of measurements

The problem of rescuing the events which are lost due to fluctuations is solved by varying the measured objects energies and momentum directions. This increases the efficiency

of finding a solution of the system of equations (8.1–8.6) (see Appendix A). The idea was implemented by reconstructing each event 100 times, each time varying relevant observables according to their resolution determined from the Monte Carlo simulation. The energies and directions of leptons and jets are smeared. All variations are done randomly, independently and simultaneously for each quantity.

The energy variation was performed through multiplication of the reconstructed energy value by a correction factor determined from the detector energy response distribution $f = \frac{E_{true}}{E_{reco}}$. Here E_{reco} is the reconstructed lepton or b-jet energy taken from the MC signal simulation and E_{true} is the true energy of the same object on the particle level. The response distributions which are used for the random choice of the correction factors are shown in Fig. 8.2. The response is determined from the signal MC simulation using b-jets and leptons matched to the particle level b-quarks and leptons arising from the decay chain $t \to WB \to l\nu b$. The binning of the response distribution was chosen such that the bin width is significantly smaller than the root mean square (RMS) deviation of these distributions. The distributions shown in Fig. 8.2 have a bin width three times smaller than the RMS[1].

The response distributions for electrons and muons almost do not differ. Their shape is similar, the mean value is the same and the RMS deviation determined in the region $[0.9,\ 1.2]$ is about 5% different. That is why for simplicity the combined distribution for electrons and muons (shown in Fig. 8.2) was used for this analysis.

If, due to the energy smearing, the lepton or jet p_T is reduced to the value beyond the selection criteria (see sec. 7.3), they are still accepted.

The directional smearing is applied by rotating the actual momentum vectors relatively to the nominal vector direction as shown in Fig. 8.3.

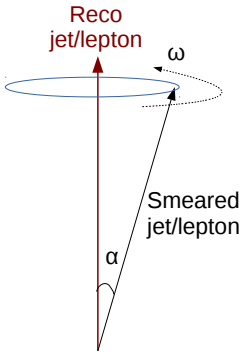

Figure 8.3: Sketch of the directional smearing of leptons and jets as applied in the $t\bar{t}$ kinematic reconstruction.

A smearing of the polar angle α is performed by choosing a random value from the MC distributions presented in Fig. 8.4. The azimuthal angle ω is taken randomly from 0 to 2π. These distributions do not depend on the ϕ coordinate of leptons and b-quarks and have a slight dependence on η. For example, for b-quarks with $\eta \in [-2.5,\ -1.5]$

[1]For this estimation the RMS was determined for the range $[0.5,\ 1.5]$ for the response distribution of jets and $[0.9,\ 1.2]$ for the response distribution of leptons.

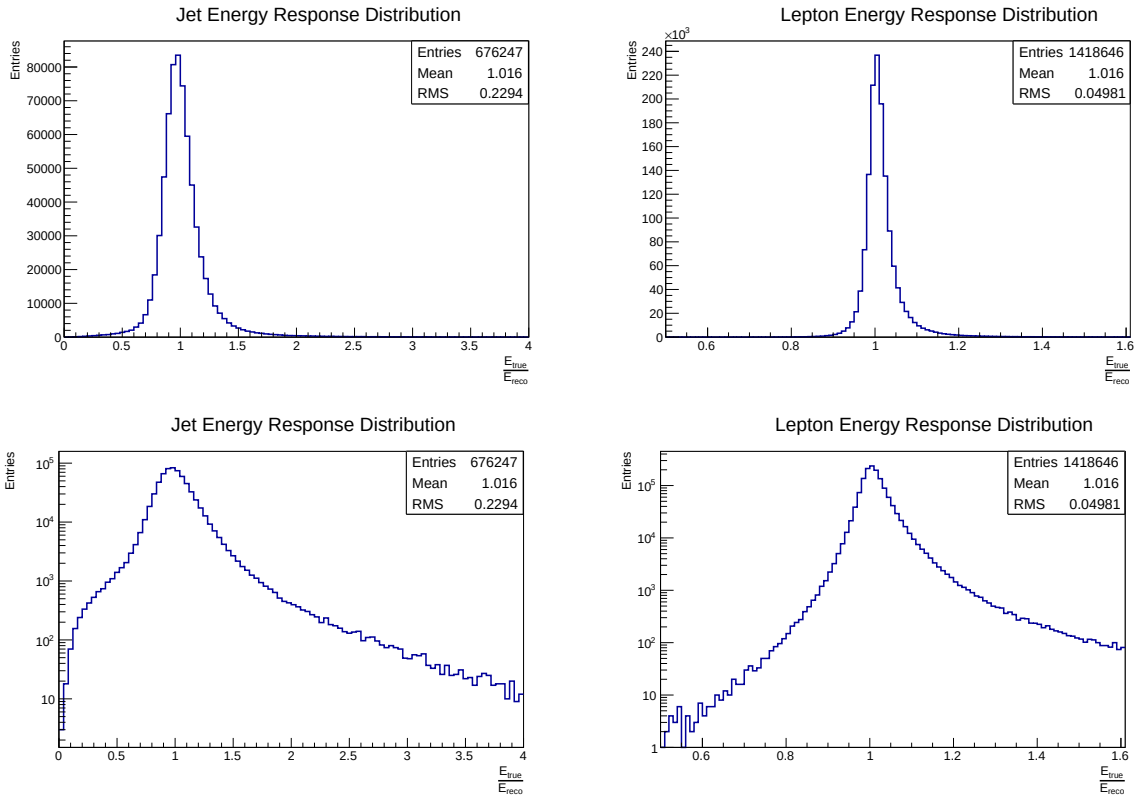

Figure 8.2: Energy response distributions for b-jets (left) and for leptons (right) for the energy smearing in the kinematic reconstruction of the top-quark kinematics. The plots are shown in linear scale (top) and logarithmic scale (bottom).

the mean value of the distributions is 0.025 and RMS is 0.042, while for the b-quarks with $\eta \in [-0.5, 0]$ the mean value is 0.05 and RMS is 0.07. Again, for the simplicity, the response distribution obtained for the total η range was taken for the smearing.

In each of the 100 variations of the jet and lepton kinematics, the transverse missing energy E_T^{miss} has to be recalculated. This is done assuming the transverse energy component, which does not refer to the leptons and jets forming a $t\bar{t}$ candidate, to be constant. Thus the missing transverse energy for the i^{th} smearing will be expressed as following:

$$E_{T_{x,y}}^{miss\ i} = E_{T_{x,y}}^{miss\ from\ reco} + (p_{x,y}^{jets\ reco} - p_{x,y}^{jets\ i}) + (p_{x,y}^{leptons\ reco} - p_{x,y}^{leptons\ i}). \tag{8.9}$$

Here the $E_{T_{x,y}}^{miss\ from\ reco}$, $p_{x,y}^{jets\ reco}$ and $p_{x,y}^{leptons\ reco}$ are the missing transverse energy and momenta components taken directly from the detector reconstruction (see chapt. 6 and 7) without applying any variations; the $p_{x,y}^{jets\ i}$ and $p_{x,y}^{leptons\ i}$ are the smeared jets and leptons momenta respectively on the i^{th} of the 100 variation step.

8.2.2 Single solution choice

The equation 8.8 is solved for every of the 100 event reconstructions. Each equation may have up to four solutions, thus each event has up to $(100 \times 4 \times N_{jet}!)$ reconstructed $t\bar{t}$

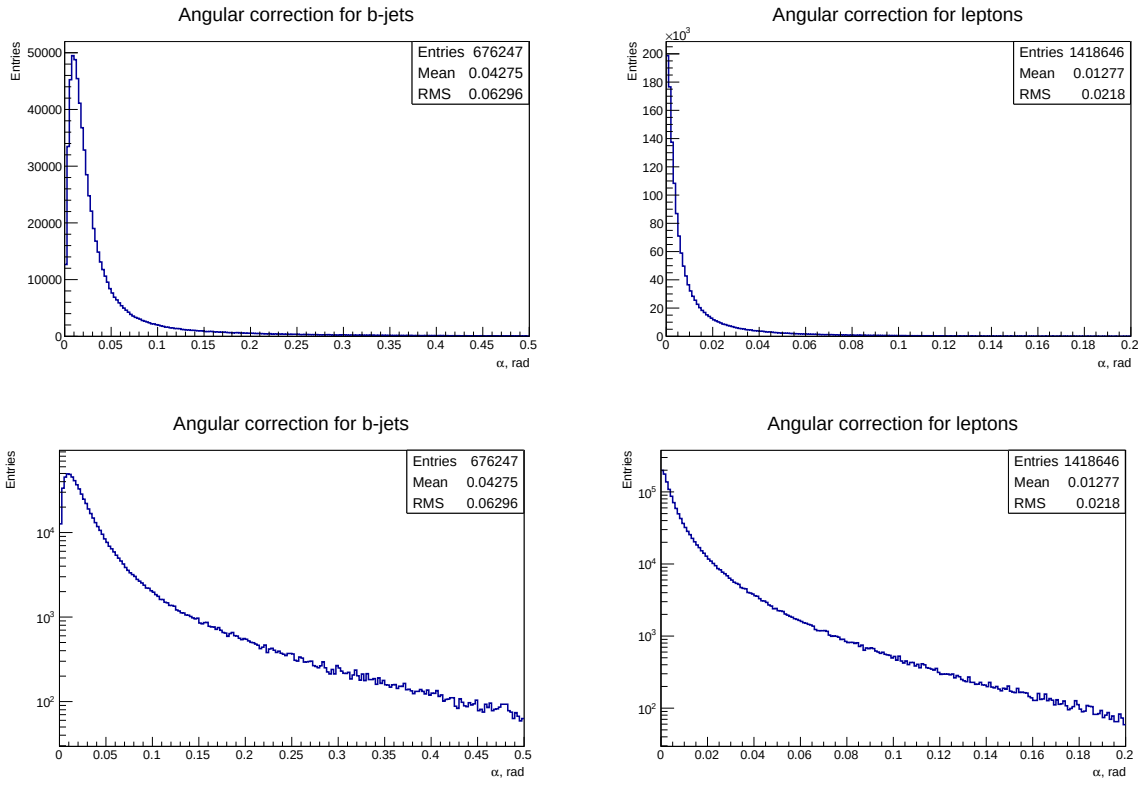

Figure 8.4: Distributions of the angle between the particle level direction and the detector level direction. The angle distribution for the b-quarks is shown on the left and for the leptons (electrons and muons) on the right. The plots are shown in linear scale (top) and logarithmic scale (bottom).

candidates (the factor $N_{jet}!$ has already been discussed is sec. 8.2). To obtain one $t\bar{t}$ pair out of this candidate variety, the following steps are applied:

– First, the single combination of leptons and jets is selected (getting rid of the combinatorics part $N_{jet}!$). If solution with two b-tagged jets (see sec. 6.2.3) are found then combinations with only one b-tagged jet are not considered. Then for each combination a following weight is assigned:

$$\omega = \sum_{i=1}^{100} \omega^i = \sum_{i=1}^{100} \omega^i_{m^{\bar{l}b}} \cdot \omega^i_{m^{l\bar{b}}}. \tag{8.10}$$

Here i is the number of smearing of the event (see sec. 8.2.1), $m^{\bar{l}b}$ and $m^{l\bar{b}}$ are the reconstructed invariant masses of the smeared lepton-jet pairs from the top and the anti-top decays, respectively. These weights are calculated according to spectrum of the correct lepton-jet pairs in top decays obtained from the signal MC on the particle level after all kinematic cuts described in chapter 7 and express the probability of obtaining an invariant mass $m^{\bar{l}b}$ or $m^{l\bar{b}}$ out of the top decay products. The spectrum of $m^{\bar{l}b}$ and $m^{l\bar{b}}$ is shown in Fig. 8.5. A combination of leptons and jets with the

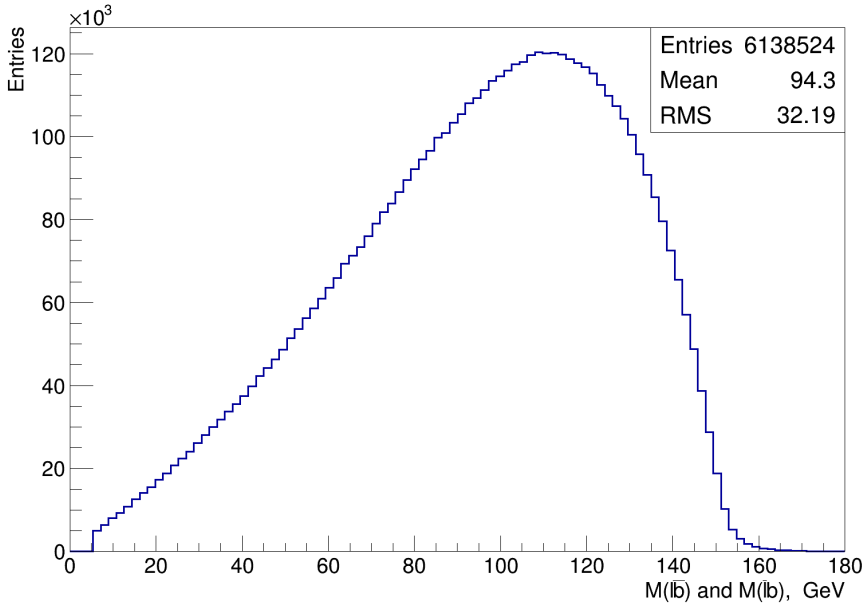

Figure 8.5: Distribution of the invariant mass of the lepton – b-jet system originating from one $t/\bar{t}$-quark. This distribution is obtained from the generator level $t\bar{t}$ signal MC.

highest weight ω is taken for the further analysis. This reduces the number of the possible candidates to maximum 100×4.

– For each of the four solutions of equation 8.8 the invariant mass of the $t\bar{t}$ pair, $m(t\bar{t})$, is calculated. Only the solution with the smallest $m(t\bar{t})$ is taken. The detailed study of the smallest $m(t\bar{t})$ criterion is presented in Appendix B.

– For the remaining up to 100 candidates (these number is related only to the energy and directional smearing, see sec. 8.2.1), the $t(\bar{t})$ momentum is constructed as a weighted average of all smeared solutions as following:

$$\langle \vec{p}(t/\bar{t}) \rangle = \frac{\sum_{i=1}^{100} \omega_i \vec{p}(t/\bar{t})_i}{\omega}. \tag{8.11}$$

Here $\vec{p}(t/\bar{t})_i$ is the t or $\bar{t}$ momentum three vector for the i^{th} variation in the event. The weights (ω and ω_i are taken according to the eq. 8.10). In case that for the i^{th} variation no solution of the kinematic equations is found, both weight and momentum three vector are set to zero. To complete the kinematics, the t and $\bar{t}$ energies are calculated taking $\langle \vec{p}(t/\bar{t}) \rangle$ and assuming the top mass $m(t) = m(\bar{t}) = 172.5$ GeV.

8.3 Performance

Only the events in which solutions of kinematic equations are found are accepted for this analysis. In Fig. 8.6 the efficiencies and scale factors (as defined in chapter 7) for the $t\bar{t}$ kinematic reconstruction procedure depending on jet multiplicity in the event, lepton and b-jets kinematics and missing transverse energy for the data after the full event selection (see sec. 7.3) and the $t\bar{t}$ signal simulation are shown. The integrated efficiency of the kinematic reconstruction method is 93 %. One of the identified sources (from the $t\bar{t}$ signal MC) is the effect that at least one b-jet from t or $\bar{t}$ decay has failed the transverse momentum or rapidity cut and instead a wrong jet was selected.

Overall, the scale factors show a flat behavior depending on different variables, thus a value of 0.99 for the scale factor is used for the analysis. This value was determined from the total number of reconstructed events in data and MC on reconstructed level ($t\bar{t}$ signal and all the background samples) before and after kinematic reconstruction.

The scatter plots in Fig. 8.7 show the correlation between the kinematic variables of the t or $t\bar{t}$ system on the reconstructed and generated levels of the $t\bar{t}$ signal MC. There are no shifts and trends observed, thus showing the trustful behavior of the kinematic reconstruction algorithm.

This kinematic reconstruction method is an alternative to the kinematic reconstruction utilized in the measurement of the single differential $t\bar{t}$ production cross sections in the dilepton channel at $\sqrt{s}$ =7 TeV [119], where no smearing of the leptons and jets energies and directions were performed, and on the other hand the top-quark mass was scanned. The kinematic reconstruction method described in this chapter has a 50% lower inefficiency compared to the previous method.

The control distributions in bins of $M(t\bar{t})$ and $p_T(t)$ obtained using the kinematic reconstruction algorithm described in [119] (previous method) and the method elucidated in this chapter are shown in Fig. 8.8. The $p_T(t)$ spectra obtained with the previous method are softer than the ones obtained with the method used for this analysis. However, this difference in shape between the results determined using different kinematic reconstruction methods was not observed on the cross section level. This cross check shows that the observed differences between data and MC are genuine and not an artifact of the specific kinematic reconstruction algorithm used in the analysis.

8.4 Control Distributions

The kinematic reconstruction method shows good results over the complete kinematic range of the top system. The Fig. 8.9 shows the control distributions of the kinematic quantities of the top quark system. The distribution of the transverse momentum of the top quark shows a good agreement between experimental data and simulation at small and intermediate p_T. However the higher p_T range is not well described by the MC. The measured spectrum in p_T is overall softer than the simulation. The rapidity is well described by the simulation in the central region, whereas for the edges MC slightly underestimates the data – the simulation is more central. An overall good agreement is

observed in the x_1[2] distribution.

In figure 8.10 the control distributions of the kinematic variables of the $t\bar{t}$ system are presented. The transverse momentum is overall well described by the simulation. A slight data excess is observed in central rapidity $y^{t\bar{t}}$ and the edges have also slightly worse agreement between experimental data and MC. The invariant mass of the $t\bar{t}$ system is reasonably well described by the simulation for the complete mass range – in the region of 800-1000 GeV the simulation is a bit lower than data.

8.5 Usage of the Kinematic Reconstruction

Apart of this work, the kinematic reconstruction as described in this chapter has also been implemented into the analysis, which measured the single differential $t\bar{t}$ production cross sections in the dilepton channel at $\sqrt{s}$ =8 TeV, TOP-12-028 [4] [120].

The results obtained in TOP-12-028 [4] [120] exploiting the kinematic reconstruction are presented in Fig. 8.11.

[2] x_1 is a fraction of a proton momentum transfered to a t quark

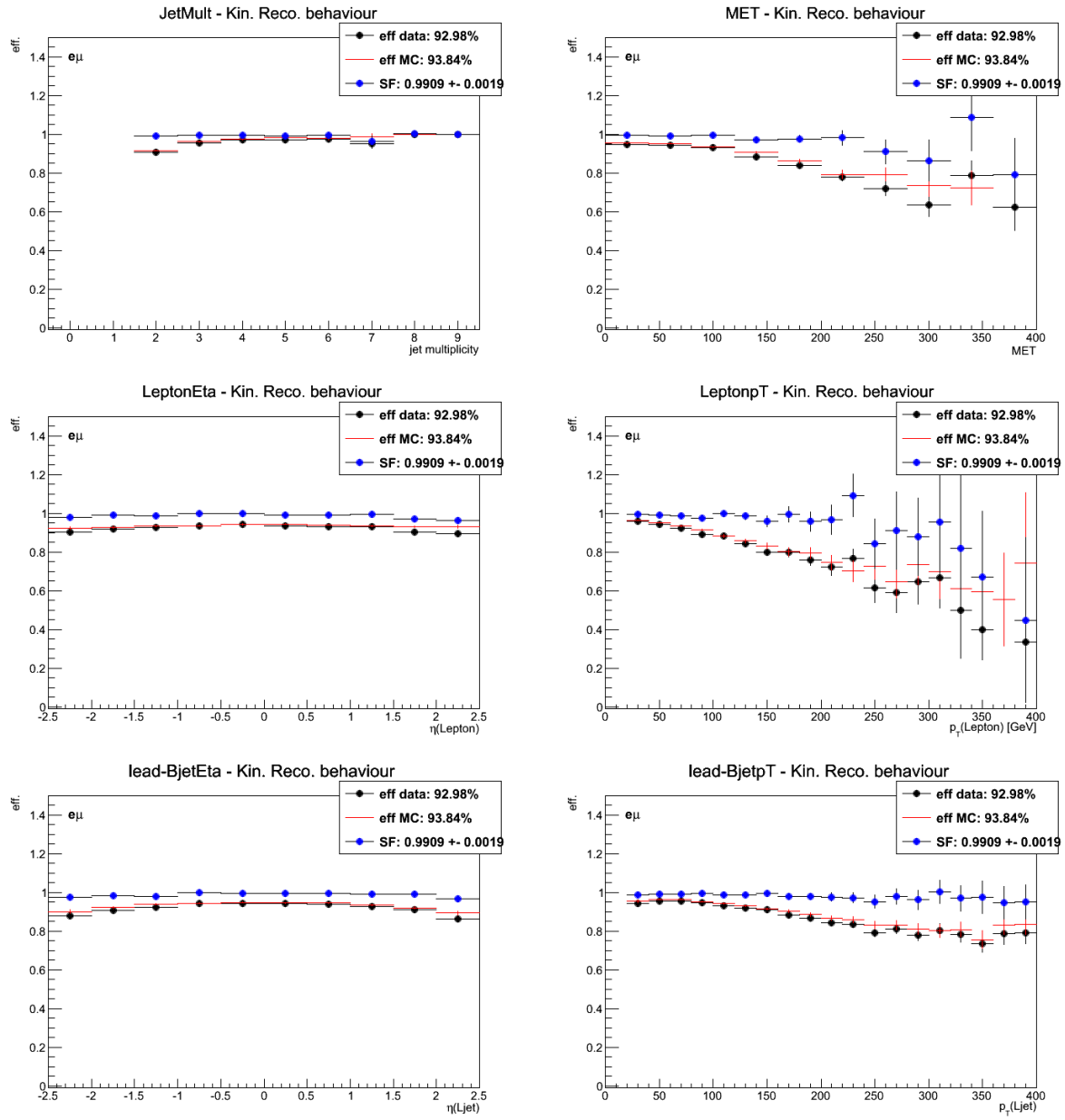

Figure 8.6: The efficiencies and scale factors for the $t\bar{t}$ kinematics reconstruction procedure in bins of the jet multiplicity in the event (top left), missing transverse energy (top right), lepton pseudorapidity (middle left) and transverse momentum (middle right) and b-jet pseudorapidity (bottom left) and transverse momentum (bottom right). The efficiencies in the data are marked with black dots, efficiencies in MC simulations are red lined and the scale factors (ratio of data and MC efficiencies) are plotted with the blue dots. The simulated MC samples contain $t\bar{t}$ signal and the backgrounds.

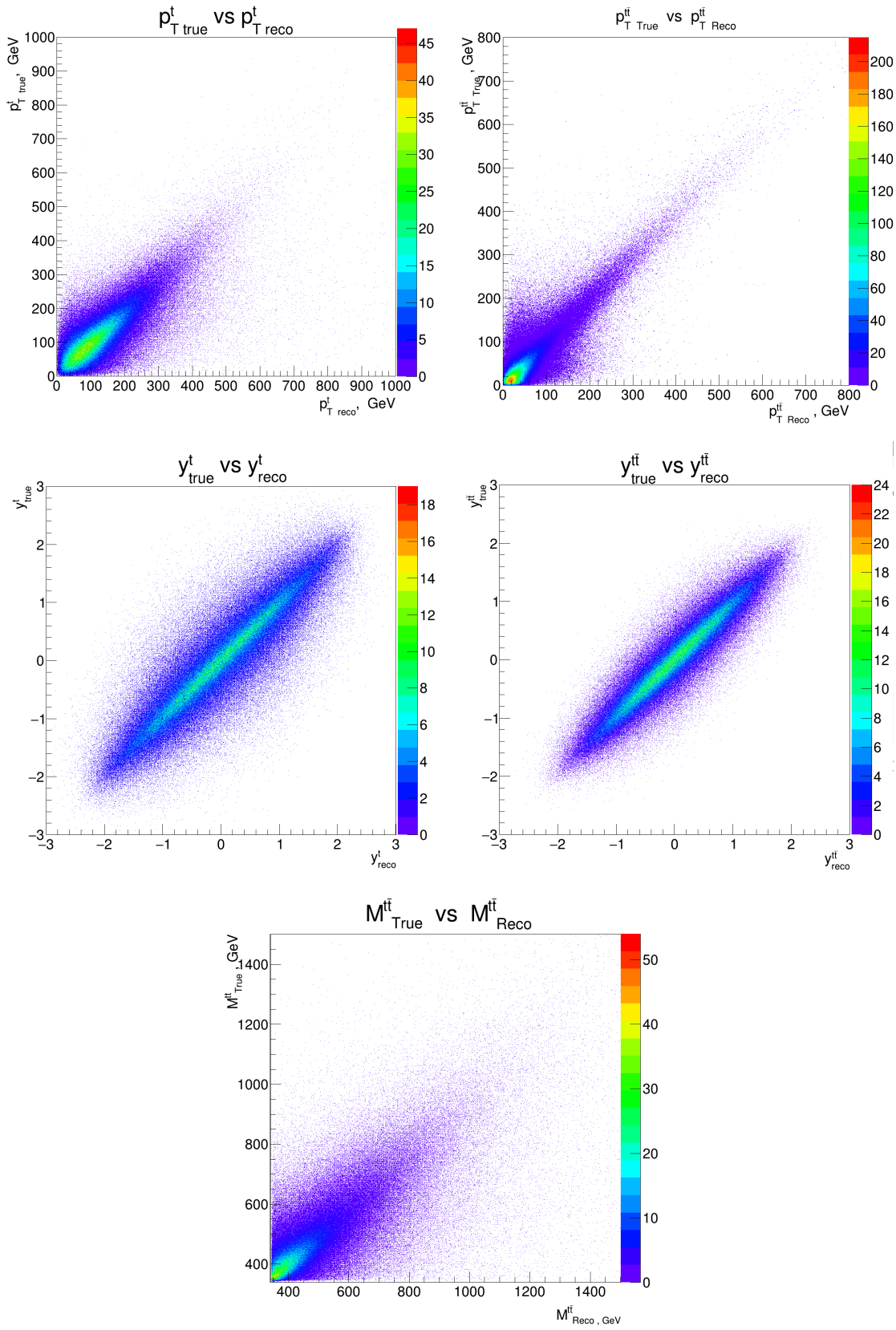

Figure 8.7: Plots which show the reconstructed vs. generated variables: the transverse momentum of the t and $t\bar{t}$ (top left and right respectively), the rapidity of the t and $t\bar{t}$ (middle left and right respectively) and the invariant mass of the $t\bar{t}$ system, obtained from the signal MC.

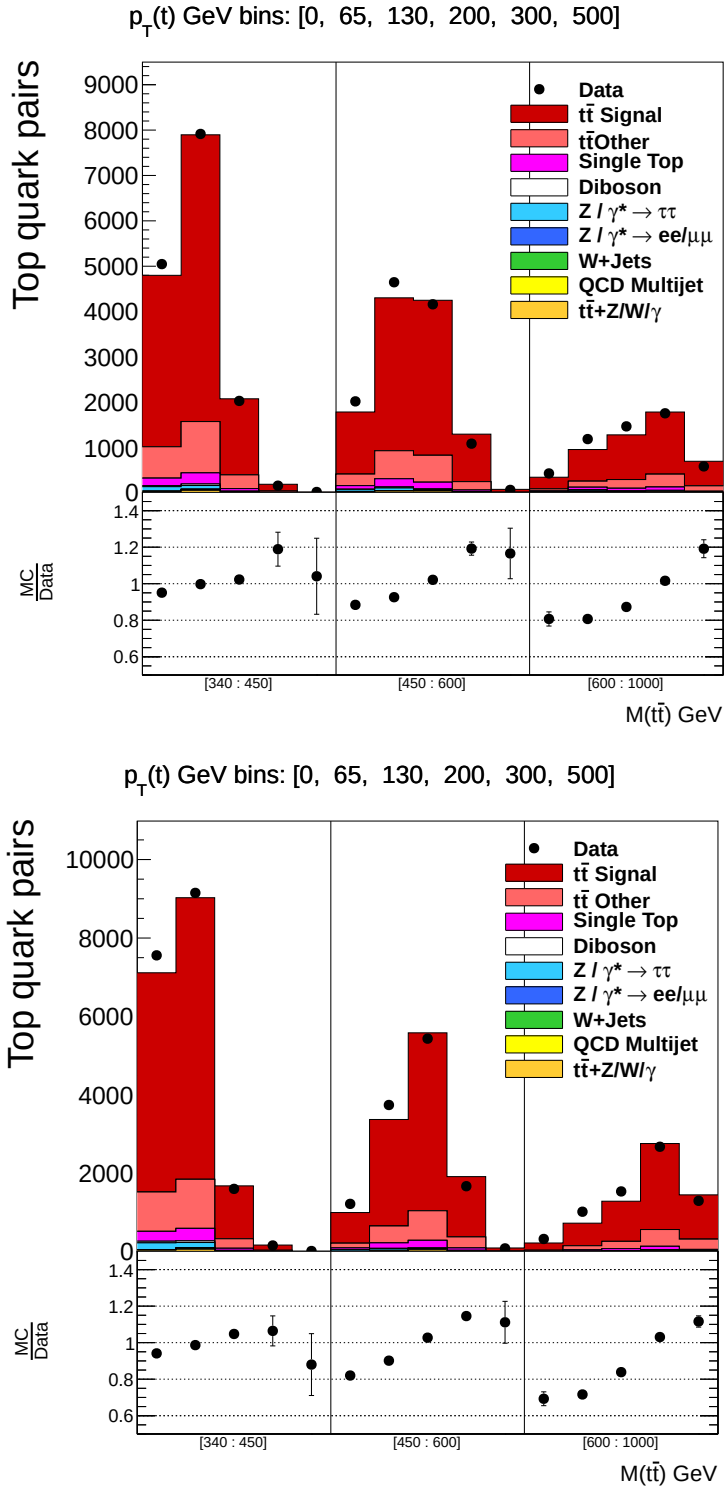

Figure 8.8: Control distribution of the $M(t\bar{t})$ in bins of the p_T of the top quark reconstructed using the kinematic reconstruction described in [119] (top) and the algorithm described in this chapter (bottom). The $p_T(t)$ bins are shown on the top of the plot. The experimental data are marked with black dots with error bars representing the statistical uncertainties only. The simulated distributions of signal and different backgrounds are represented with colored histograms. On the bottom part of the plot the ratio between MC and data yields in each bin is shown with the error bars representing the statistical uncertainties of the data only.

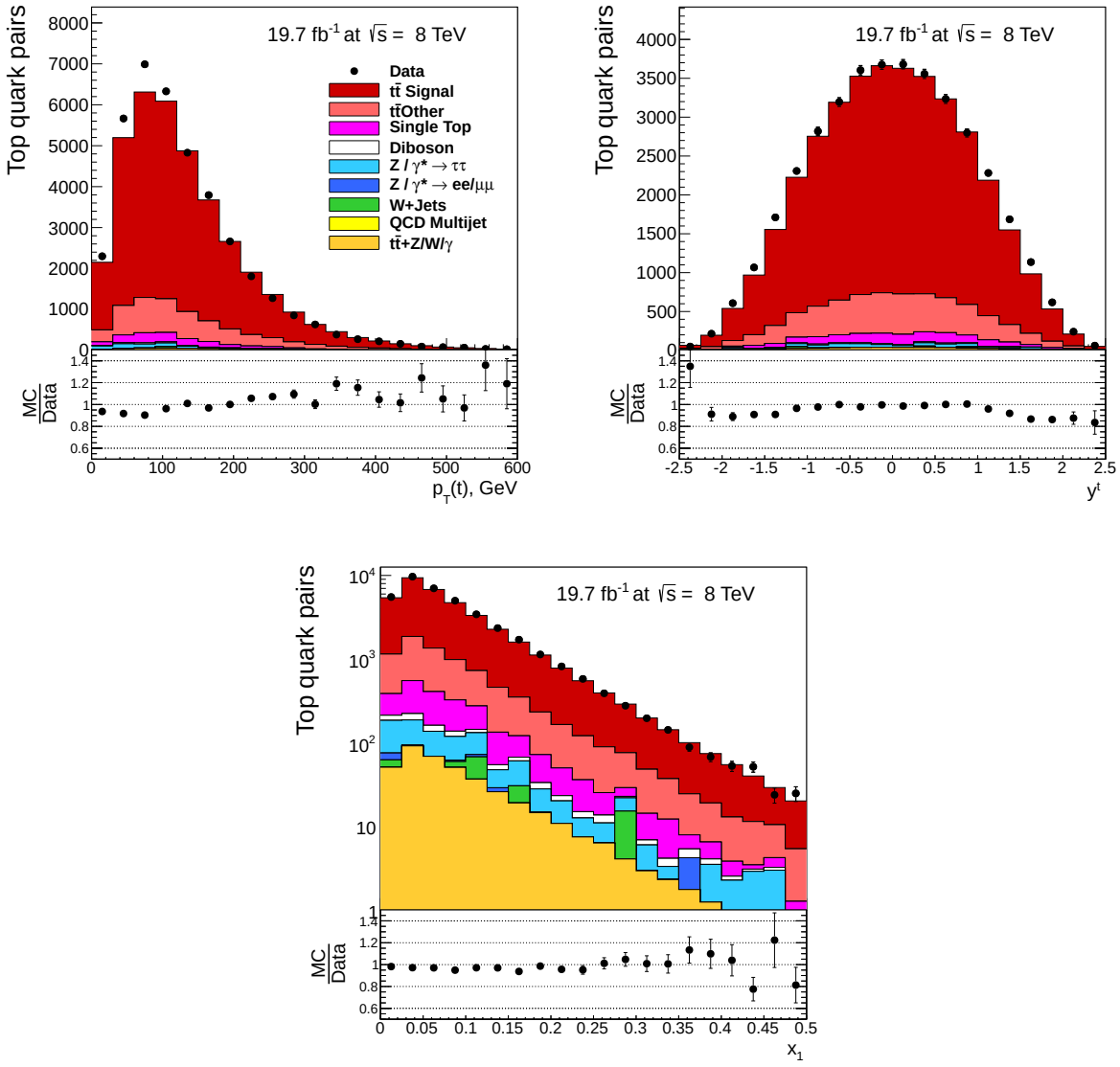

Figure 8.9: Control distributions of the top quark p_T (top left), rapidity (top right) and x_1 in the events after the kinematic reconstruction. The experimental data with the error bars corresponding to the statistical uncertainties and simulated distributions of signal and different background are plotted. Each of the plots show in the bottom panel the MC-to-data yield ratio distributions. The distributions are presented for the t quark only.

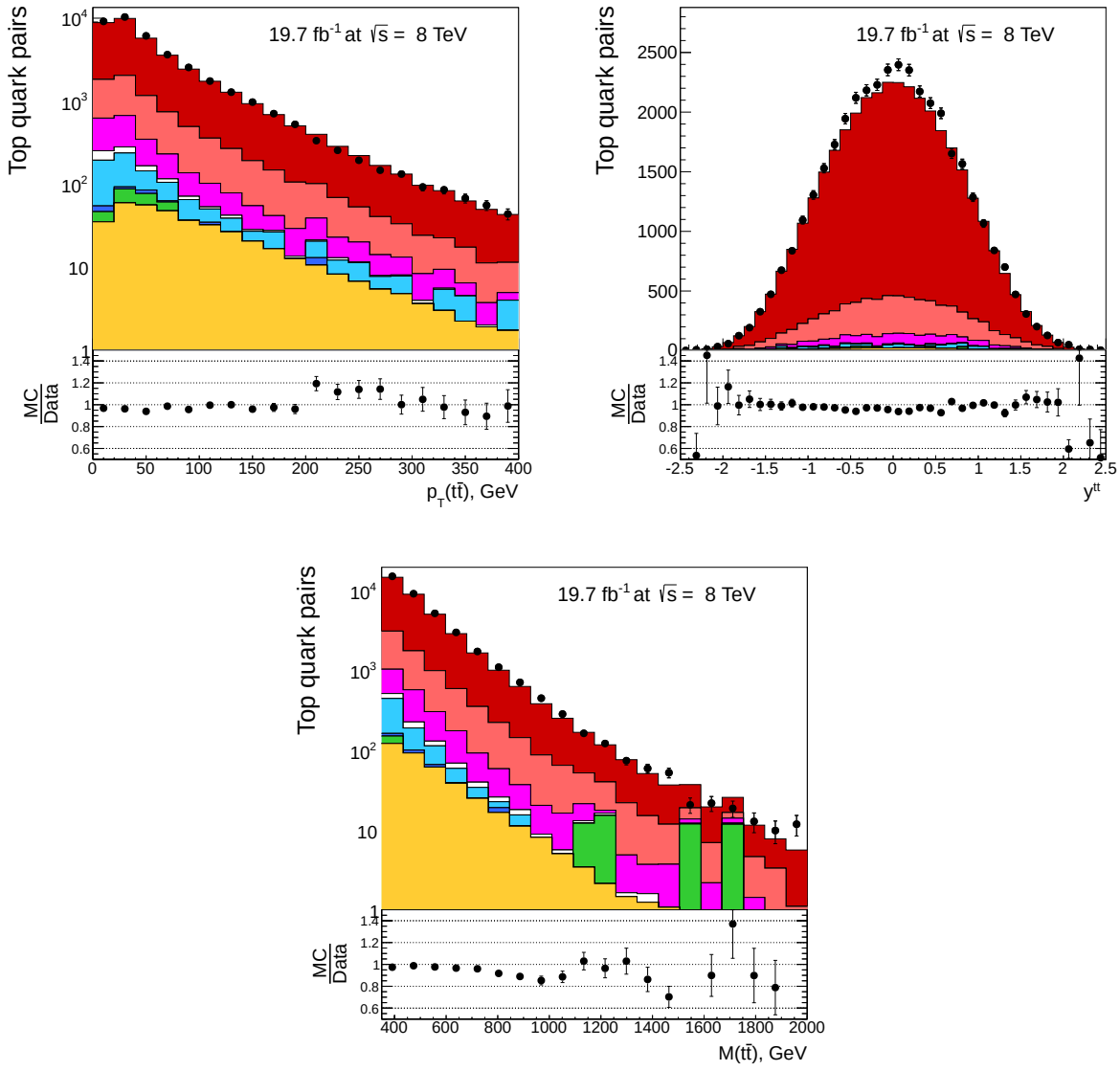

Figure 8.10: Control distributions of the p_T (top left), rapidity (top right) and invariant mass of the $t\bar{t}$ system in the events after the kinematic reconstruction. Other details as in Fig. 8.9.

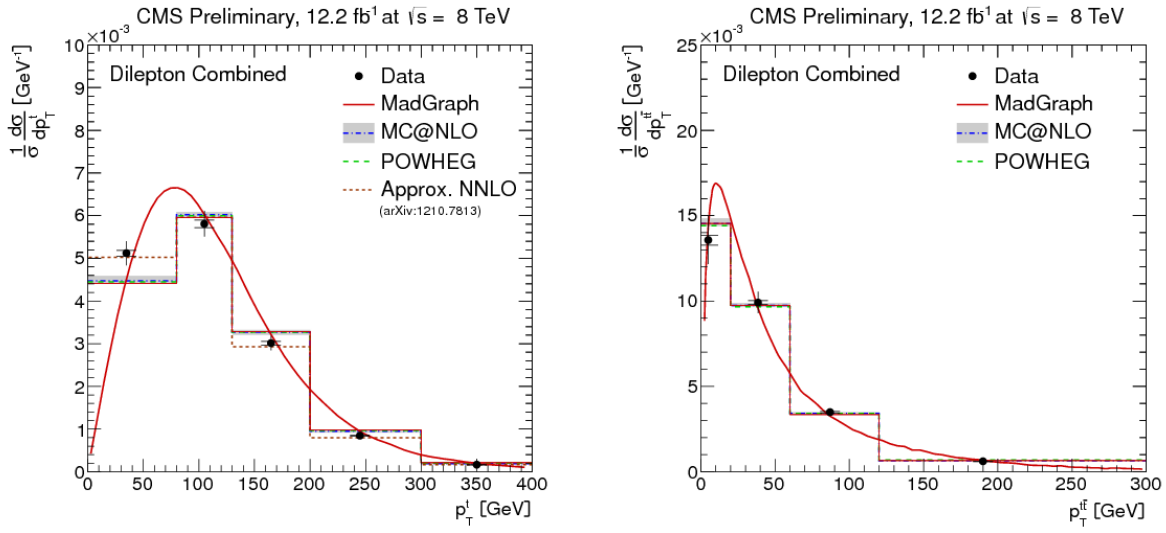

Figure 8.11: Normalised differential $t\bar{t}$ production cross section as a function of the p_T of the top quarks or antiquarks and $t\bar{t}$-pairs. The superscript 't' refers to both top quarks and antiquarks. The inner (outer) error bars indicate the statistical (combined statistical and systematic) uncertainty. The measurement is compared to predictions from MadGraph, Powheg and MC@NLO Monte Carlo generators. The MadGraph prediction is shown both as a curve and as a binned histogram. The figures are taken from [120] [4].

Chapter 9

Cross Section Measurement

The cross section measurement procedure is explained in this section. After applying selection criteria, performing the kinematic reconstruction and subtracting background one can count the events to determine the rate of the $t\bar{t}$ production process.

The cross sections were measured double differentially in bins of the kinematic variables of the top-quark and the $t\bar{t}$ system. The first section shortly describes the way how the background yields were subtracted. The two dimensional unfolding applied to correct for the detector resolution effects and fluctuations is described in the second section. The double differential cross sections definitions are elucidated in the last section of the chapter.

9.1 Background Subtraction

The first step of the cross sections measurement is the counting of the events which fulfill certain criteria (e.g. given in chapter 7 and chapter 8) and subtracting background:

$$N_{reco}^{signal\ measured} = N_{reco}^{selected} - N^{BG} \tag{9.1}$$

Here N^{BG} corresponds to the estimated number of background events, except for the $t\bar{t} \to other$ events. The background sources were introduced in sec. 7.1.

After subtracting all the non-$t\bar{t}$ backgrounds, the number of signal events is multiplied by a factor in each each cross section bin individually to correct for the contribution from other $t\bar{t}$ decay channels:

$$N_{reco}^{signal} = N_{reco}^{signal\ measured} \cdot \frac{N_{reco}^{t\bar{t}\to e\mu}}{N_{reco}^{t\bar{t}\to e\mu} + N_{reco}^{t\bar{t}\to other}}. \tag{9.2}$$

The factor $\frac{N_{reco}^{t\bar{t}\to e\mu}}{N_{reco}^{t\bar{t}\to e\mu}+N_{reco}^{t\bar{t}\to other}}$ was derived from the simulated data.

9.2 Unfolding of the Experimental Results

The signal yields after the background subtraction 9.2 are grouped to the bins in different variables. However, the kinematic properties of the events are measured with finite pre-

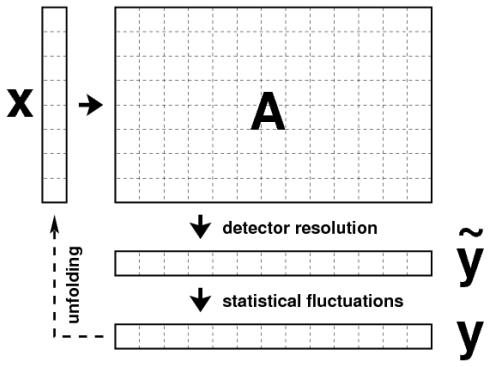

Figure 9.1: Schematic view of the problem of migration effects due to the finite precision of the detector and statistical fluctuations. Plot taken from [121].

cision due to inevitable detector effects and imperfect reconstruction algorithms. Thus, some fraction of events may be reconstructed in the wrong bins. To present the results independent of the detector effects, one needs to correct them back.

The whole problem can be described as

$$\tilde{y}_i = \sum_{j=1}^{m} A_{ij}\tilde{x}_j + b_i, \quad 1 \leq i \leq n. \tag{9.3}$$

Here the $\tilde{x}_j$ in m bins denotes the true distribution, independent of the detector effects, which is the aim of the measurement; $\tilde{y}_i$ in n bins is the distribution which one gets out of the detector and A_{ij} is a matrix of probabilities describing the migrations from true level bin j to detector level bin i to different bins on the detector level; b_i is the background in the bin i. However, the observed event counts y_i may be different from $\tilde{y}_i$ due to the statistical fluctuations. A schematic view of the problem is given in Fig. 9.1.

The process of estimating the true distribution $\tilde{x}_j$ from the observed distribution y_i which was influenced by detector effects and statistical fluctuations is called *unfolding*. The estimated unfolded distribution is called x_j in the following. To suppress statistical fluctuations of imprecisely determined high frequency components of the solution x a smoothing *regularisation* procedure is applied. The TUnfold [121] algorithm was used for the unfolding in this analysis.

9.2.1 TUnfold Minimization

The TUnfold algorithm [121] is using a method based on least square minimization plus Tikhonov regularization [122]. One of the ingredients for a good performance of the method is that the number of degrees of freedom for the minimization $(n - m)$ has to be positive, or $n > m$. This means that the unfolded distribution x_j will have coarser binning than the measured one, y_i.

The unfolding algorithm of the TUnfold determines the stationary point or minimum of the following Lagrangian:

$$\mathcal{L}(x,\lambda) = \mathcal{L}_1 + \mathcal{L}_2 + \mathcal{L}_3, \qquad \text{where} \tag{9.4}$$

$$\mathcal{L}_1 = (\mathbf{y} - \mathbf{A}\mathbf{x})^T \mathbf{V_{yy}}^{-1} (\mathbf{y} - \mathbf{A}\mathbf{x}), \tag{9.5}$$

$$\mathcal{L}_2 = \tau^2 (\mathbf{x} - f_b \mathbf{x_0})^T (\mathbf{L^T L})(\mathbf{x} - f_b \mathbf{x_0}), \tag{9.6}$$

$$\mathcal{L}_3 = \lambda(Y - \mathbf{e}^T \mathbf{x}) \qquad \text{with} \tag{9.7}$$

$$Y = \sum_i y_i, \tag{9.8}$$

$$e_j = \sum_i A_{ij}. \tag{9.9}$$

The bold symbols here correspond to matrices and vectors.

The term $\mathcal{L}_1$ is expected for a least square minimization. The vectors $\mathbf{y}$, $\mathbf{x}$ and the matrix $\mathbf{A}$ were described in the previous section. Representing the migrations into different bins of $\mathbf{y}$, the matrix $\mathbf{A}$ is defined from the $t\bar{t}$ signal Monte Carlo simulation using the information from the generator particle level and on the reconstructed level. It describes how many migrations there are out and into a certain bin. An extra "zero" row is added to the matrix $\tilde{\mathbf{A}}$ containing the information about the count of Monte Carlo events which were generated in some bin of $\mathbf{x}$, but were not reconstructed in any of the $\mathbf{y}$ bins. The matrix $\mathbf{A}$, which enters the unfolding, is the normalized $\tilde{\mathbf{A}}$ defined as $\mathbf{A}_{ij} = \frac{\tilde{A}_{ij}}{\sum_{j=0} \tilde{A}_{ij}}$ (the normalization includes the "zero" row). An example of such a matrix is shown in Fig. 9.2.

The term $\mathcal{L}_2$ is responsible for the regularization. It is reducing the effect of the statistical fluctuations present in $\mathbf{y}$ on high frequency components of $\mathbf{x}$ during the search of the stationary point of the Lagrangian $\mathcal{L}$. The τ^2 is the regularization strength. The matrix $\mathbf{L}$ represents the so-called regularization conditions. In this work the regularization of the second derivative of $\mathbf{x}$ is performed. This corresponds to the initialization of $\mathbf{L}$ matrix with three non-zero elements ($L_{i,i} = 1$, $L_{i,i+1} = -2$ and $L_{i,i+2} = 1$) and $m - 2$ rows. The quantity f_b is a normalization factor and $\mathbf{x_0}$ is the bias vector. In this work the bias vector is taken from the signal simulation on the generator level and $f_b = 1$ is used. It is very important to choose the optimal regularization strength, as a very weak strength would not damp the fluctuation effects from $\mathbf{y}$, whereas a very strong one will bias $\mathbf{x}$ towards $f_b \mathbf{x}_0$. The L-curve method [123] and the minimization of correlation coefficients [124] are implemented in TUnfold for an optimal regularization strength choice.

The idea of the L-curve method is to look at the graph L_x^{curve} vs L_y^{curve} and choose the τ from the point with maximal curvature. The L_x^{curve} and L_y^{curve} are expressed as follows:

$$L_x^{curve} = \log \mathcal{L}_1, \tag{9.10}$$

$$L_y^{curve} = \log \frac{\mathcal{L}_2}{\tau^2}. \tag{9.11}$$

The L-curve graph is in fact comparing the two terms of the Lagrangian: the minimization term $\mathcal{L}_1$ and the regularization term $\mathcal{L}_2$. The maximum curvature point of this

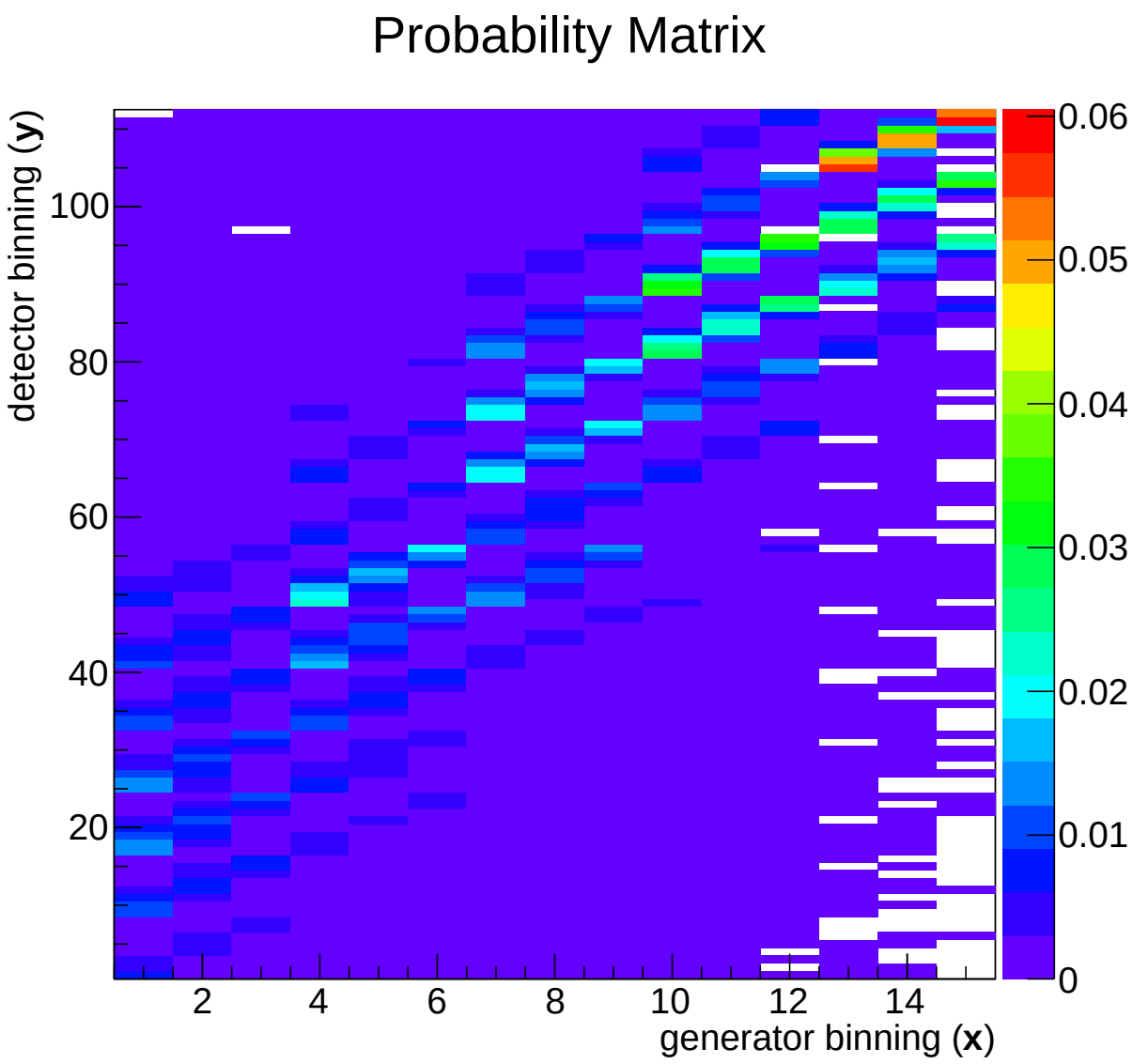

Figure 9.2: Normalized migration matrix **A** (probability matrix) in bins of $p_T(t)$ and $|y(t)|$. The generator binning consists of five groups of three bins (1-3, 4-6, 7-9, 10-12, 13-15). It corresponds to the five $p_T(t)$ bins ([0 .. 65 .. 130 .. 200 .. 300 .. 500] GeV) having three $|y(t)|$ bins ([0 .. 0.6 .. 1.2 .. 2.5]) in each $p_T(t)$ bin. Detector binning consists of fourteen groups of eight bins (1-8, 9-16, 17-24, 25-32, 33-40, 41-48, 49-56, 57-64, 65-72, 73-80, 81-88, 89-96, 97-104, 105-112). It corresponds to fourteen $p_T(t)$ bins ([0 .. 20 .. 35 .. 50 .. 65 .. 80 .. 100 .. 130 .. 145 .. 170 .. 200 .. 240 .. 300 .. 350 .. 500] GeV) having eight $|y(t)|$ bins ([0.0 .. 0.2 .. 0.4 .. 0.6 .. 0.8 .. 1.0 .. 1.2 .. 1.5 .. 2.5]) in each $p_T(t)$ bin. The matrix is obtained from the MadGraph + Pythia6 $t\bar{t}$ signal sample.

L-curve is a point of compromise between the size of the $\mathcal{L}_1$ and $\mathcal{L}_2$ contributions to the total Lagrangian.

The method of minimizing the global correlation coefficients chooses the τ at the point where the average correlation coefficient $\sum_i \frac{\rho_i}{m}$ is minimal. Here i is the component of $\mathbf{x}$ with size m. The correlation coefficient ρ_i is given as follows:

$$\rho_i = \sqrt{1 - \frac{1}{(\mathbf{V}_{xx}^{-1})_{ii}(\mathbf{V}_{xx})_{ii}}}. \tag{9.12}$$

$\mathbf{V}_{xx}$ is the covariance matrix[1] for $\mathbf{x}$ which is a key result of the unfolding. In the TUnfold this matrix is determined by error propagation from $\mathbf{V}_{yy}$:

$$\mathbf{V}_{xx} = \mathbf{D}^{xy}\mathbf{V}_{yy}(\mathbf{D}^{xy})^{\mathbf{T}}, \tag{9.13}$$

where $(\mathbf{D}^{xy})_{ki} = \frac{\delta x_k}{\delta y_i}$ is the propagator matrix from $\mathbf{y}$ to $\mathbf{x}$. A detailed description of how the propagation is done is documented in [121]. An example of a normalized covariance matrix is shown in Fig.9.3. All covariance matrices determined in this analysis are shown in Appendix H.

In Fig. 9.4 examples of the choices of regularization strength for the L-curve and minimizing global correlation coefficients methods are shown.

The term $\mathcal{L}_3$ is an orthogonal area constraint with a Lagrangian parameter λ. If λ is not set to zero, which means the area constraint is used, the $\mathbf{x}$ is forced to match the total event count Y corrected for the efficiencies $\mathbf{e}$. This is used to limit the normalization biases if the data $\mathbf{y}$ follow Poisson's statistics [125].

The stationary point of the Lagrangian $\mathcal{L}(\mathbf{x}, \lambda)$ is defined by setting the first derivatives to zero. In case no area normalization is performed, the Lagrangian $\mathcal{L}$ depends only on $\mathbf{x}$ and the $\mathcal{L}_3$ term is zero.

The multidimensional unfolding can be done in the TUnfold algorithm in a way that the multidimensional arrays are mapped to the one-dimensional arrays and the unfolding is performed as described in this section.

Regularization Strength Studies

The regularization aims to minimize fluctuations effects. To check the performance of the regularization as implemented in TUnfold, the reconstructed signal MC sample was unfolded. The outcome of this unfolding should be the generated signal distributions. The number of entries in the reconstructed signal MC distributions were fluctuated randomly in each bin independently within the statistical uncertainties of the real data in the corresponding bin. These statistical uncertainties were assumed to be Gaussian. The fluctuations were performed 3000 times. Each of the 3000 fluctuated distributions was unfolded and the following quantities were checked:

- τ **scan**. The regularization strength τ is determined using either an L-curve scan or the minimization of correlation coefficients, for each of the 3000 fluctuated distributions. The regularization strength distributions are shown in Fig. 9.5. The

[1] The *covariance matrix* of the vector $\mathbf{v}$ is the matrix in which each element with position ij represents the covariance between the i^{th} and j^{th} element of the vector $\mathbf{v}$.

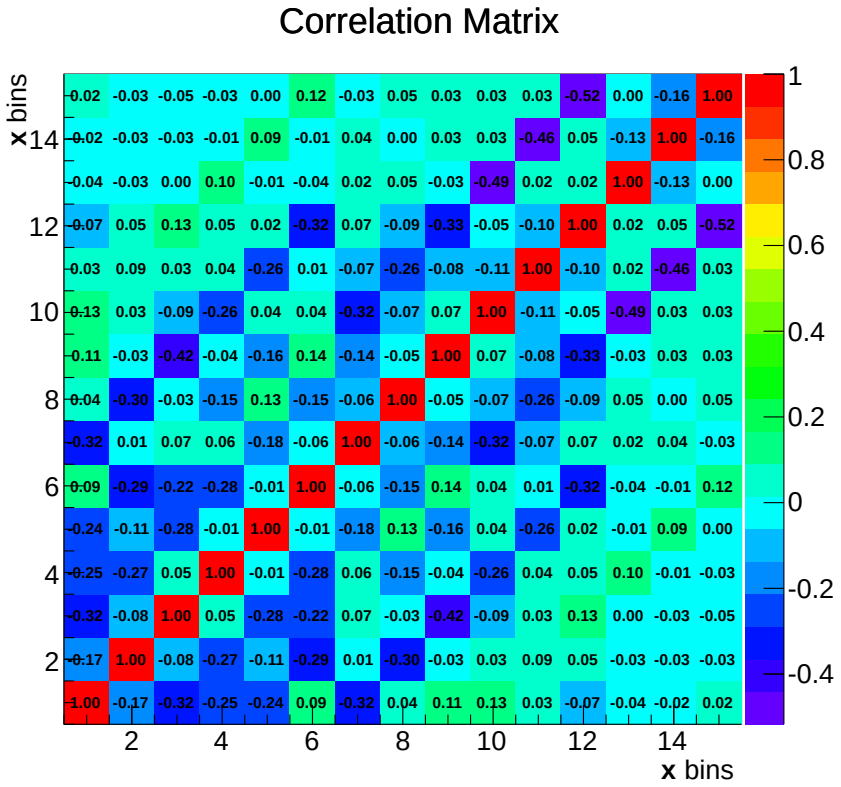

Figure 9.3: Correlation matrix $\mathbf{V}_{xx}$ for the bins of $p_T(t)$ and $|y(t)|$. The binning is the following: the five sequences of three bins (1-3, 4-6, 7-9, 10-12, 13-15) correspond to the five $p_T(t)$ bins [0..65..130..200..300..500] GeV. There are three $|y(t)|$ bins – [0..0.6..1.2..2.5] – in each $p_T(t)$ bin.

regularization strength defined in the L-curve method has multiple peaks which shows an instability of the τ choice. Such a phenomenon is not observed for the global correlation coefficients minimization. Here a single value of the regularization strength is preferred for all the unfolded distributions. Thus, the minimization of the global correlation coefficients is used for the cross section determination.

- **Relative difference between unfolded and generated values.** The mean number of entries in one bin determined from 3000 fluctuated and unfolded distributions is compared to the number of entries in the corresponding generated distribution. The quantity which evaluates this comparison is $\frac{\mathbf{x}-\mathbf{x}_0}{\mathbf{x}_0}$, where $\mathbf{x}_0$ is the bias vector and $\mathbf{x}$ is the unfolded fluctuated signal. The distributions of this quantifier in different $p_T(t)$ and $|y(t)|$ bins obtained using the L-curve method and minimizing the correlation coefficients are shown in Fig. 9.6. For both methods the overall relative deviations from zero are not higher than 3%, which means there are no big discrepancies in the unfolding outcome.

- **RMS over mean error distribution**. For each bin each of the 3000 toy experiment results will differ. To quantify if the spread of the values is not disagreeing

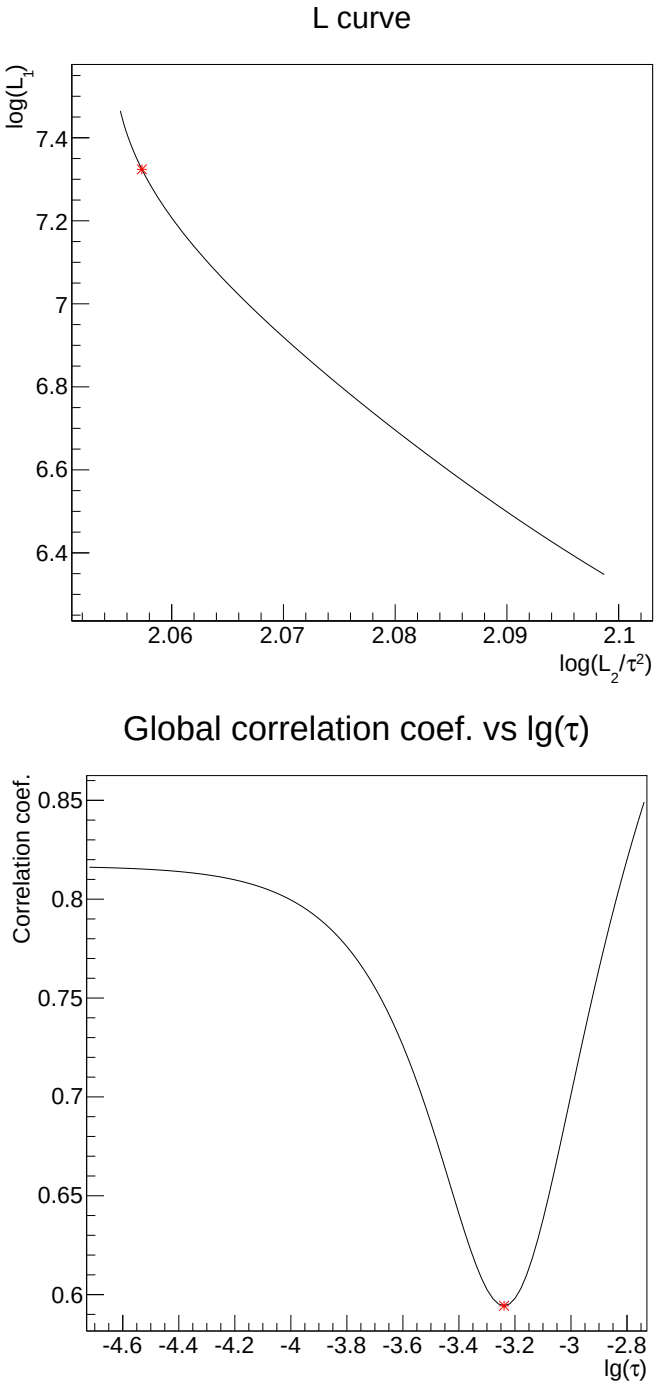

Figure 9.4: Illustration of the choice of the optimal regularization strength with the L-curve method (top) and minimization of correlation coefficient (bottom). The red dots represent the points corresponding to the finally chosen values of τ.

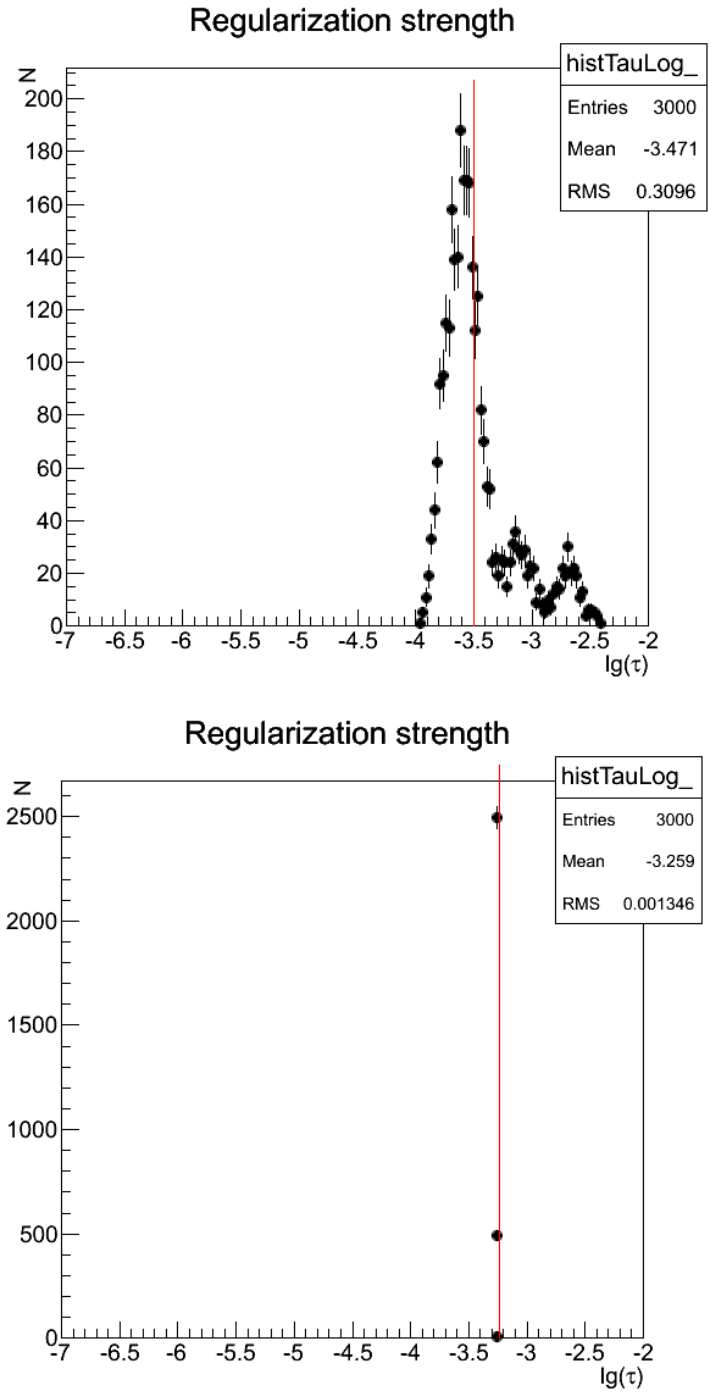

Figure 9.5: Distribution of the regularization strength τ found in MC toy experiments with the L-curve method (top) and the minimization of correlation coefficients (bottom). The red line represents the regularization strength value found by the corresponding method when unfolding the real data.

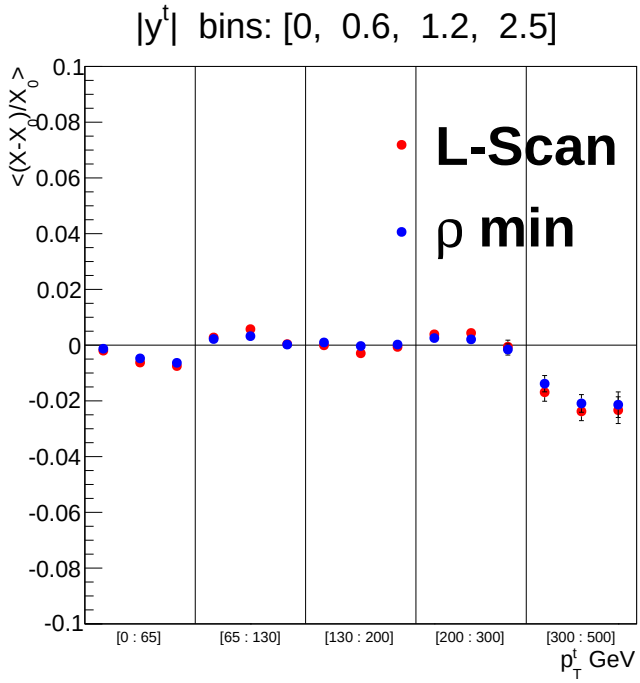

Figure 9.6: Relative difference between unfolded and generated values for the 3000 fluctuated and unfolded reconstructed MC signal samples in bins of top $p_T(t)$ and $y(t)$. The results obtained with the L-curve method are marked with red points and for the correlation coefficient minimization with blue points.

with the statistical uncertainties, one can look at the RMS (root mean square) of the values in a certain bin divided by the mean errors[2] of these values. This value is expected to be equal to unity. The distributions of the RMS over mean error in different $p_T(t)$ and $|y(t)|$ bins obtained using the L-curve method and minimizing the correlation coefficients are shown in the Fig. 9.7. The results obtained with the L-curve method overshoot unity. This means that the unfolded $\mathbf{x}$ value for the L-curve method underestimates the errors. On the other hand, the results obtained with minimizing the global correlation coefficients are in agreement with unity.

As a consequence of these studies the minimization of the correlation coefficients method for the regularization strength determination was chosen in this analysis.

A study of the influence of the regularization strength on the result of the measurement was performed by manually setting the regularization strength to zero. This study is described in Appendix C.

[2]The mean error for each bin is defined as an arithmetic mean over the error of each of the 3000 unfolded measurements in this bin. Each particular error is derived using the $\mathbf{V}_{xx}$ (see eq. 9.13) and taking the square root of the respective diagonal element.

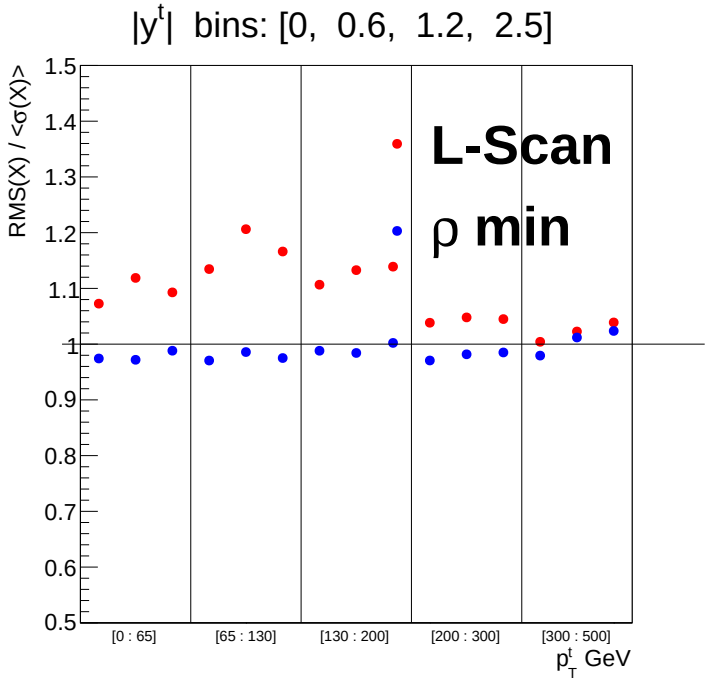

Figure 9.7: RMS over mean error for the 3000 fluctuated and unfolded reconstructed MC signal samples in bins of top $p_T(t)$ and $|y(t)|$. The results obtained with the L-curve method are marked with red points and for the correlation coefficient minimization with blue points.

Closure Tests

The unfolding procedure with all its assumptions should be able to reproduce distributions which are different in the shape compared to simulated $t\bar{t}$ signal data, from which the migration matrix for unfolding was extracted. To test this, *pseudo-data* are unfolded.

The pseudo-data are created by reweighting the $t\bar{t}$ signal MadGraph + Pythia distributions in bins of $p_T(t)$ and $|y(t)|$ with the following weights:

$$\omega(p_T(t)) = max(0.1, \quad a_1 \cdot p_T(t) + b_1), \tag{9.14}$$

$$\omega(|y(t)|) = a_2 \cdot |y(t)|^2 + b_2. \tag{9.15}$$

Here the $a_{1,2}$ and the $b_{1,2}$ are arbitrary parameters. For the studies presented in this work the values for the parameters were the following:

- For the $p_T(t)$ distribution reweighting: $a_1 = 0.0015$, $b_1 = 0.8$ and $a_1 = -0.0015$, $b_1 = 1.2$.
- For the $|y(t)|$ distribution reweighting: $a_2 = 0.17$, $b_2 = 0.7$ and $a_2 = -0.17$, $b_2 = 1.3$.

The parameter values were chosen such that the resulting shape variations are significant compared to the statistical uncertainties of the data.

The results of the unfolding of the pseudo-data are presented in Appendix D. They show that the unfolding is reproducing the shape of the distorted pseudo-data without

any biases towards the distributions, which were exploited to construct the migration matrices.

9.3 The Double Differential $t\bar{t}$ Production Cross Sections

9.3.1 Cross Section Definition

After all corrections are performed, the signal events grouped to different bins are used to define the normalized double differential cross sections of the $t\bar{t}$ production process:

$$\Delta\, y_j : \qquad (\frac{1}{\sigma}\frac{d\sigma}{dx})_i = \frac{1}{\sigma} \cdot \frac{1}{\Delta x_i} \cdot \frac{N_{ij}^{signal\ \ unfolded}}{\epsilon_{ij} \cdot BR \cdot L} \tag{9.16}$$

Here σ denotes the total cross section, ϵ_{ij} the analysis efficiency, BR the branching ratio of the $t\bar{t}$ $e\mu$ decay channel and L the luminosity of the data collected by the CMS detector, which corresponds to 19.7 fb^{-1}. The x and y are the kinematic variables in which the cross sections are measured. The i and j are the indices of the bins of the variables x and y with widths Δx_i and Δy_j. The quantity $N_{ij}^{signal\ \ unfolded}$ denotes the number of corrected and unfolded signal events in the ij^{th} bin. Taking to account that the migration matrix is already normalized to the efficiency (see the construction of the matrix in sec. 9.2.1), the ratio $N_{ij}^{signal\ \ unfolded}/\epsilon_{ij}$ is directly extracted from the unfolding.

The total production cross section σ is defined as follows:

$$\sigma = \frac{N^{signal\ \ unfolded}}{\epsilon \cdot BR \cdot L}. \tag{9.17}$$

Here $N^{signal\ \ unfolded}$ denotes the total number of the signal events extracted from the unfolding.

9.3.2 Phase Space Definition

The analysis efficiency determination ϵ_{ij} (from eq. 9.16) is based on the $t\bar{t}$ signal Monte Carlo simulation. It may be defined in two different ways:

- In the **full phase space**, taking to account the selection and the detector efficiencies:

$$\epsilon = \mathcal{A} \cdot \epsilon^{det}, \tag{9.18}$$

  where $\mathcal{A}$ is the *acceptance* which defines the effect of the kinematic selection and ϵ_{ij}^{det} is the detector efficiency part. The acceptance is determined on the generator level:

$$\mathcal{A} = \frac{N_{gen}^{PS\ selection}}{N_{gen}^{total}}. \tag{9.19}$$

Here N_{gen}^{total} is the total number of all generated $t\bar{t}$ signal events, The $N_{gen}^{PS\ selection}$ is the number of generated $t\bar{t}$ signal events which pass the so-called phase space selection for the generated leptons and b-jets. This selection fully corresponds to the one applied on the reconstruction level (see sec. 7.3) and requires:

- Two leptons from the W from the top decays with $p_T \geq 20$ GeV and $|\eta| \leq 2.4$;
- Two b-jets from the top decays with $p_T \geq 30$ GeV and $|\eta| \leq 2.4$.

The acceptance extrapolates the measurements outside the phase space selection criteria to the full phase space, relying on the theory model of the MC generators. The jets on the generator level are defined analogously to the reconstructed jets (see sec. 6.2.3) applying the anti-k_T algorithm with the cone of $\Delta R = 0.5$ on the all stable particles after the hadronization. The jets containing the B-hadrons originating from the b quarks from the top decay are the b-jets used for the phase space selection.
The detector efficiency is defined by the following ratio:

$$\epsilon^{det} = \frac{N_{reco}^{selected}}{N_{gen}^{PS\ selection}}. \tag{9.20}$$

Here $N_{reco}^{selected}$ is the number of simulated reconstructed events. Thus, combining the equation 9.18, 9.19 and 9.20, the analysis efficiency is expressed as following:

$$\epsilon = \frac{N_{reco}^{selected}}{N_{gen}^{total}}. \tag{9.21}$$

- In the **visible phase space**. This efficiency does not take into account the selection efficiency, it consists only of the detector efficiency:

$$\epsilon = \epsilon^{det} = \frac{N_{reco}^{selected}}{N_{gen}^{PS\ selection}}. \tag{9.22}$$

This efficiency definition does not rely on the theoretical predictions for the region outside the visible phase space, but the measured cross section will depend on the selection criteria.

The cross sections are measured in the full phase spaces, normalized and not normalized to the total cross section σ.

9.3.3 Efficiency, Purity and Stability

The quality of the reconstruction in each bin can be characterized by three quantities – *efficiency* ϵ, *purity* p and *stability* s. They are defined in the following way:

$$\epsilon_{ij} = \frac{N^{reco} \cup N_{ij}^{gen}}{N_{ij}^{gen\ tot}}, \tag{9.23}$$

$$p_{ij} = \frac{N_{ij}^{gen} \cup N_{ij}^{reco}}{N_{ij}^{reco}}, \tag{9.24}$$

$$s_{ij} = \frac{N_{ij}^{gen} \cup N_{ij}^{reco}}{N_{ij}^{gen}}. \tag{9.25}$$

All of these quantities are determined from the signal MC. Here ij are the bin numbers in the two dimensions of the variables in which the cross section is measured. The efficiency ϵ_{ij} is defined as the number of events in intersection of all reconstructed events and events generated in the bin ij, $N^{reco} \cup N_{ij}^{gen}$, divided by the total number of the generated events $N_{ij}^{gen\,tot}$. The efficiency contains the effects of the detector acceptance and the reconstruction efficiency.

The purity p_{ij} is the fraction of the number of the events which were generated and reconstructed in the same bin ($N_{ij}^{gen} \cup N_{ij}^{reco}$) and the total number of the reconstructed events in this bin (N_{ij}^{reco}). The purity describes migrations into the bin. The higher the purity is, the less events migrate into the bin from the other bins. The highest possible purity value is 1. The migrations of the events to the different bins are caused by detector resolution and reconstruction effects.

The stability s_{ij} is the quotient of the number of events generated and reconstructed in the same bin ($N_{ij}^{gen} \cup N_{ij}^{reco}$) over the number of the generated events inside this bin (N_{ij}^{gen}). The stability is quantifying migrations out of the bin. The higher the stability is the less events migrate to other bins. The highest possible stability value is 1.

The efficiency, purity and stability are shown as an example in Fig. 9.8 in bins of p_T and $|y|$ of the top quark. The reconstruction efficiency and stability are better in the high p_T. Although the high rapidity bins have low reconstruction efficiency, the purity and stability there do not drop. The level of purity is stable for all of the $p_T(t)$ bins and reaches roughly 40%. The stability is at the same level as purity, however in the highest $p_T(t)$ bin it raises up to 60%. This means that all the bins have the same level of migrations in and out of the bin, except for the highest $p_T(t)$ bin, where there are less migrations out of the bins.

In general in this analysis the bins for the double differential measurements were chosen such that the purities and stabilities are above 30% for all bins (except for some very few cases). Smaller bins and correspondingly smaller purities and stabilities would lead to stronger anticorrelations of the unfolded cross section results for neighboring bins and to a stronger dependency on the applied regularization.

The plots with efficiencies, purities and stabilities in bins of the other variables, in which the cross sections were measured, are shown in Appendix E.

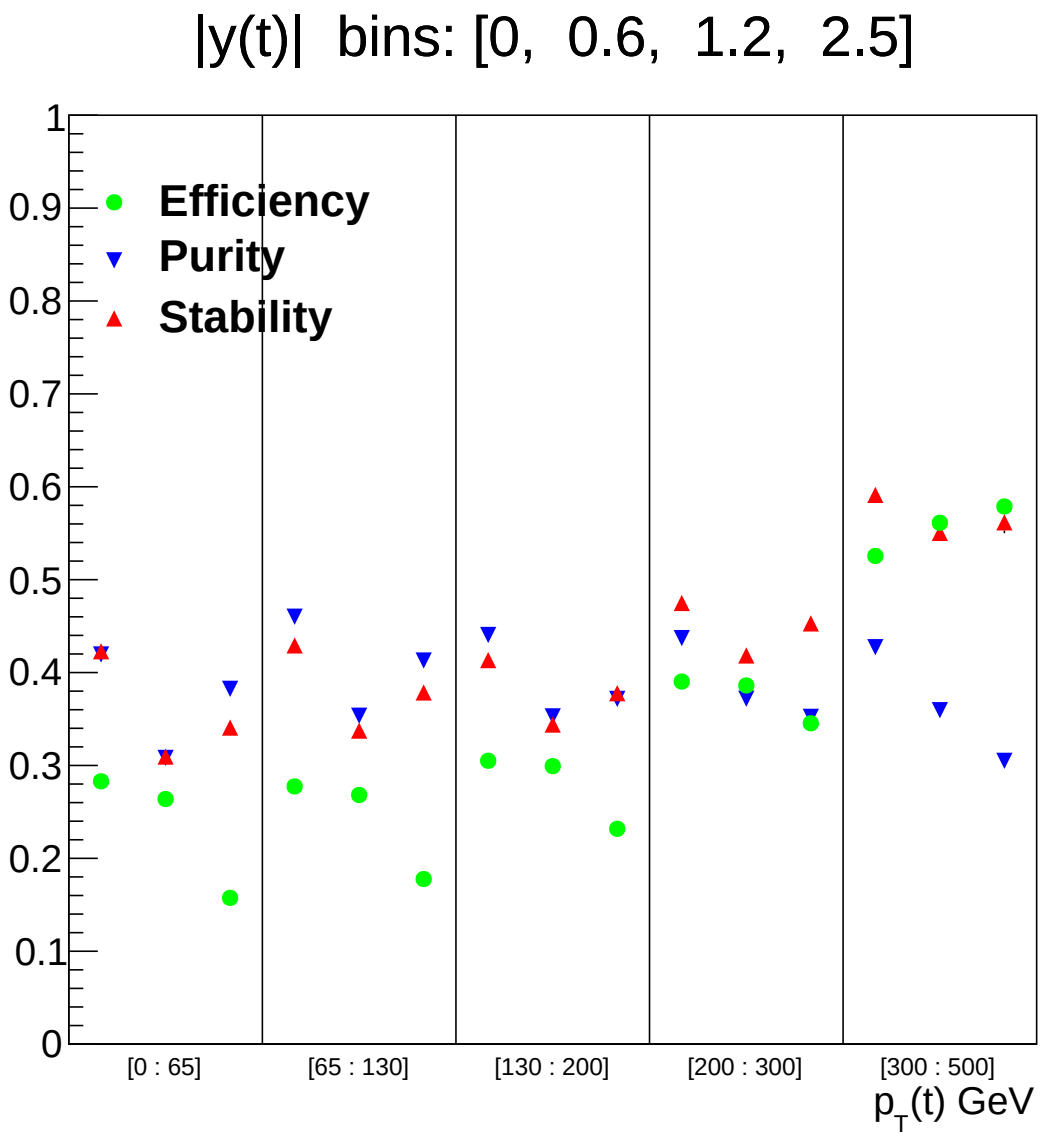

Figure 9.8: The efficiency (green circles), purity (blue triangles) and stability (red triangles) in bins of the p_T and $|y|$ of the top quark.

Chapter 10

Systematic Uncertainties

Due to the limited knowledge of detector features and theory predictions some assumptions and corrections are made, which may lead to systematic deviations of the analysis outcome. These are the sources of systematic uncertainties.

To determine the systematic uncertainties the analysis is repeated with changed assumptions or corrections and compared to the nominal result. The systematic variations are applied on the MC only.

The systematic uncertainties may be divided into two classes:

- Experimental uncertainties: variations of the correction factors connected with some reconstruction procedure.
- Model uncertainties: variations of the assumption entering the simulation model.

This chapter gives a detailed overview of the systematic variations performed in the analysis which closely follow the procedure applied in the measurement of single differential $t\bar{t}$ production cross sections [110]. The way of determining the total systematic uncertainty is presented. The systematic uncertainties, which are taken into account in this analysis, cover all the sources of the systematics for the normalized differential cross sections measurements.

For every variation discussed in the following the full cross section determination procedure including background subtraction and unfolding (using the regularization strength τ obtained in the nominal measurement) was repeated.

10.1 Experimental Uncertainties

The experimental systematic uncertainties are determined by varying the correction and scale factors applied during the analysis procedure within their uncertainty values.

10.1.1 Trigger Efficiency

The trigger scale factor is described in sec. 7.3. The typical precision of its determination is of the order of 1%. The variation of the factor is performed within this uncertainty.

10.1.2 Pileup Correction

For the pileup correction (described in sec. 7.3, vertex requirement) the total pp inelastic cross section was varied by $\pm 5\%$ [113].

10.1.3 Luminosity

The measurement of the luminosity delivered to the CMS experiment in 2012 was done utilizing the pixel cluster counting algorithm [112, 126]. The uncertainty of this measurement reaches 2.6% [126]. For the systematic variation, the luminosity value was varied up and down by it's uncertainty.

10.1.4 Uncertainty on the Lepton Selection

The lepton scale factors (described in sec. 7.3, lepton isolation) were determined using a tag and probe method which results in an uncertainty of 0.3% [110]. However, this method was performed using a Drell-Yan sample. To account for the uncertainty of the method and the possible differences between the Drell-Yan and $t\bar{t}$ event topologies, the scale factors were conservatively varied up and down by 1% [127].

10.1.5 Jet Energy Scale

The p_T and η dependent jet energy scale correction uncertainties are taken from [128] and are of the order of a few percent. The simulated jet energy was scaled up and down by the values of these uncertainties. The missing energy in the event is recalculated correspondingly to the change of the jet energy values.

10.1.6 Jet Energy Resolution

The jet energy resolution has been rescaled up by η dependent factors (1.052, 1.057, 1.096, 1.134, 1.288 for the $|\eta|$ ranges [0.0, 0.5, 1.1, 1.7, 2.3, 5.0]) following the prescriptions of the Jet/MET group [129].

10.1.7 b-tagging Efficiency Uncertainty

The uncertainties due to the b-tagging algorithm is taken into account by the b-tag scale factors (described in sec. 7.3, b-jet selection) variations within their estimated uncertainties [103]. The variations are performed depending on the p_T and $|\eta|$ of the jets. The variation "up" is done such that if the p_T of the jet was greater than a median value (65 GeV for b- and c-jets and 45 GeV for light-jets) then the b-tagging scale factor was varied up by it's uncertainty, and if the p_T of the jet is lower than the median then the b-tagging scale factor was varied down by it's uncertainty. The inverse logics was applied for the systematic "down" variation of the b-tagging scale factors. Analogous variations were performed versus the $|\eta|$ of the jets. The median value for the jet $|\eta|$ is 0.75 for all the jets flavours.

The variations of the b-tagging scale factors in p_T and η are considered as fully uncorrelated. The variations were also done separately for different jet flavours. The uncertainties for c and b flavours are considered to be fully correlated and they are varied simultaneously, while the variations for the light jet flavour are treated as uncorrelated to c- and b-jets.

10.1.8 Missing Transverse Energy Uncertainty

No specific MET variation for the systematic uncertainty was performed. The reason for this is that the missing energy is recalculated after each variation connected to the jets or leptons kinematics. This matches with the recommendations of the experts [104].

10.1.9 Uncertainty Related to the $t\bar{t}$ Kinematic Reconstruction

The uniform scale factor related to the $t\bar{t}$ kinematic reconstruction was presented in sec. 8.3. It was varied up and down by 1%, which corresponds to the value of its error, to estimate the related systematic uncertainty.

10.1.10 Uncertainty on the Background Normalization

The normalization of each background is scaled up and down by 30% [110]. This conservative variation covers both the total normalization uncertainty and local deficiencies due to mismodelling of the shapes of the distributions.

10.1.11 Branching Ratio

The uncertainties on the branching ratios of the W decays are propagated from their individual uncertainties [16]. They cancel for the normalized cross sections.

10.2 Model Uncertainties

The model uncertainty is defined by using for the unfolding of double differential cross sections different $t\bar{t}$ signal simulations obtained from different generators and/or setting different parameters for the generator input[1]. A summary of all the uncertainties taken to account in this analysis is presented in this section.

10.2.1 Uncertainties Related to PDFs

The systematic uncertainty due to the chosen PDF model is estimated by reweighting the $t\bar{t}$ signal sample according to the 44 errors of the CTEQ66 PDF set evaluated at the 90%

[1]For each discussed variation the full unfolding procedure was repeated

confidence level [83]. The effect of each of these variations of the same sign[2] are added in quadrature.

10.2.2 Uncertainties Related to the Hard Scattering Model

The nominal $t\bar{t}$ MC sample used for this analysis is generated with MadGraph+Pythia. The hard scattering model is simulated in MadGraph with LO precision. A systematic variation was performed using Powheg instead of MadGraph for the hard scattering simulation. Powheg is also interfaced with Pythia for the showering simulation. All the differences between the results produced with MadGraph+Pythia and Powheg+Pythia are assumed to originate only from the difference in the hard scattering model. The performance of Pythia is assumed to be the same in both samples.

10.2.3 Hadronization and Parton Showering Model Uncertainties

As discussed in chapter 5, Pythia and Herwig generators have different algorithms for parton showering and hadronization. Thus, the generated $t\bar{t}$ signal samples interfaced with Pythia and Herwig are compared to measure this uncertainty. In this work the samples generated with Powheg+Herwig and Powheg+Pythia were compared. All the differences in the results measured exploiting the Powheg+Herwig and Powheg+Pythia $t\bar{t}$ signal samples are assumed to originate from the differences between parton showering and hadronization models.

10.2.4 Top Quark Mass Assumption

The nominal $t\bar{t}$ simulated sample used in this analysis was generated with the top mass $m(t) = 172.5$ GeV. The experimentally measured value (world average) of this mass is $m_{exp}(t) = 172.4 \pm 0.74$ GeV [130]. To account for the experimental uncertainty of the top-quark mass, two additional $t\bar{t}$ signal samples were generated, in which the masses of the top-quark were assumed to be $m(t) = 171.5$ GeV and $m(t) = 173.5$ GeV. The results were recalculated using these samples and the differences to the nominal results are assumed to be the uncertainties related to the top quark mass assumption.

The procedure of the full kinematic reconstruction of the $t\bar{t}$ system applied in this analysis (see chapter 8) assumes a fixed top-quark mass of 172.5 GeV. This mass was varied separately for the kinematic reconstruction procedure by $\pm$ 1 GeV. This variation produced only minor difference to the nominal results, which can be neglected.

10.2.5 Matching Scale Variation

The scale at which the parton shower is matched to the hard process was varied up and down by factor 2 compared to the nominal value of 20 GeV. The resulting variations in

[2]The sign of the systematic variation is determined by the deviation caused by this variation. If the variation gave higher cross section results than the nominal ones, then the sign of this variation is "+". If the variation resulted in lower cross section values, then the sign of this variation is "-".

cross sections are the corresponding systematic uncertainties.

10.2.6 Hard Scale Variation

The hard scale Q was varied by factor 2 up and down compared to the nominal value. This variation follows the convention adopted by the CMS experiment.

10.3 Determination of the Total Systematic Uncertainties

The total systematic uncertainty consists of the different experimental and model variations described above. Some of them give results with lower values compared to the nominal ones, and some of them higher ones. The deviations to lower and to higher cross section values are independently summed up in quadrature as follows:

$$\delta^{pos}_{syst.\,total,\,ij} = \sqrt{\sum_{s} \delta^{high^2}_{s,\,ij}}, \tag{10.1}$$

$$\delta^{neg}_{syst.\,total,\,ij} = \sqrt{\sum_{s} \delta^{low^2}_{s,\,ij}}. \tag{10.2}$$

Here $\delta_{syst.\,total,\,ij}$ is the total systematic uncertainty in the bin ij from s different sources. The $\delta^{high/low}_{s,\,ij}$ are expressed the following way:

$$\delta^{m}_{s,\,ij} = \text{Varied Result}_{s,\,ij} - \text{Nominal result}_{ij}, \tag{10.3}$$

where $m = high$ if $\delta^{m}_{s,\,ij} \geq 0$ and $m = low$ if $\delta^{m}_{s,\,ij} < 0$.

In case all the variations of a certain correction factor or assumption result only in higher (or lower) values compared to the nominal result, the largest deviation is taken for the higher (lower) uncertainty and the corresponding lower (higher) uncertainty is set to zero. These numbers are presented in tables from appendix I.

10.4 Summary of Systematic Uncertainties

An example of the systematic uncertainties is presented in the table **??**. It shows the systematic uncertainties for the double differential $t\bar{t}$ production cross sections in bins of $p_T(t)$ and $|y(t)|$. The total uncertainties result in mainly symmetric positive and negative uncertainties. The table also shows the statistical uncertainties in the same bins for comparison.

The biggest contributions to the total systematic uncertainties are the JES (up to $\sim$ 5%), top quark mass variation (up to $\sim$ 13%), hard scale variation (up to $\sim$ 12%), matching scale variation (up to $\sim$ 8%), hadronization model (up to $\sim$ 13%) and hard scattering model ($\sim$ 22%) uncertainties. A large value of the uncertainty related to the b-tagging in the high $p_T(t)$ bin is caused by statistical effects.

The uncertainties related to the kinematic reconstruction scale factor variation, background variation and PDF variation are small for each cross section bin.

The following uncertainties are slightly increasing with $p_T(t)$: JER (up to $\sim$ 7%), JES (up to $\sim$ 5%), pile up reweighting (up to $\sim$ 1.5%), matching scale (up to $\sim$ 5 – 8%). The uncertainties related to the top quark mass variation, hard scale variation and hadronization model variation are more increasing with the $p_T(t)$. On the other hand, the uncertainties related to the trigger and lepton scale factor variations are slightly decreasing with $p_T(t)$ – from 0.4% to $\sim$ 0%.

All the uncertainties derived from the experimental and model systematic sources described in this chapter are listed in the tables in appendix J, for all the normalized cross sections described in sec. 11.1 and unnormalized cross sections shown in appendix G.

$p_T(t)$ [GeV]	0 to 65			65 to 130			130 to 200			200 to 300			300 to 500		
$\|y(t)\|$	0 to 0.6	0.6 to 1.2	1.2 to 2.5	0 to 0.6	0.6 to 1.2	1.2 to 2.5	0 to 0.6	0.6 to 1.2	1.2 to 2.5	0 to 0.6	0.6 to 1.2	1.2 to 2.5	0 to 0.6	0.6 to 1.2	1.2 to 2.5
Source	Uncertainty [%]														
Lumi Up	0.1	-0.5	0.2	0.2	-0.3	0.3	0	-0.2	-0.1	-0.1	0.2	-0	-0.1	-0.2	-0.1
Down	-0.1	0.5	-0.2	-0.2	0.3	-0.3	-0	0.2	0.1	0.1	-0.2	0	0.1	0.2	-0.1
b-tagging Pos.	0.7	0.7	0.7	0.7	0.3	0.5	0.8	0.9	0.6	0.9	4.1	0.8	1	1.5	1.6
Neg.	0.5	1.5	0.5	0.4	0.6	0.6	0.8	1	0.7	0.5	0.6	1.4	1.4	8.7	0.5
Kin Up	0.01	-0.04	0.02	0.02	-0.03	0.03	0	-0.01	-0.01	-0.01	0.02	0.01	-0	-0.01	-0.1
Down	-0.01	0.04	-0.02	-0.02	0.03	-0.03	-0	0.01	0	0.01	-0.02	0.03	0	0.03	-0.11
JER Up	1.1	-0.2	1.1	-0.4	0.2	-0.3	-1.5	-0.6	0.1	2.1	1.9	-2.2	-3.1	-4.3	7
Down	1.2	-1.5	1.3	-0.2	0.4	-0.3	-0.7	0.1	-2.3	-1.2	4.6	0.4	2.9	-2	1.5
JES Up	2.9	0.2	-0.3	-0.2	-1.4	-0.6	-0.7	-3.2	-0.2	2.1	5.4	1.1	1.3	-3	4.4
Down	-0.8	-0.9	0	-0.1	2.2	1	-1.4	-0.4	-0.2	1.2	1.8	-2.2	-4.7	-3.4	-4.4
PU Up	-0.1	0.1	0.2	0.2	0.2	-0	-0.1	-0.3	0.5	-1	-0.3	-1.5	0.6	-0.6	1.3
Down	0.2	-0.2	-0.1	-0.2	-0.2	0	0.1	0.3	-0.4	0.9	0.4	1.6	-0.7	0.4	-1.5
Trig Up	0.2	-0.2	-0.3	0.3	-0.1	-0.1	0.2	0	-0.3	0.1	0.2	-0.2	0.2	0	-0.2
Down	-0.2	0.2	0.3	-0.3	0.1	0.1	-0.2	-0	0.3	-0.1	-0.2	0.3	-0.2	-0.1	-0
Lept Up	0.1	-0.4	0.2	0.2	-0.4	0.3	0.1	-0.1	-0.1	-0.1	0.2	-0.1	0	-0.2	-0.1
Down	-0.1	0.5	-0.2	-0.2	0.4	-0.3	-0.1	0.2	0	0.1	-0.2	0.1	-0	0.2	-0.2
BG Up	0	-0.1	0.3	0.1	-0.3	0.1	0.2	-0	-0.1	-0.7	0.1	-0.4	0.1	-1.2	-0.1
Down	-0.1	0.1	-0.3	-0.1	0.3	-0.1	-0.2	-0	0.1	0.7	0.1	0.5	-0.1	1.1	-0.2
DY Up	-0.3	-0.8	-0.4	0.2	0	-0	0.4	0.5	0	0.1	0.3	0.4	0.6	0.6	0.6
Down	0.4	0.8	0.5	-0.3	-0.1	-0	-0.5	-0.5	-0.1	-0.1	-0.3	-0.4	-0.6	-0.6	-0.9
Mass Up	3.1	-2.6	-6.2	-0.6	4.3	1.2	-3.7	-1.3	1.5	3.9	6.9	-7.3	-1	-3.4	13.3
Down	0.2	-3.7	-1.1	-0.6	3.9	0.1	0.9	2.1	1.3	-3.4	0.4	-3.4	1.5	-9	-13
Match Up	1.3	0.7	-2.8	-1.7	0.9	0.9	0	-1.2	0.1	1.3	8.4	-2.8	-6.2	-1.6	5.1
Down	1.2	-0	0.6	-1.3	0.1	-1.4	0.3	-0.9	2.3	1.7	0.5	-0	-2	4.9	-1.4
Scale Up	-2.8	3.5	0.6	-1.7	1.3	0.4	0.4	-1.5	1.9	-0.9	4.7	-5	-7.2	-3.8	12.1
Down	1.9	-0.2	-1.2	-1.1	-0.3	0.1	-1.4	-0.9	-0.3	2.9	6.6	0.3	2.2	-0.8	2.9
PDF Pos.	0.5	0.9	1.3	0.4	0.7	1.4	0.2	0.6	1.1	0.2	0.3	1.4	0.7	0.4	0.6
Neg.	0.6	0.7	1.6	0.4	0.5	1.9	0.2	0.4	1.4	0.1	0.2	1	0.7	0.4	0.5
Hadronization	-1.1	-1	4.2	-0	-2.2	2.5	0.5	-2	0.1	4.5	-7.1	2.6	-11.8	11.1	-14.9
Hard Scat.	0.5	2	2.1	-1.4	1.4	-1.4	0.2	1.9	-4.2	0.3	2.2	-2.4	0.1	-12.1	-9.1
Statistical	3.6	4.4	4.9	2.2	3	2.9	3.1	4.4	4.8	6.2	8.3	10.5	9.7	14.8	21.3
Total Syst. Pos.	5.2	4.5	5.2	1.7	5.8	3.8	1.5	3.7	5.5	7.6	16.9	4.4	12.6	17.3	27
Total Syst. Neg.	3.3	5.1	8.5	3	3.1	3.8	4.6	5	5.1	6	7.4	10.6	16.3	21.8	22.3

Table 10.1: Summary of all the statistical and systematic uncertainties (for each source separately and total) for the **normalized** double differential cross sections in bins of $|y(t)|$ for different $p_T(t)$ bins.

Chapter 11

Results and Discussion

11.1 Normalized Double Differential $t\bar{t}$ Production Cross Sections

The normalized $t\bar{t}$ production cross sections were measured double differentially as a function of variables (see Fig.11.23) related to the dynamics of the t, of the $t\bar{t}$ system or to both of them. The studied observables are: top transverse momentum and rapidity, $t\bar{t}$ mass, rapidity and transverse momentum and the azimuthal and pseudorapidity difference between the t and the $\bar{t}$. In addition, for the first time ever in CMS, the cross sections are studied as function of x_1 (see sec. 2.4.1, eq. 2.14), which in the leading order QCD picture is equal to the proton longitudinal momentum fraction carried by one of the incoming partons (gluon or quark). The study of this observable might be particularly interesting to show the sensitivity of the data to constrain the proton PDFs at large values of x_1 where in particular the knowledge on the gluon density in the proton is not so precise.

The binning for the detector level distributions was chosen to have enough statistics in each bin so that the statistics could be treated as Gaussian. It was also checked if the purity and stability in each bin are not too low. The regularization strengths used to determine each set of the cross sections are listed in Appendix F.

This sections is presenting only the normalized double differential $t\bar{t}$ production cross sections. The corresponding unnormalized cross sections are shown in Appendix G.

All numerical values for the normalized and unnormalized cross sections and their uncertainties are listed in Appendix I.

Cross sections in bins of $|y(t)|$ versus $p_T(t)$

The $t\bar{t}$ production cross sections in bins of the rapidity and the transverse momentum of the top quark was measured in the bins presented in Fig. 11.1. The shown control distribution is also demonstrating the agreement between the data and the MC estimated $t\bar{t}$ signal and background contributions. The MC slightly underestimates the data for the lower $p_T(t)$ bins and in the outer $y(t)$ bins for all the transverse momenta values. There is a trend that the p_T spectrum for the MC is harder than for the data.

Fig. 11.10 represents the production cross sections of the $t\bar{t}$ pair in bins of top rapidity and top transverse momentum. The experimentally measured cross sections are compared

to the MadGraph +Pythia, Powheg +Pythia, Powheg +Herwig and MC@NLO +Herwig predictions. An overall good agreement between theory predictions and experimental results is observed. However, all the simulation models tend to have harder transverse momenta than data. This disagreement is the strongest between the data and MadGraph +Pythia model and is more pronounced in the central rapidity bins. The best description is provided by Powheg + Herwig.

Cross sections in bins of $p_T(t\bar{t})$ versus $|y(t\bar{t})|$

Another pair of variables in bins of which the cross section was measured is the p_T and $|y|$ of the $t\bar{t}$ system. The control distribution in bins of the $p_T(t\bar{t})$ and $|y(t\bar{t})|$ is presented in the Fig. 11.2. The agreement between data and MC is overall nice, except for the highest $p_T(t\bar{t})$ bin. The MC slightly underestimates the data for the first three $p_T(t\bar{t})$ bins, while for the highest measured $p_T(t\bar{t})$ bin the MC overestimates the data.

The production cross sections in bins of $p_T(t\bar{t})$ and $|y(t\bar{t})|$ are shown in Fig. 11.11. These plots show that the cross sections from the models are a bit less central in $|y(t\bar{t})|$ than the data except in the high $p_T(t\bar{t})$ region when the models generally overestimate the cross sections. Also, in the high $p_T(t\bar{t})$ region the difference between different models is the largest. One can observe that the $p_T(t\bar{t})$ spectrum simulated in Powheg + Pythia is a bit steeper than in the other models.

Cross sections in bins of $|y(t)|$ versus $M(t\bar{t})$

Another measurement has been performed in bins of $M(t\bar{t})$ and $|y(t)|$. Fig. 11.3 represents the control distribution in bins of these variables. The agreement between data and MC prediction is good in the lower bins of the invariant mass of the $t\bar{t}$ pair. However, the MC starts to underestimate data for the highest $M(t\bar{t})$. In general, the MC is lower for the outer rapidity bin.

The cross sections measured in bins of $M(t\bar{t})$ and $|y(t)|$ are presented in Fig. 11.12. The MC@NLO+Herwig predictions have the worst agreement with data in the smallest rapidity bin, where the model exhibits a too hard $M(t\bar{t})$ spectrum. The MC models tend to more central rapidities of the top quark in the highest $M(t\bar{t})$ bin.

Cross sections in bins of $M(t\bar{t})$ versus $p_T(t)$

The $t\bar{t}$ production cross section was also measured double differentially in bins of $p_T(t)$ and $M(t\bar{t})$. The control plot, which shows the binning and the comparison between data and simulation, is presented in Fig. 11.4. The MC shows harder $p_T(t)$ spectra than data and this discrepancy increases with $M(t\bar{t})$.

The cross sections in bins of $M(t\bar{t})$ and $p_T(t)$ are presented in Fig. 11.13. MadGraph+ Pythia predicts harder $p_T(t)$ spectra and this effect is much enhanced at high $M(t\bar{t})$. All the other models describe the data a bit better, but also predict a too hard $p_T(t)$ spectrum, in particular at the highest $M(t\bar{t})$.

Cross section in bins of $M(t\bar{t})$ versus $\Delta\eta(t\bar{t})$

The cross section has been measured double differentially in bins of $\Delta\eta(t\bar{t})$ and $M(t\bar{t})$, where $\Delta\eta(t\bar{t}) = \eta(t) - \eta(\bar{t})$ denotes the difference in pseudorapidity between the top and the antitop.

The control distribution in Fig. 11.5 shows that the simulation slightly overestimates the experimental data in the lowest $M(t\bar{t})$ bin. However, there is a strong disagreement between MC and data in the $\Delta\eta(t\bar{t})$ spectra for the two higher $M(t\bar{t})$ bins. The MC predicts a too small pseudorapidity separation between t and $\bar{t}$ for high $M(t\bar{t})$.

The double differential production cross sections in bins of $\Delta\eta(t\bar{t})$ and $M(t\bar{t})$ is presented in Fig. 11.14. The MadGraph + Pythia prediction shows the worst agreement. There is a tendency that the higher the $M(t\bar{t})$ is, the more too small $\Delta\eta(t\bar{t})$ values are predicted by the models.

Cross section in bins of $M(t\bar{t})$ versus $\Delta\phi(t\bar{t})$

The measurement of the cross section has been also performed in bins of the azimuthal angle between the top and the antitop, $\Delta\phi(t\bar{t})$, and the mass of the $t\bar{t}$ system, $M(t\bar{t})$.

The control distribution in bins of these variable pair is presented in Fig. 11.6. The MC is a bit more back-to-back than the data for the two highest $M(t\bar{t})$ bins, while the lowest $M(t\bar{t})$ bin has a good description of the data by the MC model.

The Fig. 11.15 presents the double differential production cross sections of the $t\bar{t}$ pairs in bins of $\Delta\phi(t\bar{t})$ and $M(t\bar{t})$. All the predictions provide a reasonable description of the measured cross sections. However, the agreement is getting slightly worse for the higher bins of the $M(t\bar{t})$. MadGraph + Pythia provides the worst description of the data.

Cross section in bins of $|y(t\bar{t})|$ versus $M(t\bar{t})$

The control distribution in bins of $|y(t\bar{t})|$ and $M(t\bar{t})$ is shown in Fig. 11.7. The agreement between MC and data is overall nice. For higher masses the MC tends to a bit less central rapidity.

The normalized double differential $t\bar{t}$ production cross sections in bins of $M(t\bar{t})$ and $|y(t\bar{t})|$ are presented in fig. 11.16. MadGraph + Pythia provides the best agreement with the data. The other theoretical predictions tend to be less central in $|y(t\bar{t})|$ than the data. The description at the highest $M(t\bar{t})$ bins is the worst.

Cross section in bins of $|p_T(t\bar{t})|$ versus $M(t\bar{t})$

Another measurement of the cross sections was performed in bins of $|p_T(t\bar{t})|$ and $M(t\bar{t})$. The control distribution in bins of $|p_T(t\bar{t})|$ and $M(t\bar{t})$ is presented in Fig. 11.8. In all of the $M(t\bar{t})$ bins there is the same trend in the way how the simulation describes the experimentally measured $p_T(t\bar{t})$ spectrum. The MC slightly underestimates the data for the lower $p_T(t\bar{t})$, while for the highest transverse momentum of the top-pair a significant overestimation is observed.

Fig. 11.17 shows the double differential $t\bar{t}$ production cross section in bins of $|p_T(t\bar{t})|$ and $M(t\bar{t})$. All the theoretical predictions describe the measured cross sections well.

However, the predictions are higher than data at higher $p_T(t\bar{t})$.

Cross section in bins of $M(t\bar{t})$ versus x_1

The control distributions of x_1 in bins of $M(t\bar{t})$ are shown in Fig. 11.9. A discrepancy in the medium x_1 bins for the high $M(t\bar{t})$ are observed. The MC is a bit lower than data in this region.

The double differential $t\bar{t}$ production cross sections are shown in Fig. 11.18. In general a reasonable description of data by the MC models is observed. In the two highest $M(t\bar{t})$ bins the predictions tend to be a bit higher than data at the lowest x_1 values.

It is interesting to investigate how much sensitivity these cross sections vs x_1 could have for constraining the proton PDFs. In order to test this the PDF uncertainties on the MadGraph cross sections were evaluated, using the 44 CTEQ66 PDF variations (see sec. 10.2.1). The resulting uncertainties (adding the effects in quadrature) on the cross section predictions are listed in Table I.18. One can see that the uncertainties increase from a minimum of 5% at small x_1 to up to 20% at the highest x_1 bin [0.4, 1]. This is what one had hoped for, namely that the PDF uncertainty is larger at high x which is probably (further studies would be needed) directly related to the worsening of the knowledge of the gluon PDF at high x from fits to HERA and other data used in CTEQ6. Unfortunately the total uncertainties of the measured $t\bar{t}$ cross sections are still a factor two (or more) higher at large x_1 than the PDF uncertainties on the prediction. However, to understand the impact of the data one would need to take into account the correlations (full covariance matrix) between the measurement bins. It remains a task for the future to include these data in a PDF fit and thereby evaluating their full impact on PDFs.

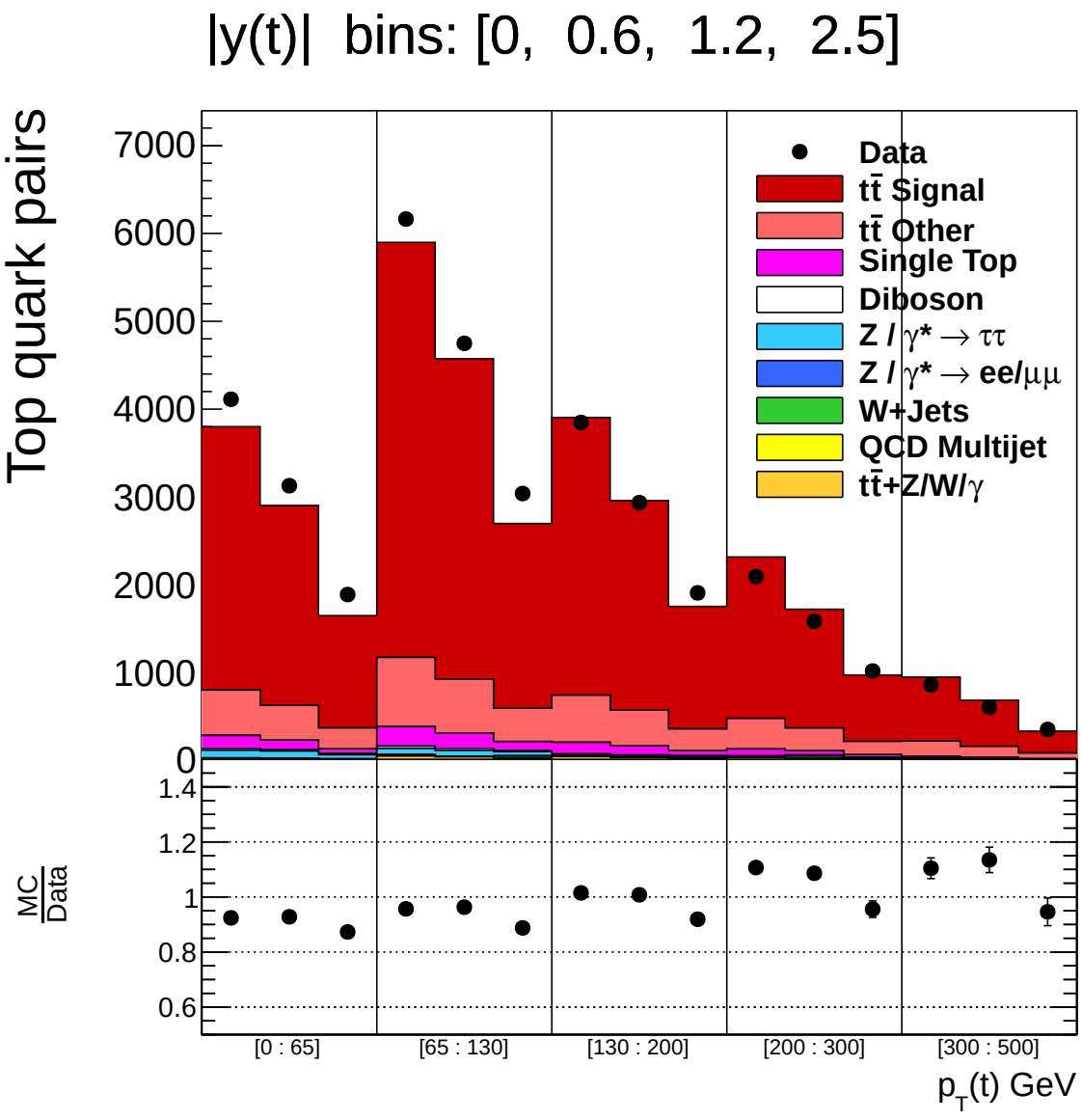

Figure 11.1: Control distribution of the $|y|$ of the top quark in bins of the p_T of the top quark. The $|y|$ bins are shown on the top of the plot. The experimental data are marked with black dots with error bars representing the statistical uncertainties only. The simulated distributions of signal and different backgrounds are represented with colored histograms. On the bottom part of the plot the ratio between MC and data yields in each bin is shown with the error bars representing the statistical uncertainties of the data only.

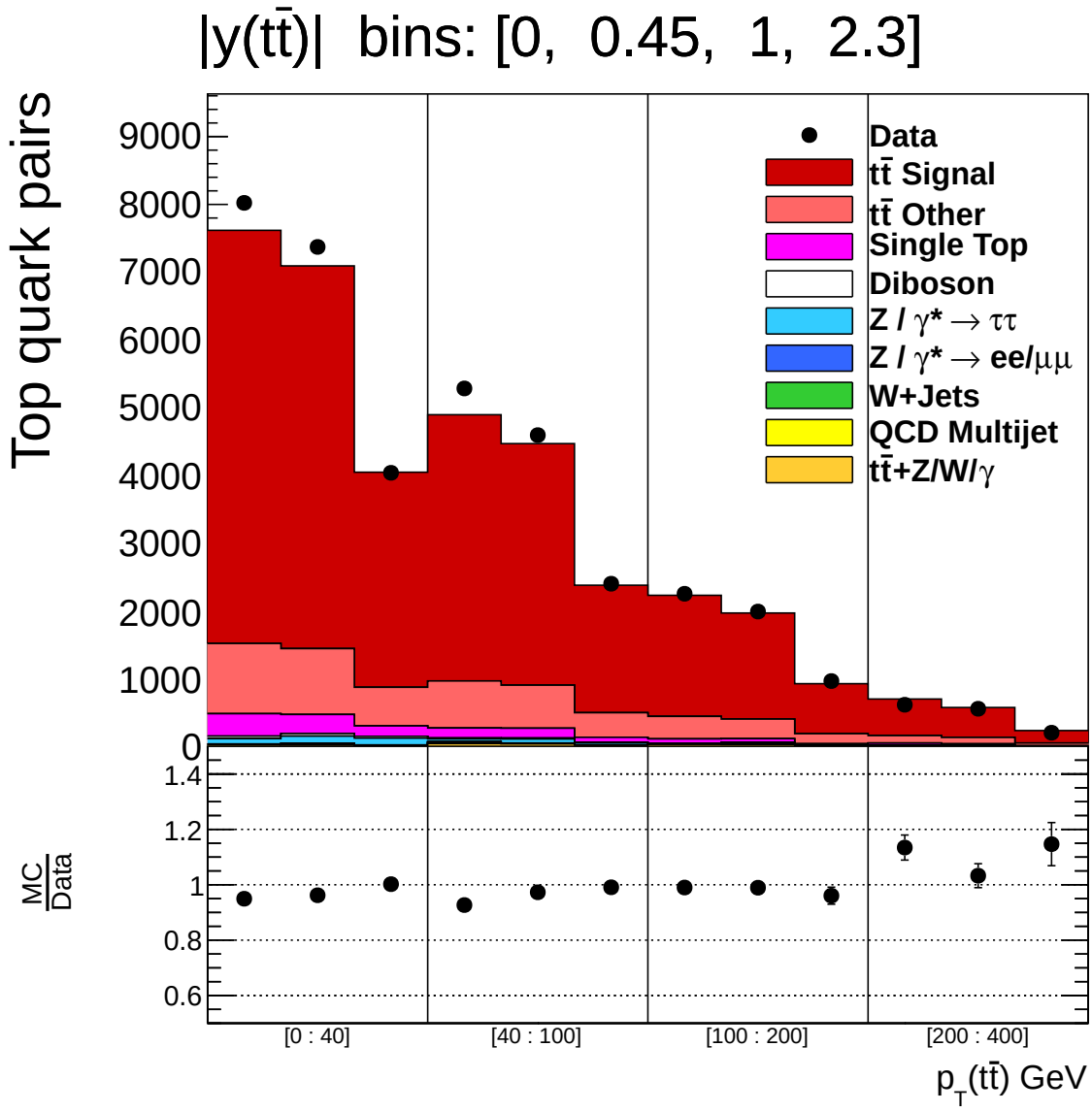

Figure 11.2: Control distribution of the $p_T(t\bar{t})$ in bins of the $|y(t\bar{t})|$. The $|y(t\bar{t})|$ bins are shown on the top of the plot. Other details as in Fig. 11.1.

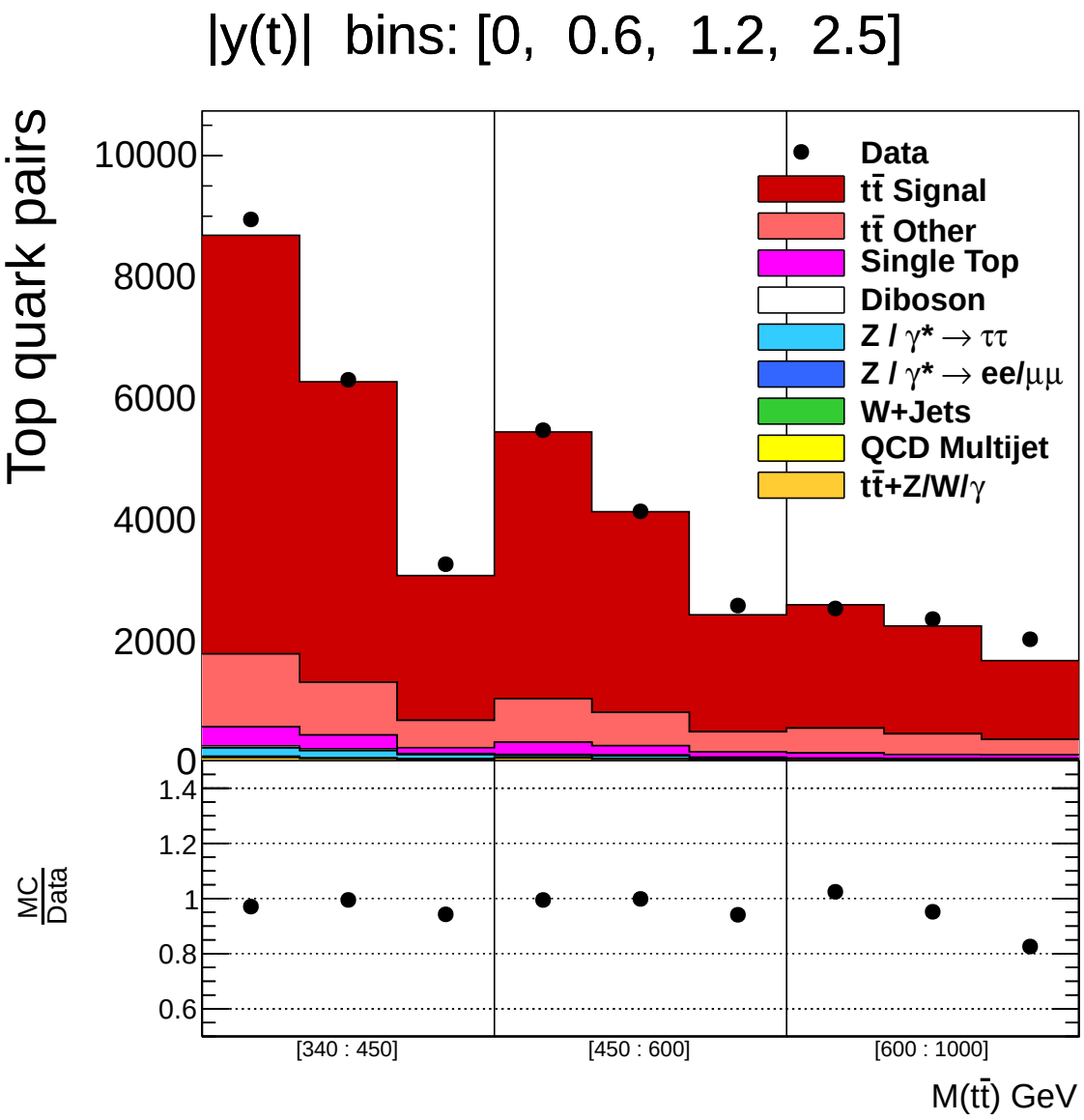

Figure 11.3: Control distribution of the $M(t\bar{t})$ in bins of the $|y(t)|$. The $|y(t)|$ bins are shown on the top of the plot. Other details as in Fig. 11.1.

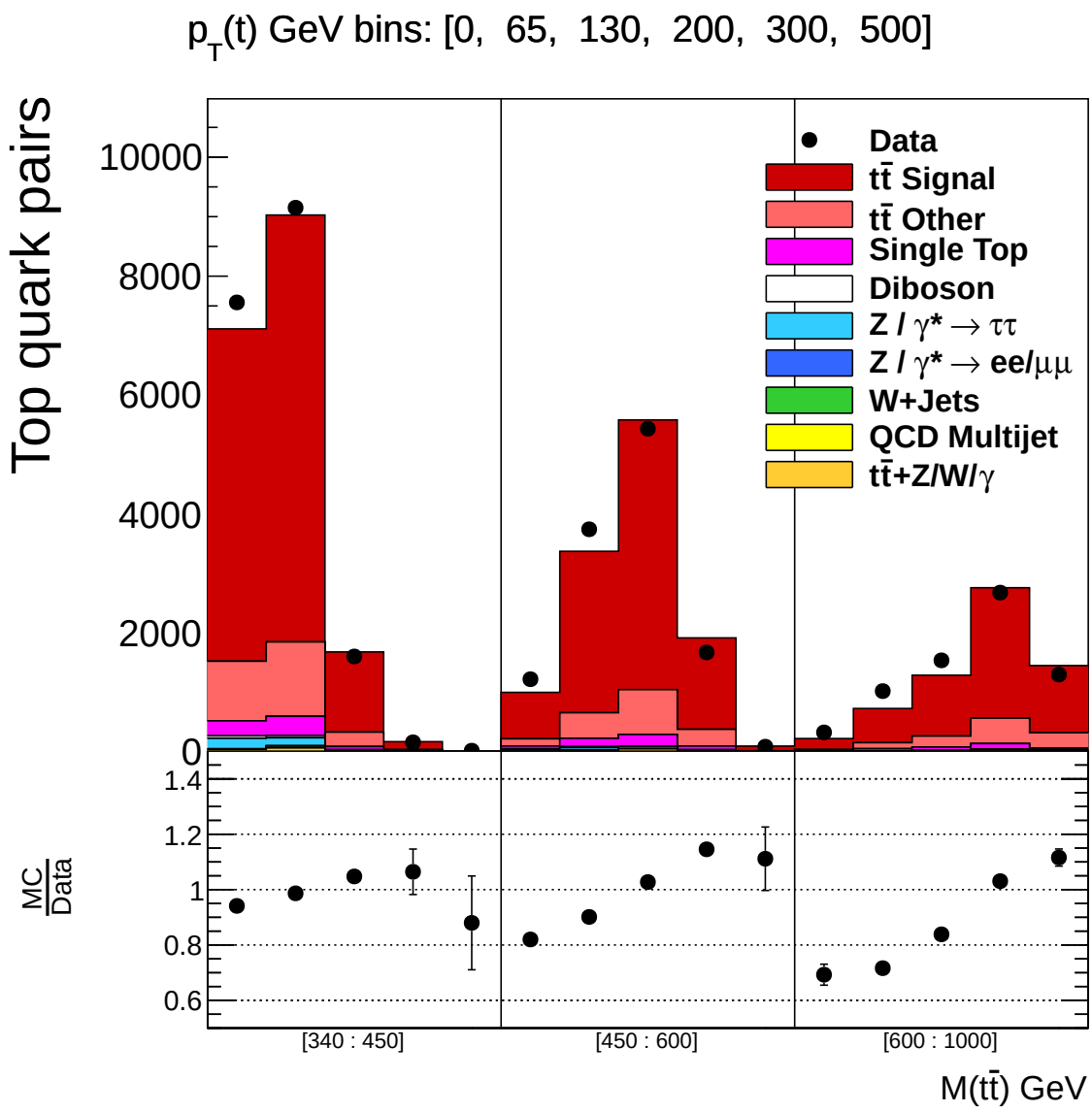

Figure 11.4: Control distribution of the $M(t\bar{t})$ in bins of the p_T of the top quark. The $p_T(t)$ bins are shown on the top of the plot. Other details as in Fig. 11.1.

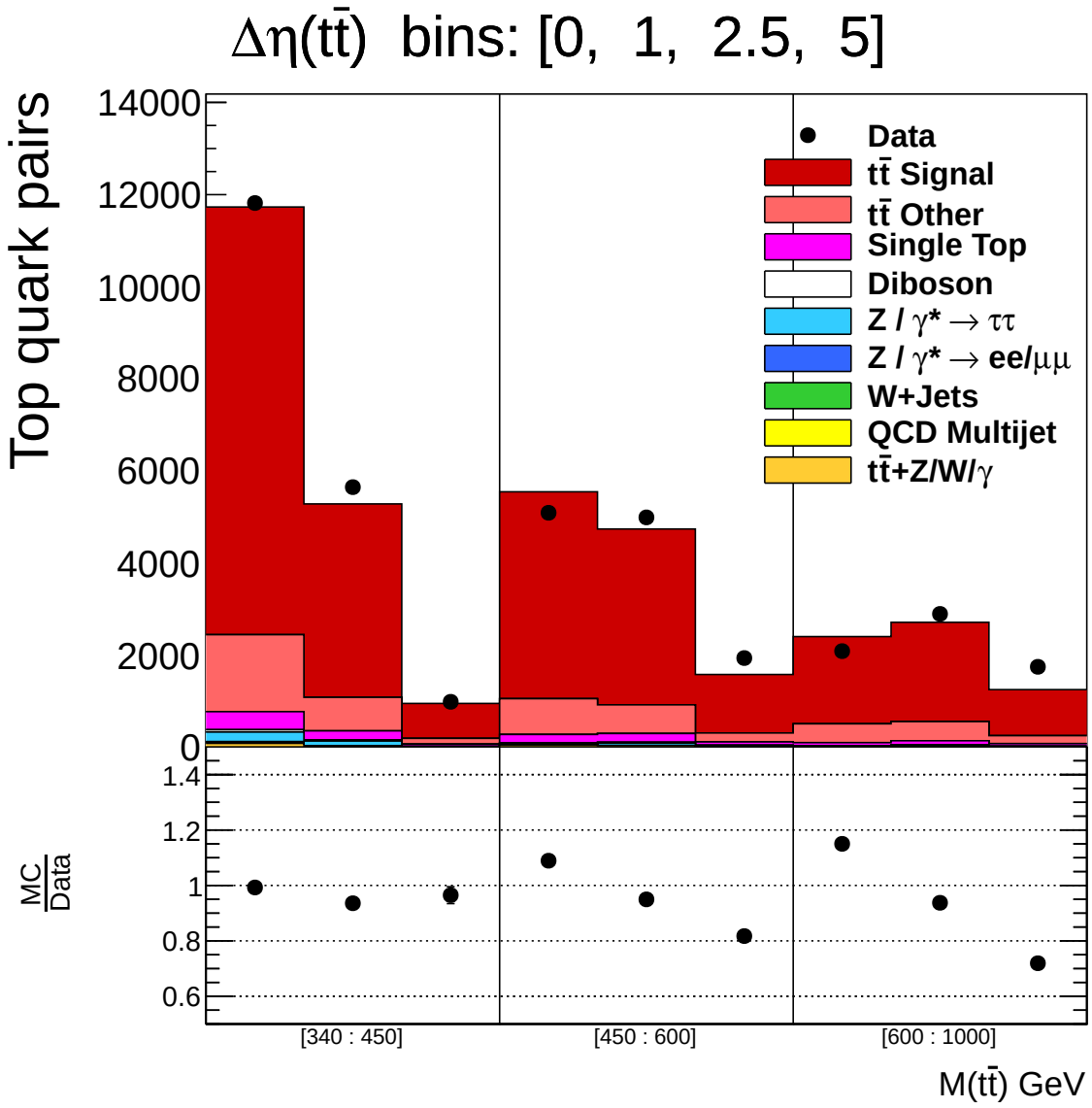

Figure 11.5: Control distribution of the $\Delta\eta$ between the t and $\bar{t}$ in bins of the $M(t\bar{t})$. The $\Delta\eta$ bins are shown on the top of the plot. Other details as in Fig. 11.1.

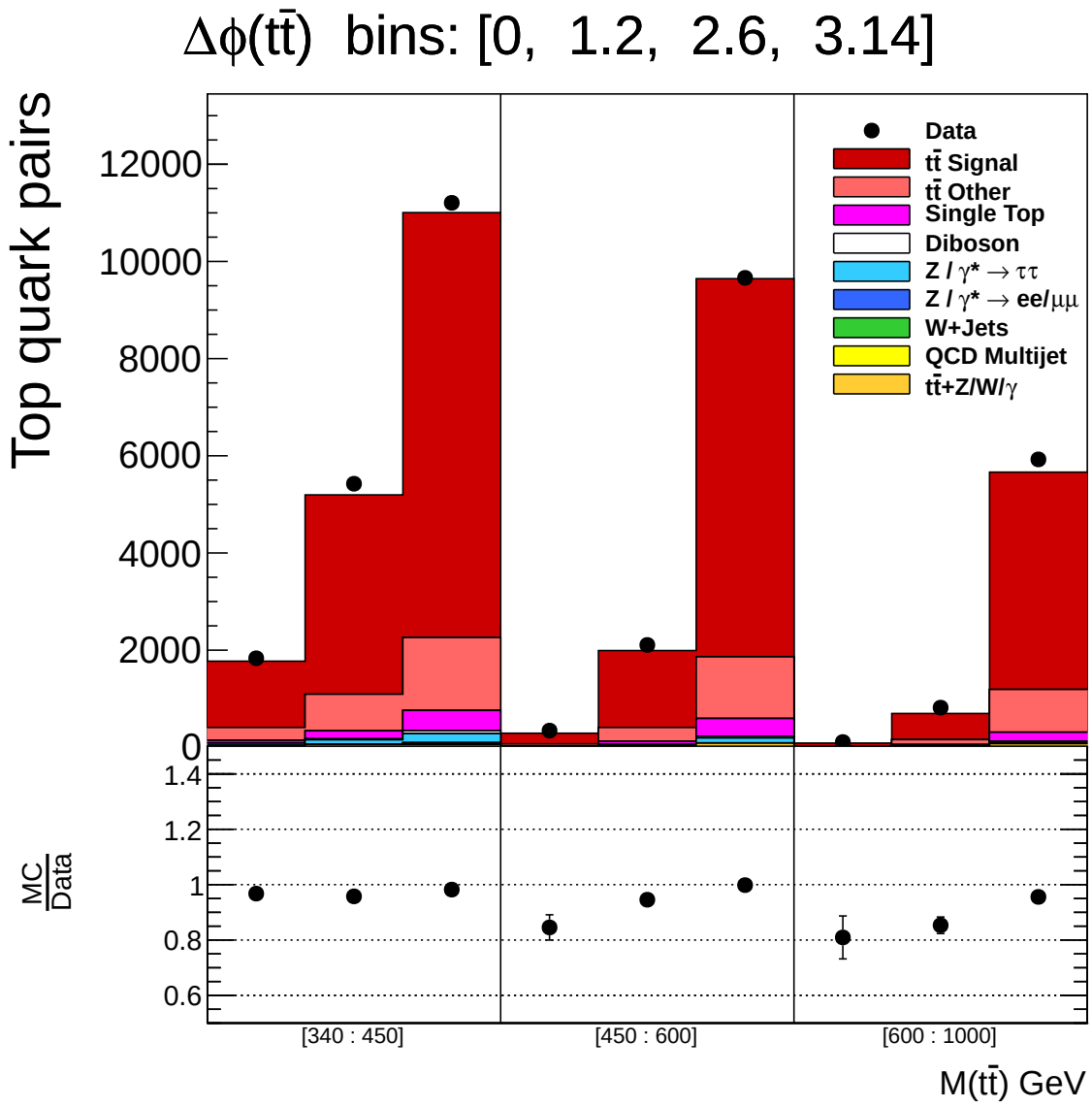

Figure 11.6: Control distribution of the $\Delta\phi$ between the t and $\bar{t}$ in bins of the $M(t\bar{t})$. The $\Delta\phi$ bins are shown on the top of the plot. Other details as in Fig. 11.1.

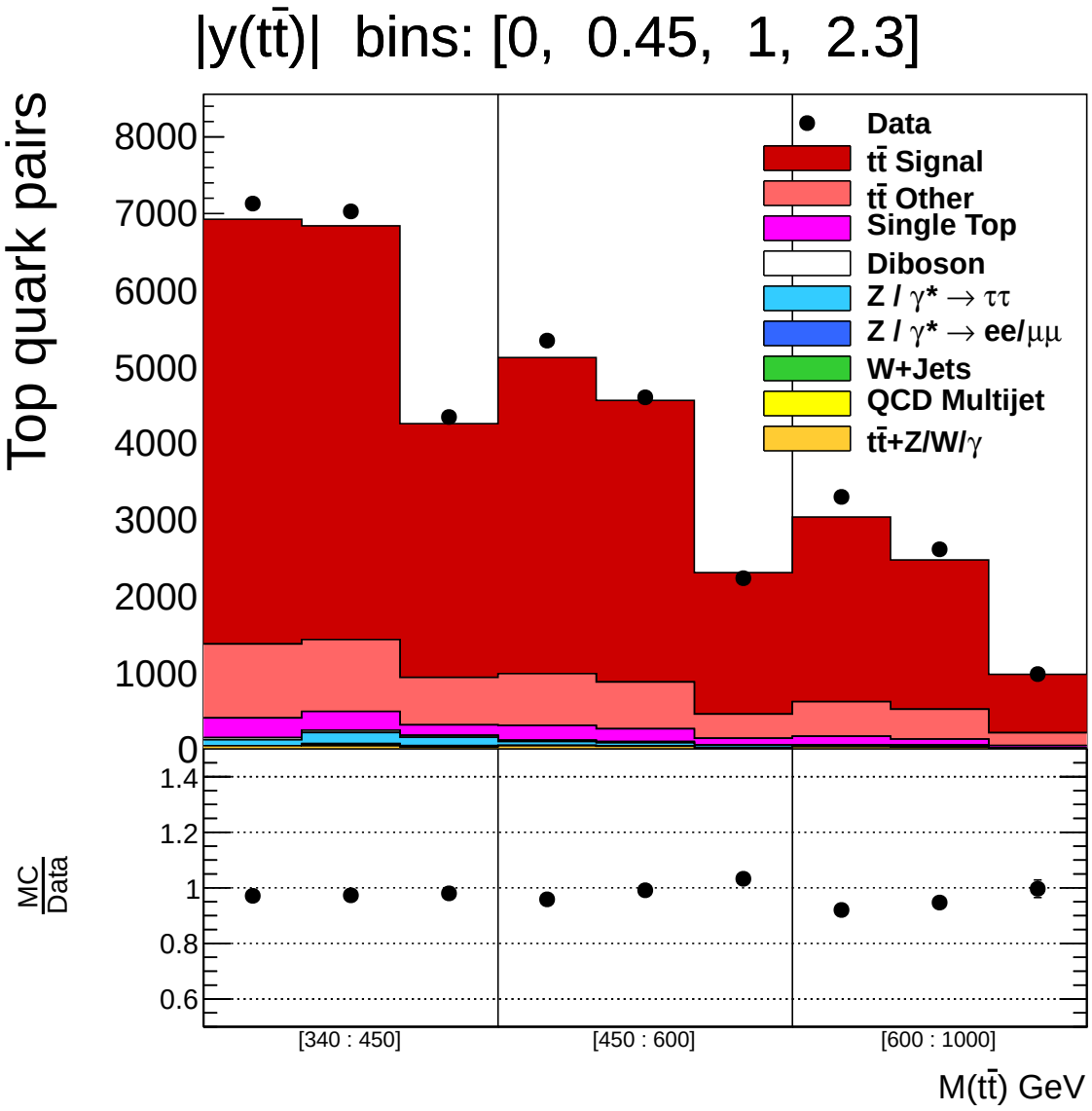

Figure 11.7: Control distribution of the $|y(t\bar{t})|$ in bins of the $M(t\bar{t})$. The $|y(t\bar{t})|$ bins are shown on the top of the plot. Other details as in Fig. 11.1.

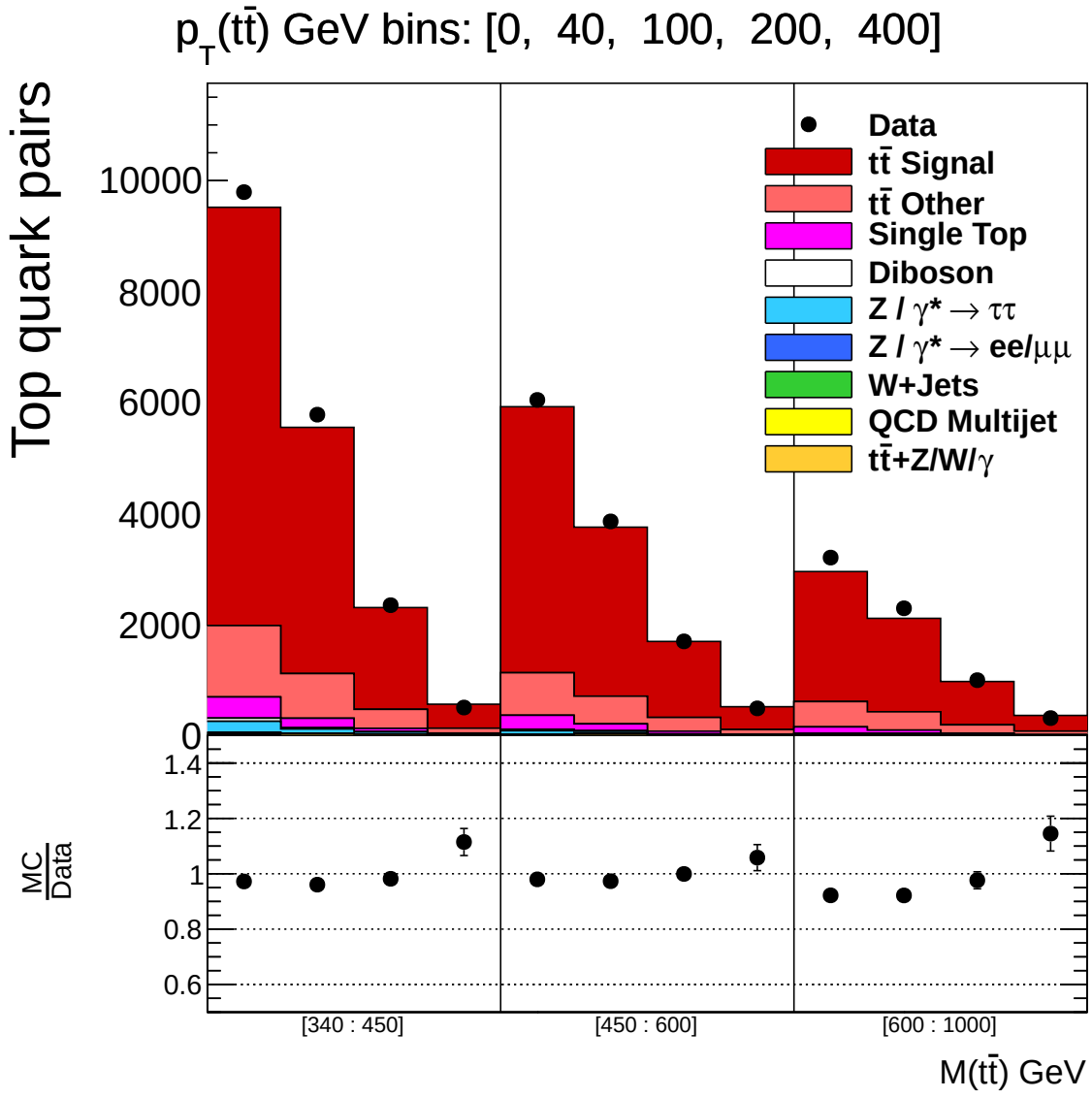

Figure 11.8: Control distribution of the $|p_T(t\bar{t})|$ in bins of the $M(t\bar{t})$. The $|p_T(t\bar{t})|$ bins are shown on the top of the plot. Other details as in Fig. 11.1.

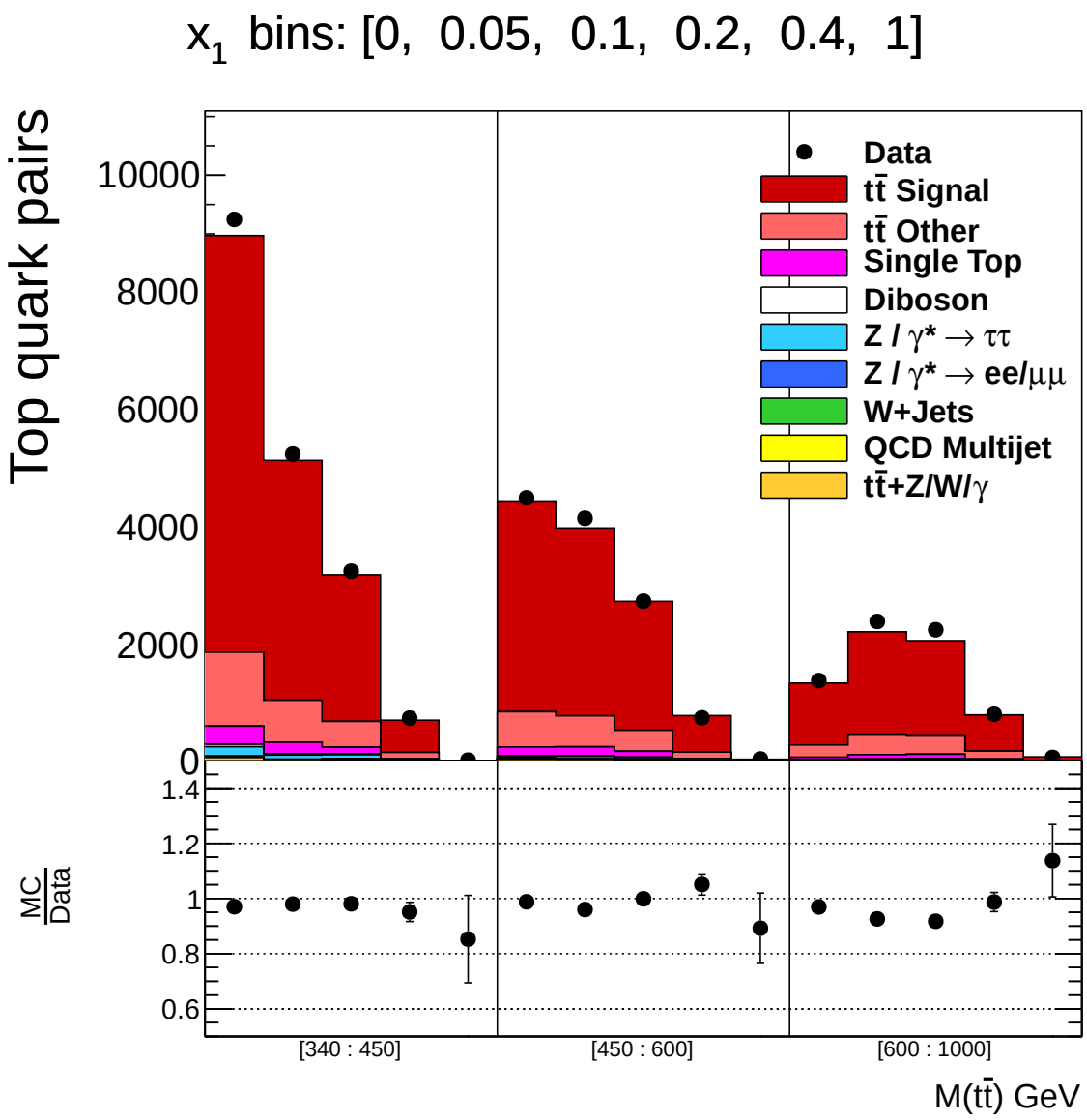

Figure 11.9: Control distribution of x_1 in bins of $M(t\bar{t})$. The x_1 bins are shown on the top of the plot. Other details as in Fig. 11.1.

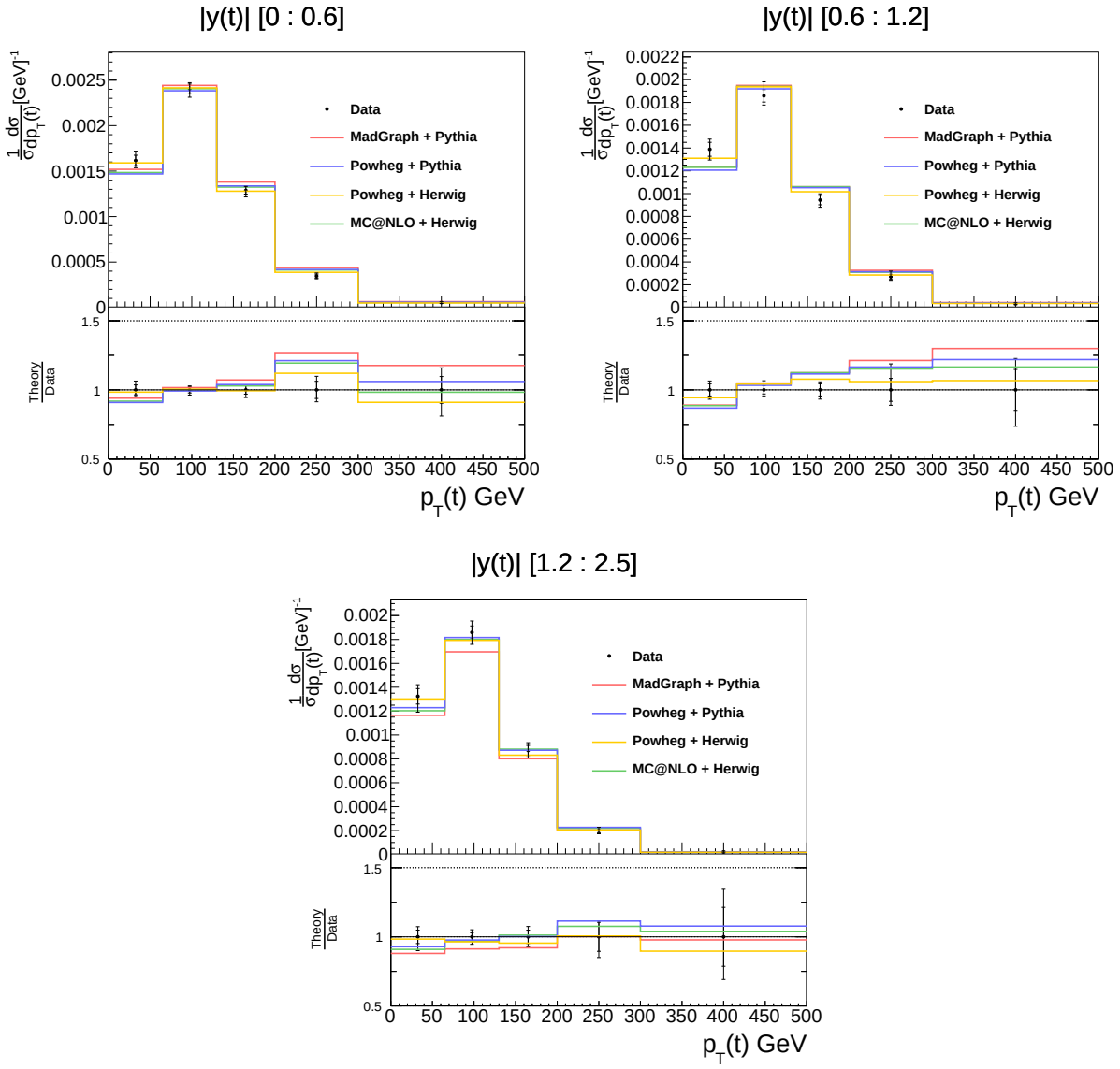

Figure 11.10: Normalized differential cross sections in bins of $|y(t)|$ and $p_T(t)$. The inner error bars show the statistical uncertainties from the data. The outer error bars are the combined statistical and systematical uncertainties on the data. The predicted cross sections from four different models are also presented: MadGraph + Pythia (red line), Powheg + Pythia (blue line), Powheg + Herwig (orange line) and MC@NLO + Herwig (green line). The ratio of the predictions over measured cross sections are shown in the bottom panels with the error bars corresponding to the measurement uncertainties.

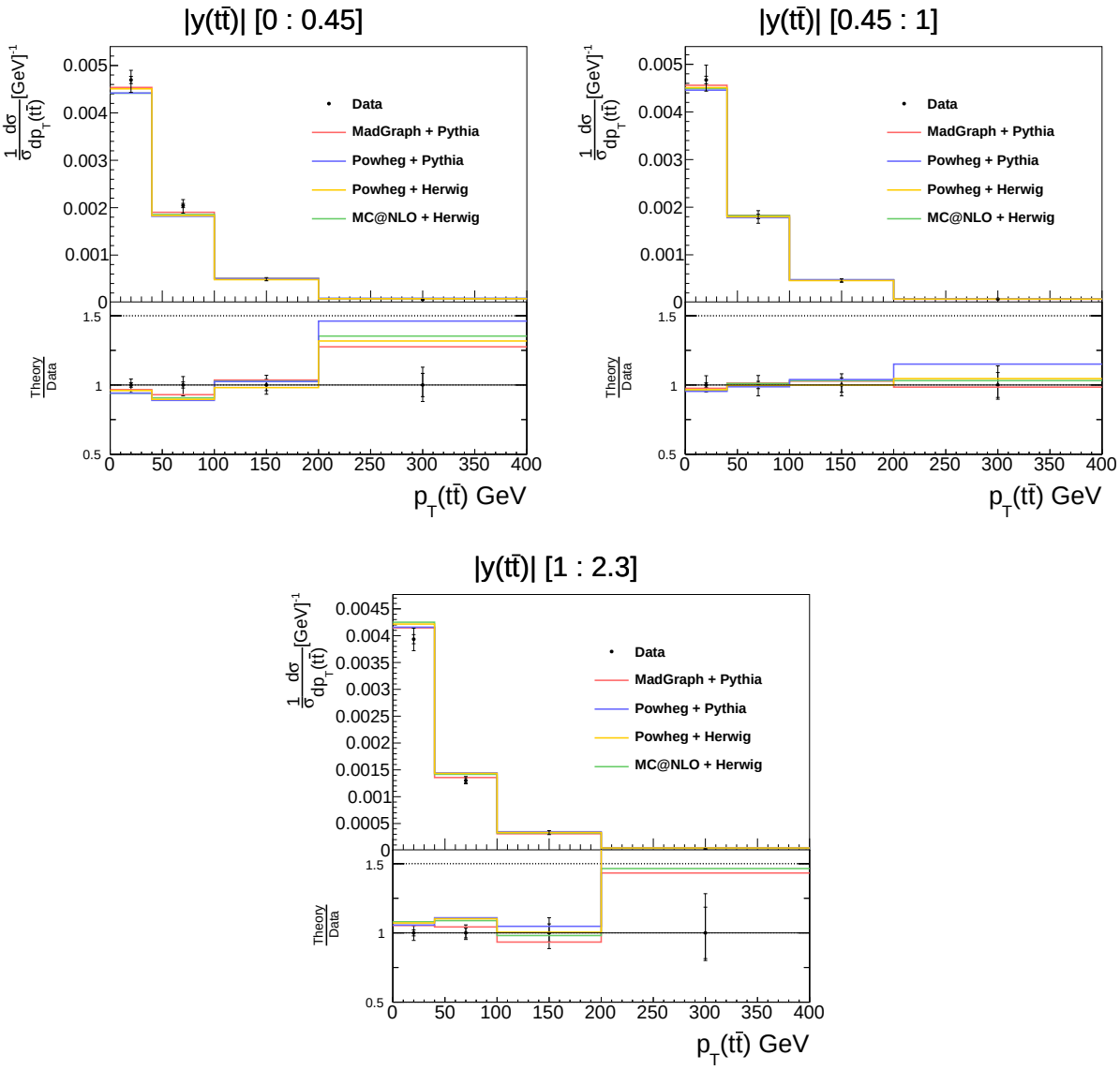

Figure 11.11: Normalized differential cross sections in bins of top pair absolute rapidity and transverse momentum. Other details as in Fig. 11.10.

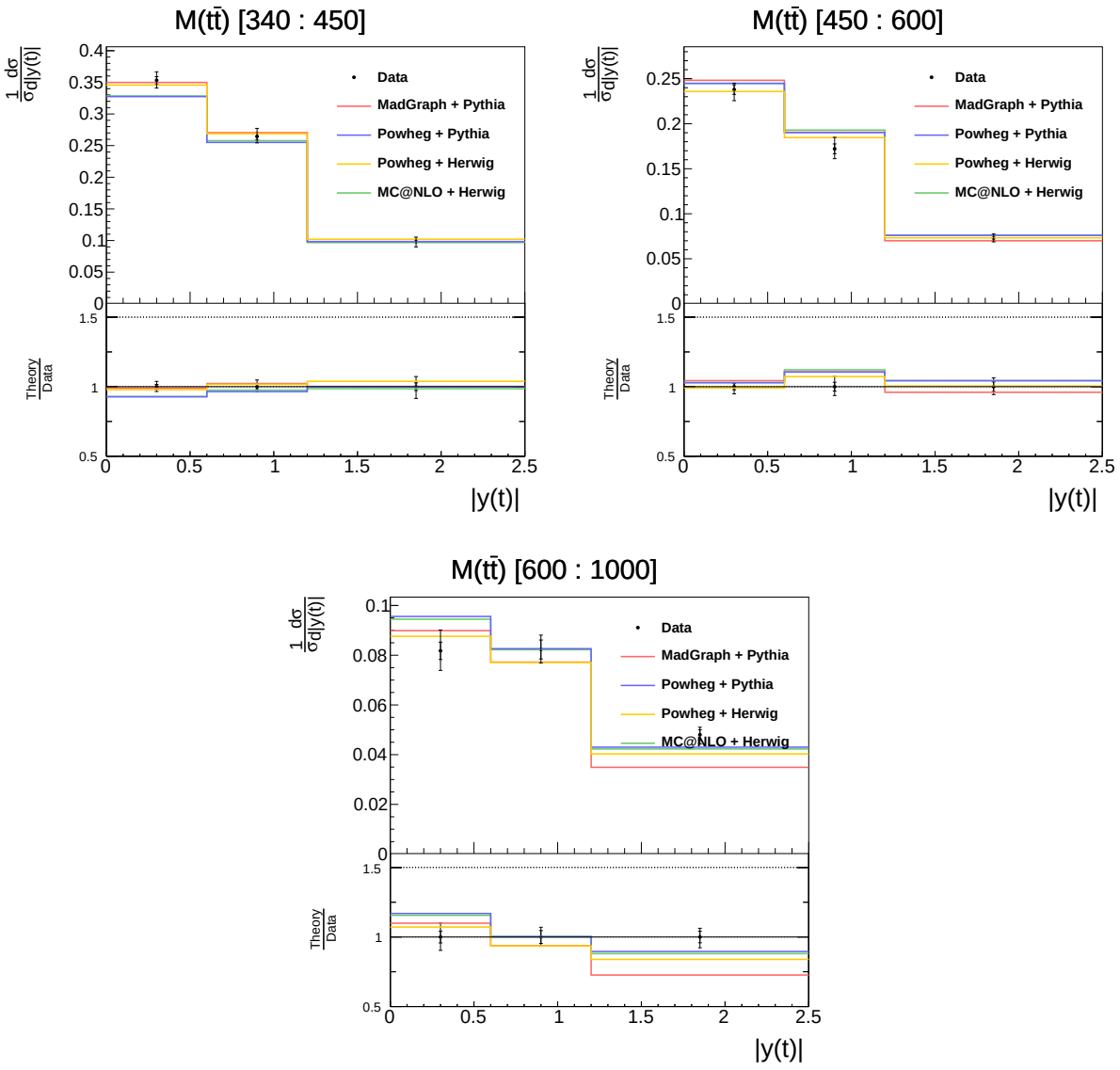

Figure 11.12: Normalized differential cross sections in bins of $M(t\bar{t})$ and $|y(t)|$. Other details as in Fig. 11.10.

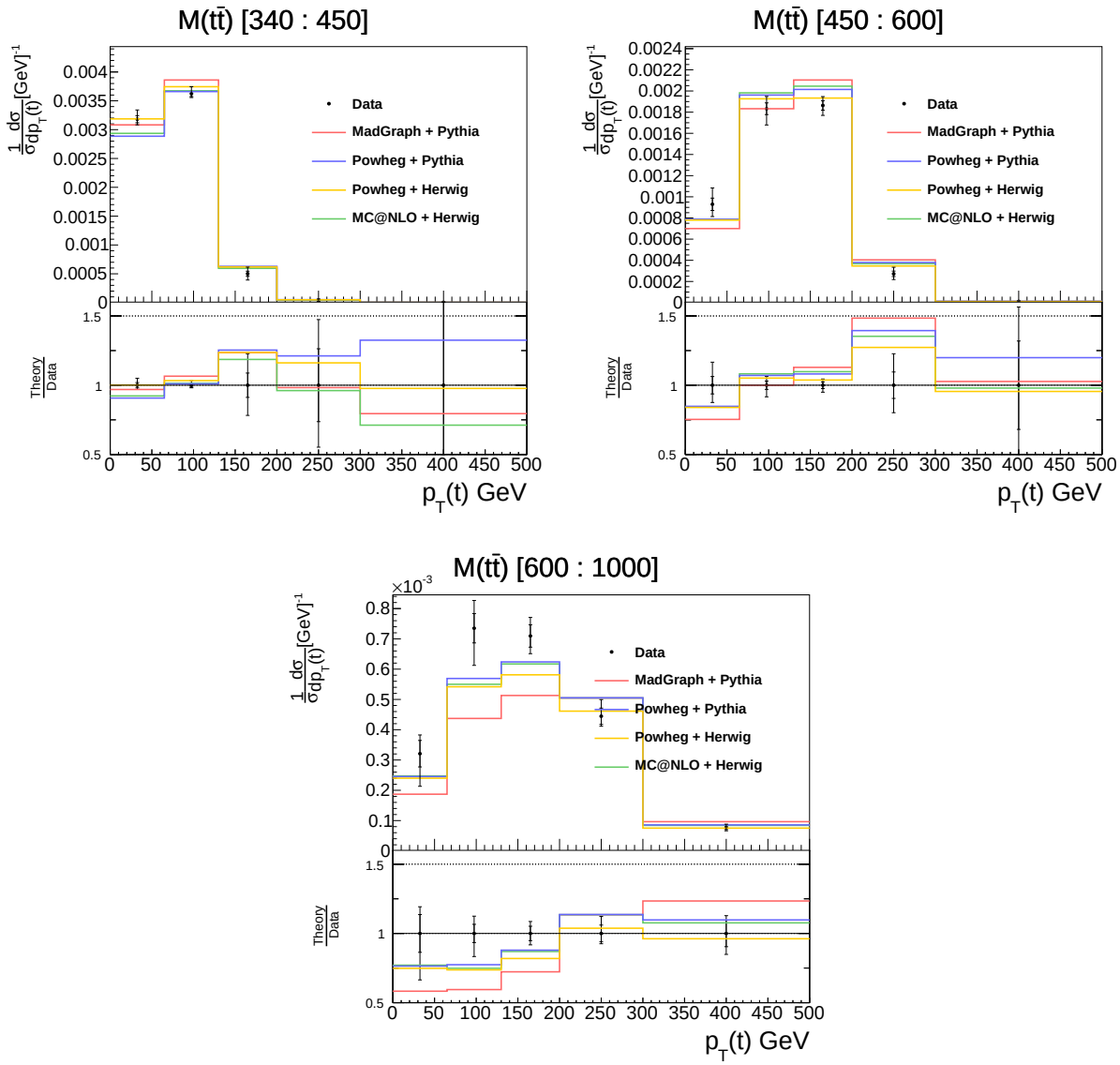

Figure 11.13: Normalized differential cross sections in bins of $M(t\bar{t})$ and $p_T(t)$. Other details as in Fig. 11.10.

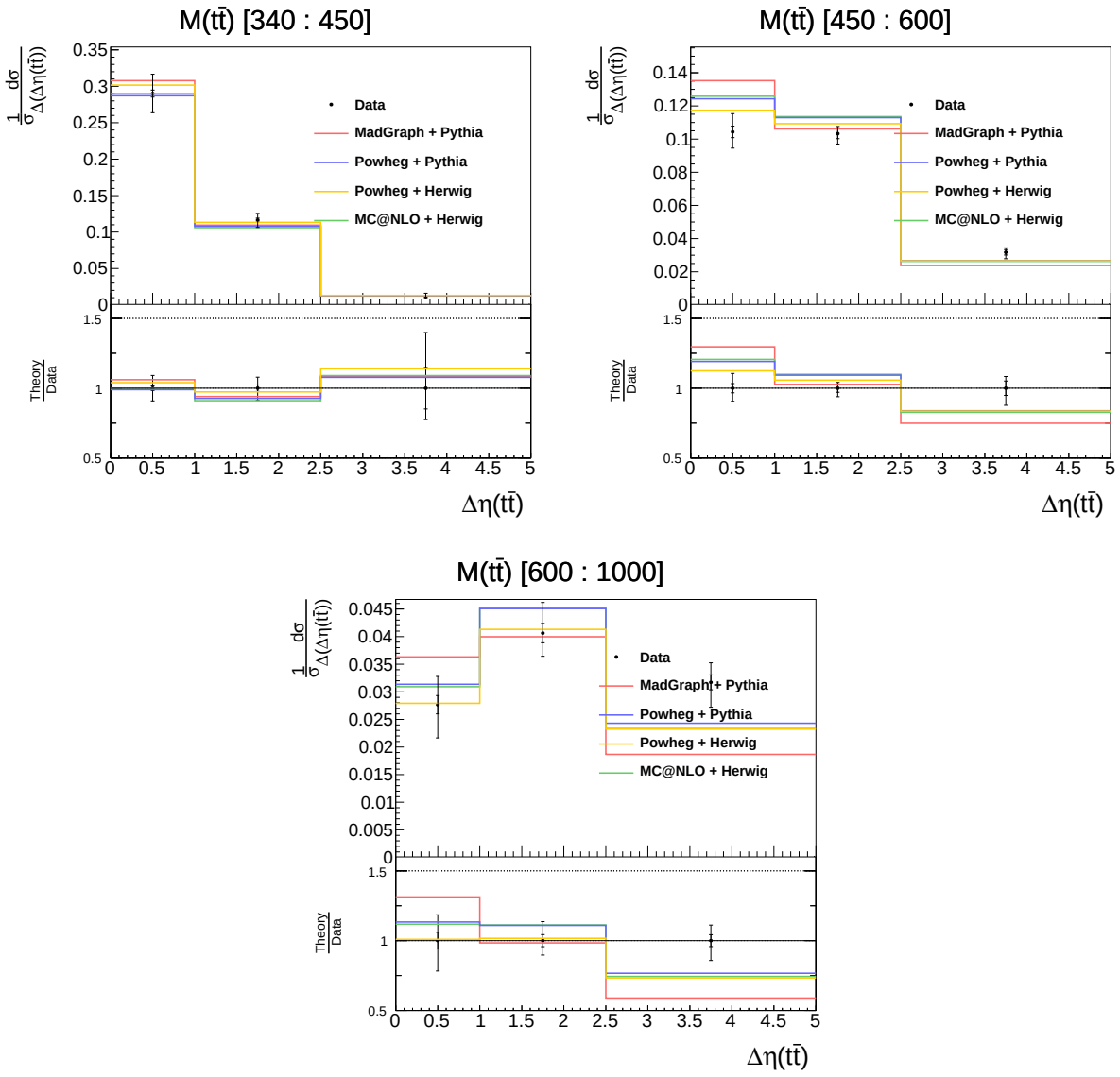

Figure 11.14: Normalized differential cross sections in bins of $M(t\bar{t})$ and $\Delta\eta(t\bar{t})$. Other details as in Fig. 11.10.

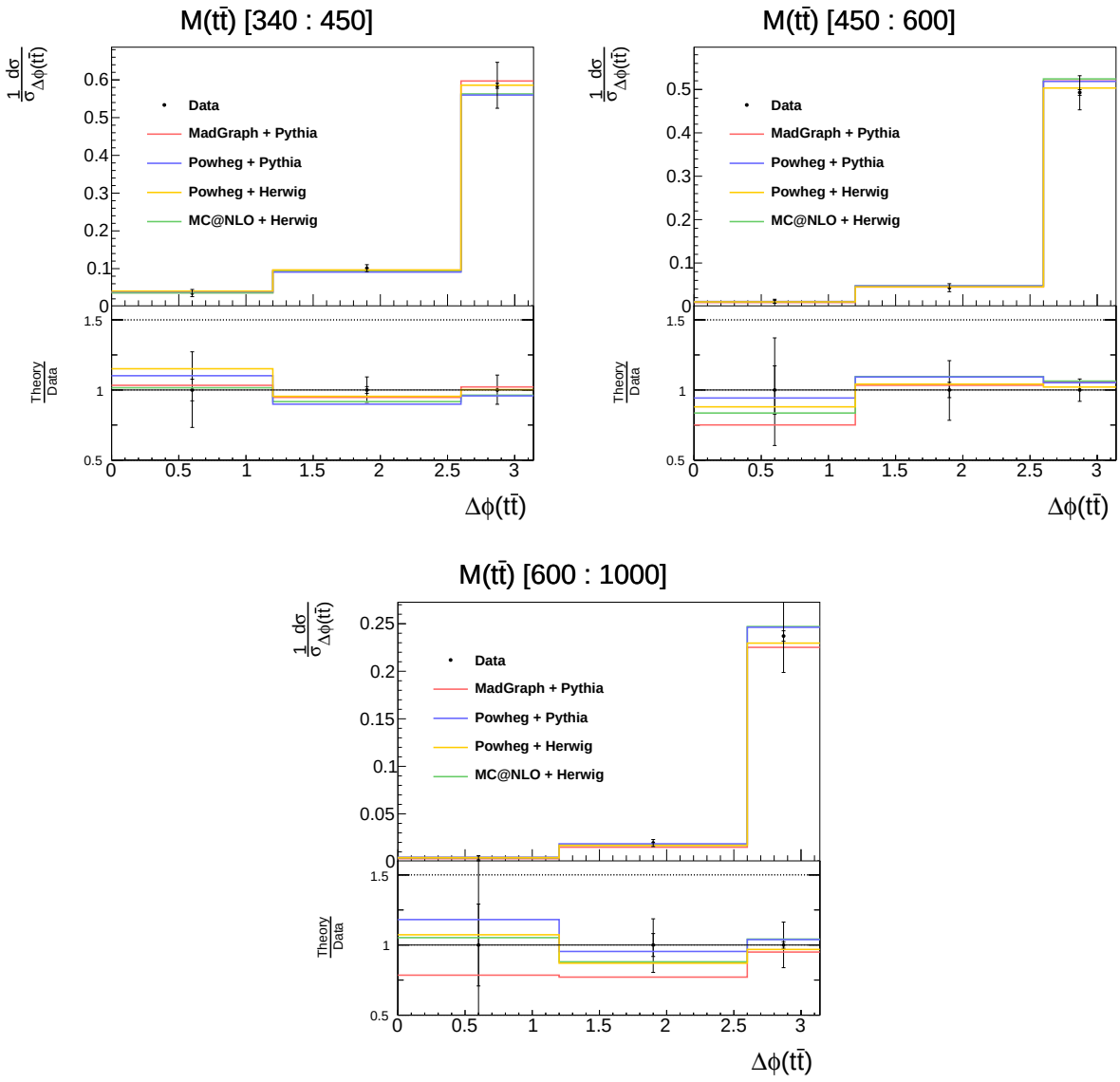

Figure 11.15: Normalized differential cross sections in bins of $M(t\bar{t})$ and $\Delta\phi(t\bar{t})$. Other details as in Fig. 11.10.

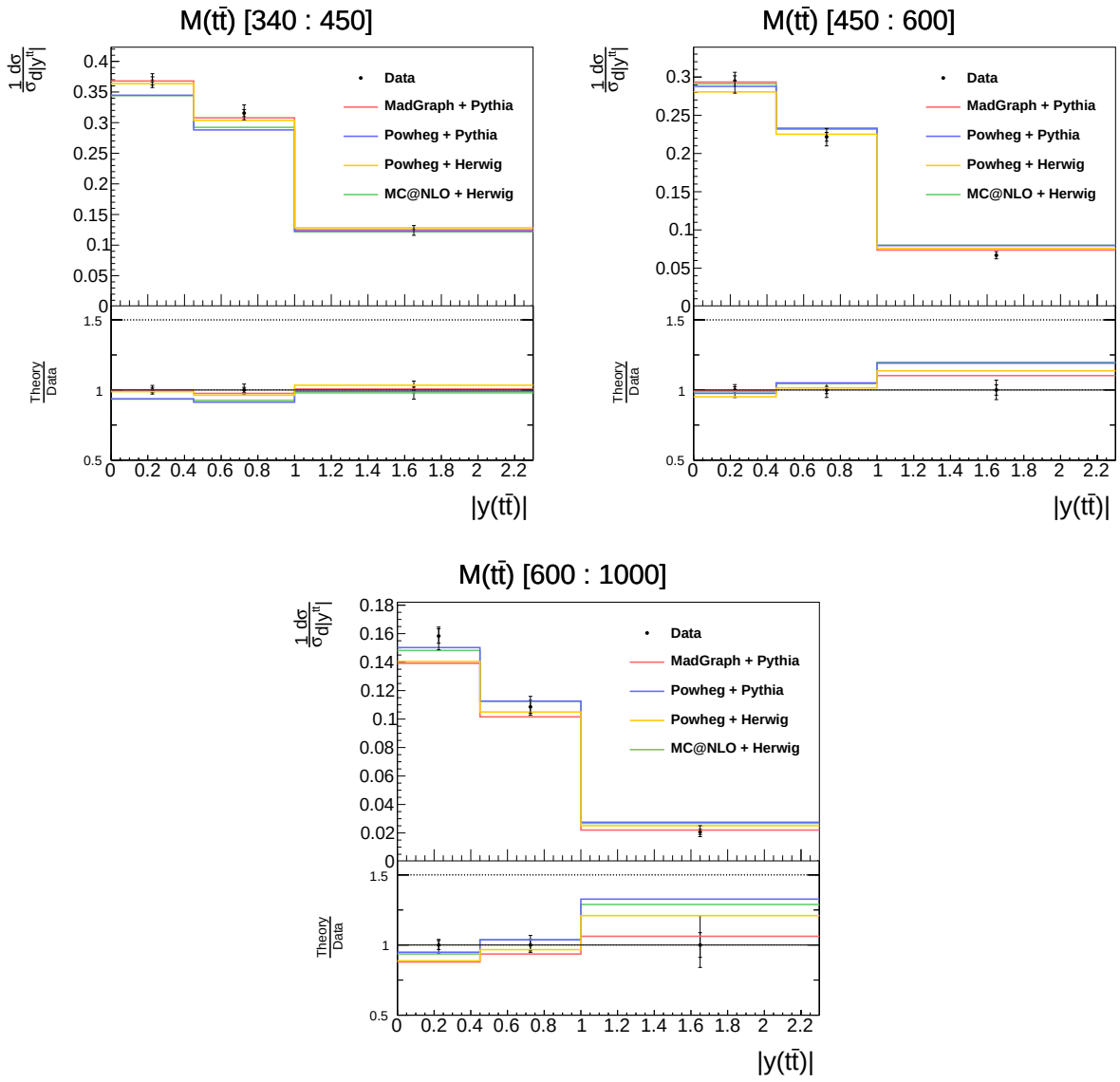

Figure 11.16: Normalized differential cross sections in bins of $M(t\bar{t})$ and $|y(t\bar{t})|$. Other details as in Fig. 11.10.

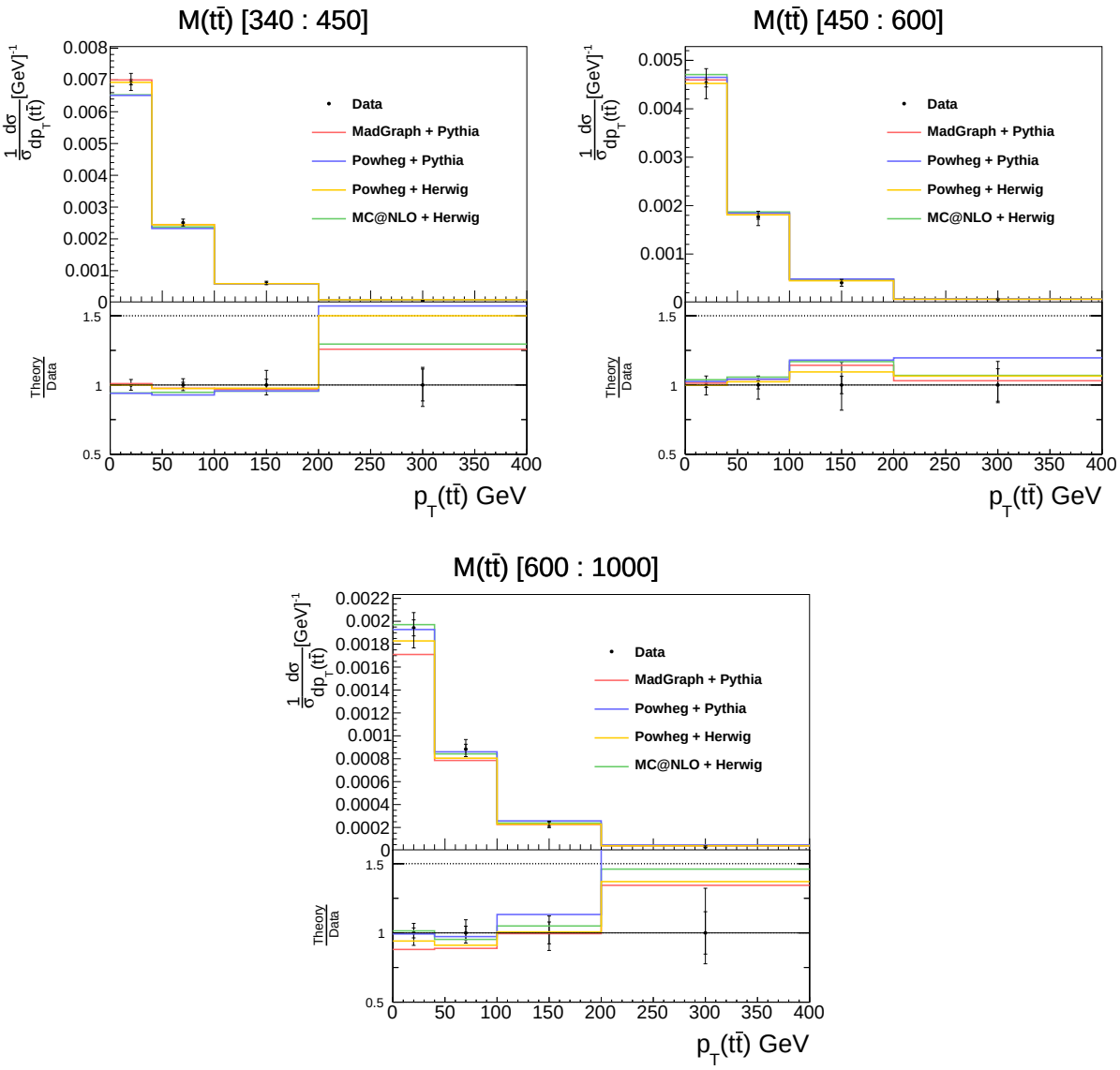

Figure 11.17: Normalized differential cross sections in bins of $M(t\bar{t})$ and $p_T(t\bar{t})$. Other details as in Fig. 11.10.

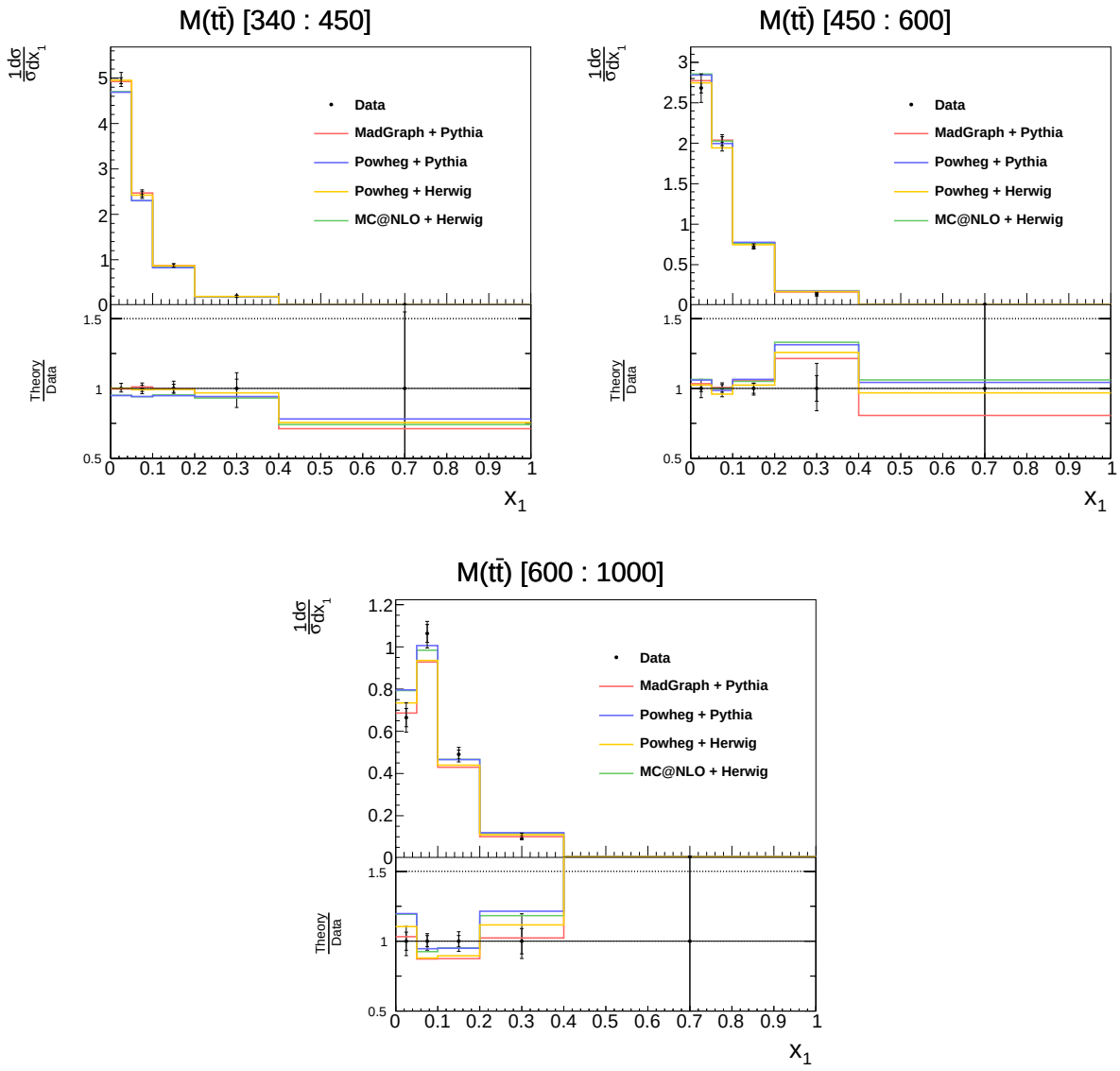

Figure 11.18: Normalized differential cross sections in bins of x_1 and $M(t\bar{t})$. Other details as in Fig. 11.10.

11.2 Discussion

In general, the cross sections measured and presented in this work are in general in reasonable agreement with LO and NLO predictions implemented in differential MC event generators (LO MadGraph+Pythia and NLO Powheg+Herwig, Powheg+Pythia and MC@NLO + Herwig). However, there are some disagreements and trends observed in particular cross sections bins and control distributions. These should be discussed in more detail.

Additionally, the double differential distributions provide a detailed check of the tendencies observed in the single differential cross sections, measured in the dilepton channel

at a center-of-mass energy $\sqrt{s} = 8$ TeV (TOP-12-028) [4].

11.2.1 Comparison to the Single Differential Cross Sections

The results of the measurement of single differential $t\bar{t}$ production cross sections [4, 110] showed some tendencies in the way how the theoretical predictions describe the measurements. The following table summarizes these observations:

Cross Sections	$\frac{\textbf{Theory}}{\textbf{Measurement}}$ **tendency**
In bins of $p_T(t)$	Theoretical predictions are harder than measurement
In bins of $y(t)$	Theoretical predictions are more central than measurement
In bins of $p_T(t\bar{t})$	Theory predicts more $t\bar{t}$ pairs with high p_T
In bins of $y(t\bar{t})$	Theoretical predictions are more central in $y(t\bar{t})$
In bins of $M(t\bar{t})$	Theory predictions are overall in agreement with measurement

The corresponding single differential $t\bar{t}$ cross section plots are shown in Fig. 11.19

It is interesting to see how the double differential cross sections measured in this analysis shed more light on these effects.

The double differential cross sections in bins of $p_T(t)$ and $|y(t)|$ (see Fig. 11.10) show that the effect observed in the single differential cross sections in bins of $y(t)$ is stronger for the middle and high $p_T(t)$. That means, that there is a slight tendency that the top quarks with higher p_T tend to be more central in the theoretical predictions compared to the measurements.

The effect observed for the single differential $p_T(t\bar{t})$ spectrum may be explained by an overestimation of the amount of hard radiation in the predictions since such a radiation is usually accompanied by a recoiling $t\bar{t}$ system with high $p_T(t\bar{t})$. This effect is the weakest for MadGraph + Pythia, is equal for MC@NLO + Herwig and Powheg + Herwig and is the strongest for Powheg + Pythia. The tendency that the measurements are more central in $y(t\bar{t})$ can originate from the PDF effects: it shows that the measurements favour an overall smaller ratio of $\frac{\text{PDF(low}x)}{\text{PDF(high}x)}$ which corresponds to a more equal x for the incoming partons. This results in an overall smaller total rapidity. This effect is the smallest for the MadGraph+Pythia model, and similarly high for Powheg+Pythia and Powheg+Herwig predictions. The double differential cross sections in bins of $p_T(t\bar{t})$ and $|y(t\bar{t})|$ (see Fig. 11.11) show overall the same tendencies.

11.2.2 Observations on the Double Differential Measurements in the Highest M($t\bar{t}$) Region

The region with the high invariant masses of the $t\bar{t}$ system shows a clear disagreement between data and predictions in different observables.

The double differential cross sections in bins of $M(t\bar{t})$ and p_T (see Fig. 11.13) shows that in the region with $M(t\bar{t}) > 600$ GeV, predictions have a harder p_T spectrum than the measurements.

An obviously related effect is the $\Delta\eta(t\bar{t})$ spectrum (see Fig. 11.14), where in the high $M(t\bar{t})$ bin the $\Delta\eta(t\bar{t})$ for the predictions tends to smaller values compared to the measurements.

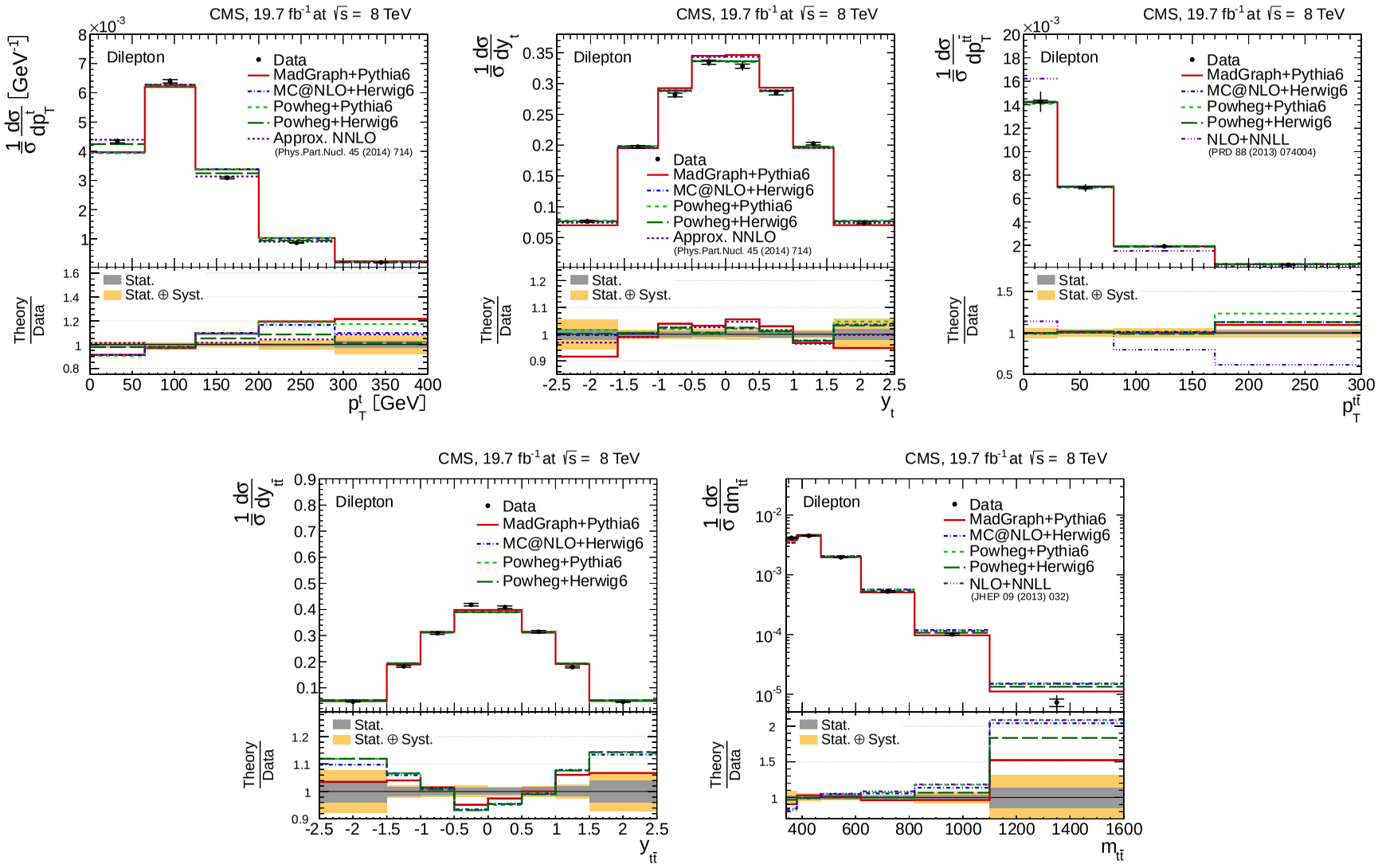

Figure 11.19: Normalized differential $t\bar{t}$ production cross section in the dilepton channels as a function of the $p_T(t)$ (upper left), $y(t)$ (upper middle), $p_T(t\bar{t})$ (upper right), $y(t\bar{t})$ (lower left) and $M(t\bar{t})$ (lower right). The data points are placed at the midpoint of the bins. The inner (outer) error bars indicate the statistical (combined statistical and systematic) uncertainties. The measurements are compared to predictions from MadGraph + Pythia, Powheg + Pythia, Powheg + Herwig and MC@NLO + Herwig, and to NLO+NNLL [131, 132] calculations, when available. The lower part of each plot shows the ratio of the predictions to data. Plots are taken from [4].

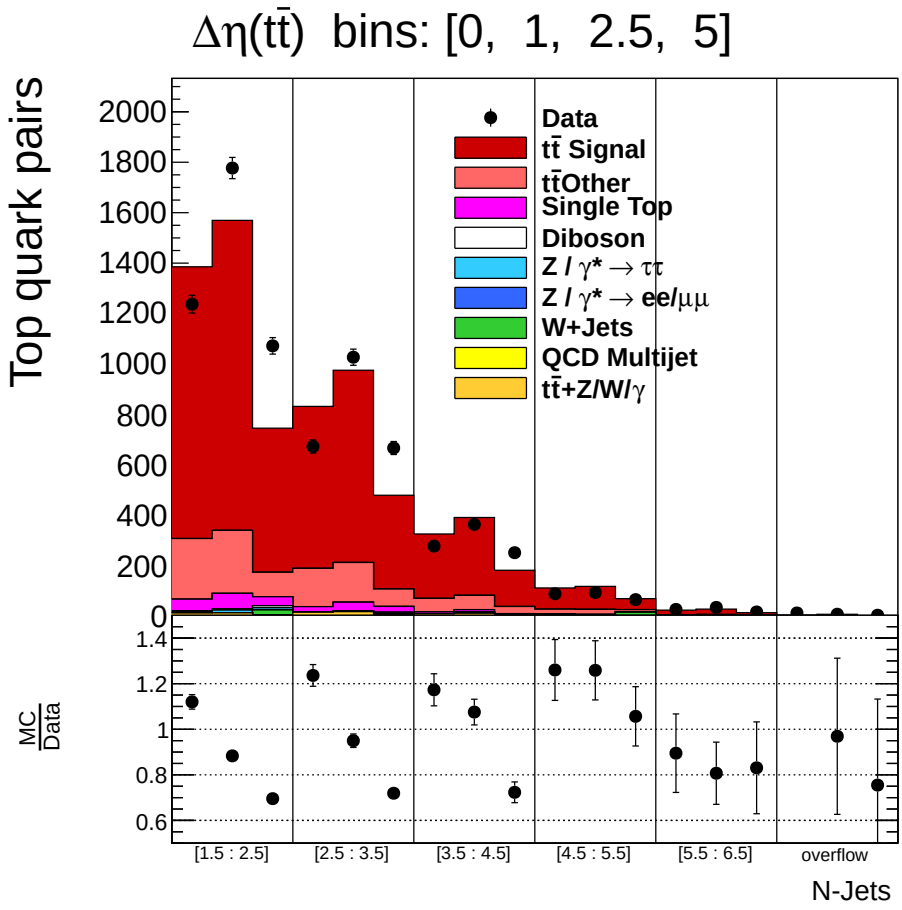

Figure 11.20: Control distribution of $\Delta\eta(t\bar{t})$ in bins of jet multiplicity for $\mathbf{M(t\bar{t}) > 600\ GeV}$. The $|\Delta\eta(t\bar{t})|$ bins are shown on the top of the plot. The experimental data are marked with the black dots and the reconstructed MC signal is marked with the red area. The error bars on the data points represent the statistical uncertainty only. The different background contributions are also shown. On the bottom part of the plot the ratio between MC and data statistics in each bin is presented.

For both cases the largest discrepancies between the measurements and the predicted cross section values are observed for the MadGraph + Pythia model.

There are no strong effects seen in the cross sections in bins of $M(t\bar{t})$ and $\Delta\phi(t\bar{t})$ (see Fig. 11.15).

To investigate the guesses about the nature of the smaller $\Delta\eta(t\bar{t})$ (see Fig. 11.14), the distribution of $\Delta\eta(t\bar{t})$ in bins of multiplicity of hard jets (with $p_T > 30$ GeV) is studied and presented in Fig. 11.20. As one observes from the plot, the ratio between theory predictions and measurements does not depend on the jet multiplicity (not taking to account the high multiplicity bin where the statistics is low). The conclusion is that it is not the hard radiation i.e. the number of hard radiations in the events, in the predictions, which is causing the effect.

The effect on the $\Delta\eta(t\bar{t})$ in the highest $M(t\bar{t})$ bin is also checked in the systematic variations of matching and hard scales in the nominal MadGraph + Pythia sample

(see sec. 10.2.5 and sec. 10.2.6). The control distributions of $\Delta\eta(t\bar{t})$ in the finer binning are shown in Fig. 11.21 for the matching scale variations and in Fig. 11.22 for the hard scale variations. All the varied distributions are compared to the nominal unvaried spectrum. This comparison shows that the effect of the MC tending towards smaller $\Delta\eta(t\bar{t})$ compared to the measurements is getting smaller for the variation of the matching scale up by factor 2 and for the variation of the hard scale down by factor 0.5. This might give some indication on the origin of the deficiency of the MC model. It seems that the discrepancy might be related to the mixture of matrix element hard radiation and parton showering.

11.3 Summary on the Results

After presenting the normalized[1] double differential top-quark-pair production cross sections in bins of nine different combinations of variables, one can summarize that overall the theoretical description of the measured data points is reasonable. The precision of the measurements allows a meaningful visual comparison of the experimental results to different theoretical models.

All the double differential distributions and normalized cross sections, shown in previous section, can be divided into three groups (see Fig. 11.23):

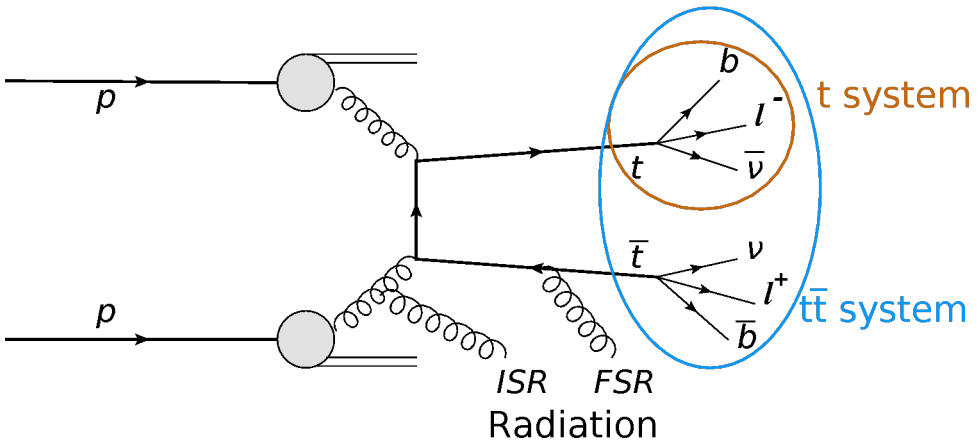

Figure 11.23: Diagram, which presents the $t\bar{t}$ production process via gluon-gluon fusion. Different groups of objects in the final state, which may be regarded as one system, are marked with circles.

- results, which describe the t dynamics;
- results, which describe the $t\bar{t}$ system dynamics;
- results on combined t and $t\bar{t}$ dynamics.

[1] As the analysis presented in this work was tuned to measure the normalized cross sections, the unnormalized cross sections are not discussed in this section. The results with unnormalized double differential top-quark-pair production cross sections are presented in Appendices G and I

The results presented in bins of $p_T(t)$ and $|y(t)|$ (fig. 11.10) are describing the t dynamics. The observation, made previously in the measurement of top-quark-pair differential cross sections in dileptonic channel at $\sqrt{s} = 8$ TeV [110], was that the top-quark transverse momentum spectrum is softer in data than in most of the predictions. The best description was provided by POWHEG + HERWIG predictions. However, as shown in the present analysis this effect is very weak in the highest $|y(t)|$ bin. One can also conclude that the POWHEG + HERWIG predictions provide the best description of the data, except for the highest $|y(t)|$ regions.

When talking about the $t\bar{t}$ system dynamics, the results in bins of $p_T(t\bar{t})$ and $|y(t\bar{t})|$ (fig. 11.11) show overall good agreement with the predictions. MADGRAPH + PYTHIA describe experimental points best. However, slight tendencies to a softer $p_T(t\bar{t})$ and more central $y(t\bar{t})$ in the measured data are observed. The same tendency towards softer $p_T(t\bar{t})$ in the measurements is observed for the distributions in bins of $p_T(t\bar{t})$ and $M(t\bar{t})$ (fig. 11.17).

The distributions, which represent the combined dynamics of t and $t\bar{t}$, are the distributions of $M(t\bar{t})$ in different bins of $p_T(t)$, $|y(t)|$, $\Delta\eta(t\bar{t})$ and $\Delta\phi(t\bar{t})$ (fig. 11.13, fig. 11.12, fig. 11.14 and fig. 11.15). The general observation is that the highest $M(t\bar{t})$ bin has the worst description of data by the predictions. In this region the effect of softer $p_T(t)$ is much more pronounced which is probably kinematically related to the simultaneous observation of a larger pseudorapidity separation $\Delta\eta(t\bar{t})$ between t and $\bar{t}$ in the data and less central $y(t)$ in the data.

One would also think of the possibility of wrong modeling of spin effects. However, MADGRAPH includes spin effects. From this point of view strong discrepancies due to spin mismodeling are not expected. Spin effects are expected to affect decay angle distributions of t and $\bar{t}$ decay products, for instance the angle of b emission in top restframe with the $\bar{t}$ direction defining the $-z$ axis. One would need to study if the spin effects could also affect the $\Delta\eta$ which should reflect the spin properties of incoming partons and exchange gauge bosons involved in the $t\bar{t}$ production process.

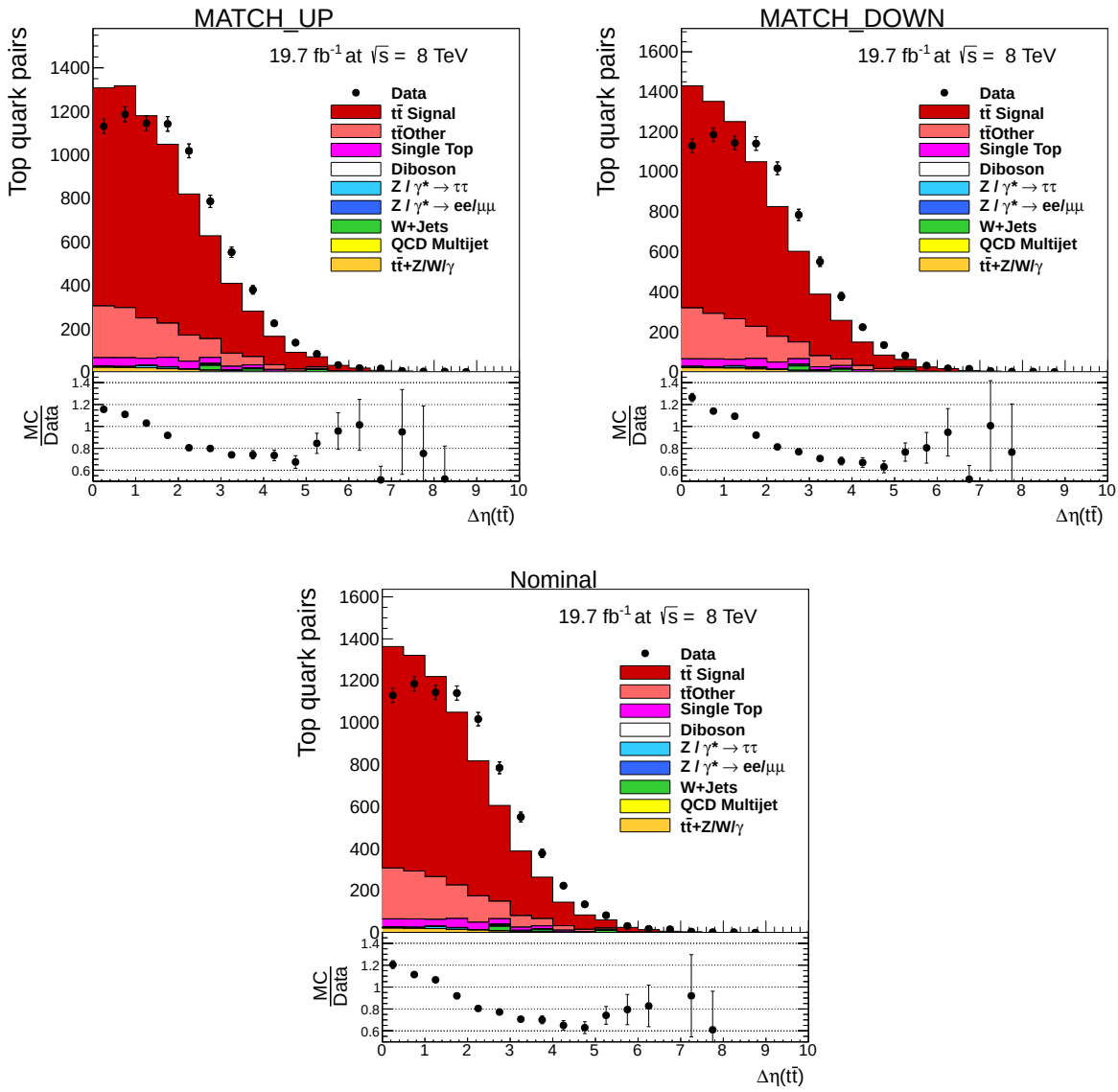

Figure 11.21: Control distribution of $\Delta\eta(t\bar{t})$ compared to the MC with matching scale variation by factor 2 (top left), to the MC with matching scale variation by factor 0.5 (top right) and to the nominal unvaried MC (bottom) for $\mathbf{M(t\bar{t}) > 600\ GeV}$. The experimental data are marked with the black dots and the reconstructed MC signal is marked with the red area. The error bars on the data points represent the statistical uncertainty only. The different background contributions are also shown. On the bottom part of the plot the ratio between MC and data statistics in each bin is presented.

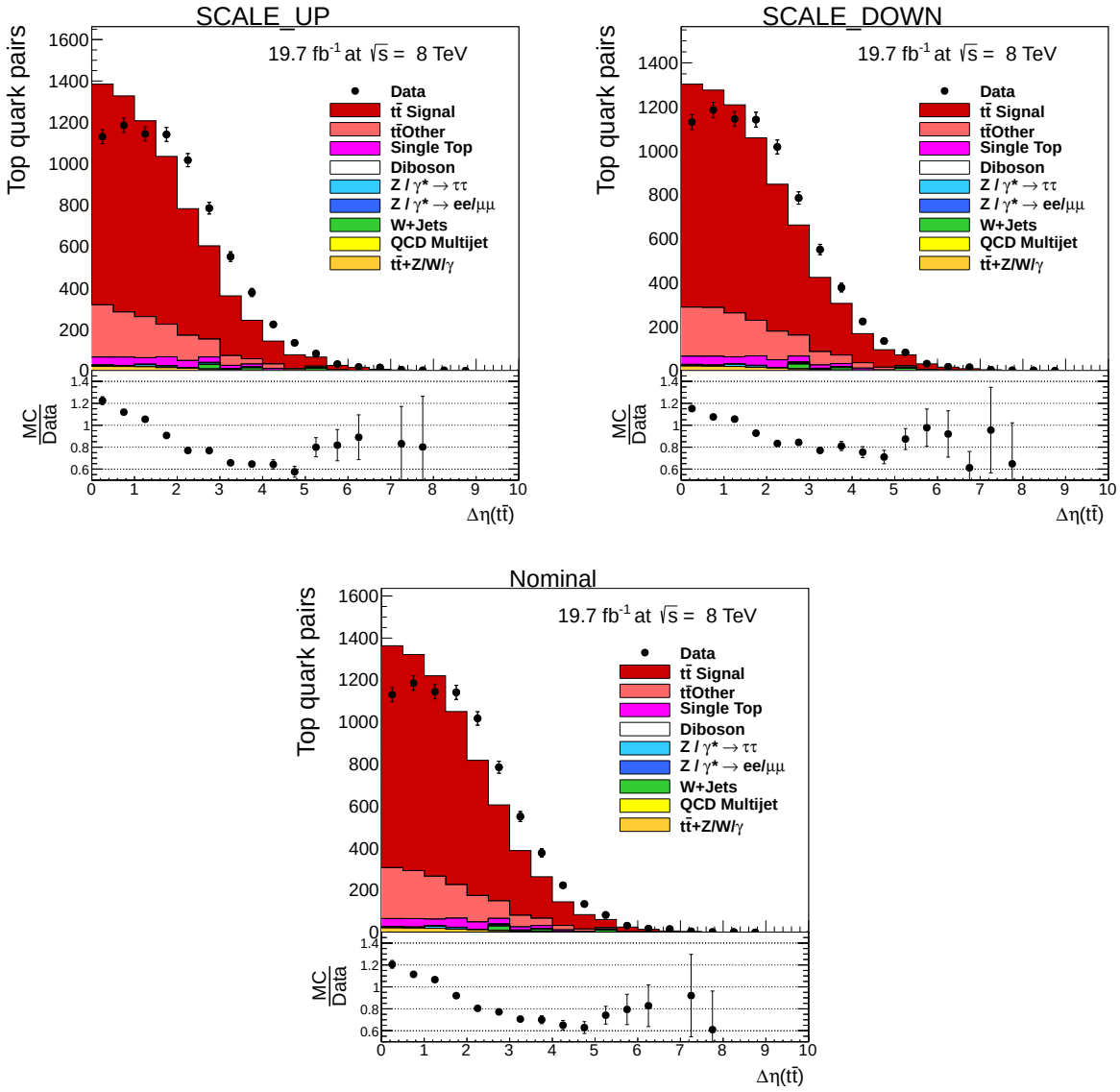

Figure 11.22: Control distribution of $\Delta\eta(t\bar{t})$ compared to the MC with hard scale variation by factor 2 (top left), to the MC with hard scale variation by factor 0.5 (top right) and to the nominal unvaried MC (bottom) for $\mathbf{M(t\bar{t}) > 600\ GeV}$. The experimental data are marked with the black dots and the reconstructed MC signal is marked with the red area. The error bars on the data points represent the statistical uncertainty only. The different background contributions are also shown. On the bottom part of the plot the ratio between MC and data statistics in each bin is presented.

Chapter 12

Summary and Outlook

12.1 Summary

The top-quark is the heaviest known elementary particle. It provides possibilities for unique tests of the Standard Model due to its properties. The top-quark has a lifetime, which is shorter than the typical hadronization time. It decays before it can hadronize. Thus, studies of the top-quark provide the knowledge of bare quark properties.

In this work, normalized double differential cross sections for the $t\bar{t}$ production in the electron-muon final state in proton-proton collisions at 8 TeV are presented. The results were obtained after analyzing a data set collected with the CMS detector at the LHC in 2012, which corresponds to a luminosity of 19.7 fb^{-1}.

A kinematic reconstruction procedure was employed to reconstruct the full final state of the $t\bar{t}$ pair. It is based on six constraints: top- and antitop-quark mass constraint, $W^{\pm}$ mass constraint and the assumption that all the MET in the event is arising only from the neutrinos from the top decay. These assumptions allow to solve the system of kinematic equations analytically. The kinematic reconstruction algorithm requires lepton, antilepton, b-jet, $\bar{b}$-jet momenta and MET as an input. To account for possible fluctuations due to detector effects, the energies and directions of leptons and b-jets were smeared 100 times. The output of the kinematic reconstruction algorithm are neutrino and antineutrino momenta.

The kinematic reconstruction algorithm is performing with 93% efficiency. The reconstructed kinematics of the top- and antitop-quarks show, according to MC simulations, no biases and trends. This kinematic reconstruction algorithm was also employed to obtain the results in the recent publication related to the measurement of the single differential $t\bar{t}$ production cross sections in the dilepton channel at $\sqrt{s}$ =8 TeV at CMS [4].

To account for the migrations between different bins, a two-dimensional unfolding is performed. In this work the TUnfold algorithm [121] (based on χ^2 minimization and Tikhonov regularization [122]) is utilized. The minimum global correlation coefficient method [124] is exploited to choose the optimal regularization strength. The unfolding is performed simultaneously in bins of two variables in which the cross sections are measured.

The central topic of this work is the first measurement of the normalized double differential $t\bar{t}$ production cross sections at $\sqrt{s} = 8$ TeV. This measurement is important to test Standard Model predictions. Detailed knowledge of the top-pair production properties is

also important for searches beyond the SM.

The normalized double differential $t\bar{t}$ production cross sections were measured in bins of nine different combinations of variables, which describe the top or top-pair kinematics. The precision of these measurements allows a visual comparison to different Standard Model predictions as implemented in MadGraph + Pythia, Powheg + Pythia, Powheg+Herwig and MC@NLO+Herwig Monte Carlo event generators. In general, the Standard Model predictions agree with the measured double differential $t\bar{t}$ production cross sections.

The results show that the top-quark transverse momentum is generally softer in data than in the MC predictions for the central top-quark rapidity bins. The best description of the top-quark transverse momentum spectra is provided by the Powheg + Herwig model.

For the higher invariant masses of the top-quark pairs, The cross sections in bins of $p_T(t)$ and $|y(t)|$ are generally poorly described by the models.

The top and antitop quarks in data have a larger separation in η than in Monte Carlo predictions. This effect is more pronounced in MadGraph + Pythia.

The relevant sources of systematic uncertainties for the normalized cross section measurement were taken into account in this analysis. The result showed that the measurement is dominated by statistical uncertainties.

This measurement confirmed the observations made previously in single differential $t\bar{t}$ production cross section measurement at $\sqrt{s} = 8$ TeV [110] in dileptonic final state. The same tendency to the softer p_T of the top-quark in data is seen similarly to what has been presented in this work. However, the double differential studies reveal more: they show that the softer $p_T(t)$ is related to the effect that at high $M(t\bar{t})$ the pseudorapidity separation $\Delta\eta(t\bar{t})$ is larger in data than in MC (which is also reflected by a broader $y(t)$ distribution in data than in MC). It seems that the discrepancy might be related to the mixture of matrix element hard radiation and parton showering. It will be the tasks mainly for the theorists to relate this discrepancies to deficiencies in their models and to improve their predictions.

12.2 Outlook

The measurement of double differential $t\bar{t}$ production cross section, as presented in this work, lacks statistics in some bins. There is a room for improvement with exploiting the upcoming data set, which is going to be collected at the high-energy LHC run with the collision center-of-mass energy of $\sqrt{s}$ = 13-14 TeV. A more intense top-pair production is expected, which will ensure a higher statistics in the data samples to be analyzed. A better precision gained in this way will allow to confirm the tendencies observed in this analysis and to perform the test of Standard Model predictions in more detail.

One could also measure the $t\bar{t}$ production cross section in a fiducial range at particle level. This can be done by taking out the acceptance correction in eq. 9.18. By doing so one avoids the kinematic extrapolation from fiducial to total cross section range represented by $\mathcal{A}$. This reduces the dependence of the measurement on the MC which was used to calculate the acceptance.

On the theory side it will be very interesting to compare NNLO models to the double differential data, once they are available for the double differential observables.

It would be also intersting to try including the measured cross sections in a proton PDF fit. Here the presented measurements (sec. results) as function of the observable $\times 1$ might be particular interesting because they provide (in the leading order QCD picture) access to the PDFs at different momentum fractions. With the presented tt data also large momentum fractions (> 0.4) are being probed with at least some sensitivity and this could help to constrain the gluon density in this region.

Appendix A

Smearing of the Measured Objects

As a part of the actions performed for the $t\bar{t}$ kinematic reconstruction, each jet and lepton energy and momentum direction is smeared 100 times to make the kinematic equations 8.1-8.6 for each event for at least a few smearings solvable. This increases the efficiency to reconstruct an event, as shown in Fig. A.1. However, one should also test the quality of the solutions obtained with the smearing procedure.

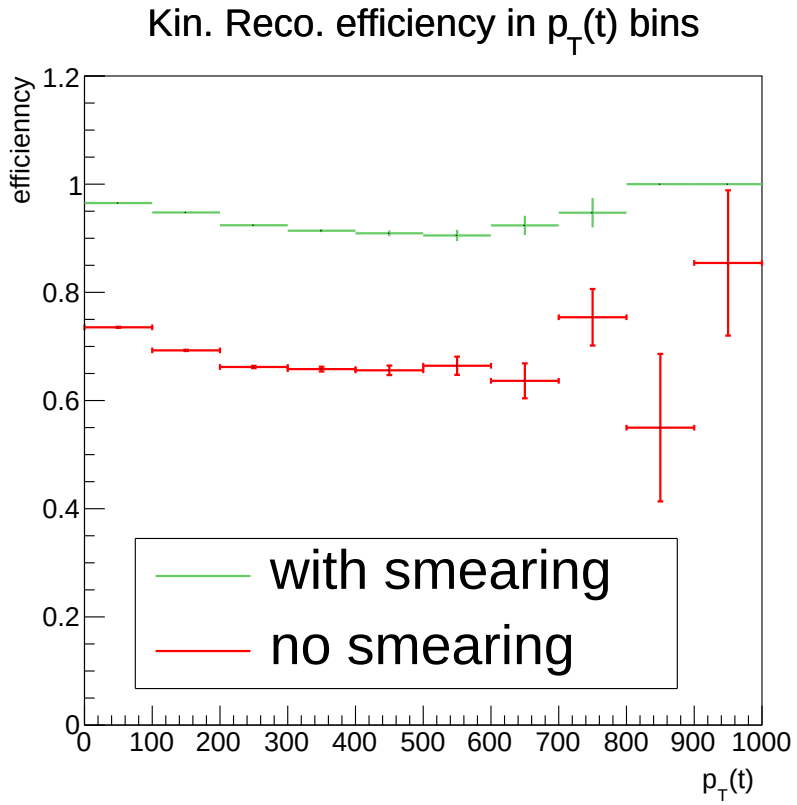

Figure A.1: Efficiency of the kinematic reconstruction procedure if the smearing of the reconstructed objects is applied (green) and if no smearing is applied (red).

The figure A.2 shows the relative resolution of the t-quark transverse momentum obtained from the event solutions, which appear only because of smearing, compared to

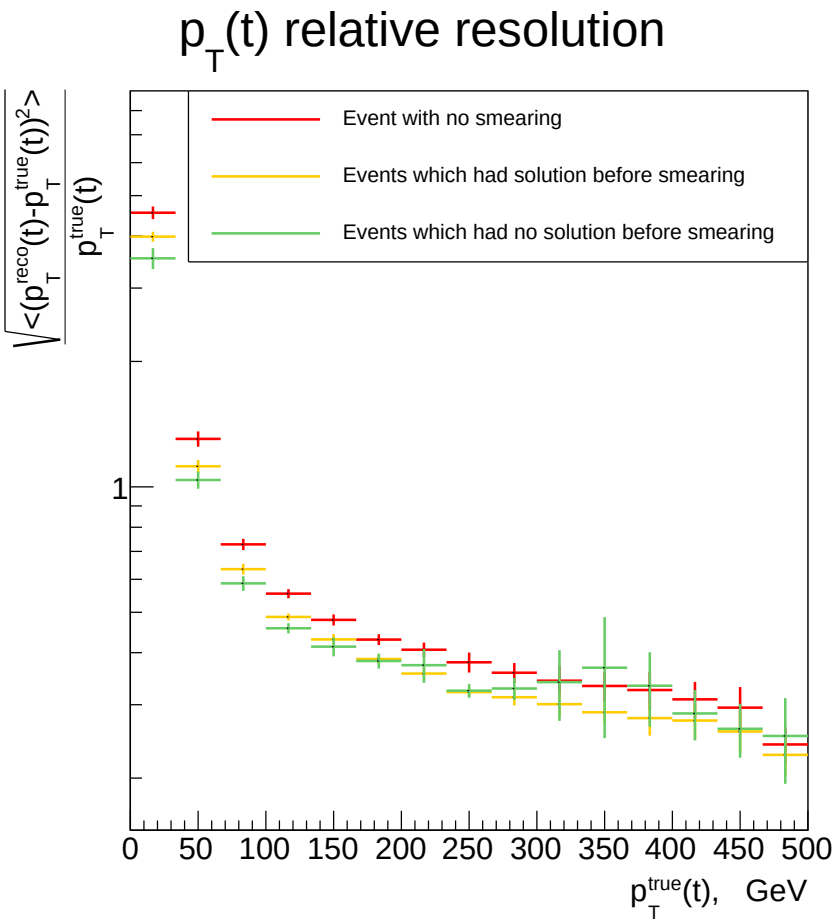

Figure A.2: Relative resolution of the solutions which appear only due to smearing (green), smeared solutions which appear in the event even without smearing (yellow) and solutions if no smearing is applied (red).

the one from the smeared solutions for events which had a solution before smearing and to the one from the central measured values events with no smearing. The relative $p_T(t)$ resolution is defined as $\frac{\sqrt{\langle (p_T^{reco}(t) - p_T^{true}(t))^2 \rangle}}{p_T^{true}(t)}$. It appears that the resolution of the event solutions which are only found due to the smearing procedure have the best resolution. The resolution of the non-smeared event solutions is the worst.

Appendix B

Kinematic Reconstruction Solution with the Smallest M($t\bar{t}$)

Only the solution of the kinematic equations 8.1-8.6 with minimal $m(t\bar{t})$ is taken for the further analysis. Studies which show the advisability of this criterion were performed.

The studies were performed on the generated $t\bar{t}$ signal events. The correct solution of the kinematic equations was defined by comparing the solution neutrino momentum, $p^{sol}_{\nu/\bar{\nu}}$, to the generated one, $p^{gen}_{\nu/\bar{\nu}}$, and choosing a solution with minimum χ^2. This χ^2 is defined as follows [133]:

$$\chi^2 = (p^{gen}_{\nu_x} - p^{sol}_{\nu_x})^2 + (p^{gen}_{\nu_y} - p^{sol}_{\nu_y})^2 + (p^{gen}_{\nu_z} - p^{sol}_{\nu_z})^2 + (p^{gen}_{\bar{\nu}_x} - p^{sol}_{\bar{\nu}_x})^2 + (p^{gen}_{\bar{\nu}_y} - p^{sol}_{\bar{\nu}_y})^2 + (p^{gen}_{\bar{\nu}_z} - p^{sol}_{\bar{\nu}_z})^2. \tag{B.1}$$

The fraction of correct solutions with minimal, second minimal, third minimal and fourth minimal invariant $t\bar{t}$ mass are shown in Figure B.1. In 60% of the cases the correct solution has a minimal $m(t\bar{t})$. One might tend to average all the solutions to include always the correct solutions. However, the figures B.2 show that the relative resolution[1] for the average and weighted average[2] solutions are worth than the one of the smallest $m(t\bar{t})$.

These studies show the advisability of selecting the solution with the smallest $m(t\bar{t})$ for the further analysis.

[1] The relative resolution is defined as in appendix A.

[2] The average solution calculated over the up to four solutions of the equations 8.1-8.6 is determined as an arithmetic average for each component of the momenta of the solutions, and the weighted average is determined by averaging the solutions momenta components with the weights according to the order of the $m(t\bar{t})$ of the solution, or from the distribution in Fig. B.1. To complete the kinematics, the top mass is assumed to be $m(t) = m(\bar{t}) = 172.5$ GeV.

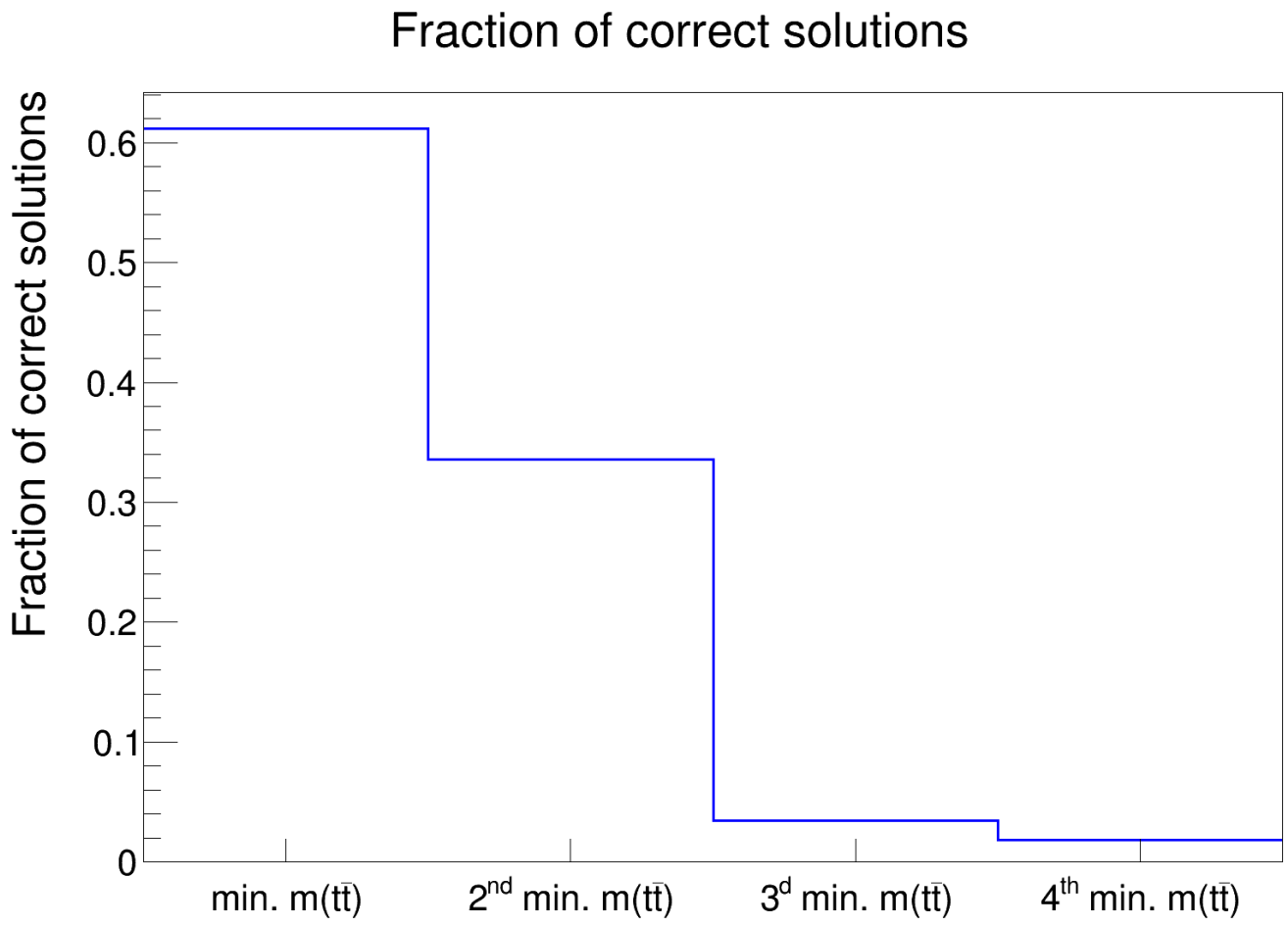

Figure B.1: Fraction of correct solutions depending on the order of minimum $m(t\bar{t})$ of the solutions.

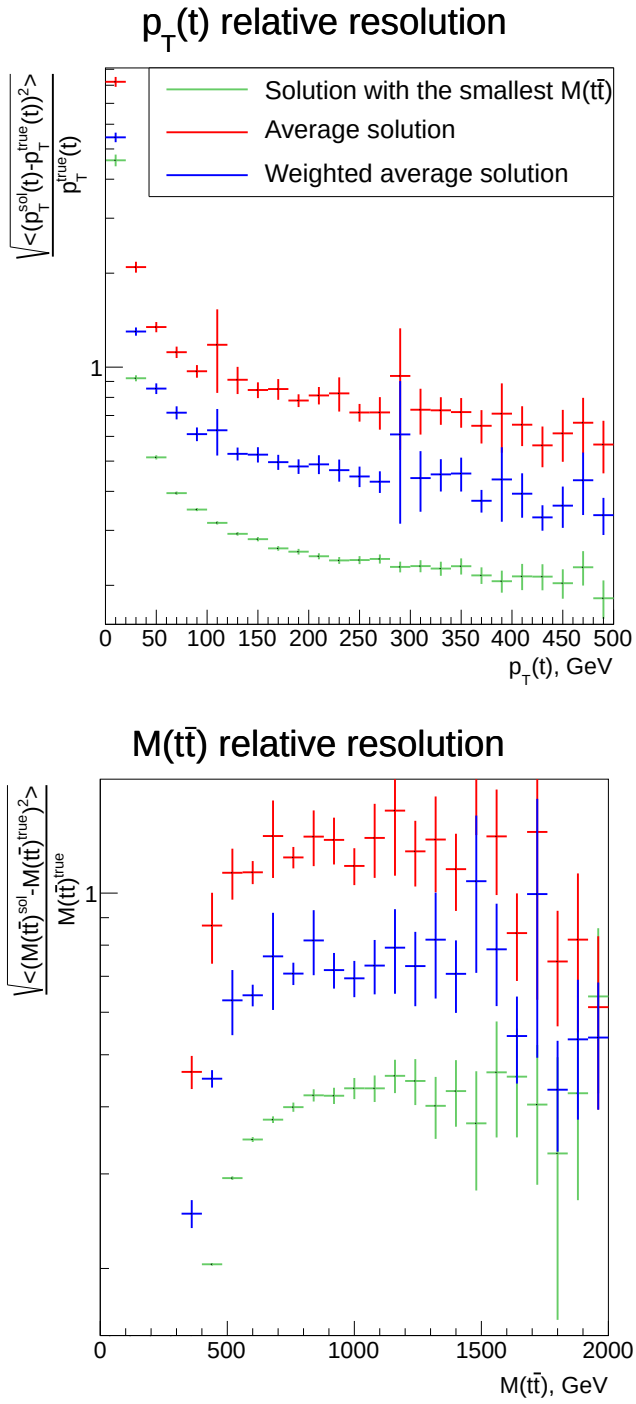

Figure B.2: Profile plot of the RMS relative to the top p_T versus transverse momentum of the t-quark (top) and invariant mass of the $t\bar{t}$ (bottom). The distribution for the solution of the kinematic equation with the smallest mass of the $t\bar{t}$ system is plotted as green points, the weighted average solution as blue points and the average solution as red points.

Appendix C

Measurement without Regularization

To check the how much the regularization (see sec. 9.2.1) influences the results, a measurement of the normalized double differential cross sections in bins of $p_T(t)$ and $|y(t)|$ was performed with manually setting the regularization strength τ to zero.

Fig. C.1 shows the correlation matrices for the measurement in bins of $p_T(t)$ and $|y(t)|$ for the cases when the regularization strength is optimal (see Appendix F) and when the regularization strength is zero. One can conclude that without the regularization one also obtains a meaningful result. The comparison of the two correlation matrices shows that for the case with a non-zero optimal τ the anticorrelations are moved a bit from the directly neighboring bins to more distant bins.

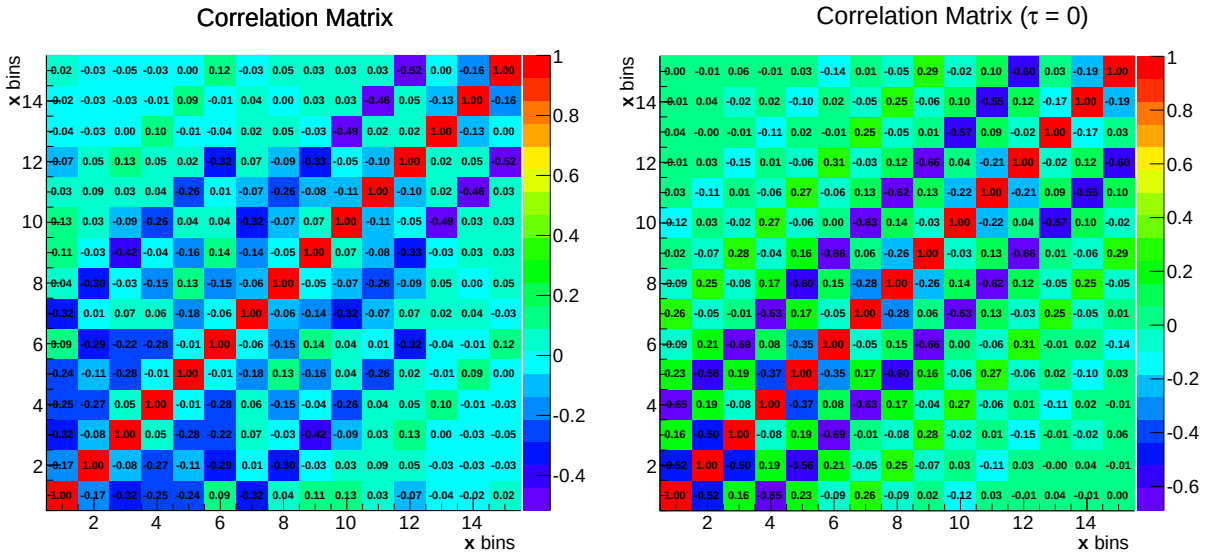

Figure C.1: Correlation matrix $\mathbf{V}_{xx}$ for the bins of $p_T(t)$ and $|y(t)|$ with regularization (left) and without regularization (right). The binning is the following: the five sequences of three bins (1-3, 4-6, 7-9, 10-12, 13-15) correspond to the five $p_T(t)$ bins [0, 65, 130, 200, 300, 500] GeV. There are three $|y(t)|$ bins – [0, 0.6, 1.2, 2.5] – in each $p_T(t)$ bin.

The cross section measured without the regularization in bins of $p_T(t)$ and $|y(t)|$ are shown in Fig. C.2. These cross sections can be compared to the corresponding nominal cross sections which were measured applying regularization (see Fig. 11.10). In general, the observed differences in the cross section values are within $\pm 1\sigma$ of the cross sections with regularization. Both statistical and systematic uncertainties increase for the unregularized cross sections by factor ~ 1.4, however, this is accompanied by increasing anticorrelations between neighboring bins.

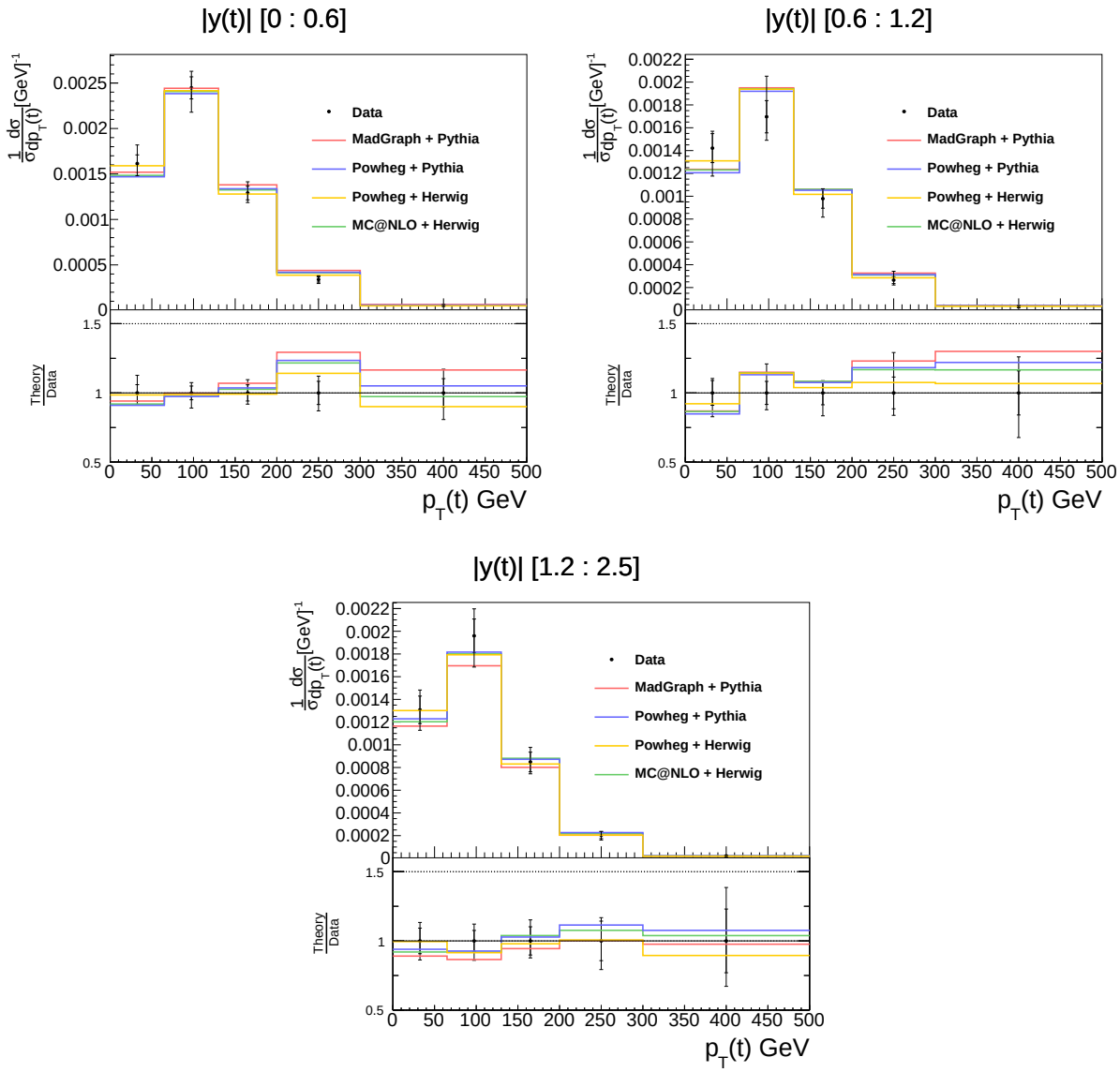

Figure C.2: Normalized differential cross sections in bins of $|y(t)|$ and $p_T(t)$ with no regularization applied. The inner error bars show the statistical uncertainties from the data. The outer error bars are the combined statistical and systematical uncertainties on the data. The predicted cross sections from four different models are also presented: MadGraph + Pythia (red line), Powheg + Pythia (blue line), Powheg + Herwig (orange line) and MC@NLO + Herwig (green line). The ratio of the predictions over measured cross sections are shown in the bottom panels with the error bars corresponding to the measurement uncertainties.

Appendix D

Closure Tests with Pseudo-data

The cross section results derived with the pseudo-data are presented in Fig. D.1. They are measured in bins of $p_T(t)$ and $|y(t)|$. The pseudo-data is generated according to the procedure described in sec. 9.2.1. The nominal MadGraph + Pythia $t\bar{t}$ signal distributions are plotted as references.

No biases between unfolded and original pseudo-data are observed.

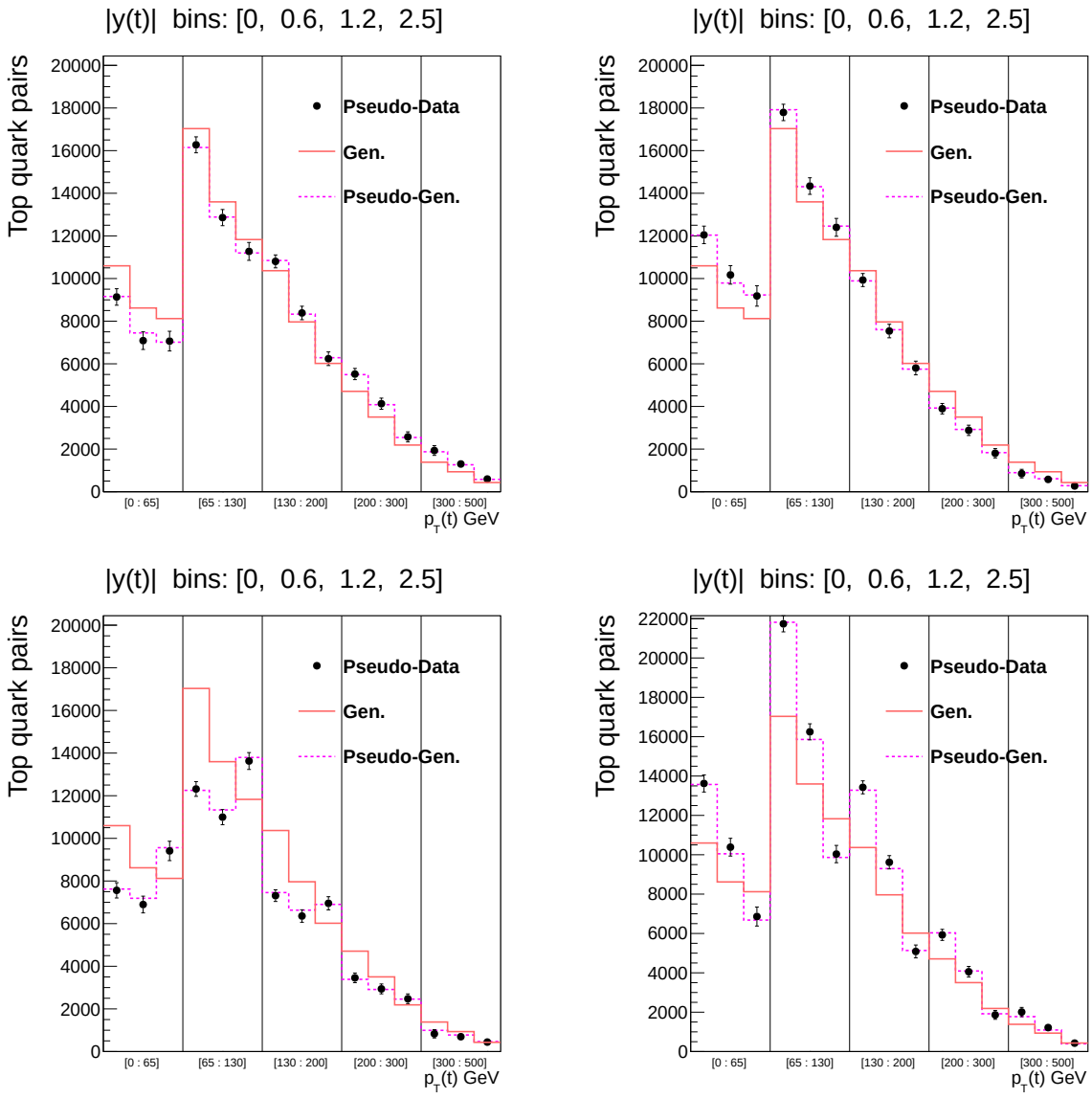

Figure D.1: Normalized double differential cross sections in bins of $p_T(t)$ and $|y(t)|$ derived from the nominal $t\bar{t}$ signal MadGraph + Pythia sample by reweighting it with the weights 9.14 and parameters $a_1 = 0.0015$, $b_1 = 0.8$ (top left), with the weights 9.14 and parameters $a_1 = -0.0015$, $b_1 = 1.2$ (top right), with the weights 9.15 and parameters $a_2 = 0.17$, $b_2 = 0.7$ (bottom left) and with the weights 9.15 and parameters $a_2 = -0.17$, $b_2 = 1.3$ (bottom right). The nominal $t\bar{t}$ signal sample, which was used to calculate the migration matrix for the unfolding, is drawn with red line. The original pseudo-data is drawn with a dashed red line and the unfolded pseudo-data is marked with black points. The error bands correspond to the statistical uncertainty of the unfolded pseudo-data.

Appendix E

Plots for Efficiencies, Purities and Stabilities

Efficiencies, purities and stabilities in bins of all the variables, in which the cross sections are measured, are shown in Fig. E.1 – E.9.

Certain tendencies are present as discussed in the following

- $p_T(t\bar{t})$ vs $|y(t\bar{t})|$ (Fig. E.2): the efficiency slightly increases towards the higher transverse momentum of top pairs and significantly grows towards central $t\bar{t}$ rapidities. It varies between 20% and 30%. Purity and stability have similar behavior and are higher for low $p_T(t\bar{t})$ and central rapidity bins. They vary between 40% and almost 70%.

- $M(t\bar{t})$ vs $|y(t)|$ (Fig. E.3: the efficiencies get higher with increasing $M(t\bar{t})$ and are always lower for the high rapidities of the top-quark. The efficiency in general alters around 30%. Purity and stabilities do not vary much between the different bins of the $M(t\bar{t})$ and are higher for the most central rapidity bin.

- $M(t\bar{t})$ vs $p_T(t)$ (Fig. E.4): the efficiencies grow with increasing $p_T(t)$ and the slope is higher with the higher $M(t\bar{t})$. Purities and stabilities alter from 20% to 50 %.

- $M(t\bar{t})$ vs $\Delta\phi(t\bar{t})$ (Fig. E.6): the purities and stabilities grow with the increase of the $\Delta\phi(t\bar{t})$. The efficiencies show the same tendency, except for the lowest invariant mass bin. There efficiencies decrease while $\Delta\phi(t\bar{t})$ increases.

- $M(t\bar{t})$ vs $|y(t\bar{t})|$ (Fig. E.7): the efficiencies are slightly larger for larger masses of the top pairs and more central $|y(t\bar{t})|$. The purity is decreasing with the growth of $M(t\bar{t})$. In general, purities and stabilities have similar behavior versus $M(t\bar{t})$ and $|y(t\bar{t})|$ and vary between 40% and 60%.

- $M(t\bar{t})$ vs $|p_T(t\bar{t})|$ (Fig. E.8): the efficiency increases in both, mass and transverse momentum of the $t\bar{t}$ system indicating that the quality of reconstruction for the system with higher energy is better. Purities and stabilities increase with transverse momentum of top pair system, not taking to account the lowest $p_T(t\bar{t})$ bin, which for all bins of $M(t\bar{t})$ shows significantly higher purities and stabilities.

- $M(t\bar{t})$ vs x_1 (Fig. E.9): the efficiencies, purities and stabilities are getting lower the higher x_1 gets. The dependence on $M(t\bar{t})$ is the opposite – efficiencies, purities and stabilities grow with $M(t\bar{t})$.

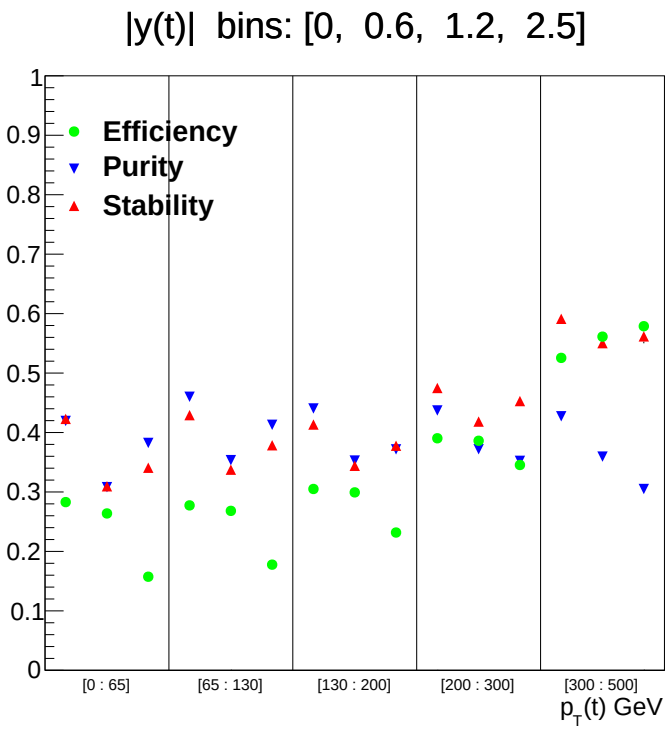

Figure E.1: The efficiency (green circles), purity (blue triangles) and stability (red triangles) in bins of the p_T and $|y|$ of the top quark.

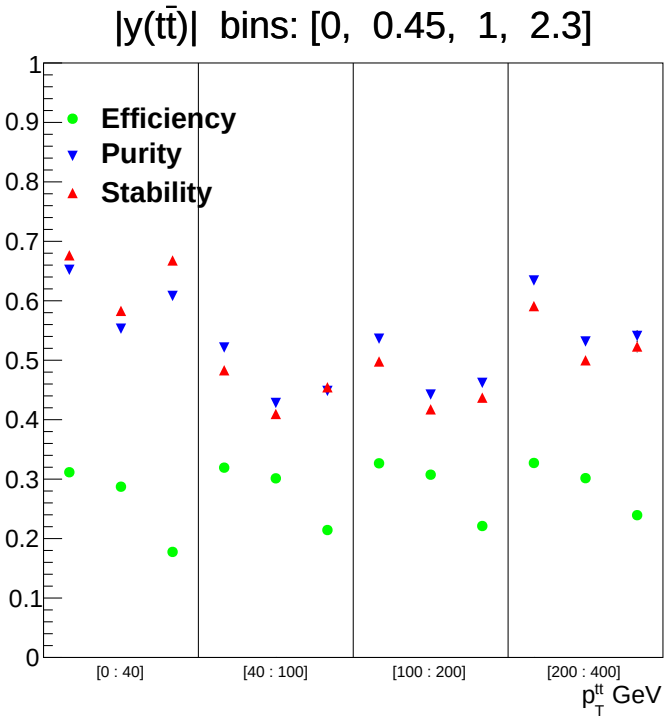

Figure E.2: The efficiency (green circles), purity (blue triangles) and stability (red triangles) in bins of the p_T and $|y|$ of the $t\bar{t}$ pair.

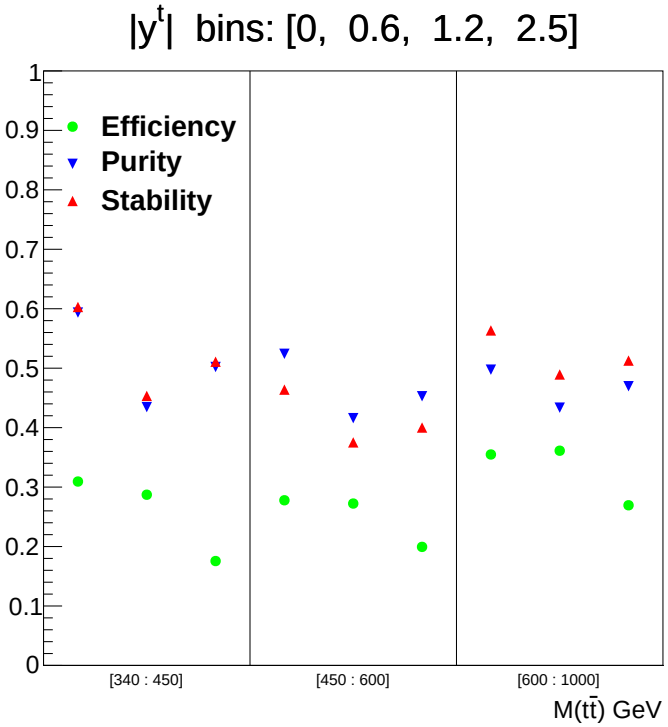

Figure E.3: The efficiency (green circles), purity (blue triangles) and stability (red triangles) in bins of the $M(t\bar{t})$ and $|y(t)|$.

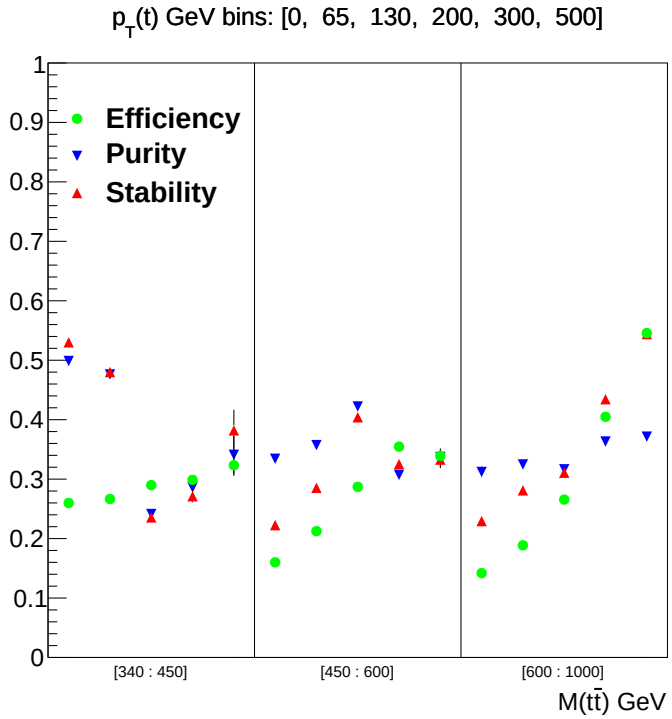

Figure E.4: The efficiency (green circles), purity (blue triangles) and stability (red triangles) in bins of the $M(t\bar{t})$ and $p_T(t)$.

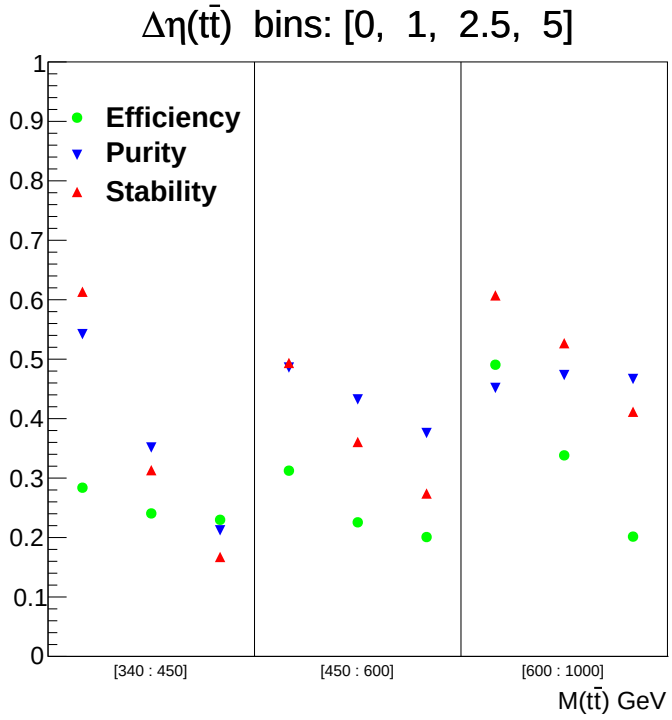

Figure E.5: The efficiency (green circles), purity (blue triangles) and stability (red triangles) in bins of the $M(t\bar{t})$ and $\Delta\eta(t\bar{t})$.

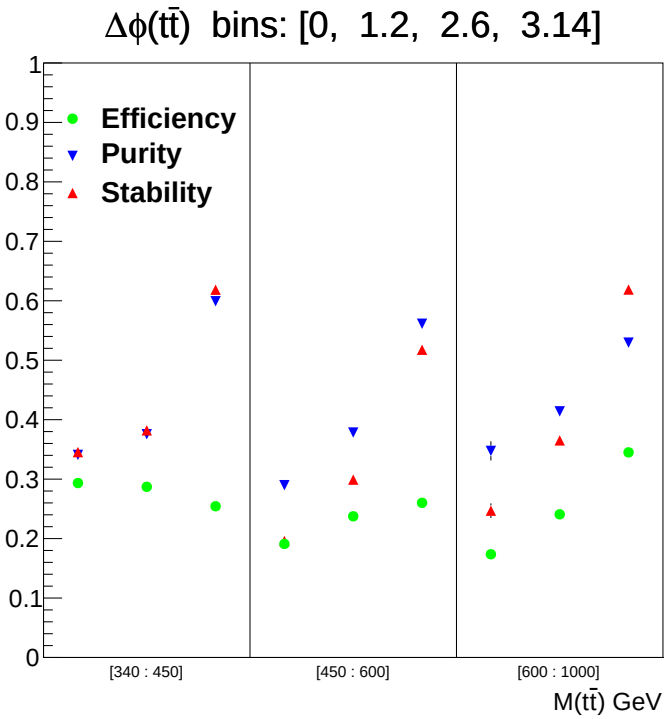

Figure E.6: The efficiency (green circles), purity (blue triangles) and stability (red triangles) in bins of the $M(t\bar{t})$ and $\Delta\phi(t\bar{t})$.

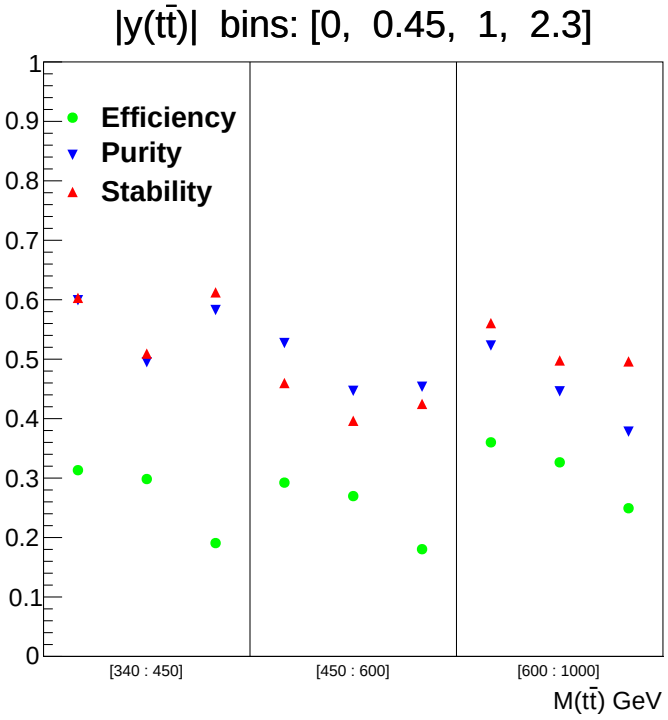

Figure E.7: The efficiency (green circles), purity (blue triangles) and stability (red triangles) in bins of $|y(t\bar{t})|$ and invariant $M(t\bar{t})$.

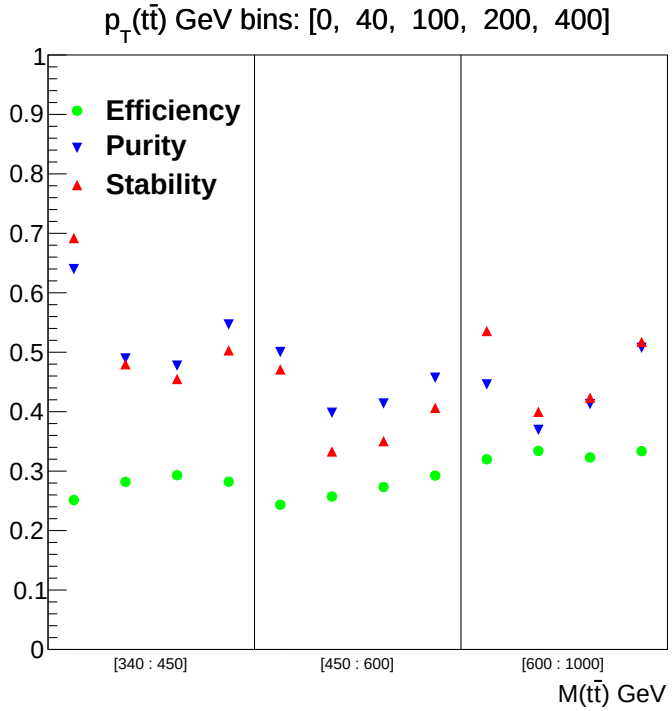

Figure E.8: The efficiency (green circles), purity (blue triangles) and stability (red triangles) in bins of $p_T(t\bar{t})$ and $M(t\bar{t})$.

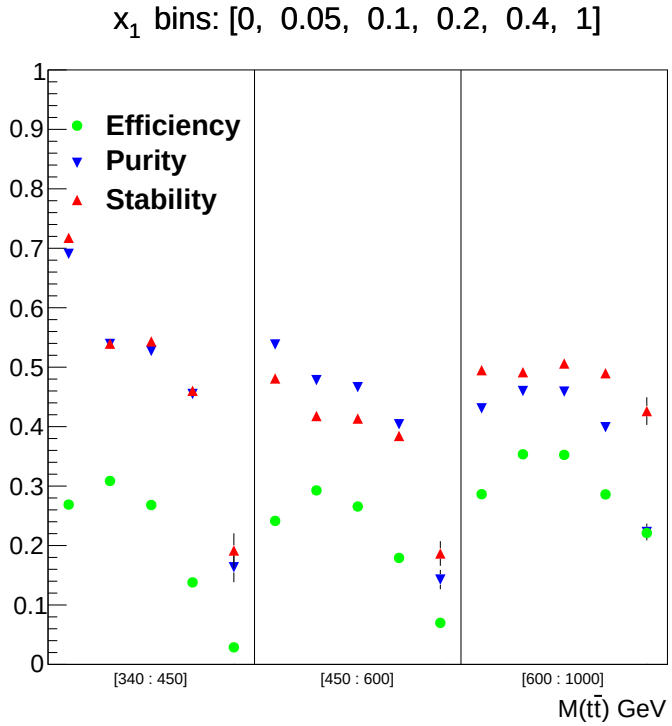

Figure E.9: The efficiency (green circles), purity (blue triangles) and stability (red triangles) in bins of $M(t\bar{t})$ and x_1.

Appendix F

Regularization Strength

To unfold every distribution a regularization strength parameter τ was defined using the minimization of correlation coefficients [124]. The resulting τ-parameters used to unfold each set of distributions is presented in the following table:

Variables	**lg(τ)**
$\|y(t)\|$ vs $p_T(t)$	-3.239
$\|y(t\bar{t})\|$ vs $p_T(t\bar{t})$	-3.137
$\|y(t)\|$ vs $M(t\bar{t})$	-3.138
$\|p_T(t)\|$ vs $M(t\bar{t})$	-3.213
$\Delta\eta(t\bar{t})$ vs $M(t\bar{t})$	-3.291
$\Delta\phi(t\bar{t})$ vs $M(t\bar{t})$	-3.166
$\|y(t\bar{t})\|$ vs $M(t\bar{t})$	-3.120
$p_T(t\bar{t})$ vs $M(t\bar{t})$	-3.150
x_1 vs $M(t\bar{t})$	-3.116

Appendix G

Unnormalized Cross Sections

The unnormalized double differential $t\bar{t}$ production cross sections are defined the following way:

$$\Delta\, y_j : \quad (\frac{d\sigma}{dx})_j = \frac{1}{\Delta x_i} \cdot \frac{N_{ij}^{signal\ \ unfolded}}{\epsilon_{ij} \cdot BR \cdot L}. \tag{G.1}$$

All the components of the eq. G.1 are described in sec. 9.3.1. The unnormalized cross sections defined by eq. G.1 differ from the normalized ones, defined in eq. 9.16, by the absence of the normalization to the inclusive $t\bar{t}$ production cross section.

In this appendix, all the unnormalized cross sections in bins of the variables listed in sec. 11.1 are presented. The behavior of these cross sections and their consistency with the theoretical predictions is the same as for the normalized cross sections. This was discussed in detail in sec. 9.3.1. The difference is in the uncertainty values.

The Fig. G.1 – G.9 present the unnormalized double differential $t\bar{t}$ production cross sections. The corresponding numbers are listed in appendix I.

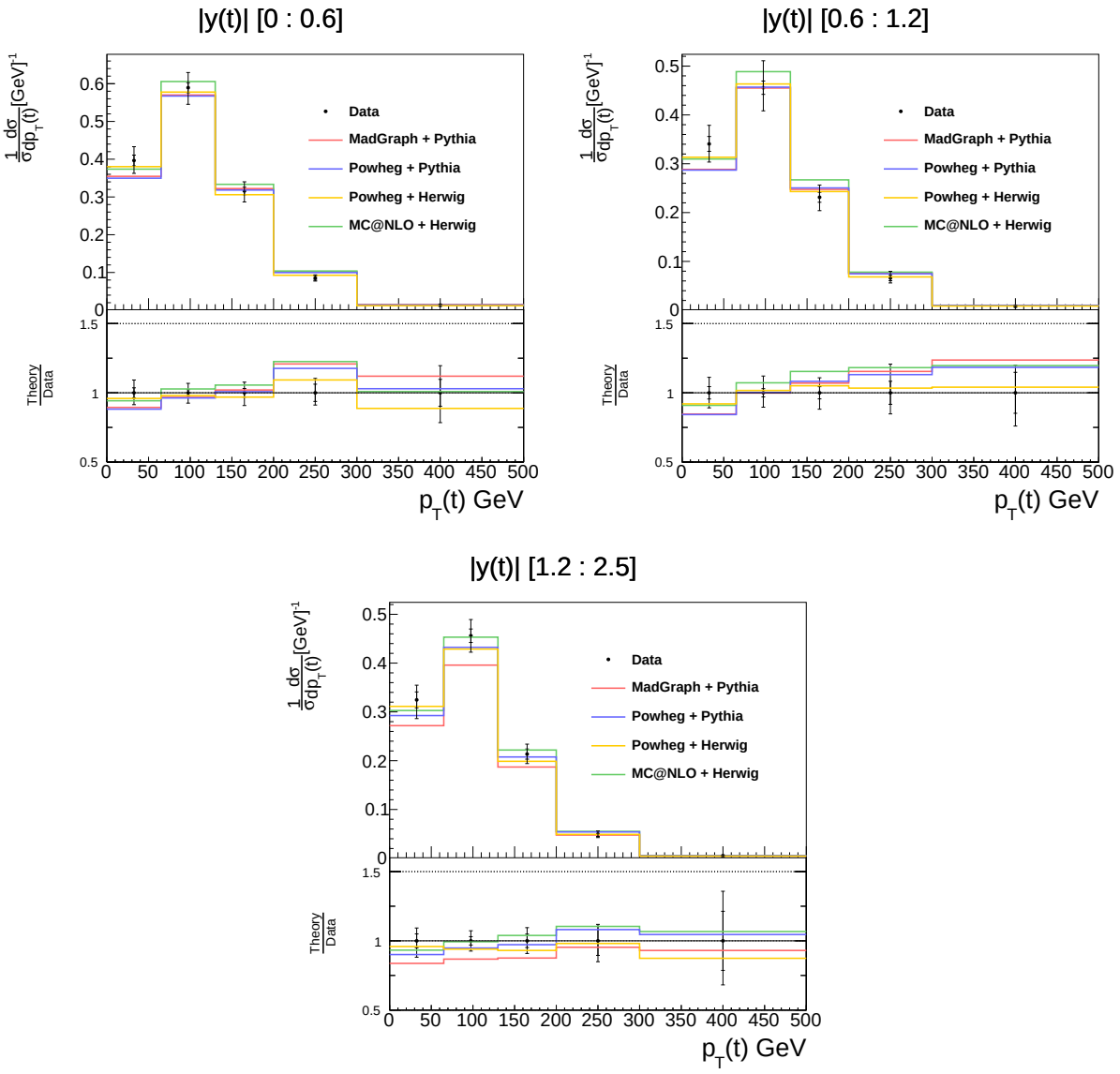

Figure G.1: Differential cross sections in bins of $|y(t)|$ and $p_T(t)$. The inner error bands are the statistical uncertainties from the data. The outer error bars are the combines statistical and systematical uncertainties on the data. The cross sections predicted different models are also presented: MadGraph + Pythia (red line), Powheg + Pythia (blue line), Powheg + Herwig (orange line) and MC@NLO + Herwig (green line).

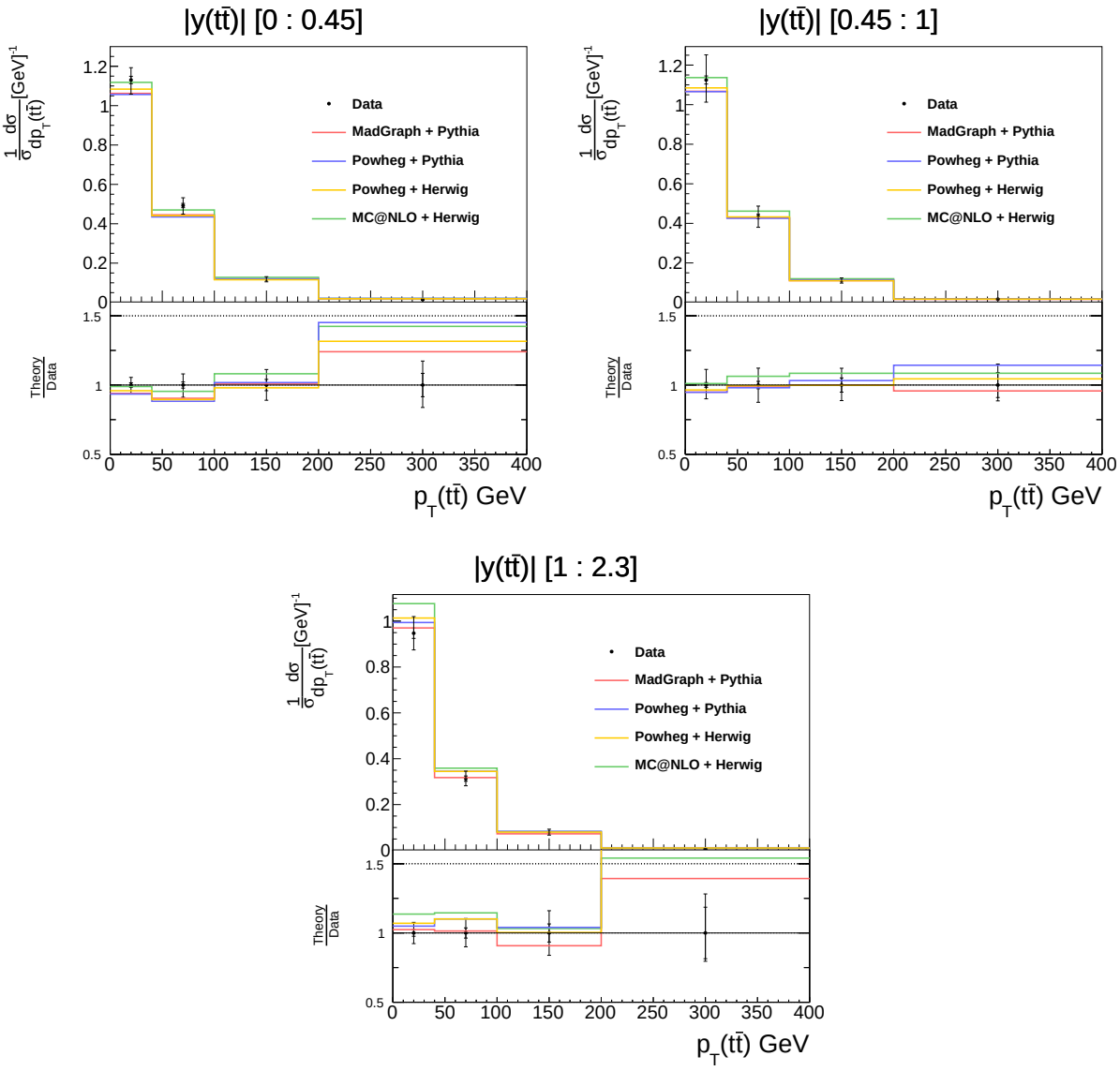

Figure G.2: Differential cross sections in bins of $|y(t\bar{t})|$ and $p_T(t)$. Other details as in Fig. G.1.

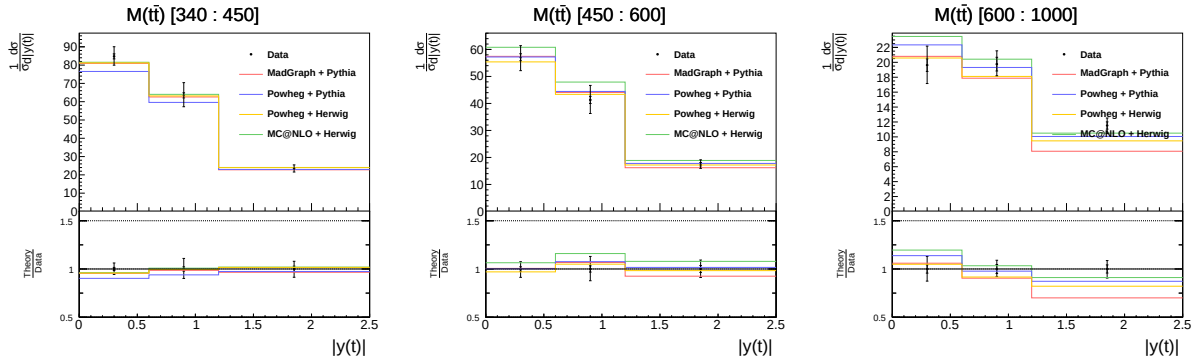

Figure G.3: Differential cross sections in bins of $M(t\bar{t})$ and $|y(t)|$. Other details as in Fig. G.1.

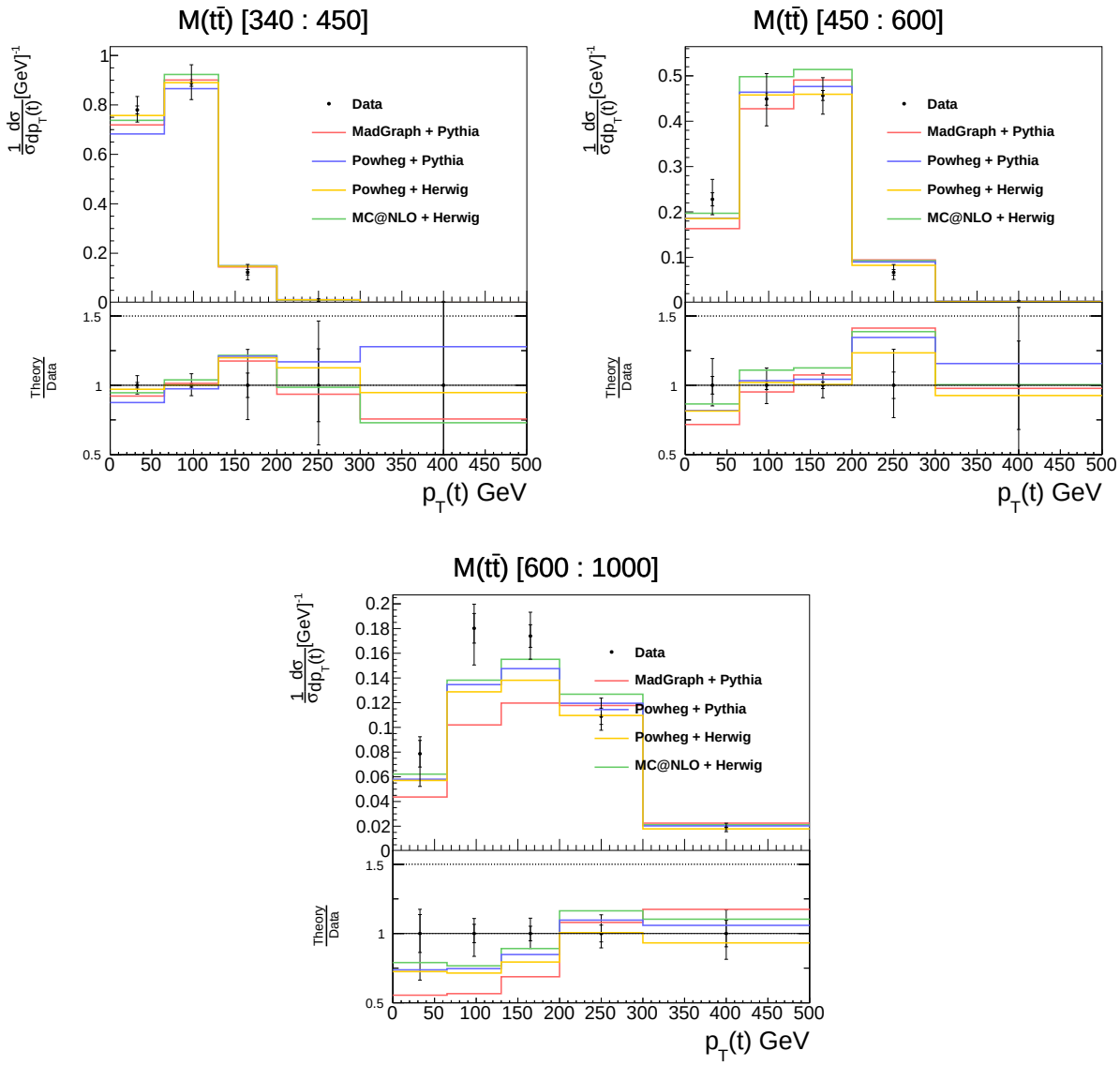

Figure G.4: Differential cross sections in bins of $M(t\bar{t})$ and $p_T(t)$. Other details as in Fig. G.1.

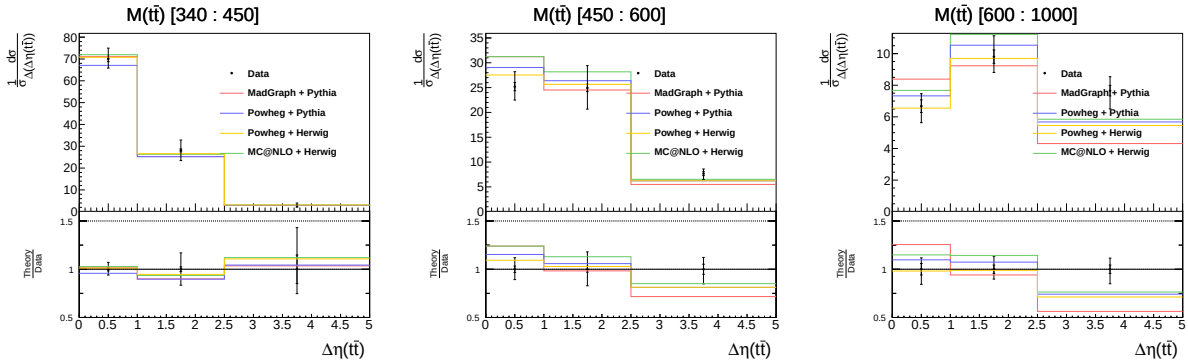

Figure G.5: Differential cross sections in bins of $M(t\bar{t})$ and $\Delta\eta(t\bar{t})$. Other details as in Fig. G.1.

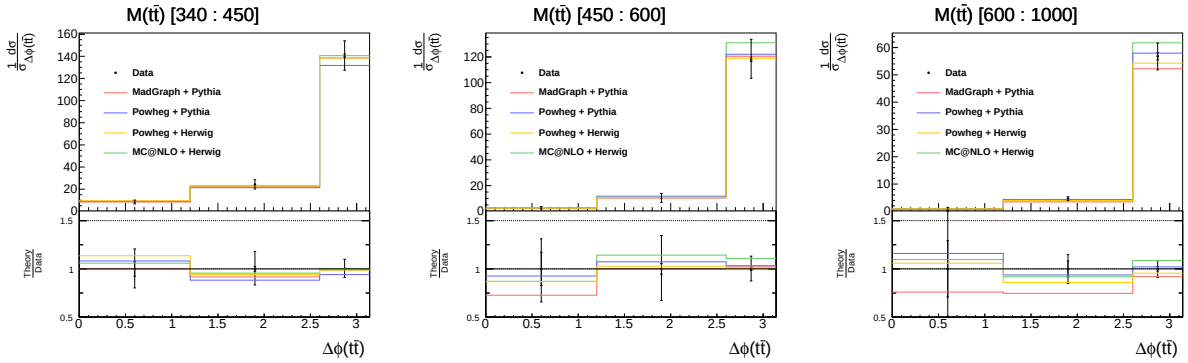

Figure G.6: Differential cross sections in bins of $M(t\bar{t})$ and $\Delta\phi(t\bar{t})$. Other details as in Fig. G.1.

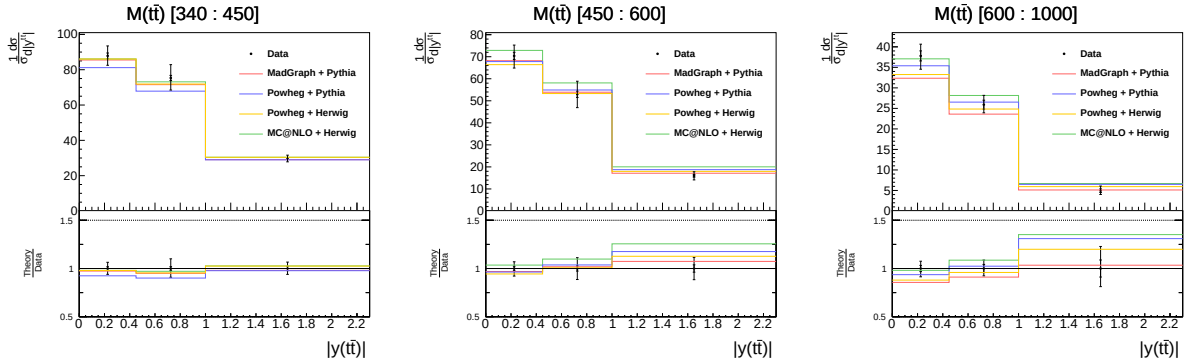

Figure G.7: Differential cross sections in bins of $M(t\bar{t})$ and $|y(t\bar{t})|$. Other details as in Fig. G.1.

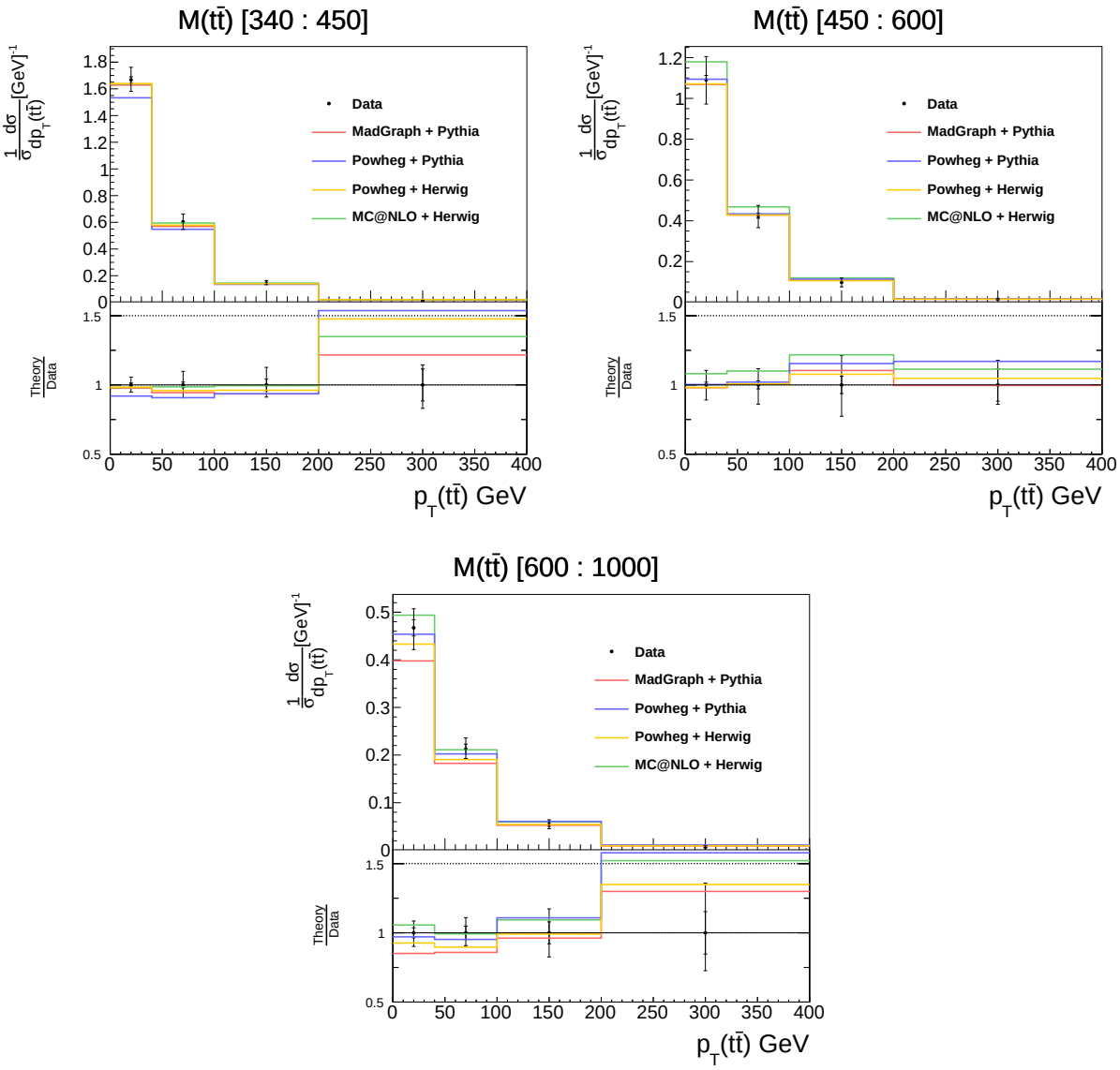

Figure G.8: Differential cross sections in bins of $M(t\bar{t})$ and $p_T(t\bar{t})$. Other details as in Fig. G.1.

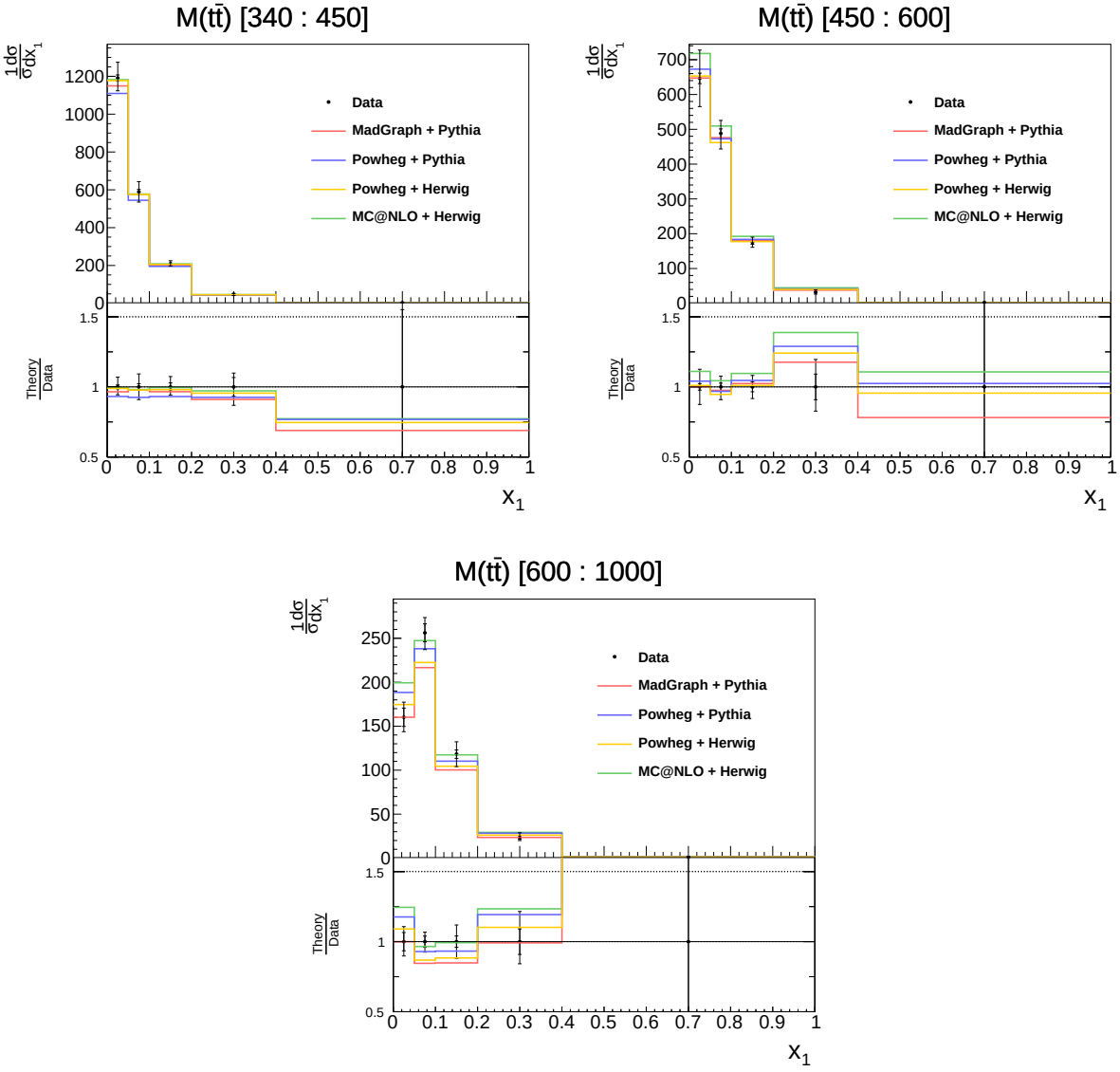

Figure G.9: Differential cross sections in bins of Bjorken x_1 and $M(t\bar{t})$. Other details as in Fig. G.1.

Appendix H

Correlation Matrices

Figures H.1 – H.8 show the correlation matrices in bins of kinematic variables in which the normalized cross sections 11.1 were measured.

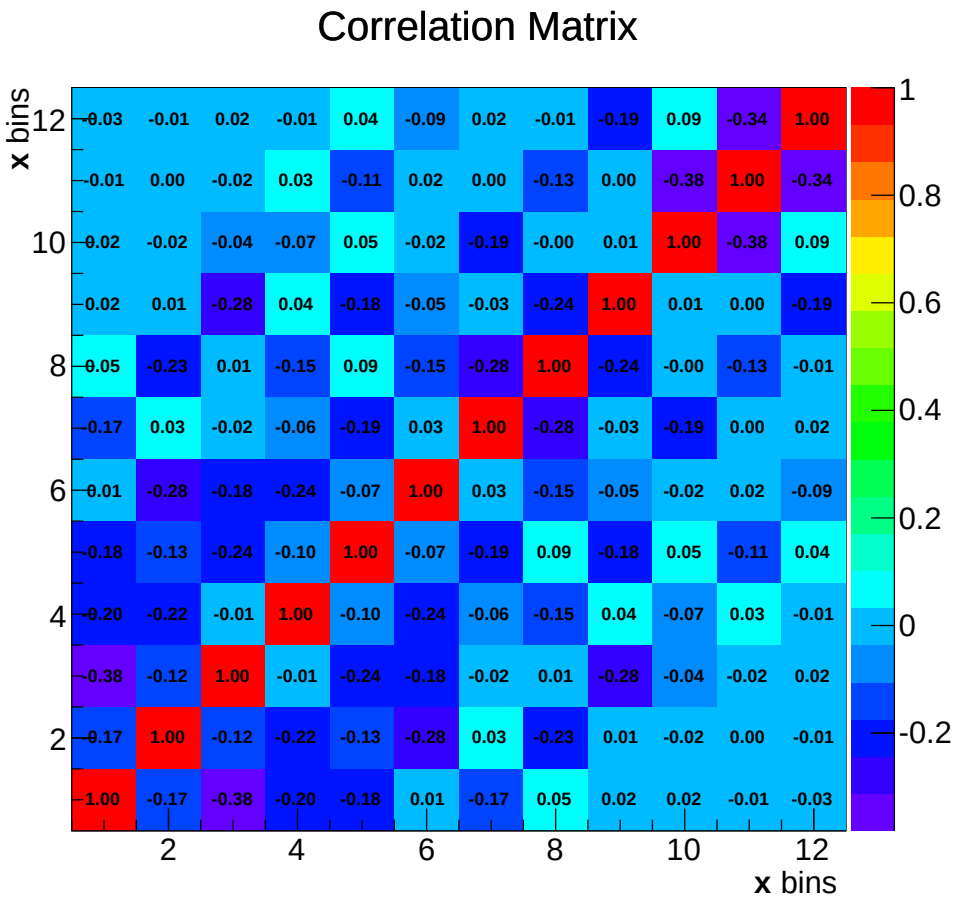

Figure H.1: Covariance matrix $\mathbf{V}_{xx}$ for the bins of $p_T(t\bar{t})$ and $|y(t\bar{t})|$. The binning is the following: the sequences of three bins (1-3, 4-6, 7-9, 10-12) correspond to the $p_T(t\bar{t})$ bins [0 40 100 200 400] GeV. There are three $|y(t\bar{t})|$ bins – [0 0.45 1.0 2.3] – in each $p_T(t\bar{t})$ bin.

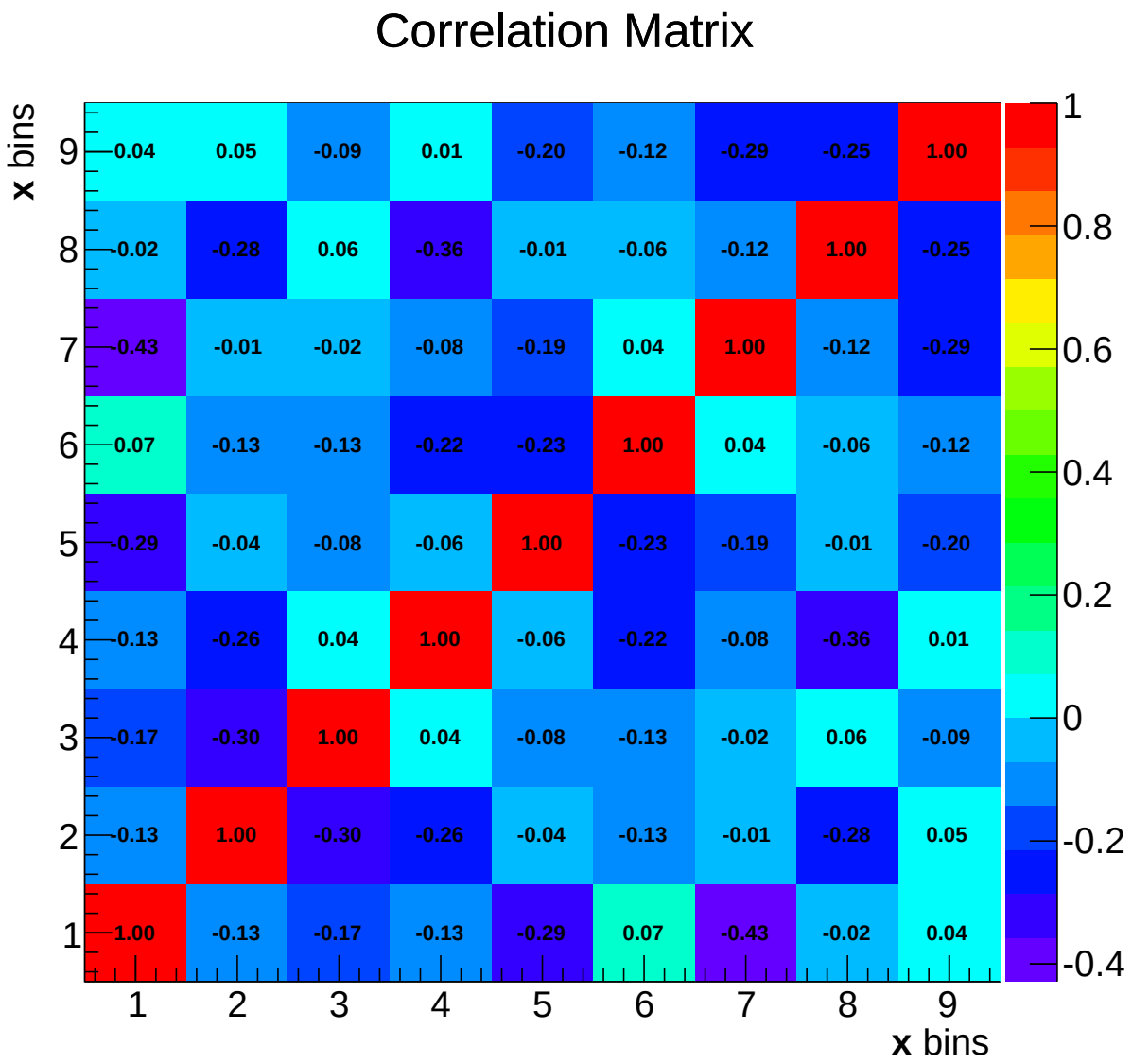

Figure H.2: Covariance matrix $\mathbf{V}_{xx}$ for the bins of $M(t\bar{t})$ and $|y(t)|$. The binning is the following: the sequences of three bins (1-3, 4-6, 7-9) correspond to the $|y(t)|$ bins [0 0.6 1.2 2.5]. There are three $M(t\bar{t})$ bins – [340 450 600 1000] GeV – in each $p_T(t)$ bin.

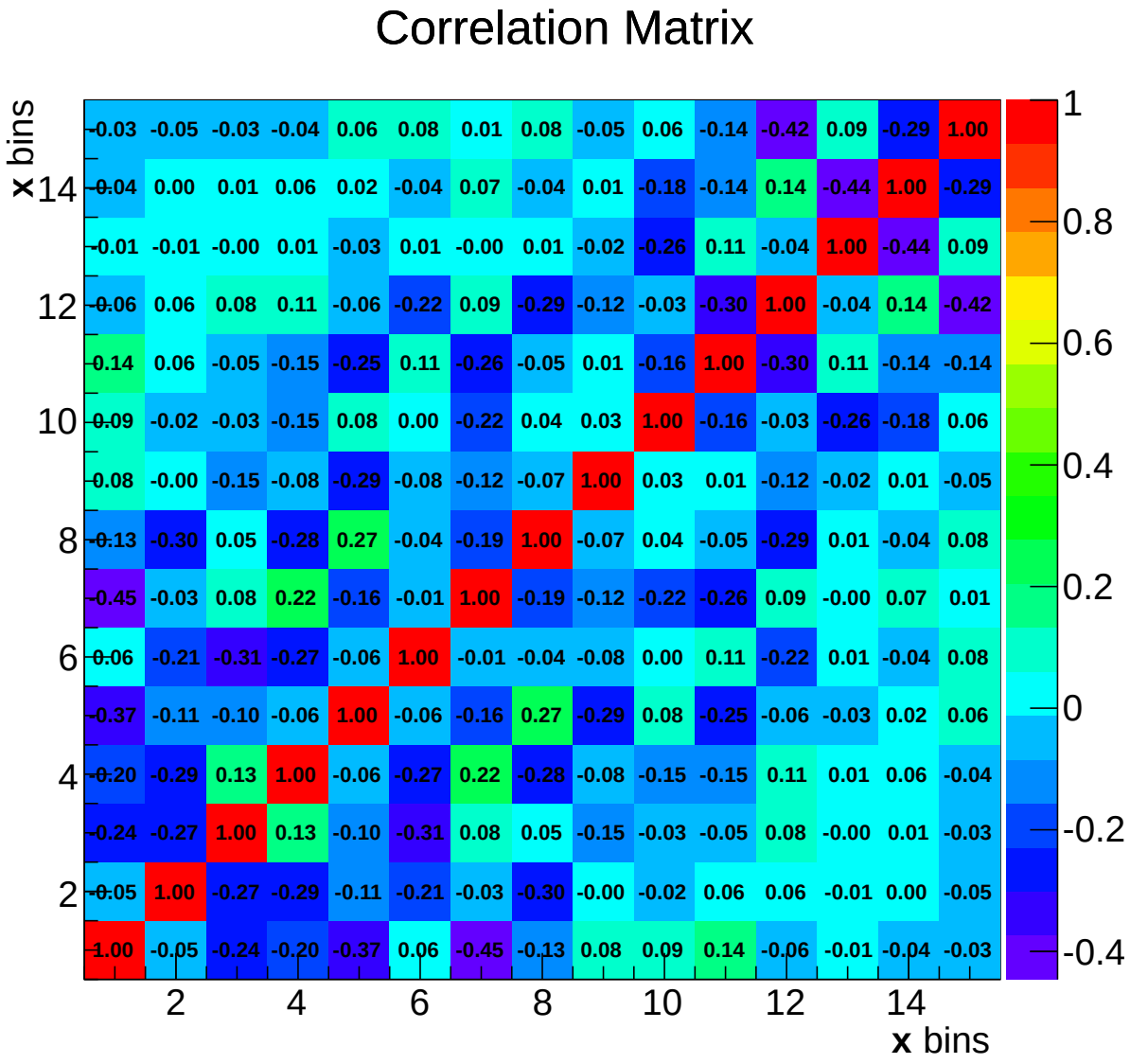

Figure H.3: Covariance matrix $\mathbf{V}_{xx}$ for the bins of $M(t\bar{t})$ and $p_T(t)$. The binning is the following: the sequences of three bins (1-3, 4-6, 7-9, 10-12, 13-15) correspond to the $p_T(t)$ bins [0 65 130 200 300 500] GeV. There are three $M(t\bar{t})$ bins – [340 450 600 1000] GeV – in each $p_T(t)$ bin.

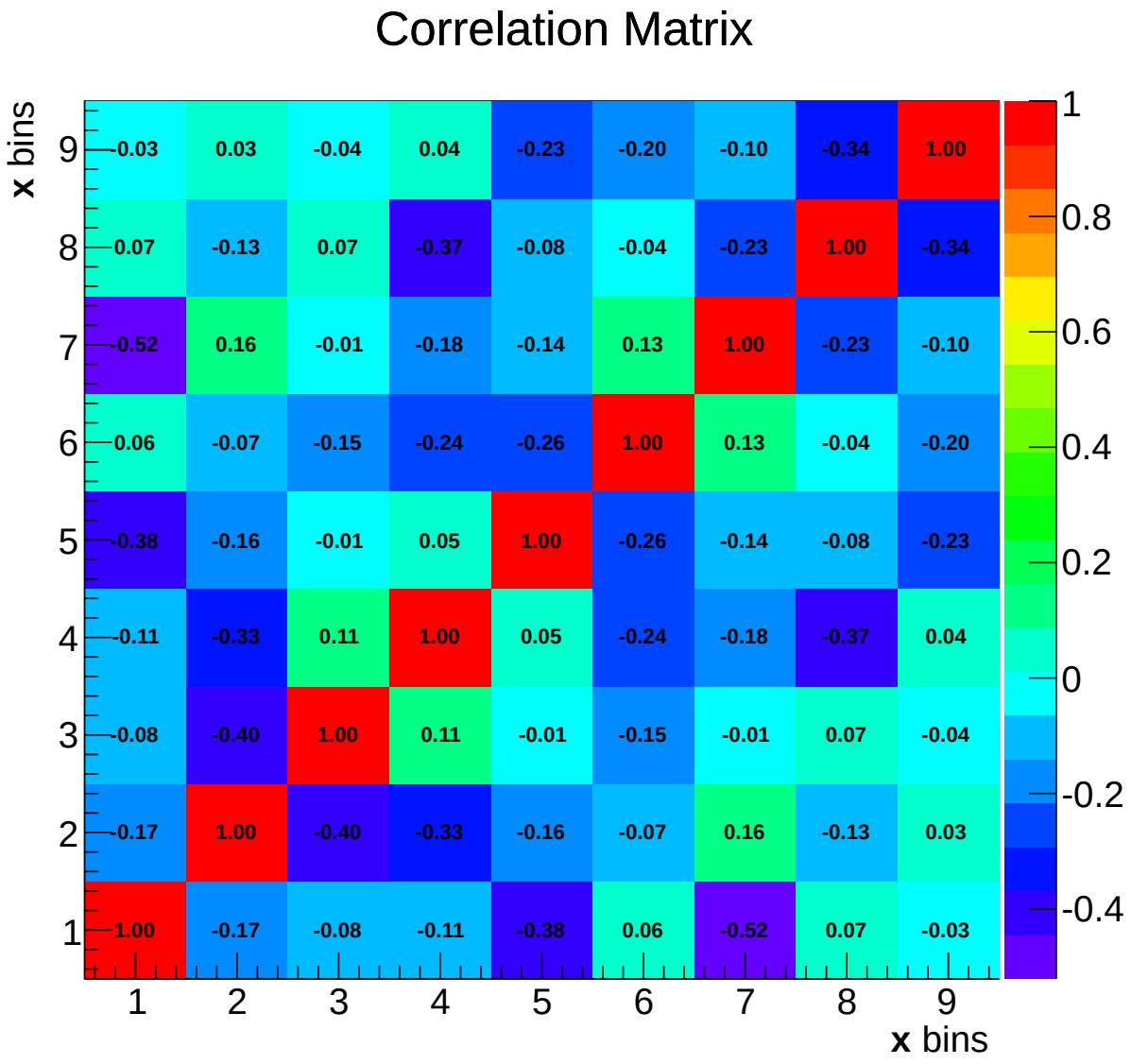

Figure H.4: Covariance matrix $\mathbf{V}_{xx}$ for the bins of $M(t\bar{t})$ and $\Delta\eta(t\bar{t})$. The binning is the following: the sequences of three bins (1-3, 4-6, 7-9) correspond to the $\Delta\eta(t\bar{t})$ bins [0 1.0 2.5 5.0]. There are three $M(t\bar{t})$ bins – [340 450 600 1000] GeV – in each $\Delta\eta(t\bar{t})$ bin.

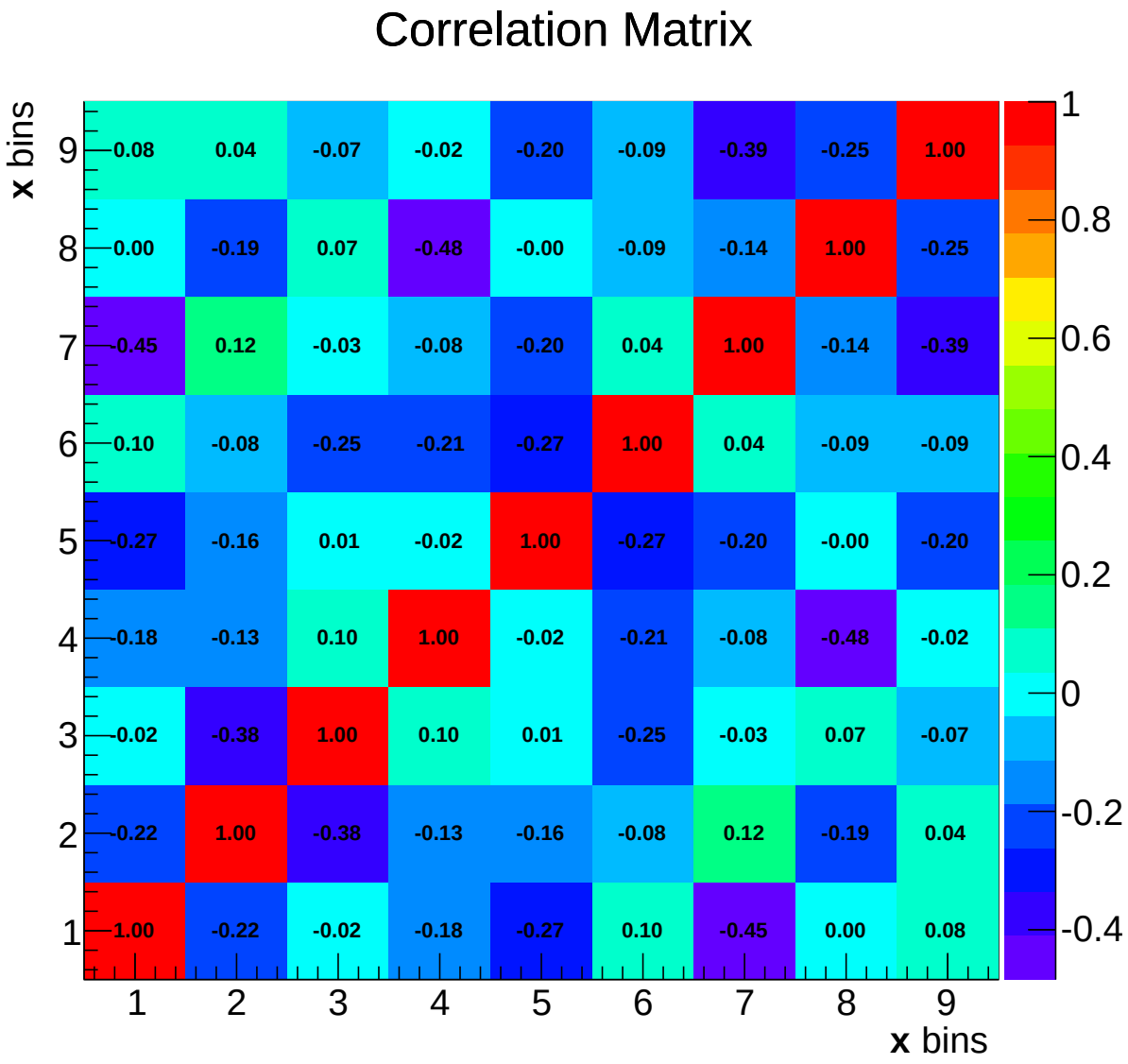

Figure H.5: Covariance matrix $\mathbf{V}_{xx}$ for the bins of $M(t\bar{t})$ and $\Delta\phi(t\bar{t})$. The binning is the following: the sequences of three bins (1-3, 4-6, 7-9) correspond to the $\Delta\phi(t\bar{t})$ bins [0 1.2 2.6 3.14] rad. There are three $M(t\bar{t})$ bins – [340 450 600 1000] GeV – in each $\Delta\phi(t\bar{t})$ bin.

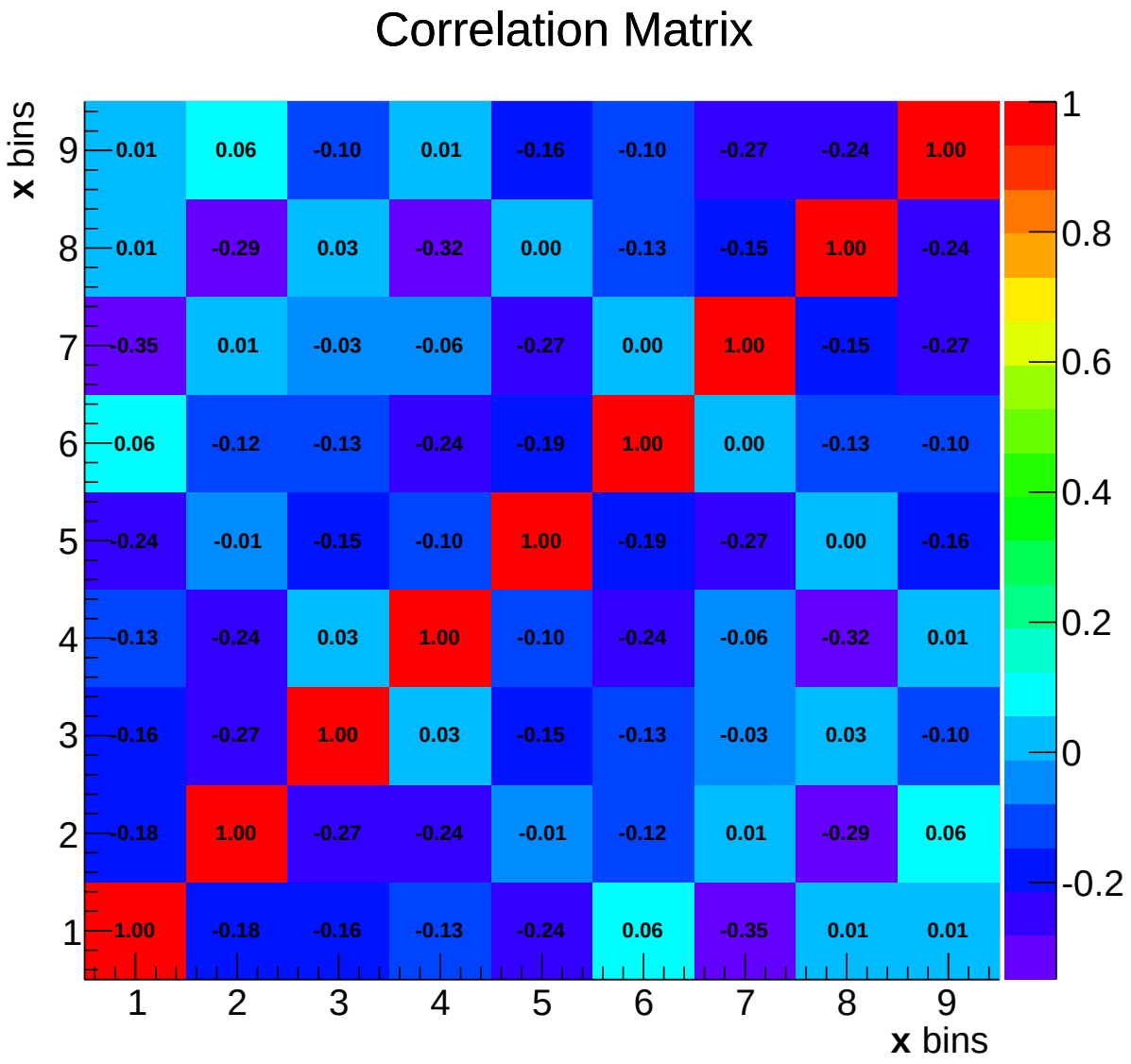

Figure H.6: Covariance matrix $\mathbf{V}_{xx}$ for the bins of $M(t\bar{t})$ and $|y(t\bar{t})|$. The binning is the following: the sequences of three bins (1-3, 4-6, 7-9) correspond to the $|y(t\bar{t})|$ bins – [0 0.45 1.0 2.3]. There are three $M(t\bar{t})$ bins – [340 450 600 1000] GeV – in each $|y(t\bar{t})|$ bin.

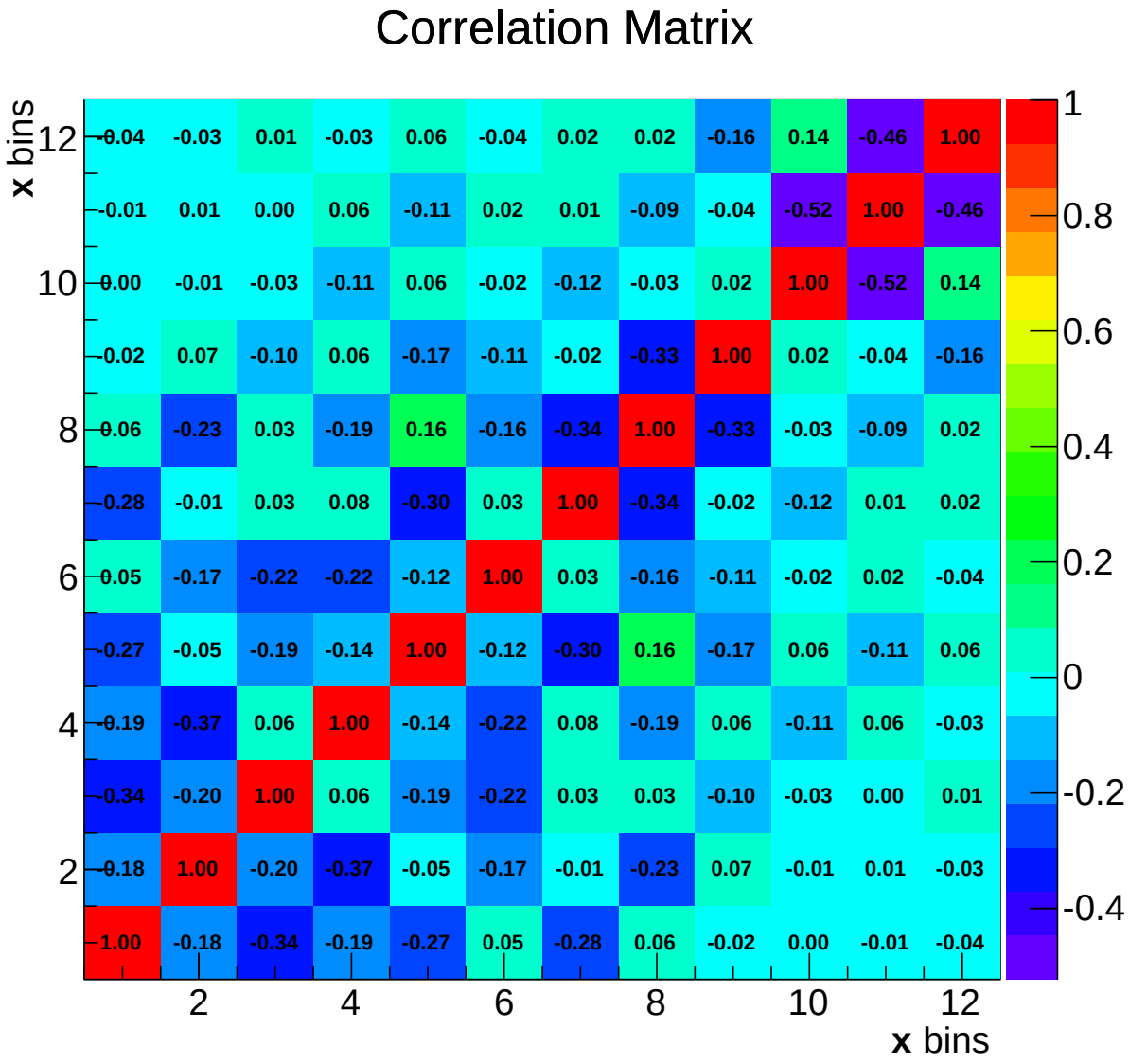

Figure H.7: Covariance matrix $\mathbf{V}_{xx}$ for the bins of $M(t\bar{t})$ and $|p_T(t\bar{t})|$. The binning is the following: the sequences of three bins (1-3, 4-6, 7-9, 10-12) correspond to the $p_T(t\bar{t})$ bins [0 40 100 200 400] GeV. There are three $M(t\bar{t})$ bins – [340 450 600 1000] GeV – in each $p_T(t\bar{t})$ bin.

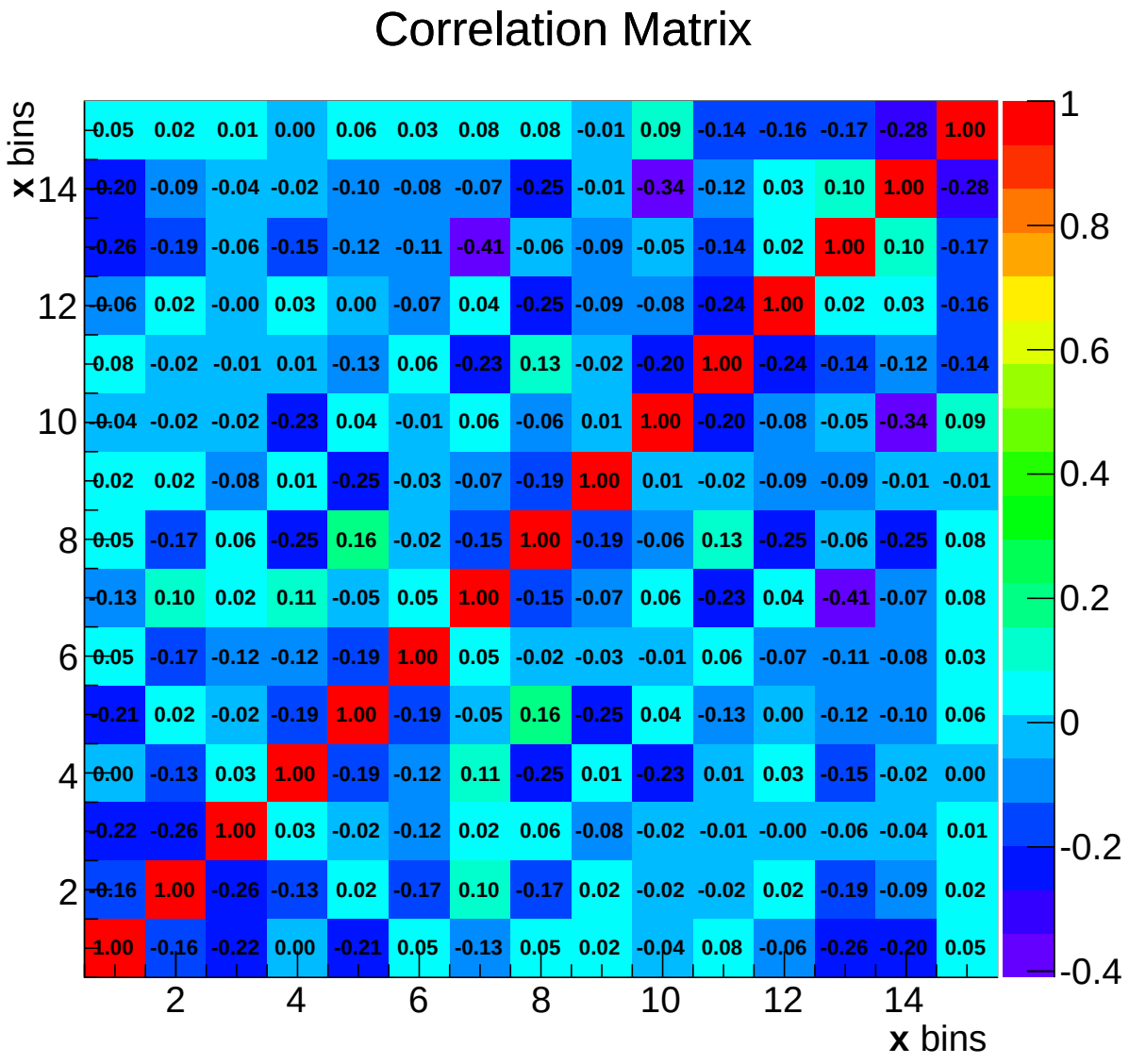

Figure H.8: Covariance matrix $\mathbf{V}_{xx}$ for the bins of $M(t\bar{t})$ and Bjorken x_1. The binning is the following: the sequences of three bins (1-3, 4-6, 7-9, 10-12, 13-15) correspond to the x_1 bins [0 0.05 0.1 0.2 0.4 1.0]. There are three $M(t\bar{t})$ bins – [340 450 600 1000] GeV – in each x_1 bin.

Appendix I

Numerical Values for the Cross Sections

In the following the numerical values of the cross sections presented in chapter 9 and appendix G and their total statistical and systematical uncertainties.

$\lvert y(t)\rvert \in$ [0 0.6]	Results	Uncertainties [%]		
$p_T(t)$ bin range [GeV]	$\frac{1}{\sigma}\frac{d\sigma}{dp_T(t)}$ [GeV^{-1}]	Stat.	Syst. Up	Syst. Down
0 to 65	0.00162	3.6	5.3	3.4
65 to 130	0.0024	2.2	1.8	3
130 to 200	0.00129	3.1	1.5	4.6
200 to 300	0.00035	6.2	7.6	6
300 to 500	5.5e-05	9.7	12.7	16.3
$\lvert y(t)\rvert \in$ [0.6 1.2]	Results	Uncertainties [%]		
$p_T(t)$ bin range [GeV]	$\frac{1}{\sigma}\frac{d\sigma}{dp_T(t)}$ [GeV^{-1}]	Stat.	Syst. Up	Syst. Down
0 to 65	0.00139	4.4	4.7	5.1
65 to 130	0.00186	3	5.9	3.2
130 to 200	0.00094	4.4	3.8	5
200 to 300	0.00027	8.3	16.9	7.4
300 to 500	3.4e-05	14.8	17.3	21.8
$\lvert y(t)\rvert \in$ [1.2 2.5]	Results	Uncertainties [%]		
$p_T(t)$ bin range [GeV]	$\frac{1}{\sigma}\frac{d\sigma}{dp_T(t)}$ [GeV^{-1}]	Stat.	Syst. Up	Syst. Down
0 to 65	0.00132	4.9	5.5	8.8
65 to 130	0.00186	2.9	4.2	4.6
130 to 200	0.00087	4.8	5.7	5.4
200 to 300	0.0002	10.5	4.8	10.7
300 to 500	2.1e-05	21.3	27	22.3

Table I.1: Double differential **normalized** $t\bar{t}$ production cross sections and uncertainties in the $e\mu$ channel in bins of $p_T(t)$ for different $|y(t)|$ bins. The uncertainties are given separately for the statistical and systematic components.

$\lvert y(t\bar{t})\rvert \in$ [0 0.45]	Results	Uncertainties [%]		
$p_T(t\bar{t})$ bin range [GeV]	$\frac{1}{\sigma}\frac{d\sigma}{dp_T(t\bar{t})}$ [GeV^{-1}]	Stat.	Syst. Up	Syst. Down
0 to 40	0.0047	1.6	4	5.3
40 to 100	0.00205	2.2	5.7	7.5
100 to 200	0.00049	4.1	5.7	5.3
200 to 400	6e-05	8.4	9.7	8.5
$\lvert y(t\bar{t})\rvert \in$ [0.45 1]	Results	Uncertainties [%]		
$p_T(t\bar{t})$ bin range [GeV]	$\frac{1}{\sigma}\frac{d\sigma}{dp_T(t\bar{t})}$ [GeV^{-1}]	Stat.	Syst. Up	Syst. Down
0 to 40	0.00467	1.7	6.5	4.7
40 to 100	0.0018	2.6	6.3	7.4
100 to 200	0.00046	5.1	6.3	5.9
200 to 400	6.9e-05	9	10.4	5
$\lvert y(t\bar{t})\rvert \in$ [1 2.3]	Results	Uncertainties [%]		
$p_T(t\bar{t})$ bin range [GeV]	$\frac{1}{\sigma}\frac{d\sigma}{dp_T(t\bar{t})}$ [GeV^{-1}]	Stat.	Syst. Up	Syst. Down
0 to 40	0.00393	2.2	4.7	5
40 to 100	0.0013	3.6	4.5	3.1
100 to 200	0.00033	6.5	8.8	9.3
200 to 400	2.5e-05	18.6	21.4	7.3

Table I.2: Double differential **normalized** $t\bar{t}$ production cross sections and uncertainties in the $e\mu$ channel in bins of $p_T(t\bar{t})$ for different $|y(t\bar{t})|$ bins. The uncertainties are given separately for the statistical and systematic components.

$M(t\bar{t}) \in$ [340 450] [GeV]	Results	Uncertainties [%]		
$\lvert y(t)\rvert$ bin range	$\frac{1}{\sigma}\frac{d\sigma}{d\lvert y(t)\rvert}$	Stat.	Syst. Up	Syst. Down
0 to 0.6	0.353	1.6	3.4	3.1
0.6 to 1.2	0.264	2.1	4.4	3.2
1.2 to 2.5	0.098	2.7	6.8	8
$M(t\bar{t}) \in$ [450 600] [GeV]	Results	Uncertainties [%]		
$\lvert y(t)\rvert$ bin range	$\frac{1}{\sigma}\frac{d\sigma}{d\lvert y(t)\rvert}$	Stat.	Syst. Up	Syst. Down
0 to 0.6	0.238	2.2	2	4.7
0.6 to 1.2	0.172	3.2	6.7	5.5
1.2 to 2.5	0.073	3.5	5.3	4.5
$M(t\bar{t}) \in$ [600 1000] [GeV]	Results	Uncertainties [%]		
$\lvert y(t)\rvert$ bin range	$\frac{1}{\sigma}\frac{d\sigma}{d\lvert y(t)\rvert}$	Stat.	Syst. Up	Syst. Down
0 to 0.6	0.082	4.3	9.3	8.6
0.6 to 1.2	0.082	4.6	5.3	4.7
1.2 to 2.5	0.048	4.2	4.7	6.5

Table I.3: Double differential **normalized** $t\bar{t}$ production cross sections and uncertainties in the $e\mu$ channel in bins of $|y(t)|$ for different $M(t\bar{t})$ bins. The uncertainties are given separately for the statistical and systematic components.

$M(t\bar{t})$ ∈ [340 450] [GeV]	Results	Uncertainties [%]		
$p_T(t)$ bin range [GeV]	$\frac{1}{\sigma}\frac{d\sigma}{dp_T(t)}$ [GeV^{-1}]	Stat.	Syst. Up	Syst. Down
0 to 65	0.00318	1.9	4.6	2.4
65 to 130	0.00362	1.4	3	1.3
130 to 200	0.0005	8.8	20.9	20
200 to 300	4e-05	26.3	39.4	36.2
300 to 500	3e-06	66.9	37.1	34.1
$M(t\bar{t})$ ∈ [450 600] [GeV]	Results	Uncertainties [%]		
$p_T(t)$ bin range [GeV]	$\frac{1}{\sigma}\frac{d\sigma}{dp_T(t)}$ [GeV^{-1}]	Stat.	Syst. Up	Syst. Down
0 to 65	0.00093	6.3	15.4	10.8
65 to 130	0.00183	3	5.6	7.8
130 to 200	0.00186	2.4	3.8	4.4
200 to 300	0.00027	9.5	20.6	17.4
300 to 500	1.1e-05	31.9	46.6	47.9
$M(t\bar{t})$ ∈ [600 1000] [GeV]	Results	Uncertainties [%]		
$p_T(t)$ bin range [GeV]	$\frac{1}{\sigma}\frac{d\sigma}{dp_T(t)}$ [GeV^{-1}]	Stat.	Syst. Up	Syst. Down
0 to 65	0.00032	13.6	13.6	30.7
65 to 130	0.00074	6.6	10.6	15.3
130 to 200	0.00071	5.2	6.9	6.4
200 to 300	0.00044	6.1	10.7	4.3
300 to 500	7.8e-05	9.6	8.6	11.7

Table I.4: Double differential **normalized** $t\bar{t}$ production cross sections and uncertainties in the $e\mu$ channel in bins of $p_T(t)$ for different $M(t\bar{t})$ bins. The uncertainties are given separately for the statistical and systematic components.

$M(t\bar{t}) \in$ [340 450] [GeV]	Results	Uncertainties [%]		
$\Delta\eta(t\bar{t})$ bin range	$\frac{1}{\sigma}\frac{d\sigma}{d\Delta\eta(t\bar{t})}$	Stat.	Syst. Up	Syst. Down
0 to 1	0.29	1.6	9	8.9
1 to 2.5	0.116	2.3	7.6	8.3
2.5 to 5	0.011	14.9	37	16.9
$M(t\bar{t}) \in$ [450 600] [GeV]	Results	Uncertainties [%]		
$\Delta\eta(t\bar{t})$ bin range	$\frac{1}{\sigma}\frac{d\sigma}{d\Delta\eta(t\bar{t})}$	Stat.	Syst. Up	Syst. Down
0 to 1	0.104	3.3	10	8.8
1 to 2.5	0.103	2.9	2.9	5.3
2.5 to 5	0.032	5.2	6.6	11.1
$M(t\bar{t}) \in$ [600 1000] [GeV]	Results	Uncertainties [%]		
$\Delta\eta(t\bar{t})$ bin range	$\frac{1}{\sigma}\frac{d\sigma}{d\Delta\eta(t\bar{t})}$	Stat.	Syst. Up	Syst. Down
0 to 1	0.028	6	17.5	20.9
1 to 2.5	0.041	4.3	12.9	9.4
2.5 to 5	0.032	4.2	10.3	13.6

Table I.5: Double differential **normalized** $t\bar{t}$ production cross sections and uncertainties in the $e\mu$ channel in bins of $\Delta\eta(t\bar{t})$ for different $M(t\bar{t})$ bins. The uncertainties are given separately for the statistical and systematic components.

$M(t\bar{t}) \in$ [340 450] [GeV]	Results	Uncertainties [%]		
$\Delta\phi(t\bar{t})$ bin range	$\frac{1}{\sigma}\frac{d\sigma}{d\Delta\phi(t\bar{t})}$	Stat.	Syst. Up	Syst. Down
0 to 1.2	0.035	7.7	26.1	25.5
1.2 to 2.6	0.101	2.4	9	8.5
2.6 to 3.14	0.584	1.2	10.6	10.1
$M(t\bar{t}) \in$ [450 600] [GeV]	Results	Uncertainties [%]		
$\Delta\phi(t\bar{t})$ bin range	$\frac{1}{\sigma}\frac{d\sigma}{d\Delta\phi(t\bar{t})}$	Stat.	Syst. Up	Syst. Down
0 to 1.2	0.012	17.2	32.9	35.6
1.2 to 2.6	0.043	5.4	20.2	20.9
2.6 to 3.14	0.493	1.3	7.7	8
$M(t\bar{t}) \in$ [600 1000] [GeV]	Results	Uncertainties [%]		
$\Delta\phi(t\bar{t})$ bin range	$\frac{1}{\sigma}\frac{d\sigma}{d\Delta\phi(t\bar{t})}$	Stat.	Syst. Up	Syst. Down
0 to 1.2	0.004	29.2	55	51.5
1.2 to 2.6	0.019	8.2	16.8	17.7
2.6 to 3.14	0.237	2.3	16.2	16

Table I.6: Double differential **normalized** $t\bar{t}$ production cross sections and uncertainties in the $e\mu$ channel in bins of $\Delta\phi(t\bar{t})$ for different $M(t\bar{t})$ bins. The uncertainties are given separately for the statistical and systematic components.

$M(t\bar{t}) \in$ [340 450] [GeV]	Results	Uncertainties [%]		
$\lvert y(t\bar{t})\rvert$ bin range	$\frac{1}{\sigma}\frac{d\sigma}{d\lvert y(t\bar{t})\rvert}$	Stat.	Syst. Up	Syst. Down
0 to 0.45	0.368	1.9	2.7	2.2
0.45 to 1	0.316	1.8	3.8	2.9
1 to 2.3	0.124	2.1	6	6.2
$M(t\bar{t}) \in$ [450 600] [GeV]	Results	Uncertainties [%]		
$\lvert y(t\bar{t})\rvert$ bin range	$\frac{1}{\sigma}\frac{d\sigma}{d\lvert y(t\bar{t})\rvert}$	Stat.	Syst. Up	Syst. Down
0 to 0.45	0.295	2.3	3.1	4.9
0.45 to 1	0.222	2.6	4.2	4.7
1 to 2.3	0.067	3.7	6	5.8
$M(t\bar{t}) \in$ [600 1000] [GeV]	Results	Uncertainties [%]		
$\lvert y(t\bar{t})\rvert$ bin range	$\frac{1}{\sigma}\frac{d\sigma}{d\lvert y(t\bar{t})\rvert}$	Stat.	Syst. Up	Syst. Down
0 to 0.45	0.158	3.2	2.4	5.2
0.45 to 1	0.109	4.2	5.4	3.4
1 to 2.3	0.021	8.8	19	13.4

Table I.7: Double differential **normalized** $t\bar{t}$ production cross sections and uncertainties in the $e\mu$ channel in bins of $|y(t\bar{t})|$ for different $M(t\bar{t})$ bins. The uncertainties are given separately for the statistical and systematic components.

$M(t\bar{t}) \in$ [340 450] [GeV]	Results	Uncertainties [%]		
$p_T(t\bar{t})$ bin range [GeV]	$\frac{1}{\sigma}\frac{d\sigma}{dp_T(t\bar{t})}$ [GeV^{-1}]	Stat.	Syst. Up	Syst. Down
0 to 40	0.00693	1.2	3.8	3.6
40 to 100	0.00251	2	4.1	3.5
100 to 200	0.0006	4.2	9.7	5.8
200 to 400	5.7e-05	11.5	5.4	10.3
$M(t\bar{t}) \in$ [450 600] [GeV]	Results	Uncertainties [%]		
$p_T(t\bar{t})$ bin range [GeV]	$\frac{1}{\sigma}\frac{d\sigma}{dp_T(t\bar{t})}$ [GeV^{-1}]	Stat.	Syst. Up	Syst. Down
0 to 40	0.00453	1.8	6.2	6.9
40 to 100	0.00177	2.8	5.8	9.8
100 to 200	0.00041	6.3	15.2	17.1
200 to 400	6.4e-05	11.7	12.3	5.2
$M(t\bar{t}) \in$ [600 1000] [GeV]	Results	Uncertainties [%]		
$p_T(t\bar{t})$ bin range [GeV]	$\frac{1}{\sigma}\frac{d\sigma}{dp_T(t\bar{t})}$ [GeV^{-1}]	Stat.	Syst. Up	Syst. Down
0 to 40	0.00194	3.6	5.8	8.3
40 to 100	0.00088	4.8	8.1	5.5
100 to 200	0.00023	7.9	9.3	9.9
200 to 400	2.9e-05	15.3	28.4	16.2

Table I.8: Double differential **normalized** $t\bar{t}$ production cross sections and uncertainties in the $e\mu$ channel in bins of $p_T(t\bar{t})$ for different $M(t\bar{t})$ bins. The uncertainties are given separately for the statistical and systematic components.

$M(t\bar{t}) \in$ [340 450] [GeV]	Results	Uncertainties [%]		
x_1 bin range	$\frac{1}{\sigma}\frac{d\sigma}{dx_1}$	Stat.	Syst. Up	Syst. Down
0 to 0.05	4.94	1.3	3.4	2.2
0.05 to 0.1	2.44	2.2	3.2	3.1
0.1 to 0.2	0.87	2.9	4.3	3
0.2 to 0.4	0.2	6.6	9.1	11.9
0.4 to 1	0.013	54.8	29.8	43.3
$M(t\bar{t}) \in$ [450 600] [GeV]	Results	Uncertainties [%]		
x_1 bin range	$\frac{1}{\sigma}\frac{d\sigma}{dx_1}$	Stat.	Syst. Up	Syst. Down
0 to 0.05	2.68	2.3	6.1	6.2
0.05 to 0.1	2.03	2.7	2.9	5.4
0.1 to 0.2	0.73	3.5	1.6	3.2
0.2 to 0.4	0.13	9.2	15.4	13.1
0.4 to 1	0.009	64.3	57.7	45.7
$M(t\bar{t}) \in$ [600 1000] [GeV]	Results	Uncertainties [%]		
x_1 bin range	$\frac{1}{\sigma}\frac{d\sigma}{dx_1}$	Stat.	Syst. Up	Syst. Down
0 to 0.05	0.66	6.5	8.4	8.1
0.05 to 0.1	1.06	4	3.6	5.1
0.1 to 0.2	0.49	4	5.4	6
0.2 to 0.4	0.098	9.1	17.4	8.4
0.4 to 1	0.001	144.1	521.7	556.1

Table I.9: Double differential **normalized** $t\bar{t}$ production cross sections and uncertainties in the $e\mu$ channel in bins of x_1 for different $M(t\bar{t})$ bins. The uncertainties are given separately for the statistical and systematic components.

$\lvert y(t)\rvert \in [0\ 0.6]$	Results	Uncertainties [%]		
$p_T(t)$ bin range [GeV]	$\frac{d\sigma}{dp_T(t)}$ $[\frac{pb}{\text{GeV}}]$	Stat.	Syst. Up	Syst. Down
0 to 65	0.4	3.6	8.5	7.8
65 to 130	0.59	2.3	6.4	7.1
130 to 200	0.316	3.1	7	8.7
200 to 300	0.085	6.2	8.3	6.3
300 to 500	0.013	9.7	17	19.2
$\lvert y(t)\rvert \in [0.6\ 1.2]$	Results	Uncertainties [%]		
$p_T(t)$ bin range [GeV]	$\frac{d\sigma}{dp_T(t)}$ $[\frac{pb}{\text{GeV}}]$	Stat.	Syst. Up	Syst. Down
0 to 65	0.34	4.5	10.3	9.9
65 to 130	0.46	3	11.7	10
130 to 200	0.23	4.4	9.9	11
200 to 300	0.066	8.3	19	12.8
300 to 500	0.008	14.8	13.4	18.9
$\lvert y(t)\rvert \in [1.2\ 2.5]$	Results	Uncertainties [%]		
$p_T(t)$ bin range [GeV]	$\frac{d\sigma}{dp_T(t)}$ $[\frac{pb}{\text{GeV}}]$	Stat.	Syst. Up	Syst. Down
0 to 65	0.32	5	7.8	10.7
65 to 130	0.46	3	6.6	6.7
130 to 200	0.21	4.9	8.2	7.7
200 to 300	0.05	10.5	5.5	10.8
300 to 500	0.005	21.3	28.7	23.6

Table I.10: Double differential **unnormalized** $t\bar{t}$ production cross sections and uncertainties in the $e\mu$ channel in bins of $p_T(t)$ for different $|y(t)|$ bins. The uncertainties are given separately for the statistical and systematic components.

$\lvert y(t\bar{t})\rvert \in$ [0 0.45]	Results	Uncertainties [%]		
$p_T(t\bar{t})$ bin range [GeV]	$\frac{d\sigma}{dp_T(t\bar{t})}$ $[\frac{pb}{\text{GeV}}]$	Stat.	Syst. Up	Syst. Down
0 to 40	1.13	1.7	5.3	6.1
40 to 100	0.49	2.2	7.7	8.6
100 to 200	0.118	4.1	10.4	10.2
200 to 400	0.014	8.4	15.1	13.8
$\lvert y(t\bar{t})\rvert \in$ [0.45 1]	Results	Uncertainties [%]		
$p_T(t\bar{t})$ bin range [GeV]	$\frac{d\sigma}{dp_T(t\bar{t})}$ $[\frac{pb}{\text{GeV}}]$	Stat.	Syst. Up	Syst. Down
0 to 40	1.12	1.8	11.1	9.8
40 to 100	0.43	2.7	11.9	12.2
100 to 200	0.111	5.1	11	10
200 to 400	0.017	9	12.1	7
$\lvert y(t\bar{t})\rvert \in$ [1 2.3]	Results	Uncertainties [%]		
$p_T(t\bar{t})$ bin range [GeV]	$\frac{d\sigma}{dp_T(t\bar{t})}$ $[\frac{pb}{\text{GeV}}]$	Stat.	Syst. Up	Syst. Down
0 to 40	0.95	2.4	7.3	7.3
40 to 100	0.31	3.7	9.8	9.3
100 to 200	0.08	6.5	14.7	14.8
200 to 400	0.006	18.6	21.2	8.5

Table I.11: Double differential **unnormalized** $t\bar{t}$ production cross sections and uncertainties in the $e\mu$ channel in bins of $p_T(t\bar{t})$ for different $|y(t\bar{t})|$ bins. The uncertainties are given separately for the statistical and systematic components.

$M(t\bar{t}) \in$ [340 450] [GeV]	Results	Uncertainties [%]		
$\lvert y(t)\rvert$ bin range	$\frac{d\sigma}{d\lvert y(t)\rvert}$ $[pb]$	Stat.	Syst. Up	Syst. Down
0 to 0.6	84.8	1.6	6	5.4
0.6 to 1.2	63.5	2.2	10.7	9.6
1.2 to 2.5	23.6	2.9	7.4	8.1
$M(t\bar{t}) \in$ [450 600] [GeV]	Results	Uncertainties [%]		
$\lvert y(t)\rvert$ bin range	$\frac{d\sigma}{d\lvert y(t)\rvert}$ $[pb]$	Stat.	Syst. Up	Syst. Down
0 to 0.6	57.1	2.3	7.2	8.4
0.6 to 1.2	41.3	3.2	12.6	11.8
1.2 to 2.5	17.5	3.6	8.6	8.1
$M(t\bar{t}) \in$ [600 1000] [GeV]	Results	Uncertainties [%]		
$\lvert y(t)\rvert$ bin range	$\frac{d\sigma}{d\lvert y(t)\rvert}$ $[pb]$	Stat.	Syst. Up	Syst. Down
0 to 0.6	19.6	4.3	12.2	11.8
0.6 to 1.2	19.8	4.6	7.8	6.3
1.2 to 2.5	11.5	4.2	7.6	8.4

Table I.12: Double differential **unnormalized** $t\bar{t}$ production cross sections and uncertainties in the $e\mu$ channel in bins of $|y(t)|$ for different $M(t\bar{t})$ bins. The uncertainties are given separately for the statistical and systematic components.

$M(t\bar{t})$ ∈ [340 450] [GeV]	Results	Uncertainties [%]		
$p_T(t)$ bin range [GeV]	$\frac{d\sigma}{dp_T(t)}$ $[\frac{pb}{\text{GeV}}]$	Stat.	Syst. Up	Syst. Down
0 to 65	0.78	2	6.6	6
65 to 130	0.89	1.5	8.2	7.4
130 to 200	0.12	8.8	24.3	23.2
200 to 300	0.01	26.3	38.2	34.1
300 to 500	0.0007	66.9	32.5	29.1
$M(t\bar{t})$ ∈ [450 600] [GeV]	Results	Uncertainties [%]		
$p_T(t)$ bin range [GeV]	$\frac{d\sigma}{dp_T(t)}$ $[\frac{pb}{\text{GeV}}]$	Stat.	Syst. Up	Syst. Down
0 to 65	0.23	6.3	18.2	13.5
65 to 130	0.45	3.1	12	12.9
130 to 200	0.46	2.4	8.2	8.7
200 to 300	0.067	9.5	24.2	21.3
300 to 500	0.0026	31.9	46.2	48.2
$M(t\bar{t})$ ∈ [600 1000] [GeV]	Results	Uncertainties [%]		
$p_T(t)$ bin range [GeV]	$\frac{d\sigma}{dp_T(t)}$ $[\frac{pb}{\text{GeV}}]$	Stat.	Syst. Up	Syst. Down
0 to 65	0.08	13.7	10.9	30.7
65 to 130	0.18	6.6	8.6	15.1
130 to 200	0.174	5.2	9.8	9.4
200 to 300	0.109	6.1	12.1	8.4
300 to 500	0.019	9.6	14	15.9

Table I.13: Double differential **unnormalized** $t\bar{t}$ production cross sections and uncertainties in the $e\mu$ channel in bins of $p_T(t)$ for different $M(t\bar{t})$ bins. The uncertainties are given separately for the statistical and systematic components.

$M(t\bar{t}) \in$ [340 450] [GeV]	Results	Uncertainties [%]		
$\Delta\eta(t\bar{t})$ bin range	$\frac{d\sigma}{d\Delta\eta(t\bar{t})}$ [pb]	Stat.	Syst. Up	Syst. Down
0 to 1	70	1.8	6.9	5.8
1 to 2.5	28.1	2.5	16.7	16.4
2.5 to 5	2.8	14.8	40.5	20.5
$M(t\bar{t}) \in$ [450 600] [GeV]	Results	Uncertainties [%]		
$\Delta\eta(t\bar{t})$ bin range	$\frac{d\sigma}{d\Delta\eta(t\bar{t})}$ [pb]	Stat.	Syst. Up	Syst. Down
0 to 1	25.2	3.3	11.5	10.2
1 to 2.5	24.9	3	17.8	16.9
2.5 to 5	7.7	5.2	11.1	14.3
$M(t\bar{t}) \in$ [600 1000] [GeV]	Results	Uncertainties [%]		
$\Delta\eta(t\bar{t})$ bin range	$\frac{d\sigma}{d\Delta\eta(t\bar{t})}$ [pb]	Stat.	Syst. Up	Syst. Down
0 to 1	6.7	6	10.2	14.5
1 to 2.5	9.8	4.3	12.7	9.2
2.5 to 5	7.7	4.4	10.7	14.4

Table I.14: Double differential **unnormalized** $t\bar{t}$ production cross sections and uncertainties in the $e\mu$ channel in bins of $\Delta\eta(t\bar{t})$ for different $M(t\bar{t})$ bins. The uncertainties are given separately for the statistical and systematic components.

$M(t\bar{t}) \in$ [340 450] [GeV]	Results	Uncertainties [%]		
$\Delta\phi(t\bar{t})$ bin range	$\frac{d\sigma}{d\Delta\phi(t\bar{t})}$ [pb]	Stat.	Syst. Up	Syst. Down
0 to 1.2	8.4	7.7	19.2	18.1
1.2 to 2.6	24.2	2.5	17.9	16.5
2.6 to 3.14	140	1.3	9.9	8.9
$M(t\bar{t}) \in$ [450 600] [GeV]	Results	Uncertainties [%]		
$\Delta\phi(t\bar{t})$ bin range	$\frac{d\sigma}{d\Delta\phi(t\bar{t})}$ [pb]	Stat.	Syst. Up	Syst. Down
0 to 1.2	2.9	17.2	25.9	29.6
1.2 to 2.6	10.4	5.5	34.2	32.2
2.6 to 3.14	118.1	1.4	13.1	12.4
$M(t\bar{t}) \in$ [600 1000] [GeV]	Results	Uncertainties [%]		
$\Delta\phi(t\bar{t})$ bin range	$\frac{d\sigma}{d\Delta\phi(t\bar{t})}$ [pb]	Stat.	Syst. Up	Syst. Down
0 to 1.2	0.9	29.2	55.2	51.5
1.2 to 2.6	4.6	8.2	12.3	12.8
2.6 to 3.14	56.8	2.4	8.3	8.5

Table I.15: Double differential **unnormalized** $t\bar{t}$ production cross sections and uncertainties in the $e\mu$ channel in bins of $\Delta\phi(t\bar{t})$ for different $M(t\bar{t})$ bins. The uncertainties are given separately for the statistical and systematic components.

$M(t\bar{t}) \in$ [340 450] [GeV]	Results	Uncertainties [%]		
$\lvert y(t\bar{t})\rvert$ bin range	$\frac{d\sigma}{d\lvert y(t\bar{t})\rvert}$ $[pb]$	Stat.	Syst. Up	Syst. Down
0 to 0.45	87.8	1.9	6.2	5.7
0.45 to 1	75.3	1.9	9.9	8.9
1 to 2.3	29.6	2.2	6.3	5.7
$M(t\bar{t}) \in$ [450 600] [GeV]	Results	Uncertainties [%]		
$\lvert y(t\bar{t})\rvert$ bin range	$\frac{d\sigma}{d\lvert y(t\bar{t})\rvert}$ $[pb]$	Stat.	Syst. Up	Syst. Down
0 to 0.45	70.4	2.3	6.6	7.5
0.45 to 1	52.9	2.7	10.9	11.1
1 to 2.3	16	3.8	10.9	10.9
$M(t\bar{t}) \in$ [600 1000] [GeV]	Results	Uncertainties [%]		
$\lvert y(t\bar{t})\rvert$ bin range	$\frac{d\sigma}{d\lvert y(t\bar{t})\rvert}$ $[pb]$	Stat.	Syst. Up	Syst. Down
0 to 0.45	37.8	3.2	6.8	8
0.45 to 1	25.9	4.2	7.7	6.4
1 to 2.3	5	8.8	21.1	16.6

Table I.16: Double differential **unnormalized** $t\bar{t}$ production cross sections and uncertainties in the $e\mu$ channel in bins of $|y(t\bar{t})|$ for different $M(t\bar{t})$ bins. The uncertainties are given separately for the statistical and systematic components.

$M(t\bar{t}) \in$ [340 450] [GeV]	Results	Uncertainties [%]		
$p_T(t\bar{t})$ bin range [GeV]	$\frac{d\sigma}{dp_T(t\bar{t})}$ $[\frac{pb}{\text{GeV}}]$	Stat.	Syst. Up	Syst. Down
0 to 40	1.67	1.4	5.5	5
40 to 100	0.6	2	9.6	9.1
100 to 200	0.145	4.2	12	7.7
200 to 400	0.014	11.5	8.6	12.4
$M(t\bar{t}) \in$ [450 600] [GeV]	Results	Uncertainties [%]		
$p_T(t\bar{t})$ bin range [GeV]	$\frac{d\sigma}{dp_T(t\bar{t})}$ $[\frac{pb}{\text{GeV}}]$	Stat.	Syst. Up	Syst. Down
0 to 40	1.09	2	10.3	10.7
40 to 100	0.43	2.9	11.4	13.6
100 to 200	0.099	6.3	20.2	21.8
200 to 400	0.015	11.7	13.5	7.6
$M(t\bar{t}) \in$ [600 1000] [GeV]	Results	Uncertainties [%]		
$p_T(t\bar{t})$ bin range [GeV]	$\frac{d\sigma}{dp_T(t\bar{t})}$ $[\frac{pb}{\text{GeV}}]$	Stat.	Syst. Up	Syst. Down
0 to 40	0.47	3.6	7.7	9.1
40 to 100	0.21	4.9	9.9	7.9
100 to 200	0.055	7.9	15.4	15.5
200 to 400	0.007	15.3	32.5	22.7

Table I.17: Double differential **unnormalized** $t\bar{t}$ production cross sections and uncertainties in the $e\mu$ channel in bins of $p_T(t\bar{t})$ for different $M(t\bar{t})$ bins. The uncertainties are given separately for the statistical and systematic components.

$M(t\bar{t}) \in$ [340 450] [GeV]	Results	Uncertainties [%]			PDF unc. on MadGraph theory pred. [%]	
x_1 bin range	$\frac{d\sigma}{dx_1}$ $[pb]$	Stat.	Syst. Up	Syst. Down	Pos.	Neg.
0 to 0.05	1191	1.4	6.9	5.5	5.8	5.1
0.05 to 0.1	589	2.2	9	8.8	6.4	5.5
0.1 to 0.2	209.8	2.9	6.8	5	6.3	5.7
0.2 to 0.4	47.6	6.7	7.3	11.3	10.0	9.1
0.4 to 1	3.1	55.2	33.1	44.4	20.4	13.3
$M(t\bar{t}) \in$ [450 600] [GeV]	Results	Uncertainties [%]			PDF unc. on MadGraph theory pred. [%]	
x_1 bin range	$\frac{d\sigma}{dx_1}$ $[pb]$	Stat.	Syst. Up	Syst. Down	Pos.	Neg.
0 to 0.05	646	2.3	12.4	12.3	7.1	6.4
0.05 to 0.1	488	2.7	7.2	8.7	7.5	6.6
0.1 to 0.2	175.6	3.5	7.4	7.6	7.5	6.7
0.2 to 0.4	32.2	9.1	17.3	14.7	10.6	9.5
0.4 to 1	2.1	64.5	57.8	46.8	24.3	15.3
$M(t\bar{t}) \in$ [600 1000] [GeV]	Results	Uncertainties [%]			PDF unc. on MadGraph theory pred. [%]	
x_1 bin range	$\frac{d\sigma}{dx_1}$ $[pb]$	Stat.	Syst. Up	Syst. Down	Pos.	Neg.
0 to 0.05	160	6.5	8.5	7.9	9.4	8.7
0.05 to 0.1	256	4	5.5	6.3	9.4	8.5
0.1 to 0.2	118.2	4.1	11.2	11.3	9.4	8.6
0.2 to 0.4	23.7	9.1	19.5	12.9	11.4	10.1
0.4 to 1	0.3	144	497.1	533.4	23.5	14.5

Table I.18: Double differential **unnormalized** $t\bar{t}$ production cross sections and uncertainties in the $e\mu$ channel in bins of x_1 for different $M(t\bar{t})$ bins. The uncertainties are given separately for the statistical and systematic components. Additionally the PDF uncertainties on MadGraph theory predictions.

Appendix J

Numerical Values for the Systematics Uncertainties

In the following the numerical values of systematic uncertainties for the normalized 11.1 and unnormalized G double differential $t\bar{t}$ production cross sections are listed in the tables. The tables contain the systematic uncertainties components for each systematic source and the total uncertainties. The suffixes "UP" or "DOWN" show the direction of the variation compared to the nominal parameter/scale factor value. The signs of the uncertainties represent the change of the result caused by the variation compared to nominal. The suffixes "Positive" and "Negative" are described in sec. 10.3.

$\lvert y(t\bar{t})\rvert$	0 to 0.45				0.45 to 1				1 to 2.3			
$p_T(t\bar{t})$ [GeV]	0 to 40	40 to 100	100 to 200	200 to 400	0 to 40	40 to 100	100 to 200	200 to 400	0 to 40	40 to 100	100 to 200	200 to 400
Source	Uncertainty [%]											
Lumi Up	0.2	-0	0.1	-0.3	-0.2	-0.4	-0	-0.2	0.4	-0.1	0.1	-0.5
Down	-0.2	0	-0.1	0.3	0.2	0.4	0	0.2	-0.4	0.1	-0.1	0.2
b-tagging Pos.	0.3	0.5	0.5	1.1	0.1	0.3	0.7	0.4	0.5	0.7	1.5	0.2
Neg.	0.3	0.2	0.8	0.2	0.3	0.4	0.9	0.5	0.5	0.6	1	2.2
Kin Up	0.01	0	0	-0.03	-0.01	-0.04	-0	0.01	0.03	-0.01	0.02	-0.16
Down	-0.01	-0	-0	0.01	0.02	0.04	0	0.03	-0.03	0.01	-0	-0.1
JER Up	-0.1	0.1	-0	1	0.3	-0.8	-0.1	-0.3	0.6	-0.5	-0.2	1.2
Down	-0.5	0.8	-0.2	-0.4	-0.8	0.9	1	1.2	-0.3	1	-0.6	0.7
JES Up	0.7	-0.1	-2.1	-0	1	-1.1	-1.3	0.3	1.1	-1.6	-1.6	-3
Down	-1	0.5	0.6	-0.5	-0.7	0.5	2.8	2.7	-0.4	0.4	1.9	-2.8
PU Up	0.2	-0.4	-0.3	-0.4	0.4	-0.4	-0.1	-0.6	0.2	-0.3	-0.4	0.5
Down	-0.3	0.4	0.2	0.5	-0.4	0.4	0.1	0.8	-0.2	0.3	0.5	-1
Trig Up	0.2	0.2	0.1	0	-0	-0.1	0.1	0.1	-0.1	-0.4	-0.2	-0.7
Down	-0.2	-0.2	-0.1	-0	0	0.1	-0.1	-0	0.1	0.4	0.3	0.5
Lept Up	0.2	0.1	0	-0.2	-0.2	-0.4	-0	-0.1	0.3	-0.1	0.1	-0.5
Down	-0.2	-0.1	-0	0.2	0.2	0.4	0	0.1	-0.3	0.1	-0.1	0.3
BG Up	0	0.3	0.2	-1.9	-0.1	-0.2	-0	-1	0.2	0	0.2	-1.8
Down	-0	-0.3	-0.2	1.8	0.1	0.2	0	1	-0.2	-0.1	-0.2	1.5
DY Up	0.2	0.2	0.4	0.1	-0.1	-0.1	-0	-0	-0.3	-0.1	0.6	-1.2
Down	-0.2	-0.3	-0.4	0	0.1	0.1	0.1	0.1	0.4	0.1	-0.6	1.2
Mass Up	-0.8	-0.6	0.5	3.1	1	0.3	0.1	2.5	-1.2	-0.7	3.4	3.6
Down	-1.5	-1.9	1.4	5.6	0.8	1.9	2.1	-2.4	-0.8	0.8	0.6	1.8
Match Up	-0.4	-1.8	1	4.2	-0.5	1.1	2.8	-2.6	-1.6	2.7	1.7	12.3
Down	0.7	-1.2	-1.9	-0.5	1.5	-1.6	-2.4	7.9	-0.4	0.6	0.3	2.4
Scale Up	-3.5	3.3	4.8	-6.1	-4.1	2.8	3.9	4.4	-0.1	2.2	2.1	16
Down	1.7	-5.4	-3.7	3	5.7	-4.8	-4.9	3.8	1.1	1.3	-5.4	3.1
PDF Pos.	0.3	0.1	0.3	0.8	0.3	0.2	0.2	0.3	0.5	0.2	0.5	0.7
Neg.	0.3	0.1	0.2	0.7	0.2	0.2	0.2	0.3	0.9	0.2	0.5	0.7
Hadronization	2.2	-1.4	-2.1	-4.7	-0.3	-5.1	-1.5	3.2	4	0.7	-4.8	4.8
Hard Scat.	-2.6	-4.3	0.6	2.7	1.9	0.2	0.1	-0.3	1.3	2.3	5.3	-2.8
Statistical	1.6	2.2	4.1	8.4	1.7	2.6	5.1	9	2.2	3.6	6.5	18.6
Total Syst. Pos.	4	5.7	5.7	9.7	6.5	6.3	6.2	10.4	4.6	4.5	8.8	21.4
Total Syst. Neg.	5.3	7.5	5.3	8.4	4.7	7.3	5.9	4.9	4.9	3.1	9.2	7.2

Table J.1: Summary of all the statistical and systematic uncertainties (for each source separately and total) for the **normalized** double differential cross sections in bins of $p_T(t\bar{t})$ for different $\lvert y(t\bar{t})\rvert$ bins.

$\lvert y(t)\rvert$	0 to 0.6			0.6 to 1.2			1.2 to 2.5		
$M(t\bar{t})$ [GeV]	340 to 450	450 to 600	600 to 1000	340 to 450	450 to 600	600 to 1000	340 to 450	450 to 600	600 to 1000
Source	Uncertainty [%]								
Lumi Up	0.4	-0.1	0.1	-0.5	-0.8	0.3	0.5	-0	0.1
Down	-0.4	0.1	-0.1	0.5	0.8	-0.3	-0.5	0	-0.1
b-tagging Pos.	0.6	0.7	0.8	0.4	0.5	0.4	0.8	0.3	0.2
Neg.	0.5	0.5	0.4	0.6	0.6	0.8	0.5	0.6	0.6
Kin Up	0.03	-0.01	0.01	-0.03	-0.07	0.03	0.05	-0.01	0.01
Down	-0.03	0.01	-0.01	0.03	0.07	-0.02	-0.05	0.01	-0.02
JER Up	0.1	-0.2	-1.2	-0.2	0.4	0.4	0.2	0.4	-0.3
Down	0.1	-0.3	-0.1	-0.2	0.5	0	-0.1	-0.4	0.7
JES Up	1.1	-0.6	1.5	-0.4	-2.3	1.4	0.9	-1.3	0.5
Down	-0.9	0.1	-1.8	0.9	2.4	-2.6	0.2	0.7	-1.3
PU Up	0.1	-0.3	-0.1	0.1	-0.2	-0.2	0.2	0.1	-0
Down	-0.1	0.3	0.1	-0.1	0.2	0.1	-0.2	-0.1	-0
Trig Up	0.4	0.1	0.1	-0.2	-0.3	0.2	-0.1	-0.3	-0
Down	-0.4	-0.1	-0.1	0.2	0.3	-0.2	0.1	0.3	-0
Lept Up	0.3	-0.1	0.1	-0.4	-0.7	0.3	0.5	-0.1	0.2
Down	-0.3	0.1	-0.1	0.4	0.8	-0.3	-0.5	0.1	-0.2
BG Up	0.3	-0.2	-0	-0.3	-0.6	0.5	0.3	-0	0.1
Down	-0.3	0.2	0	0.3	0.6	-0.5	-0.3	0	-0.1
DY Up	-0	0.3	0.5	-0.5	0.2	0.5	-0.5	0.2	0.2
Down	0	-0.3	-0.5	0.5	-0.2	-0.5	0.5	-0.2	-0.2
Mass Up	-0.3	-1.8	2.2	0.4	3.2	1.4	-3.5	2.7	-1.1
Down	1.1	-2.9	-1.9	2.2	0.4	-2.8	1.2	-0.1	-2.3
Match Up	-0.5	-1.2	-0.7	1.3	-0.4	3.3	0.1	0.7	-1.4
Down	1.1	-1.3	-1.3	0.2	-0.9	-0.3	0	1.5	-0.8
Scale Up	-0.7	-2.9	-1.5	1.2	2.4	2.4	1.2	1.6	-3.4
Down	0.1	-2.4	4	1.3	-1.6	-0.4	0.6	1.3	-1.5
PDF Pos.	0.9	0.7	0.7	0.3	1	1	2.6	1	1.1
Neg.	0.8	0.5	0.7	0.2	0.7	1	3.2	1.4	1.3
Hadronization	0.3	-0.8	1.9	-2.4	-3.6	-0.2	4.5	2.9	-2
Hard Scat.	-2.2	-1	7.6	1.8	2.3	-1.8	-1.3	2.1	-3.7
Statistical	1.6	2.2	4.3	2.1	3.2	4.6	2.7	3.5	4.2
Total Syst. Pos.	3.2	1.7	9.2	4.3	6.6	5.1	5.8	5.1	4.5
Total Syst. Neg.	2.9	4.6	8.6	3.2	5.4	4.5	6.8	4.1	6.3

Table J.2: Summary of all the statistical and systematic uncertainties (for each source separately and total) for the **normalized** double differential cross sections in bins of $M(t\bar{t})$ for different $\lvert y(t)\rvert$ bins.

$M(t\bar{t})$ [GeV]	340 to 450					450 to 600					600 to 1000				
$p_T(t)$ [GeV]	0 to 65	65 to 130	130 to 200	200 to 300	300 to 500	0 to 65	65 to 130	130 to 200	200 to 300	300 to 500	0 to 65	65 to 130	130 to 200	200 to 300	300 to 500
Source	Uncertainty [%]														
Lumi Up	0.1	0.5	-1.9	1.6	-1.3	-1	-0.7	0.5	-0.4	-0.1	1	0.6	-0.2	-0	-0.2
Down	-0.1	-0.4	1.9	-1.6	1.2	1	0.7	-0.5	0.4	0.1	-1	-0.6	0.2	0	0.1
b-tagging Pos.	0.5	0.3	1.6	3.5	3.4	0.9	0.5	0.9	1.1	0	1.6	0.3	0.6	0.5	1.4
Neg.	0.5	0	0.8	0.8	2.4	1.7	0.5	0.6	0.5	5	1.8	1.5	0.5	0.7	0.5
Kin Up	0.01	0.03	-0.12	0.11	-0.1	-0.08	-0.06	0.03	-0.03	0.01	0.08	0.04	-0	-0	-0.03
Down	-0.01	-0.03	0.12	-0.11	0.08	0.08	0.06	-0.03	0.03	0.03	-0.08	-0.04	0	0.01	-0.02
JER Up	0.6	-0.1	-3.1	-3.8	15.2	1	0.1	-0.5	3.7	-2.6	0.2	-0.7	-0.7	0.3	-2.6
Down	0.3	-0.1	-0.1	-3.5	2.2	-0.6	-0.3	-0.2	1.8	-5.7	3.1	0.1	-1.1	0.5	-0.6
JES Up	2.3	0.4	-6.1	2.2	-5.7	-2.4	-1.9	-0.2	2.1	-2.8	-6.5	0.9	-0.5	2	1.3
Down	-1.3	0.2	2.4	3.3	0.5	3.3	2.2	-0.9	1.6	-2.8	0.3	-1.8	-2.2	-0	-4.5
PU Up	0.1	0	0.1	-0.9	-3	-0	0.2	-0.2	-1.1	-1.1	-0.8	0.6	0.3	-0.5	0.3
Down	-0.1	-0	-0	0.9	3.9	0.1	-0.2	0.2	1.1	1.2	1.2	-0.7	-0.4	0.5	-0.4
Trig Up	0.1	0.2	-0.8	0.8	-0.5	-0.5	-0.3	0.2	-0.1	0	-0.1	0.1	-0	0	0
Down	-0.1	-0.2	0.8	-0.9	0.5	0.5	0.4	-0.2	0.1	-0	0.1	-0.1	0	-0	-0.1
Lept Up	0.1	0.4	-1.4	1.2	-1	-0.9	-0.7	0.3	-0.3	-0.1	0.8	0.5	-0	-0.1	-0.1
Down	-0.1	-0.4	1.4	-1.3	1	0.9	0.7	-0.3	0.3	0.1	-0.9	-0.5	0	0.1	0
BG Up	0.3	0.3	-1.1	-1.8	-1.1	-1.2	-0.6	0.3	-0.7	-1	0.7	0.5	0.3	-0.1	-0.1
Down	-0.3	-0.3	1	1.8	1.5	1.2	0.6	-0.3	0.7	1	-0.6	-0.5	-0.3	0.1	0
DY Up	-0.6	0.1	0.2	-1	1.8	-1.2	0.2	0.5	0.2	0.2	0.9	0.4	0.1	0.2	0.6
Down	0.6	-0.1	-0.2	1.3	-2	1.2	-0.2	-0.5	-0.3	-0.2	-0.8	-0.4	-0.1	-0.2	-0.7
Mass Up	-0.2	-0.2	-6.3	-11.9	-2.2	0.4	2.5	-0.8	2	13.5	-2.2	-3.1	1.1	5.3	-3.5
Down	0.4	1.7	10.7	2.2	1.5	-4.5	-2	0.1	-0.3	-0.1	-3.1	-1.6	-0.5	-3	-3.4
Match Up	1.3	0.4	3.3	-3	6.4	1.7	-2.4	-0.7	9.7	-18.5	-22	-0.2	0.8	0.3	-1.6
Down	1.5	-0.1	-2	1.5	8.7	1	-4	0.6	6.7	11.7	-4.4	0	0.9	0.5	-4.3
Scale Up	-0.9	-0.4	16	24.5	-8.3	14.4	-4.3	-3.7	0.8	0.6	-14.1	-2.9	3.9	-0.2	-2.8
Down	3.3	2.1	-16.1	-14.9	-4.2	-8.5	0.8	3.1	2.1	-5.9	-15.1	-10.4	-2.2	8.5	-1.5
PDF Pos.	0.2	0.2	0.2	0.7	1.1	0.6	0.4	0.3	1.1	0.5	1.9	0.9	0.9	0.5	2.2
Neg.	0.2	0.2	0.2	0.8	1.1	0.6	0.4	0.2	1.1	0.6	1.9	0.9	0.9	0.5	2.4
Hadronization	1.5	-0.4	4.2	11	27	1.6	-2.5	-1.4	2.4	-11.5	4.7	2.7	-2.1	-2.4	-5.6
Hard Scat.	-0	0.8	4.8	-28.1	-17.4	-2.3	3.3	0.8	17.1	-41.4	-11.7	-10	-4.8	-1.5	4.9
Statistical	1.9	1.4	8.8	26.3	66.9	6.3	3	2.4	9.5	31.9	13.6	6.6	5.2	6.1	9.6
Total Syst. Pos.	4.6	3	20.9	39.4	37.1	15.4	5.6	3.8	20.5	46.6	13.4	10.5	6.8	10.7	8
Total Syst. Neg.	2.4	1.2	20	36.2	34	10.7	7.8	4.4	17.3	47.9	30.6	15.3	6.3	4.3	11.3

Table J.3: Summary of all the statistical and systematic uncertainties (for each source separately and total) for the **normalized** double differential cross sections in bins of $p_T(t)$ for different $M(t\bar{t})$ bins.

$M(t\bar{t})$ [GeV]	340 to 450			450 to 600			600 to 1000		
$\Delta\eta(t\bar{t})$	0 to 1	1 to 2.5	2.5 to 5	0 to 1	1 to 2.5	2.5 to 5	0 to 1	1 to 2.5	2.5 to 5
Source	Uncertainty [%]								
Lumi Up	0.6	-0.8	0.5	-0.3	-0.2	0	0.2	0.2	-0.1
Down	-0.6	0.7	-0.5	0.3	0.2	-0	-0.3	-0.2	0.1
b-tagging Pos.	0.2	0.4	1.5	0.9	0.6	0.9	0.6	0.8	0.4
Neg.	0.1	0.4	3.1	0.7	0.4	1.3	0.5	0.5	1.1
Kin Up	0.04	-0.03	0.01	-0.02	-0.02	-0.01	0.01	0.01	0
Down	-0.04	0.04	-0	0.03	0.01	0.01	-0.04	-0.01	-0
JER Up	0.2	-0.7	3.9	0.8	-0.3	-0	-1.9	0.7	-0.9
Down	0.1	0.1	0.6	0.1	-0.2	-0.5	0.5	-0.4	0.2
JES Up	1.5	-0.6	2.5	-0.6	-1.5	-3.1	2.1	2	-0.4
Down	-0.5	-0.4	3.1	0.8	0.8	2.3	-3.2	-1.5	-0.9
PU Up	-0	0.3	0.3	-0.5	-0.1	0.1	-0	-0.3	0.3
Down	0	-0.3	-0.1	0.5	0.2	-0.2	-0	0.3	-0.3
Trig Up	0.2	-0.2	0.4	-0.2	-0	-0.1	0.3	0.1	-0.2
Down	-0.2	0.2	-0.4	0.2	0	0.1	-0.3	-0.1	0.2
Lept Up	0.4	-0.4	0.1	-0.3	-0.2	-0.1	0.3	0.1	0
Down	-0.4	0.4	-0.1	0.3	0.2	0.1	-0.3	-0.1	-0
BG Up	0.5	-0.2	-1.1	-0.4	-0.4	-0.1	0	0.2	0.1
Down	-0.5	0.2	1	0.4	0.3	0.1	-0.1	-0.2	-0.1
DY Up	-0.1	-0.6	-0.2	0.5	0.3	-0.1	0.4	0.4	0.2
Down	0.1	0.5	0.5	-0.4	-0.3	0.1	-0.4	-0.4	-0.2
Mass Up	-0.7	-1.9	7.1	2.4	-0.7	0.7	0.3	5.2	-2.6
Down	1	0.7	13.9	-0	-1.9	-1.9	-10.2	2.8	-2.9
Match Up	0	-0.5	17.8	3.8	-3.2	-4	-2.2	4.1	-2.6
Down	1	-2.2	17.9	2.8	-3	-3.3	-3.1	1.8	0.1
Scale Up	0.1	-2.2	23.5	-0.3	-0.7	-1.1	-1.5	4.5	-4.1
Down	0.6	1.6	13.2	2.4	-2.2	-7.3	3	6.1	-7.7
PDF Pos.	0.6	0.3	2.1	0.1	0.2	0.2	0.4	0.3	0.3
Neg.	0.6	0.4	2.4	0.1	0.1	0.2	0.4	0.2	0.3
Hadronization	3.4	-5.8	4	0.2	-1.5	2.2	-2.6	-1.3	1.8
Hard Scat.	-2.2	3.5	15.3	3.3	0.2	-3.9	0.4	2.3	-8.3
Statistical	1.6	2.3	14.9	3.3	2.9	5.2	6	4.3	4.2
Total Syst. Pos.	4.7	7.1	36.8	6.3	1.9	5.2	4.7	9.7	8.5
Total Syst. Neg.	4.2	7.8	16.4	3.6	4.9	10.3	11.8	3.1	12.2

Table J.4: Summary of all the statistical and systematic uncertainties (for each source separately and total) for the **normalized** double differential cross sections in bins of $\Delta\eta(t\bar{t})$ for different $M(t\bar{t})$ bins.

$M(t\bar{t})$ [GeV]	340 to 450			450 to 600			600 to 1000		
$\Delta\phi(t\bar{t})$	0 to 1.2	1.2 to 2.6	2.6 to 3.1415	0 to 1.2	1.2 to 2.6	2.6 to 3.1415	0 to 1.2	1.2 to 2.6	2.6 to 3.1415
Source	Uncertainty [%]								
Lumi Up	1.4	-0.4	0.7	2	-1.1	-0.1	-0.4	0.7	0.1
Down	-0.9	1.3	-0.1	-0.9	1.8	0	1.3	-0	-0.2
b-tagging Pos.	2.4	1.7	0.8	3.2	1.3	0.4	3	0.9	0.4
Neg.	0.6	0	0	1.4	0.3	0.5	2.3	0.4	0.5
Kin Up	0.33	0.42	0.33	0.66	0.25	-0.06	0.37	0.38	-0.02
Down	0.21	0.51	0.27	0.43	0.48	-0.03	0.51	0.32	-0.06
JER Up	0.6	0.6	0.3	-0.8	-0.1	0.1	1.3	1.1	-0.5
Down	4.4	0.5	-0.2	-1.9	-0.7	-0	4	2.2	0.1
JES Up	2.4	0.1	1.1	-6.9	-4.4	-0.4	4.3	-0.1	1.4
Down	2.4	0.9	-0.5	-1.5	4.2	0.2	4.6	2.6	-2.2
PU Up	0	0.5	0.5	-2.4	0.2	-0	2	-0.4	-0.1
Down	0.6	0.4	0.1	3.4	0.6	-0.1	-1.2	1.1	-0
Trig Up	0.7	0.2	0.5	1.4	-0.3	-0.1	-0.5	0.4	0.1
Down	-0.2	0.8	0.1	-0.3	1.1	0	1.4	0.3	-0.2
Lept Up	1	-0.1	0.6	1.9	-0.9	-0.2	-0.4	0.7	0.2
Down	-0.5	1	-0	-0.9	1.7	0.1	1.3	-0	-0.3
BG Up	1.1	0.2	0.6	0.5	-0.9	-0.2	-1.3	0.2	0.3
Down	-0.5	0.7	0.1	0.6	1.6	0.1	2.1	0.5	-0.3
DY Up	-0.5	0	0.2	-0.2	1.1	0.1	1.7	0.2	0.4
Down	1.2	0.9	0.4	1.4	-0.4	-0.2	-0.8	0.5	-0.5
Mass Up	5.6	-0.3	-2	3.8	1.5	0.4	28.1	-2.1	0.9
Down	1.5	2.6	1.1	-7	-2.5	-1.1	-7.3	7.2	-3.2
Match Up	4.2	0.4	-0.5	-0.7	-0.4	-0.5	5.3	2.9	-0
Down	0.7	0.3	0.8	5.4	-4.8	0.1	17.1	-3.6	-1
Scale Up	10.2	0.6	-1.9	-11	17.3	-2.8	-27.5	3.5	-0.2
Down	-12.3	0.6	3.3	0.8	-17.1	1.7	8.6	-10	1.5
PDF Pos.	1.5	0.5	5.5	1.9	0.6	0.6	11.5	1	1.1
Neg.	1.4	0.5	5.8	1.6	0.5	0.7	12	1	1.1
Hadronization	14.2	-5.3	1.2	16.9	-4.8	-0.3	-36.7	3.5	0.7
Hard Scat.	-11.1	3.5	-1	-24.4	2.2	1.5	-18.4	-2.8	2.1
Statistical	7.7	2.4	1.2	17.2	5.4	1.3	29.2	8.2	2.3
Total Syst. Pos.	22.8	7.5	7	31	19	2.5	55.1	10.5	3.4
Total Syst. Neg.	21.9	6.3	6.7	33.3	19.3	3.6	51.5	11.8	4.8

Table J.5: Summary of all the statistical and systematic uncertainties (for each source separately and total) for the **normalized** double differential cross sections in bins of $\Delta\phi(t\bar{t})$ for different $M(t\bar{t})$ bins.

$M(t\bar{t})$ [GeV]	340 to 450			450 to 600			600 to 1000		
$\lvert y(t\bar{t})\rvert$	0 to 0.45	0.45 to 1	1 to 2.3	0 to 0.45	0.45 to 1	1 to 2.3	0 to 0.45	0.45 to 1	1 to 2.3
Source	Uncertainty [%]								
Lumi Up	0.3	-0.3	0.5	-0.1	-0.6	-0.3	0.1	0.3	0.4
Down	-0.3	0.3	-0.4	0.1	0.6	0.3	-0.1	-0.3	-0.4
b-tagging Pos.	0.6	0.4	0.7	0.5	0.4	0.5	0.3	0.4	0.6
Neg.	0.5	0.5	0.4	0.2	0.4	1.1	0.4	0.6	0.5
Kin Up	0.03	-0.01	0.03	-0.01	-0.05	-0.02	0.01	0.03	0
Down	-0.02	0.02	-0.03	0.01	0.06	0.03	-0.01	-0.02	-0.07
JER Up	0.2	-0.1	0	0.4	-0.6	0.5	-0.6	-0.4	1
Down	-0.4	0.3	0.2	0.4	-0.4	-0.9	0.1	-0.6	3.4
JES Up	0.7	0.7	0.1	-0.7	-2.1	-1.6	0.3	1.8	4
Down	-0.8	0.4	0.1	0.9	1.3	0.5	-1.3	-2.2	-1.5
PU Up	0	0.2	0.1	-0.2	-0.1	-0.2	-0	-0.1	-0.1
Down	-0	-0.2	-0.1	0.2	0.1	0.3	-0.1	0.2	0.1
Trig Up	0.4	0	-0.1	0.1	-0.2	-0.5	0.1	0.2	0.1
Down	-0.4	-0	0.1	-0.1	0.3	0.6	-0.1	-0.2	-0.2
Lept Up	0.3	-0.2	0.4	-0.1	-0.6	-0.3	0.1	0.3	0.4
Down	-0.3	0.2	-0.4	0.1	0.6	0.3	-0.1	-0.3	-0.5
BG Up	0.3	-0.1	0.4	-0.2	-0.5	-0.4	0.1	0.4	-0.3
Down	-0.3	0.1	-0.3	0.1	0.5	0.4	-0.1	-0.4	0.2
DY Up	0.1	-0.5	-0.5	0.3	0.2	0.1	0.4	0.4	0.5
Down	-0.1	0.5	0.5	-0.3	-0.2	-0.1	-0.4	-0.4	-0.6
Mass Up	-0.2	0.2	-3	-0.3	0.3	3	-1.2	2.5	6.1
Down	0.5	2.3	1.8	-1.8	0.1	-1.9	-3.3	1.1	-7.5
Match Up	0.2	-0.2	-0.1	-0.7	-0.2	-0.2	-2.6	3.4	5.4
Down	1.2	0.8	-0.5	-1	0.4	-1.2	-2.1	-1.2	5.7
Scale Up	0	-0.5	1.8	-0.4	-0.4	-0.5	-1.3	0.9	-0.7
Down	0.9	0.4	-0.8	-3.3	-1.2	1.6	-1.2	1.9	12
PDF Pos.	0.4	0.4	0.3	0.3	0.3	0.2	1.3	0.9	0.8
Neg.	0.4	0.3	0.4	0.3	0.2	0.2	1.3	1	0.8
Hadronization	-0.1	-2.6	4.6	0.4	-3	0.5	-0.5	1	0.3
Hard Scat.	-1.7	0.6	-2.5	-2.8	2.2	4.8	-0.8	0.4	10.8
Statistical	1.9	1.8	2.1	2.3	2.6	3.7	3.2	4.2	8.8
Total Syst. Pos.	2.6	3.8	6	3.1	4.2	6	1.7	5.3	19
Total Syst. Neg.	2.2	2.9	6.2	4.9	4.7	5.8	4.9	3.1	13.3

Table J.6: Summary of all the statistical and systematic uncertainties (for each source separately and total) for the **normalized** double differential cross sections in bins of $|y(t\bar{t})|$ for different $M(t\bar{t})$ bins.

$M(t\bar{t})$ [GeV]	340 to 450				450 to 600				600 to 1000			
$p_T(t\bar{t})$ [GeV]	0 to 40	40 to 100	100 to 200	200 to 400	0 to 40	40 to 100	100 to 200	200 to 400	0 to 40	40 to 100	100 to 200	200 to 400
Source	Uncertainty [%]											
Lumi Up	0.3	-0.1	0.2	-0.3	-0.3	-0.5	0	-0.1	0.3	0.2	-0.1	-0.8
Down	-0.3	0.1	-0.2	0.3	0.3	0.5	-0	0.1	-0.3	-0.2	0.1	0.7
b-tagging Pos.	0.1	0.5	1.7	0.3	0.4	0.7	1.1	0.8	0.4	0.9	0.4	0.9
Neg.	0.2	0.4	1.1	1.3	0.5	0.6	1.1	0.2	0.3	0.9	1.1	0.9
Kin Up	0.03	-0	0.02	-0.03	-0.03	-0.04	-0.01	0.03	0.03	0.02	0.01	-0.15
Down	-0.03	0	-0.02	0.02	0.03	0.04	0.01	0.03	-0.03	-0.02	0.01	-0.03
JER Up	0.2	-0.3	0.5	-1.2	0	0	-0.4	2.5	-0.2	-0.4	-1.3	1.1
Down	-0.5	0.9	0.9	-1.8	-0.8	1.3	-0.8	0.7	-0.6	0.3	0.7	4.6
JES Up	1.4	-0.6	-0.8	1.8	-0.4	-1.6	-4.6	-1.7	1.4	0.9	0	2.4
Down	-0.8	0.6	2	-0.6	-0.2	1.9	2	1.6	-2.2	-1.8	0.5	2.8
PU Up	0.2	-0.2	0.1	0.1	0.3	-0.6	-0.8	-0.9	0.3	-0.4	-0.3	-0.4
Down	-0.2	0.1	-0.1	0.2	-0.3	0.6	0.8	1	-0.4	0.3	0.4	0.1
Trig Up	0.2	-0	0.1	-0.1	-0.2	-0.3	-0	0.1	0.1	0.1	-0	-0.5
Down	-0.2	0	-0.1	0.1	0.2	0.3	0	-0	-0.1	-0.1	0	0.3
Lept Up	0.3	-0.1	0.2	-0.3	-0.3	-0.5	-0.1	0	0.3	0.2	-0	-0.7
Down	-0.3	0.1	-0.2	0.3	0.3	0.5	0.1	0	-0.3	-0.2	0	0.6
BG Up	0.1	0.2	0.5	-1.5	-0.3	-0.3	-0.3	-0.7	0.3	0.5	-0.3	-3.1
Down	-0.1	-0.2	-0.5	1.5	0.3	0.3	0.3	0.8	-0.3	-0.5	0.4	2.8
DY Up	-0.3	-0.1	0.1	-1.1	0.1	0.1	0.5	0.1	0.5	0.1	0.6	0.1
Down	0.3	0.1	0	1.4	-0.1	-0.1	-0.6	-0.2	-0.5	-0.1	-0.6	-0.2
Mass Up	-0.9	-1	1.7	-8.4	-0	0.5	2.7	6.7	1.3	0.5	-3.2	16.5
Down	0.8	1.4	6.3	1.4	-1.1	-1.5	-3.8	-1.9	-4.3	-1	2.3	9.3
Match Up	-0.5	1	1.4	-2.2	-0.3	-1.6	0.7	2.3	-1.7	1.2	3.9	11.2
Down	0.1	1	1.5	0.3	1.2	-2.9	-4.3	7.7	1.1	-2.7	-2.2	-0.6
Scale Up	0	1.5	4.9	-1.7	-6	3.3	7.9	-0.8	-5.4	7.2	-4.5	10.9
Down	1.1	-0.9	-3.4	-1.3	5.3	-8.1	-9	4.3	4.2	-2.6	2.1	6.6
PDF Pos.	0.3	0.2	0.1	0.5	0.4	0.3	0.3	0.2	1	1.1	0.6	1.6
Neg.	0.4	0.2	0.1	0.5	0.4	0.2	0.2	0.2	1.1	1.2	0.7	1.7
Hadronization	2.1	-2.9	4.3	-1.5	1.8	-4	-11.5	4.2	2.8	2.5	-6.7	-7.4
Hard Scat.	-2.3	-1.2	1.2	-4	2.3	-0.5	4.6	0.8	0.4	1	3.8	13.7
Statistical	1.2	2	4.2	11.5	1.8	2.8	6.3	11.7	3.6	4.8	7.9	15.3
Total Syst. Pos.	3.8	4.1	9.7	5.4	6.2	5.8	15.2	12.3	5.7	8	9.3	28.3
Total Syst. Neg.	3.5	3.5	5.8	10.3	6.9	9.8	17.1	5.2	8.1	5.3	9.9	16.1

Table J.7: Summary of all the statistical and systematic uncertainties (for each source separately and total) for the **normalized** double differential cross sections in bins of $p_T(t\bar{t})$ for different $M(t\bar{t})$ bins.

$M(t\bar{t})$ [GeV]	340 to 450					450 to 600					600 to 1000				
x_1	0 to 0.05	0.05 to 0.1	0.1 to 0.2	0.2 to 0.4	0.4 to 1	0 to 0.05	0.05 to 0.1	0.1 to 0.2	0.2 to 0.4	0.4 to 1	0 to 0.05	0.05 to 0.1	0.1 to 0.2	0.2 to 0.4	0.4 to 1
Source	Uncertainty [%]														
Lumi Up	0.3	-0.2	0.2	-0.1	2.8	-0.4	-0.4	-0	-0.5	1.3	0.4	0.1	0	-0.1	-2.7
Down	-0.3	0.2	-0.2	0.1	-2.7	0.4	0.4	0	0.5	-0.9	-0.4	-0.1	-0	0.1	-2.8
b-tagging Pos.	0.4	0.6	0.3	0.9	3.4	0.3	0.7	0.3	0.8	2.9	0.6	0.4	0.2	0.8	5.5
Neg.	0.3	0.5	0.4	1.1	4.3	0.3	0.3	0.2	1	5.4	0.5	0.4	0.4	1	16.4
Kin Up	0.03	-0.02	0.02	-0.01	0.22	-0.03	-0.03	-0.01	-0.03	0.29	0.03	0.01	0.01	0.02	-2.69
Down	-0.03	0.02	-0.02	-0	-0.13	0.04	0.03	0.01	0.08	0.05	-0.03	-0.01	-0.01	0.03	-2.72
JER Up	-0.1	-0.2	-0.3	-0.6	18.4	-0.3	-0.1	-0.2	0.5	19.7	-0	-0.8	-0.6	-1.3	2.6
Down	0	-0.9	0.3	0.1	17.7	-0.4	0.1	-0	-2	3.5	0.4	0.1	-0.8	1.2	26.2
JES Up	0.6	-0.1	0.5	-1.7	13	-1.6	-1.5	-1.2	-1.2	22.5	1.8	0.8	0.3	3.2	-32.5
Down	-0.2	-0.4	-0.4	-0.9	17.7	0.6	1.1	1.3	1.3	-7.8	-2.1	-2.1	-0.9	-1.6	-3.1
PU Up	0.1	0.2	0.2	0.3	-0.9	-0.1	-0.1	-0.2	-0.8	5.8	-0.2	-0.3	0.1	0.5	-14.2
Down	-0	-0.1	-0.2	-0.5	0.2	0.1	0.1	0.3	1	-4.2	0.2	0.2	-0.1	-0.5	8.9
Trig Up	0.2	0.1	0.1	-0.7	-1.1	-0.3	0	0	-0.7	-1.2	0.1	0.2	0.1	0	-3.3
Down	-0.2	-0.1	-0.1	0.7	1.3	0.3	-0	-0	0.7	1.6	-0.1	-0.2	-0.1	0	-2.1
Lept Up	0.3	-0.2	0.2	-0.1	2	-0.4	-0.3	-0.1	-0.6	1.4	0.3	0.1	0.1	-0	-2.5
Down	-0.3	0.2	-0.2	0.1	-1.9	0.4	0.4	0.1	0.6	-1.2	-0.3	-0.1	-0.1	0.1	-2.9
BG Up	0.3	-0.2	0.2	0.7	2.9	-0.2	-0.4	-0.3	-1.1	-3.5	0.1	0.2	0.2	-0.2	1
Down	-0.3	0.2	-0.2	-0.7	-2.7	0.2	0.4	0.3	1.1	4.2	-0.2	-0.2	-0.2	0.2	-6.5
DY Up	-0.2	-0.2	-0.3	-0.7	-0.7	0.3	0.2	0.1	0.7	-1.5	0.3	0.5	0.3	0.5	-3.6
Down	0.2	0.1	0.3	0.8	2.3	-0.3	-0.3	-0.1	-0.6	2.3	-0.3	-0.5	-0.3	-0.4	-2.4
Mass Up	-1	0.7	-0.3	-4.1	-35.6	1.7	-0.3	-0.4	6.4	19.1	1.1	1	-1	8.7	-28.7
Down	2.5	-0.8	2.9	0.7	-16	-1.8	-1	-1.4	6.3	16.8	-4.8	0.2	-2.4	-4	-155.2
Match Up	0	0	0.9	-2.7	-4.5	-0.7	-0.8	0.5	1.2	11.9	3.2	-2.1	-0.3	7.1	-34.5
Down	0.9	0.9	0.5	-5.4	-2.5	0.3	-1.1	-1.1	0.7	19.4	1.7	-1.9	-1.6	1.8	-51.2
Scale Up	0.4	1	0.5	2.6	-21.1	1	0.5	-2.3	-2.5	-13.4	1.5	-2.3	1.8	-2.4	-62.4
Down	0.6	0.3	0.3	-4.1	10.2	0	-4.2	-1.2	5.6	3.4	4.1	-1.6	0.4	10.9	-97.7
PDF Pos.	0.3	0.3	0.3	0.5	2.3	0.4	0.5	0.3	0.4	8.3	0.8	1.2	1.2	0.6	7.8
Neg.	0.4	0.3	0.3	0.5	2.9	0.4	0.5	0.2	0.4	11.6	0.7	1.2	1.3	0.7	7
Hadronization	1.7	-2.7	1.6	5.9	-7.7	-4	0.6	0.5	8.8	-35.3	5.3	1.6	-3.3	-3.5	509.9
Hard Scat.	-0.6	-0.4	-2.3	-6.1	4.4	3.9	-2.3	-0.3	8.9	-13.3	2.6	-2	3.3	5.6	-105.8
Statistical	1.3	2.2	2.9	6.6	54.8	2.3	2.7	3.5	9.2	64.3	6.5	4	4	9.1	144.1
Total Syst. Pos.	3.4	3.2	4.2	9	29.7	6	2.8	1.6	15.4	56.7	8.3	3.2	5.2	17.4	521.6
Total Syst. Neg.	2.1	3.1	3	11.9	43.1	6.2	5.3	3.2	13.1	43.2	8	4.8	5.8	8.4	556

Table J.8: Summary of all the statistical and systematic uncertainties (for each source separately and total) for the **normalized** double differential cross sections in bins of x_1 for different $M(t\bar{t})$ bins.

$\|y(t)\|$	0 to 0.6					0.6 to 1.2					1.2 to 2.5				
$p_T(t)$ [GeV]	0 to 65	65 to 130	130 to 200	200 to 300	300 to 500	0 to 65	65 to 130	130 to 200	200 to 300	300 to 500	0 to 65	65 to 130	130 to 200	200 to 300	300 to 500
Source	Uncertainty [%]														
Lumi Up	-2.6	-2.5	-2.7	-2.8	-2.7	-3.2	-3	-2.9	-2.5	-2.9	-2.5	-2.4	-2.8	-2.7	-2.7
Down	2.8	2.6	2.8	2.9	2.9	3.4	3.2	3	2.7	3.1	2.7	2.5	2.9	2.9	2.8
b-tagging Pos.	0.9	0.8	1	1.1	1.3	0.9	1	1.3	3.6	2	0.8	1	1.1	0.6	1.5
Neg.	0.8	0.7	1.2	0.7	1.8	1.8	1.2	1.4	0.3	9.1	0.7	1.1	1.2	1.7	0.7
Kin Up	-0.18	-0.17	-0.19	-0.2	-0.19	-0.23	-0.23	-0.21	-0.18	-0.2	-0.18	-0.17	-0.2	-0.18	-0.3
Down	0.18	0.17	0.19	0.2	0.19	0.23	0.23	0.21	0.18	0.23	0.18	0.17	0.19	0.22	0.08
JER Up	1.2	-0.3	-1.4	2.2	-3	-0.1	0.3	-0.5	2	-4.1	1.2	-0.2	0.2	-2.1	7.1
Down	1.1	-0.3	-0.7	-1.3	2.8	-1.6	0.3	0	4.5	-2.1	1.2	-0.4	-2.4	0.4	1.4
JES Up	0.6	-2.5	-2.9	-0.2	-0.9	-2	-3.6	-5.3	3.1	-5.2	-2.5	-2.8	-2.4	-1.1	2
Down	1.6	2.3	0.9	3.6	-2.5	1.4	4.6	1.9	4.2	-1.1	2.4	3.4	2.2	0.1	-2.2
PU Up	0.2	0.6	0.3	-0.6	1	0.5	0.6	0	0	-0.2	0.5	0.4	0.9	-1.1	1.7
Down	-0.2	-0.6	-0.3	0.6	-1.1	-0.6	-0.6	-0	0.1	0.1	-0.5	-0.4	-0.8	1.2	-1.9
Trig Up	-1.1	-1	-1.2	-1.2	-1.2	-1.5	-1.4	-1.3	-1.1	-1.3	-1.6	-1.4	-1.6	-1.5	-1.5
Down	1.1	1.1	1.2	1.3	1.2	1.5	1.5	1.3	1.1	1.3	1.7	1.5	1.6	1.6	1.3
Lept Up	-2.1	-2	-2.1	-2.3	-2.2	-2.6	-2.5	-2.3	-2	-2.4	-2	-1.9	-2.2	-2.3	-2.2
Down	2.1	2	2.2	2.4	2.2	2.7	2.6	2.4	2	2.5	2.1	1.9	2.3	2.4	2.1
BG Up	-1.6	-1.5	-1.4	-2.3	-1.5	-1.7	-1.9	-1.7	-1.5	-2.8	-1.3	-1.5	-1.7	-2	-1.7
Down	1.6	1.5	1.4	2.3	1.5	1.7	1.9	1.6	1.7	2.7	1.3	1.5	1.7	2.1	1.4
DY Up	-0.8	-0.2	-0	-0.4	0.1	-1.3	-0.4	-0	-0.2	0.2	-0.9	-0.5	-0.4	-0.1	0.2
Down	0.8	0.2	0	0.4	-0.2	1.3	0.4	0	0.2	-0.1	1	0.5	0.4	0.1	-0.4
Mass Up	2.8	-0.9	-4	3.6	-1.4	-2.9	4	-1.6	6.6	-3.7	-6.5	0.9	1.2	-7.6	13
Down	1.2	0.4	1.9	-2.4	2.5	-2.7	4.9	3.2	1.4	-8.1	-0.1	1.1	2.4	-2.4	-12.1
Match Up	1.1	-1.9	-0.2	1.1	-6.4	0.5	0.6	-1.4	8.2	-1.8	-3	0.7	-0.2	-3	4.8
Down	0.8	-1.7	-0.1	1.3	-2.4	-0.4	-0.3	-1.3	0.1	4.4	0.2	-1.7	1.9	-0.4	-1.8
Scale Up	-1.7	-0.6	1.5	0.2	-6.2	4.6	2.4	-0.4	5.8	-2.7	1.7	1.5	3	-3.9	13.4
Down	0.8	-2.2	-2.5	1.8	1	-1.3	-1.5	-2	5.4	-2	-2.3	-1	-1.5	-0.8	1.7
PDF Pos.	0.5	0.3	0.1	0.1	0.8	0.7	0.5	0.4	0.2	0.5	1.4	1.6	1.2	1.2	0.5
Neg.	0.6	0.3	0.1	0.1	0.8	0.6	0.4	0.3	0.2	0.6	1.8	2.1	1.6	0.9	0.4
Hadronization	-5.2	-4.2	-3.8	0.1	-15.6	-5.2	-6.3	-6.1	-11	6.4	-0.2	-1.8	-4.1	-1.8	-18.4
Hard Scat.	3.6	1.6	3.3	3.4	3.2	5.2	4.5	5.1	5.4	-9.4	5.2	1.7	-1.2	0.6	-6.3
Statistical	3.6	2.3	3.1	6.2	9.7	4.5	3	4.4	8.3	14.8	5	3	4.9	10.5	21.3
Total Syst. Pos.	8.5	6.4	7	8.3	17	10.2	11.7	9.9	19	13.4	7.6	6.3	8	5.3	28.7
Total Syst. Neg.	7.8	7.1	8.7	6.3	19.2	9.9	9.9	11	12.8	18.9	10.5	6.1	7.4	10.7	23.6

Table J.9: Summary of all the statistical and systematic uncertainties (for each source separately and total) for the **unnormalized** double differential cross sections in bins of $p_T(t)$ for different $|y(t)|$ bins.

$\lvert y(t\bar{t})\rvert$	0 to 0.45				0.45 to 1				1 to 2.3			
$p_T(t\bar{t})$ [GeV]	0 to 40	40 to 100	100 to 200	200 to 400	0 to 40	40 to 100	100 to 200	200 to 400	0 to 40	40 to 100	100 to 200	200 to 400
Source	Uncertainty [%]											
Lumi Up	-2.5	-2.7	-2.6	-3	-2.9	-3.1	-2.7	-2.8	-2.3	-2.8	-2.6	-3.2
Down	2.6	2.8	2.8	3.1	3.1	3.3	2.8	3	2.4	3	2.7	3.1
b-tagging Pos.	0.8	0.9	0.4	1.3	0.9	0.8	0.6	1	0.9	1.1	1.6	0.2
Neg.	0.8	0.6	0.9	0.4	0.9	0.9	1.1	0.9	0.9	1	1.3	2.3
Kin Up	-0.18	-0.19	-0.19	-0.22	-0.21	-0.23	-0.19	-0.18	-0.16	-0.2	-0.17	-0.36
Down	0.18	0.19	0.19	0.21	0.21	0.23	0.19	0.22	0.16	0.2	0.19	0.1
JER Up	0	0.2	0.1	1.1	0.4	-0.7	-0	-0.2	0.7	-0.4	-0.1	1.3
Down	-0.7	0.7	-0.3	-0.5	-0.9	0.7	0.9	1	-0.4	0.8	-0.8	0.6
JES Up	-1.4	-2.2	-4.1	-2.1	-1.1	-3.2	-3.3	-1.8	-1	-3.6	-3.6	-5
Down	1.1	2.6	2.8	1.7	1.4	2.7	5	4.9	1.8	2.6	4.1	-0.7
PU Up	0.6	-0	0.1	0	0.8	-0.1	0.3	-0.2	0.6	0.1	0	0.9
Down	-0.6	0	-0.2	0.1	-0.8	0	-0.3	0.4	-0.6	-0.1	0.1	-1.4
Trig Up	-1.1	-1.1	-1.2	-1.3	-1.3	-1.4	-1.2	-1.2	-1.4	-1.7	-1.5	-2
Down	1.1	1.2	1.2	1.3	1.4	1.5	1.2	1.3	1.4	1.8	1.6	1.8
Lept Up	-2	-2.1	-2.1	-2.4	-2.3	-2.6	-2.2	-2.2	-1.9	-2.3	-2	-2.7
Down	2.1	2.2	2.2	2.4	2.4	2.7	2.2	2.4	1.9	2.4	2.1	2.5
BG Up	-1.6	-1.3	-1.4	-3.5	-1.8	-1.8	-1.7	-2.6	-1.4	-1.6	-1.4	-3.4
Down	1.6	1.3	1.4	3.5	1.8	1.8	1.6	2.7	1.5	1.6	1.4	3.1
DY Up	-0.3	-0.2	-0	-0.4	-0.6	-0.5	-0.5	-0.5	-0.8	-0.6	0.1	-1.7
Down	0.3	0.2	0	0.5	0.6	0.5	0.5	0.5	0.8	0.6	-0.1	1.7
Mass Up	-1.1	-1	0.2	2.7	0.7	-0.1	-0.2	2.1	-1.6	-1	3	3.2
Down	-0.6	-0.9	2.4	6.6	1.8	2.9	3.1	-1.4	0.2	1.7	1.6	2.8
Match Up	-0.4	-1.7	1	4.3	-0.4	1.2	2.9	-2.5	-1.5	2.8	1.8	12.4
Down	0.4	-1.5	-2.2	-0.8	1.2	-1.9	-2.7	7.6	-0.7	0.3	0	2.1
Scale Up	-3.7	3	4.6	-6.3	-4.3	2.6	3.6	4.1	-0.3	2	1.9	15.7
Down	2.3	-4.8	-3.1	3.6	6.4	-4.2	-4.3	4.4	1.7	1.9	-4.9	3.7
PDF Pos.	0.3	0.2	0.3	0.8	0.3	0.2	0.2	0.3	0.6	0.2	0.4	0.7
Neg.	0.3	0.2	0.3	0.8	0.2	0.2	0.2	0.3	0.9	0.2	0.4	0.7
Hadronization	-1.6	-5.1	-5.8	-8.3	-4.1	-8.6	-5.2	-0.7	0.1	-3.1	-8.4	0.8
Hard Scat.	1.4	-0.3	4.8	7	6.1	4.3	4.3	3.8	5.5	6.5	9.6	1.2
Statistical	1.7	2.2	4.1	8.4	1.8	2.7	5.1	9	2.4	3.7	6.5	18.6
Total Syst. Pos.	5.3	7.7	10.4	15.1	11.1	11.9	11	12.1	7.3	9.8	14.7	21.2
Total Syst. Neg.	6.1	8.6	10.2	13.8	9.8	12.2	10	7	7.2	9.3	14.7	8.4

Table J.10: Summary of all the statistical and systematic uncertainties (for each source separately and total) for the **unnormalized** double differential cross sections in bins of $p_T(t\bar{t})$ for different $\lvert y(t\bar{t})\rvert$ bins.

$\lvert y(t)\rvert$	0 to 0.6			0.6 to 1.2			1.2 to 2.5		
$M(t\bar{t})$ [GeV]	340 to 450	450 to 600	600 to 1000	340 to 450	450 to 600	600 to 1000	340 to 450	450 to 600	600 to 1000
Source	Uncertainty [%]								
Lumi Up	-2.3	-2.8	-2.6	-3.1	-3.4	-2.4	-2.2	-2.7	-2.6
Down	2.5	3	2.7	3.3	3.6	2.5	2.3	2.9	2.7
b-tagging Pos.	0.7	1	1	1	1.1	0.6	1	0.8	0.6
Neg.	0.8	0.9	0.9	1.1	1	1	0.7	1.1	1
Kin Up	-0.16	-0.2	-0.18	-0.23	-0.26	-0.17	-0.15	-0.2	-0.18
Down	0.16	0.2	0.18	0.23	0.26	0.17	0.15	0.2	0.17
JER Up	0.2	-0.1	-1.1	-0.1	0.5	0.5	0.3	0.4	-0.3
Down	0	-0.4	-0.2	-0.3	0.4	-0.1	-0.1	-0.5	0.6
JES Up	-1.1	-2.7	-0.7	-2.6	-4.4	-0.8	-1.3	-3.4	-1.7
Down	1.4	2.4	0.5	3.2	4.8	-0.3	2.5	3	1
PU Up	0.5	0.1	0.3	0.5	0.2	0.2	0.5	0.5	0.4
Down	-0.5	-0.1	-0.3	-0.5	-0.2	-0.2	-0.6	-0.5	-0.4
Trig Up	-0.9	-1.2	-1.2	-1.5	-1.6	-1.1	-1.4	-1.6	-1.3
Down	0.9	1.3	1.2	1.5	1.7	1.1	1.5	1.7	1.3
Lept Up	-1.9	-2.3	-2	-2.5	-2.9	-1.9	-1.7	-2.3	-2
Down	1.9	2.3	2.1	2.6	3	1.9	1.7	2.3	2
BG Up	-1.3	-1.8	-1.6	-1.8	-2.2	-1.1	-1.3	-1.6	-1.5
Down	1.3	1.8	1.6	1.8	2.2	1.1	1.3	1.6	1.4
DY Up	-0.5	-0.2	0	-1	-0.3	0.1	-1	-0.3	-0.3
Down	0.5	0.2	-0	1	0.3	-0	1	0.3	0.3
Mass Up	-0.6	-2.1	1.9	0.1	2.9	1.1	-3.8	2.4	-1.3
Down	2.4	-1.7	-0.7	3.4	1.6	-1.7	2.5	1.1	-1.1
Match Up	-0.5	-1.2	-0.7	1.4	-0.4	3.4	0.2	0.7	-1.3
Down	0.6	-1.7	-1.8	-0.3	-1.3	-0.8	-0.4	1	-1.3
Scale Up	0.4	-1.8	-0.4	2.3	3.5	3.5	2.3	2.7	-2.3
Down	-0.8	-3.3	3.1	0.5	-2.4	-1.3	-0.2	0.4	-2.4
PDF Pos.	0.7	0.4	0.9	0.2	0.6	1.2	2.8	1.1	1.4
Neg.	0.7	0.4	1	0.2	0.5	1.2	3.5	1.7	1.6
Hadronization	-3.6	-4.7	-2.2	-6.2	-7.4	-4.1	0.4	-1.2	-5.9
Hard Scat.	0.5	1.7	10.6	4.6	5.2	1	1.5	5	-1
Statistical	1.6	2.3	4.3	2.2	3.2	4.6	2.9	3.6	4.2
Total Syst. Pos.	5.9	7.2	12.2	10.7	12.6	7.6	6.5	8.4	7.4
Total Syst. Neg.	5.4	8.4	11.8	9.6	11.7	6.1	6.6	7.8	8.1

Table J.11: Summary of all the statistical and systematic uncertainties (for each source separately and total) for the **unnormalized** double differential cross sections in bins of $M(t\bar{t})$ for different $\lvert y(t)\rvert$ bins.

$M(t\bar{t})$ [GeV]	340 to 450					450 to 600					600 to 1000				
$p_T(t)$ [GeV]	0 to 65	65 to 130	130 to 200	200 to 300	300 to 500	0 to 65	65 to 130	130 to 200	200 to 300	300 to 500	0 to 65	65 to 130	130 to 200	200 to 300	300 to 500
Source	Uncertainty [%]														
Lumi Up	-2.6	-2.3	-4.6	-1.1	-3.9	-3.7	-3.4	-2.3	-3.1	-2.8	-1.7	-2.1	-2.9	-2.7	-2.9
Down	2.7	2.4	4.8	1.2	4.1	3.9	3.6	2.4	3.3	2.9	1.8	2.2	3.1	2.9	3
b-tagging Pos.	0.8	0.7	1.8	3.9	3.3	1.1	1.1	1.1	1.1	0	1.3	0.4	1.2	0.4	1.8
Neg.	0.9	0.6	1.4	0.9	2.4	2.1	1.1	0.9	0.6	5.2	1.4	1.8	1	1	0.9
Kin Up	-0.18	-0.16	-0.31	-0.09	-0.3	-0.27	-0.25	-0.17	-0.22	-0.18	-0.12	-0.15	-0.19	-0.2	-0.23
Down	0.18	0.16	0.31	0.08	0.27	0.27	0.25	0.17	0.22	0.22	0.12	0.15	0.2	0.21	0.17
JER Up	0.7	0	-3	-3.7	15.3	1.1	0.2	-0.4	3.8	-2.5	0.4	-0.6	-0.6	0.4	-2.5
Down	0.2	-0.2	-0.2	-3.6	2.1	-0.6	-0.3	-0.2	1.7	-5.8	3	0	-1.2	0.5	-0.7
JES Up	-0	-1.9	-8.2	-0.1	-7.8	-4.6	-4.1	-2.4	-0.2	-5	-8.6	-1.3	-2.7	-0.3	-0.9
Down	0.9	2.5	4.7	5.6	2.8	5.7	4.5	1.3	3.9	-0.6	2.6	0.5	0	2.3	-2.3
PU Up	0.5	0.4	0.5	-0.5	-2.7	0.3	0.6	0.2	-0.7	-0.7	-0.4	0.9	0.7	-0.1	0.7
Down	-0.5	-0.4	-0.4	0.5	3.5	-0.3	-0.6	-0.2	0.7	0.8	0.8	-1.1	-0.8	0.1	-0.8
Trig Up	-1.2	-1.1	-2	-0.5	-1.8	-1.8	-1.6	-1.1	-1.4	-1.2	-1.4	-1.2	-1.3	-1.3	-1.2
Down	1.2	1.1	2.1	0.4	1.8	1.8	1.7	1.1	1.4	1.3	1.4	1.2	1.4	1.3	1.2
Lept Up	-2.1	-1.8	-3.5	-1	-3.2	-3	-2.8	-1.9	-2.5	-2.3	-1.4	-1.7	-2.2	-2.2	-2.3
Down	2.1	1.9	3.7	0.9	3.3	3.2	2.9	1.9	2.6	2.4	1.3	1.8	2.3	2.3	2.3
BG Up	-1.3	-1.3	-2.7	-3.4	-2.7	-2.8	-2.1	-1.3	-2.3	-2.6	-0.9	-1.1	-1.3	-1.7	-1.6
Down	1.3	1.3	2.6	3.4	3.2	2.8	2.1	1.3	2.3	2.6	0.9	1.1	1.3	1.7	1.6
DY Up	-1	-0.4	-0.3	-1.5	1.3	-1.6	-0.3	0.1	-0.2	-0.3	0.4	-0.1	-0.4	-0.2	0.2
Down	1	0.4	0.3	1.8	-1.5	1.7	0.2	-0.1	0.2	0.3	-0.3	0	0.3	0.2	-0.2
Mass Up	-0.5	-0.5	-6.6	-12.2	-2.5	0.1	2.2	-1.1	1.7	13.1	-2.5	-3.4	0.7	5	-3.8
Down	1.6	3	12.1	3.4	2.7	-3.4	-0.8	1.3	0.9	1.1	-1.9	-0.4	0.7	-1.8	-2.3
Match Up	1.1	0.2	3.1	-3.2	6.2	1.5	-2.6	-0.9	9.5	-18.7	-22.2	-0.4	0.6	0.1	-1.8
Down	1	-0.6	-2.5	1	8.1	0.4	-4.5	0.1	6.1	11.1	-4.9	-0.5	0.4	-0.1	-4.8
Scale Up	0.2	0.7	17.3	25.9	-7.3	15.6	-3.2	-2.6	1.9	1.7	-13.2	-1.9	5	0.9	-1.7
Down	1.7	0.6	-17.4	-16.2	-5.6	-9.9	-0.7	1.6	0.5	-7.3	-16.3	-11.7	-3.6	6.9	-2.9
PDF Pos.	0.5	0.3	0.1	0.6	0.9	0.8	0.5	0.3	1.2	0.4	1.9	1.1	1	0.5	2.2
Neg.	0.5	0.3	0.1	0.6	0.9	0.8	0.4	0.2	1.1	0.5	2	1.1	1	0.5	2.4
Hadronization	-3.1	-4.9	-0.6	5.9	21.2	-3	-6.9	-5.8	-2.3	-15.5	-0.1	-2	-6.5	-6.9	-9.9
Hard Scat.	2.9	3.8	7.9	-26	-14.9	0.6	6.4	3.7	20.6	-39.7	-9.1	-7.4	-2	1.4	8
Statistical	2	1.5	8.8	26.3	66.9	6.3	3.1	2.4	9.5	31.9	13.7	6.6	5.2	6.1	9.6
Total Syst. Pos.	6.6	8.2	24.3	38.2	32.5	18.2	12	8.2	24.1	46.2	10.6	8.4	9.7	12.1	13.7
Total Syst. Neg.	5.9	7.4	23.2	34.1	29.1	13.4	12.9	8.7	21.3	48.2	30.6	15	9.4	8.4	15.6

Table J.12: Summary of all the statistical and systematic uncertainties (for each source separately and total) for the **unnormalized** double differential cross sections in bins of $p_T(t)$ for different $M(t\bar{t})$ bins.

$M(t\bar{t})$ [GeV]	340 to 450			450 to 600			600 to 1000		
$\Delta\eta(t\bar{t})$	0 to 1	1 to 2.5	2.5 to 5	0 to 1	1 to 2.5	2.5 to 5	0 to 1	1 to 2.5	2.5 to 5
Source	Uncertainty [%]								
Lumi Up	-2.2	-3.4	-2.3	-3	-2.9	-2.7	-2.5	-2.6	-2.8
Down	2.3	3.6	2.4	3.2	3	2.8	2.6	2.7	3
b-tagging Pos.	0.8	0.9	1.4	1.1	0.9	1.1	0.8	0.9	0.8
Neg.	0.7	0.9	2.9	1.1	1	1.6	0.8	0.8	1.5
Kin Up	-0.16	-0.23	-0.19	-0.22	-0.21	-0.2	-0.18	-0.18	-0.19
Down	0.16	0.23	0.19	0.22	0.21	0.2	0.16	0.19	0.19
JER Up	0.2	-0.6	4	0.9	-0.2	0.1	-1.8	0.8	-0.8
Down	-0	-0	0.5	0	-0.3	-0.6	0.4	-0.5	0.1
JES Up	-0.7	-2.8	0.3	-2.8	-3.7	-5.2	-0.1	-0.3	-2.6
Down	1.8	1.9	5.4	3.1	3.1	4.7	-1	0.8	1.3
PU Up	0.4	0.7	0.7	-0.1	0.3	0.5	0.3	0	0.6
Down	-0.4	-0.7	-0.5	0.1	-0.2	-0.5	-0.4	-0	-0.7
Trig Up	-1.1	-1.5	-0.9	-1.4	-1.3	-1.4	-1	-1.2	-1.5
Down	1.1	1.5	0.9	1.5	1.4	1.4	1	1.2	1.5
Lept Up	-1.8	-2.6	-2.1	-2.5	-2.3	-2.3	-1.9	-2.1	-2.2
Down	1.8	2.7	2.2	2.6	2.4	2.4	1.9	2.2	2.2
BG Up	-1.1	-1.8	-2.6	-2	-1.9	-1.7	-1.6	-1.4	-1.5
Down	1.1	1.7	2.6	2	1.9	1.7	1.5	1.4	1.5
DY Up	-0.6	-1	-0.7	0	-0.2	-0.5	-0.1	-0	-0.2
Down	0.6	1	0.9	0	0.2	0.6	0	0.1	0.2
Mass Up	-1.1	-2.3	6.7	2	-1	0.3	-0.1	4.8	-3
Down	2.2	1.9	15.3	1.2	-0.7	-0.8	-9.2	4	-1.8
Match Up	-0.1	-0.6	17.6	3.7	-3.3	-4.1	-2.3	4	-2.7
Down	0.4	-2.8	17.3	2.3	-3.6	-3.9	-3.6	1.2	-0.5
Scale Up	1.2	-1.1	24.9	0.8	0.4	-0	-0.4	5.6	-3
Down	-1	0	11.5	0.9	-3.7	-8.8	1.4	4.4	-9.1
PDF Pos.	0.3	0.6	2.3	0.3	0.3	0.5	0.2	0.3	0.6
Neg.	0.3	0.6	2.6	0.3	0.2	0.4	0.1	0.3	0.5
Hadronization	-1.2	-10	-0.6	-4.3	-5.9	-2.3	-6.9	-5.6	-2.7
Hard Scat.	0.6	6.5	18.6	6.3	3.1	-1.2	3.3	5.2	-5.7
Statistical	1.8	2.5	14.8	3.3	3	5.2	6	4.3	4.4
Total Syst. Pos.	4.9	13.3	39.8	10.5	8.7	7	8.7	12.2	7.8
Total Syst. Neg.	4	13.8	19.5	9.4	10.3	12.2	13.2	8.6	12.9

Table J.13: Summary of all the statistical and systematic uncertainties (for each source separately and total) for the **unnormalized** double differential cross sections in bins of $\Delta\eta(t\bar{t})$ for different $M(t\bar{t})$ bins.

$M(t\bar{t})$ [GeV]	340 to 450			450 to 600			600 to 1000		
$\Delta\phi(t\bar{t})$	0 to 1.2	1.2 to 2.6	2.6 to 3.1415	0 to 1.2	1.2 to 2.6	2.6 to 3.1415	0 to 1.2	1.2 to 2.6	2.6 to 3.1415
Source	Uncertainty [%]								
Lumi Up	-1.8	-3.5	-2.5	-1.2	-4.2	-3.3	-3.5	-2.5	-3
Down	1.5	3.7	2.3	1.5	4.2	2.4	3.7	2.4	2.2
b-tagging Pos.	1.2	1.1	0.5	1.7	1	0.3	2.5	0	0.1
Neg.	1.2	1	1	2.4	1.4	2	3.5	1.4	1.9
Kin Up	-0.31	-0.23	-0.31	0.02	-0.39	-0.7	-0.27	-0.26	-0.66
Down	-0.05	0.25	0.02	0.17	0.22	-0.29	0.25	0.06	-0.31
JER Up	0.3	0.2	-0.1	-1.1	-0.5	-0.3	1	0.7	-0.8
Down	3.9	0	-0.8	-2.4	-1.3	-0.6	3.4	1.6	-0.4
JES Up	-0.2	-2.5	-1.4	-9.2	-6.8	-2.9	1.6	-2.7	-1.2
Down	4.3	2.7	1.3	0.2	6.1	2	6.5	4.4	-0.5
PU Up	-0.1	0.4	0.5	-2.5	0.1	-0.1	2	-0.5	-0.2
Down	-0.3	-0.4	-0.8	2.6	-0.2	-0.9	-2	0.3	-0.8
Trig Up	-1	-1.6	-1.2	-0.4	-2.1	-1.8	-2.2	-1.3	-1.6
Down	0.7	1.6	1	0.5	2	0.9	2.2	1.1	0.7
Lept Up	-1.7	-2.7	-2	-0.8	-3.5	-2.8	-3	-1.9	-2.5
Down	1.3	2.8	1.7	0.9	3.5	1.9	3.1	1.8	1.5
BG Up	-1	-1.8	-1.5	-1.5	-2.9	-2.2	-3.3	-1.9	-1.8
Down	0.6	1.8	1.2	1.7	2.7	1.2	3.3	1.7	0.8
DY Up	-1.4	-0.9	-0.7	-1.1	0.2	-0.8	0.8	-0.7	-0.5
Down	1.2	0.9	0.4	1.4	-0.4	-0.2	-0.8	0.5	-0.5
Mass Up	5.3	-0.5	-2.2	3.5	1.2	0.1	27.7	-2.3	0.7
Down	2.8	3.9	2.4	-5.8	-1.3	0.2	-6.2	8.6	-2
Match Up	4.3	0.6	-0.4	-0.6	-0.2	-0.4	5.5	3	0.1
Down	0.1	-0.2	0.3	4.9	-5.3	-0.4	16.5	-4.1	-1.5
Scale Up	10.8	1.2	-1.3	-10.5	18	-2.2	-27.1	4.2	0.4
Down	-12.8	-0	2.7	0.2	-17.6	1.1	7.9	-10.6	0.9
PDF Pos.	0.8	1	6.1	1.1	0.4	1.3	12.2	0.8	1.3
Neg.	0.8	1.1	6.5	1	0.4	1.5	12.6	0.7	1.3
Hadronization	9.4	-9.3	-3.1	11.9	-8.9	-4.5	-39.4	-0.9	-3.6
Hard Scat.	-7.6	7.5	2.8	-21.4	6.1	5.4	-15.2	1	6
Statistical	7.7	2.5	1.3	17.2	5.5	1.4	29.2	8.2	2.3
Total Syst. Pos.	18.8	14.1	9	25.6	22.8	8.3	56.1	11.8	7.7
Total Syst. Neg.	17.9	13.3	9.3	29.2	23.4	9.9	52.6	12.7	9.2

Table J.14: Summary of all the statistical and systematic uncertainties (for each source separately and total) for the **unnormalized** double differential cross sections in bins of $\Delta\phi(t\bar{t})$ for different $M(t\bar{t})$ bins.

$M(t\bar{t})$ [GeV]	340 to 450			450 to 600			600 to 1000		
$\lvert y(t\bar{t})\rvert$	0 to 0.45	0.45 to 1	1 to 2.3	0 to 0.45	0.45 to 1	1 to 2.3	0 to 0.45	0.45 to 1	1 to 2.3
Source	Uncertainty [%]								
Lumi Up	-2.4	-3	-2.2	-2.8	-3.3	-2.9	-2.6	-2.4	-2.3
Down	2.5	3.1	2.4	2.9	3.5	3.1	2.7	2.5	2.4
b-tagging Pos.	0.8	0.8	1	1	0.9	0.9	0.6	0.8	0.7
Neg.	0.8	1	0.7	0.7	0.9	1.5	0.7	1.1	0.8
Kin Up	-0.17	-0.21	-0.16	-0.2	-0.24	-0.21	-0.18	-0.16	-0.19
Down	0.17	0.21	0.16	0.2	0.25	0.22	0.18	0.17	0.12
JER Up	0.3	0	0.1	0.5	-0.5	0.6	-0.5	-0.3	1.1
Down	-0.5	0.2	0.1	0.3	-0.5	-1	-0	-0.7	3.4
JES Up	-1.5	-1.5	-2	-2.8	-4.2	-3.7	-1.8	-0.4	1.8
Down	1.4	2.6	2.4	3.2	3.5	2.8	0.9	0	0.7
PU Up	0.4	0.6	0.5	0.2	0.3	0.2	0.3	0.2	0.2
Down	-0.4	-0.6	-0.5	-0.2	-0.3	-0.1	-0.4	-0.2	-0.3
Trig Up	-0.9	-1.3	-1.4	-1.2	-1.5	-1.8	-1.2	-1.1	-1.2
Down	1	1.3	1.4	1.2	1.6	1.9	1.2	1.1	1.1
Lept Up	-1.9	-2.3	-1.8	-2.3	-2.7	-2.4	-2.1	-1.9	-1.8
Down	1.9	2.4	1.9	2.4	2.9	2.5	2.1	1.9	1.8
BG Up	-1.3	-1.6	-1.2	-1.7	-2.1	-2	-1.5	-1.2	-1.9
Down	1.3	1.6	1.2	1.7	2.1	2	1.5	1.2	1.8
DY Up	-0.4	-0.9	-1	-0.2	-0.3	-0.3	-0.1	-0.1	0
Down	0.4	0.9	1	0.2	0.3	0.4	0.1	0.1	-0.1
Mass Up	-0.5	-0.1	-3.2	-0.5	0	2.7	-1.4	2.3	5.8
Down	1.7	3.5	3.1	-0.6	1.3	-0.7	-2.1	2.3	-6.4
Match Up	0.4	-0.1	0.1	-0.5	-0.1	-0	-2.4	3.6	5.6
Down	0.7	0.3	-1	-1.5	-0.1	-1.7	-2.6	-1.8	5.1
Scale Up	1.1	0.5	2.8	0.6	0.6	0.5	-0.3	1.9	0.3
Down	0.3	-0.2	-1.4	-3.8	-1.7	1.1	-1.8	1.4	11.4
PDF Pos.	0.4	0.4	0.3	0.2	0.2	0.2	1.4	1	0.7
Neg.	0.4	0.3	0.5	0.2	0.2	0.2	1.4	1	0.7
Hadronization	-3.9	-6.4	0.6	-3.5	-6.7	-3.4	-4.3	-2.8	-3.5
Hard Scat.	1.4	3.8	0.6	0.3	5.5	8.1	2.4	3.6	14.3
Statistical	1.9	1.9	2.2	2.3	2.7	3.8	3.2	4.2	8.8
Total Syst. Pos.	6.1	9.8	6.2	6.6	10.9	10.9	6.6	7.6	21
Total Syst. Neg.	5.7	8.8	5.6	7.5	11.1	10.9	7.7	6.2	16.5

Table J.15: Summary of all the statistical and systematic uncertainties (for each source separately and total) for the **unnormalized** double differential cross sections in bins of $|y(t\bar{t})|$ for different $M(t\bar{t})$ bins.

$M(t\bar{t})$ [GeV]	340 to 450				450 to 600				600 to 1000			
$p_T(t\bar{t})$ [GeV]	0 to 40	40 to 100	100 to 200	200 to 400	0 to 40	40 to 100	100 to 200	200 to 400	0 to 40	40 to 100	100 to 200	200 to 400
Source	Uncertainty [%]											
Lumi Up	-2.4	-2.8	-2.5	-3	-3	-3.2	-2.7	-2.7	-2.4	-2.5	-2.8	-3.5
Down	2.5	3	2.7	3.1	3.2	3.3	2.8	2.9	2.5	2.7	2.9	3.5
b-tagging Pos.	0.7	0.8	1.5	0.8	1	1.2	0.9	1	0.7	0.9	0.2	1.3
Neg.	0.8	0.8	1.1	1.8	1.1	1.1	1.2	0.5	0.7	1.3	1.3	1.1
Kin Up	-0.17	-0.2	-0.18	-0.23	-0.22	-0.23	-0.2	-0.17	-0.17	-0.18	-0.19	-0.34
Down	0.17	0.2	0.18	0.21	0.22	0.23	0.2	0.22	0.17	0.18	0.2	0.16
JER Up	0.3	-0.2	0.6	-1.1	0.1	0.1	-0.3	2.6	-0.1	-0.3	-1.2	1.2
Down	-0.7	0.7	0.7	-2	-1	1.1	-1	0.5	-0.7	0.2	0.5	4.4
JES Up	-0.7	-2.7	-2.8	-0.2	-2.4	-3.6	-6.6	-3.7	-0.6	-1.1	-2	0.3
Down	1.3	2.7	4.2	1.5	1.9	4.1	4.2	3.8	-0.1	0.3	2.7	5
PU Up	0.6	0.2	0.5	0.5	0.7	-0.2	-0.4	-0.5	0.7	0	0.1	0
Down	-0.6	-0.3	-0.5	-0.2	-0.7	0.2	0.4	0.6	-0.8	-0.1	0	-0.3
Trig Up	-1.1	-1.3	-1.1	-1.4	-1.4	-1.5	-1.3	-1.2	-1.1	-1.2	-1.3	-1.7
Down	1.1	1.3	1.2	1.4	1.5	1.6	1.3	1.3	1.2	1.2	1.3	1.6
Lept Up	-1.9	-2.2	-2	-2.5	-2.5	-2.6	-2.2	-2.1	-1.9	-2	-2.2	-2.9
Down	1.9	2.3	2	2.5	2.6	2.7	2.3	2.3	1.9	2	2.3	2.8
BG Up	-1.4	-1.4	-1.1	-3.1	-1.9	-1.9	-1.9	-2.3	-1.2	-1.1	-1.9	-4.6
Down	1.4	1.3	1.1	3.1	1.9	1.9	1.9	2.4	1.2	1.1	1.9	4.4
DY Up	-0.8	-0.6	-0.4	-1.6	-0.3	-0.3	0.1	-0.4	-0	-0.3	0.2	-0.4
Down	0.8	0.6	0.5	1.8	0.3	0.3	-0.1	0.3	-0	0.3	-0.2	0.3
Mass Up	-1.3	-1.3	1.4	-8.8	-0.4	0.1	2.3	6.3	0.9	0.2	-3.5	16.1
Down	2	2.6	7.5	2.6	0	-0.4	-2.7	-0.8	-3.2	0.2	3.5	10.5
Match Up	-0.4	1.1	1.5	-2.1	-0.2	-1.5	0.8	2.5	-1.6	1.3	4.1	11.3
Down	-0.2	0.6	1.2	-0	0.9	-3.2	-4.6	7.4	0.8	-3	-2.5	-1
Scale Up	-0.1	1.3	4.7	-1.8	-6.2	3.1	7.7	-1	-5.6	7	-4.6	10.7
Down	1.4	-0.6	-3.1	-1	5.6	-7.9	-8.7	4.6	4.5	-2.3	2.4	6.9
PDF Pos.	0.4	0.3	0.3	0.5	0.5	0.4	0.2	0.2	1.2	1.2	0.6	1.7
Neg.	0.4	0.3	0.3	0.5	0.5	0.3	0.1	0.3	1.2	1.2	0.7	1.8
Hadronization	-2.2	-6.9	-0	-5.6	-2.4	-8	-15.2	-0.1	-1.4	-1.7	-10.5	-11.3
Hard Scat.	1.5	2.7	5.2	-0.3	6.3	3.4	8.7	4.7	4.3	4.9	7.9	18.2
Statistical	1.4	2	4.2	11.5	2	2.9	6.3	11.7	3.6	4.9	7.9	15.3
Total Syst. Pos.	5.5	9.6	12	8.5	10.3	11.4	20.2	13.4	7.6	9.7	15.3	32.4
Total Syst. Neg.	4.9	9.1	7.7	12.4	10.7	13.6	21.8	7.6	9	7.7	15.5	22.6

Table J.16: Summary of all the statistical and systematic uncertainties (for each source separately and total) for the **unnormalized** double differential cross sections in bins of $p_T(t\bar{t})$ for different $M(t\bar{t})$ bins.

$M(t\bar{t})$ [GeV]	340 to 450					450 to 600					600 to 1000				
x_1	0 to 0.05	0.05 to 0.1	0.1 to 0.2	0.2 to 0.4	0.4 to 1	0 to 0.05	0.05 to 0.1	0.1 to 0.2	0.2 to 0.4	0.4 to 1	0 to 0.05	0.05 to 0.1	0.1 to 0.2	0.2 to 0.4	0.4 to 1
Source	Uncertainty [%]														
Lumi Up	-2.3	-2.9	-2.4	-2.8	0	-3.1	-3.1	-2.7	-3.2	-1.4	-2.3	-2.6	-2.7	-2.8	-5.3
Down	2.5	3.1	2.6	3	0.1	3.3	3.2	2.9	3.4	1.9	2.4	2.7	2.8	2.9	-0
b-tagging Pos.	0.6	1	0.6	1.1	3.8	0.8	1.1	0.8	1.2	2.2	0.8	0.7	0.6	1.3	5.8
Neg.	0.6	0.9	0.8	1.4	4.6	0.9	0.8	0.8	1.4	5	0.9	0.8	0.8	1.6	16.8
Kin Up	-0.16	-0.21	-0.17	-0.2	0.03	-0.23	-0.22	-0.2	-0.22	0.09	-0.16	-0.18	-0.19	-0.17	-2.88
Down	0.17	0.21	0.17	0.19	0.06	0.23	0.22	0.2	0.27	0.24	0.16	0.18	0.19	0.22	-2.54
JER Up	0.2	0.1	0	-0.3	18.8	-0	0.2	0.1	0.8	20.1	0.3	-0.5	-0.3	-1	3
Down	0.1	-0.9	0.3	0.2	17.8	-0.3	0.2	0	-2	3.5	0.5	0.1	-0.7	1.2	26.3
JES Up	-1.4	-2.1	-1.5	-3.7	10.7	-3.6	-3.4	-3.2	-3.2	20	-0.2	-1.2	-1.7	1.2	-33.8
Down	2.2	1.9	1.9	1.4	20.4	2.9	3.5	3.6	3.6	-5.7	0.2	0.2	1.4	0.7	-0.8
PU Up	0.4	0.5	0.5	0.7	-0.6	0.3	0.3	0.2	-0.4	6.2	0.2	0.1	0.4	0.9	-13.9
Down	-0.4	-0.5	-0.6	-0.8	-0.2	-0.3	-0.3	-0.1	0.6	-4.6	-0.2	-0.1	-0.5	-0.9	8.5
Trig Up	-1.1	-1.2	-1.2	-2	-2.4	-1.6	-1.3	-1.3	-2	-2.5	-1.2	-1.2	-1.2	-1.3	-4.6
Down	1.1	1.2	1.2	2.1	2.6	1.6	1.3	1.3	2.1	2.9	1.2	1.2	1.3	1.4	-0.7
Lept Up	-1.9	-2.3	-1.9	-2.2	-0.2	-2.5	-2.5	-2.3	-2.7	-0.7	-1.8	-2	-2.1	-2.2	-4.6
Down	1.9	2.4	2	2.3	0.3	2.6	2.6	2.3	2.9	1	1.9	2.1	2.2	2.3	-0.7
BG Up	-1.3	-1.7	-1.4	-0.8	1.3	-1.8	-1.9	-1.9	-2.7	-5	-1.4	-1.3	-1.4	-1.8	-0.6
Down	1.3	1.7	1.4	0.8	-1.1	1.8	1.9	1.9	2.7	5.8	1.4	1.3	1.4	1.8	-5
DY Up	-0.7	-0.6	-0.8	-1.2	-1.2	-0.2	-0.2	-0.4	0.2	-1.9	-0.2	-0	-0.2	0	-4
Down	0.7	0.6	0.8	1.3	2.8	0.2	0.2	0.4	-0.1	2.8	0.2	0	0.2	0.1	-1.9
Mass Up	-1.4	0.2	-0.8	-4.5	-35.9	1.2	-0.7	-0.9	5.9	18.6	0.7	0.5	-1.5	8.3	-29
Down	3.7	0.5	4.1	2	-15	-0.6	0.2	-0.2	7.6	18.2	-3.6	1.5	-1.2	-2.8	-155.9
Match Up	0.2	0.2	1	-2.6	-4.4	-0.5	-0.7	0.6	1.3	12.1	3.3	-2	-0.1	7.2	-34.4
Down	0.3	0.3	-0.1	-6	-3	-0.3	-1.6	-1.7	0.1	18.7	1.1	-2.5	-2.2	1.2	-51.5
Scale Up	1.2	1.8	1.3	3.4	-20.5	1.8	1.3	-1.5	-1.7	-12.7	2.3	-1.5	2.7	-1.6	-62.1
Down	-0.1	-0.4	-0.5	-4.9	9.3	-0.7	-4.9	-1.9	4.8	2.6	3.3	-2.3	-0.4	10.1	-97.8
PDF Pos.	0.5	0.3	0.2	0.4	2.2	0.5	0.5	0.2	0.3	8.2	0.8	1.3	1.3	0.5	7.8
Neg.	0.5	0.3	0.2	0.4	2.9	0.5	0.5	0.2	0.3	11.5	0.7	1.3	1.3	0.5	7
Hadronization	-2.5	-6.7	-2.6	1.5	-11.5	-8	-3.6	-3.7	4.3	-38	1	-2.6	-7.3	-7.5	484.7
Hard Scat.	2.5	2.6	0.7	-3.2	7.6	7.1	0.8	2.8	12.2	-10.6	5.8	1	6.5	8.8	-105.9
Statistical	1.4	2.2	2.9	6.7	55.2	2.3	2.7	3.5	9.1	64.5	6.5	4	4.1	9.1	144
Total Syst. Pos.	6.8	9	6.8	7.2	32.9	12.3	7.2	7.4	17.3	56.8	8.5	5.2	11.1	19.5	497
Total Syst. Neg.	5.5	8.8	5	11.3	44.2	12.3	8.7	7.6	14.7	44.4	7.8	6.1	11.1	12.9	533.3

Table J.17: Summary of all the statistical and systematic uncertainties (for each source separately and total) for the **unnormalized** double differential cross sections in bins of x_1 for different $M(t\bar{t})$ bins.

Bibliography

[1] **CDF Collaboration** Collaboration, Abe, F. and others, *Observation of Top Quark Production in $\overline{p}p$ Collisions with the Collider Detector at Fermilab*, *Phys. Rev. Lett.* **74** (Apr, 1995) 2626–2631.

[2] M. Kobayashi and T. Maskawa, *CP Violation in the Renormalizable Theory of Weak Interaction*, *Prog. Theor. Phys.* **49** (1973) 652–657.

[3] Herb, S. W. and Hom, D. C. and Lederman, L. M. and Sens, J. C. and Snyder, H. D. and Yoh, J. K. and Appel, J. A. and Brown, B. C. and Brown, C. N. and Innes, W. R. and Ueno, K. and Yamanouchi, T. and Ito, A. S. and Jöstlein, H. and Kaplan, D. M. and Kephart, R. D., *Observation of a Dimuon Resonance at 9.5 GeV in 400-GeV Proton-Nucleus Collisions*, *Phys. Rev. Lett.* **39** (Aug, 1977) 252–255.

[4] **CMS** Collaboration, V. Khachatryan et al., *Measurement of the differential cross section for top quark pair production in pp collisions at $\sqrt{s} = 8$ TeV*, *Eur. Phys. J.* **C75** (2015), no. 11 542, [arXiv:1505.0448].

[5] C. Yang, *Elementary particles*, *Princeton University Press* (1961).

[6] J. Thomson, *Cathode Rays*, *The Electrician* **39** (1897) 104.

[7] E. Rutherford, *The Scattering of α and β Particles by Matter and the Structure of the Atom*, *Phil. Mag.* **21** (1911) 669–688.

[8] "Standard Model." https://en.wikipedia.org/wiki/Standard_Model Accessed: 2015-06-02.

[9] P. A. M. Dirac, *Principles of Quantum Mechanics (4th ed.)*. Clarendon (1958 (reprinted 2011)).

[10] Griffiths, D., *Introduction to Elementary Particles*. Physics textbook. Wiley (2008).

[11] Dyson, F. J., *The Radiation Theories of Tomonaga, Schwinger, and Feynman*, *Phys. Rev.* **75** (Feb, 1949) 486–502.

[12] "9. QUANTUM CHROMODYNAMICS." http://pdg.lbl.gov/2015/reviews/rpp2015-rev-qcd.pdf

[13] Gross, David J. and Wilczek, Frank, *Ultraviolet Behavior of Non-Abelian Gauge Theories*, *Phys. Rev. Lett.* **30** (Jun, 1973) 1343–1346.

[14] H. Bohr and H. Nielsen, *Hadron production from a boiling quark soup: A thermodynamical quark model predicting particle ratios in hadronic collisions*, *Nuclear Physics B* **128** (1977), no. 2 275 – 293.

[15] Aitchison, Ian JR and Hey, Anthony JG and Brewer, Douglas F, *Gauge Theories in Particle Physics-a Practical Introduction. Volume 1: From Relativistic Quantum Mechanics to QED, ISBN-10: 0-7503-0864-8 (PB); ISBN-13 978-0-7503-0864-9 (PB). Published by Institute of Physics Publishing, Bristol, UK, 2003.* **1** (2003).

[16] **Particle Data Group** Collaboration, J. Beringer et al., *Review of particle physics*, *Phys. Rev. D* **86** (2012) 010001.

[17] S. M. Bilenky and J. Hosek, *GLASHOW-WEINBERG-SALAM THEORY OF ELECTROWEAK INTERACTIONS AND THE NEUTRAL CURRENTS*, *Phys. Rept.* **90** (1982) 73–157.

[18] P. W. Higgs, *Broken Symmetries and the Masses of Gauge Bosons*, *Physical Review Letters* **13** (oct, 1964) 508–509.

[19] G. Aad et al., *Observation of a new particle in the search for the standard model higgs boson with the {ATLAS} detector at the {LHC}*, *Physics Letters B* **716** (2012), no. 1 1 – 29.

[20] **CMS** Collaboration, S. Chatrchyan et al., *Observation of a new boson at a mass of 125 GeV with the CMS experiment at the LHC*, *Phys. Lett.* **B716** (2012) 30–61, [arXiv:1207.7235].

[21] "W. J. Stirling, "Standard Model cross sections as a function of collider energy". Private communication." http://www.hep.ph.ic.ac.uk/~wstirlin/plots/plots.html

[22] F.-P. Schilling, *Top Quark Physics at the LHC: A Review of the First Two Years*, *Int. J. Mod. Phys.* **A27** (2012) 1230016, [arXiv:1206.4484].

[23] G. Altarelli and G. Parisi, *Asymptotic Freedom in Parton Language*, *Nucl. Phys.* **B126** (1977) 298.

[24] Y. L. Dokshitzer, *Calculation of the Structure Functions for Deep Inelastic Scattering and e+ e- Annihilation by Perturbation Theory in Quantum Chromodynamics.*, *Sov. Phys. JETP* **46** (1977) 641–653. [Zh. Eksp. Teor. Fiz.73,1216(1977)].

[25] V. N. Gribov and L. N. Lipatov, *Deep inelastic e p scattering in perturbation theory*, *Sov. J. Nucl. Phys.* **15** (1972) 438–450. [Yad. Fiz.15,781(1972)].

[26] L. A. Harland-Lang, A. D. Martin, P. Motylinski, and R. S. Thorne, *Parton distributions in the LHC era: MMHT 2014 PDFs*, *Eur. Phys. J.* **C75** (2015), no. 5 204, [arXiv:1412.3989].

[27] J. Pumplin, D. R. Stump, J. Huston, H. L. Lai, P. M. Nadolsky, and W. K. Tung, *New generation of parton distributions with uncertainties from global QCD analysis*, *JHEP* **07** (2002) 012, [hep-ph/0201195].

[28] **ZEUS, H1** Collaboration, H. Abramowicz et al., *Combination of measurements of inclusive deep inelastic $e^{\pm}p$ scattering cross sections and QCD analysis of HERA data*, *Eur. Phys. J.* **C75** (2015), no. 12 580, [arXiv:1506.0604].

[29] "Useful Diagrams of Top Signals and Backgrounds." http://www-d0.fnal.gov/Run2Physics/top/top_public_web_pages/top_feynman_diagrams.html

[30] R. Scrivens, M. Kronberger, D. Kchler, J. Lettry, C. Mastrostefano, O. Midttun, M. ONeil, H. Pereira, and C. Schmitzer, *Overview of the status and developments on primary ion sources at CERN**, .

[31] F. Fayette, *Strategies for precision measurements of the charge asymmetry of the W boson mass at the LHC within the ATLAS experiment*, Ph.D. thesis, Paris U., VI-VII (2009). arXiv:0906.4260.

[32] L. Arnaudon, P. Baudrenghien, and M. e. a. Baylac, *Linac4 Technical Design Report*, . revised version submitted on 2006-12-14 09:00:40.

[33] A. Blas et al., *The PS complex as proton pre-injector for the LHC: Design and implementation report*, .

[34] "Professional website of Howard Haber, Professor of Physics at the University of California, Santa Cruz.." http://scipp.ucsc.edu/~haber/

[35] ALICE Collaboration and F. Carminati and P. Foka and P. Giubellino and A. Morsch and G. Paic and J.-P. Revol and K. Safark and Y. Schutz and U. A. Wiedemann, *ALICE: Physics Performance Report, Volume I*, *Journal of Physics G: Nuclear and Particle Physics* **30** (2004), no. 11 1517.

[36] **LHCb Collaboration** Collaboration, Alves, A Augusto et al, *The LHCb Detector at the LHC*, *J. Instrum.* **3** (2008), no. LHCb-DP-2008-001. CERN-LHCb-DP-2008-001 S08005. Also published by CERN Geneva in 2010.

[37] **ATLAS** Collaboration, G. Aad et al., *The ATLAS Experiment at the CERN Large Hadron Collider*, *JINST* **3** (2008) S08003.

[38] **CMS** Collaboration, S. Chatrchyan et al., *The CMS experiment at the CERN LHC*, *JINST* **3** (2008) S08004.

[39] T. Sakuma and T. McCauley, *Detector and Event Visualization with SketchUp at the CMS Experiment*, *J. Phys. Conf. Ser.* **513** (2014) 022032, [arXiv:1311.4942].

[40] G. Dissertori, *LHC Detectors and Early Physics*, arXiv:1003.2222. 65th Scottish Universities Summer School in Physics: LHC Physics (16 August to 29 August 2009), St. Andrews.

[41] "CMS solenoid magnet — LC Newsline." http://newsline.linearcollider.org/2011/05/05/one-hundred-years-of-superconductivity/cms-solenoid-magnet/

[42] **CMS Collaboration** Collaboration, V. Karimki, M. Mannelli, P. Siegrist, H. Breuker, A. Caner, R. Castaldi, K. Freudenreich, G. Hall, R. Horisberger, M. Huhtinen, and A. Cattai, *The CMS tracker system project: Technical Design Report*. Technical Design Report CMS. CERN, Geneva (1997).

[43] **CMS** Collaboration, S. Chatrchyan et al., *Description and performance of track and primary-vertex reconstruction with the CMS tracker*, *JINST* **9** (2014), no. 10 P10009, [arXiv:1405.6569].

[44] T. Lenzi, *Development and Study of Different Muon Track Reconstruction Algorithms for the Level-1 Trigger for the CMS Muon Upgrade with GEM Detectors*, Master's thesis, U. Brussels (main) (2013).

[45] **CMS Collaboration** Collaboration, *The CMS electromagnetic calorimeter project: Technical Design Report*. Technical Design Report CMS. CERN, Geneva (1997).

[46] **CMS Collaboration** Collaboration, P. Bloch, R. Brown, P. Lecoq, and H. Rykaczewski, *Changes to CMS ECAL electronics: addendum to the Technical Design Report*. Technical Design Report CMS. CERN, Geneva (2002).

[47] B. Isildak, *Measurement of the differential dijet production cross section in proton-proton collisions at* $\sqrt{s} = 7$ *tev*, Ph.D. thesis, Bogazici U. (2011). arXiv:1308.6064.

[48] Hobson, Peter R., *Avalanche photodiodes and vacuum phototriodes for the electromagnetic calorimeter of the CMS experiment at the Large Hadron Collider*, *Nuclear Inst. and Methods in Physics Research, A* **604** (2009), no. 1-2 193–195.

[49] Adzic, P and Alemany-Fernandez, R and Almeida et al, *Energy resolution of the barrel of the CMS Electromagnetic Calorimeter*, *JOURNAL OF INSTRUMENTATION* **2** (2007).

[50] **CMS** Collaboration, S. Chatrchyan et al., *Energy Calibration and Resolution of the CMS Electromagnetic Calorimeter in pp Collisions at* $\sqrt{s} = 7$ *TeV*, *JINST* **8** (2013) P09009, [arXiv:1306.2016].

[51] "Official XDAQ page." http://xdaq.web.cern.ch/xdaq/setup/images/

[52] V. D. Elvira, *Measurement of the Pion Energy Response and Resolution in the CMS HCAL Test Beam 2002 Experiment*, .

[53] D. E. Groom, N. V. Mokhov, and S. I. Striganov, *Muon stopping power and range tables 10-MeV to 100-TeV*, *Atom. Data Nucl. Data Tabl* **78** (2001) 183 356.

[54] CMS Collaboration, *CMS computing : Technical Design Report*, *Technical Design Report CMS* **7** (2005).

[55] P La Rocca and F Riggi, *The upgrade programme of the major experiments at the Large Hadron Collider*, *Journal of Physics: Conference Series* **515** (2014), no. 1 012012.

[56] **CMS** Collaboration, A. Dominguez, D. Abbaneo, K. Arndt, N. Bacchetta, A. Ball, E. Bartz, W. Bertl, G. M. Bilei, G. Bolla, H. W. K. Cheung, et al., *CMS Technical Design Report for the Pixel Detector Upgrade*, .

[57] P. La Rocca and F. Riggi, *The upgrade programme of the major experiments at the Large Hadron Collider*, *J. Phys. Conf. Ser.* **515** (2014) 012012.

[58] "SBA." http://sba.web.cern.ch/sba/

[59] "Deutschland grösstes Beschleunigerzentrum – Deutsches Elektronen-Synchrotron DESY." http://www.desy.de Accessed: 2015-10-21.

[60] G. Hemmie, *THE FUTURE OF SYNCHROTRONS (DESY II)*, .

[61] "DESY - DESY II - Das Synchrotron DESY II." http://desy2.desy.de/ Accessed: 2015-10-21.

[62] "Test Beams at Desy. Beam Generation." http://particle-physics.desy.de/test_beams_at_desy/beam_generation/index_ger.html Accessed: 2016-01-18.

[63] J. Aguilar et al., *The EUDET Consortium, Infrastructure for Detector Research and Development towards the International Linear Collider*, *arXiv:1201.4657* (2012).

[64] R. Turchetta, J. D. Berst, B. Casadei, G. Claus, C. Colledani, W. Dulinski, Y. Hu, D. Husson, J. P. Le Normand, J. L. Riester, G. Deptuch, U. Goerlach, S. Higueret, and M. Winter, *A monolithic active pixel sensor for charged particle tracking and imaging using standard VLSI CMOS technology*, *Nuclear Instruments and Methods in Physics Research A* **458** (Feb., 2001) 677–689.

[65] P. Fischer, W. Neeser, M. Trimpl, J. Ulrici, and N. Wermes, *Readout concepts for DEPFET pixel arrays*, *Nucl. Instrum. Meth.* **A512** (2003) 318–325, [hep-ex/0209074].

[66] G. Flucke, P. Schleper, G. Steinbrck, and M. Stoye, *CMS silicon tracker alignment strategy with the Millepede II algorithm*, *Journal of Instrumentation* **3** (2008), no. 09 P09002.

[67] V. Blobel, *A new fast track-fit algorithm based on broken lines*, *Nucl. Instrum. Meth.* **A566** (2006) 14–17.

[68] "CMS Tracker studies." http://www.desy.de/~pitzl/res.pdf

[69] G. Corcella, I. G. Knowles, G. Marchesini, S. Moretti, K. Odagiri, P. Richardson, M. H. Seymour, and B. R. Webber, *HERWIG 6: An Event generator for hadron emission reactions with interfering gluons (including supersymmetric processes)*, *JHEP* **01** (2001) 010, [hep-ph/0011363].

[70] T. Sjostrand, S. Mrenna, and P. Z. Skands, *PYTHIA 6.4 Physics and Manual*, *JHEP* **05** (2006) 026, [hep-ph/0603175].

[71] T. Gleisberg, S. Hoeche, F. Krauss, A. Schalicke, S. Schumann, and J.-C. Winter, *SHERPA 1. alpha: A Proof of concept version*, *JHEP* **02** (2004) 056, [hep-ph/0311263].

[72] A. Buckley et al., *General-purpose event generators for LHC physics*, *Phys. Rept.* **504** (2011) 145–233, [arXiv:1101.2599].

[73] X. Artru and G. Mennessier, *String model and multiproduction*, *Nucl. Phys.* **B70** (1974) 93–115.

[74] B. Andersson, *The Lund model*, *Nuclear Physics A* **461** (1987), no. 1 513 – 520.

[75] D. Amati and G. Veneziano, *Preconfinement as a Property of Perturbative QCD*, *Phys. Lett.* **B83** (1979) 87.

[76] B. R. Webber, *Fragmentation and hadronization*, *Int. J. Mod. Phys.* **A15S1** (2000) 577–606, [hep-ph/9912292]. [,577(1999)].

[77] **CMS** Collaboration, V. Khachatryan et al., *Event generator tunes obtained from underlying event and multiparton scattering measurements*, arXiv:1512.0081.

[78] **CMS** Collaboration, S. Chatrchyan et al., *Measurement of the Underlying Event Activity at the LHC with $\sqrt{s} = 7$ TeV and Comparison with $\sqrt{s} = 0.9$ TeV*, *JHEP* **09** (2011) 109, [arXiv:1107.0330].

[79] *ATLAS tunes of PYTHIA 6 and Pythia 8 for MC11*, .

[80] J. Alwall, M. Herquet, F. Maltoni, O. Mattelaer, and T. Stelzer, *MadGraph 5 : Going Beyond*, *JHEP* **06** (2011) 128, [arXiv:1106.0522].

[81] S. Mrenna and P. Richardson, *Matching matrix elements and parton showers with HERWIG and PYTHIA*, *JHEP* **05** (2004) 040, [hep-ph/0312274].

[82] S. Frixione, P. Nason, and C. Oleari, *Matching NLO QCD computations with Parton Shower simulations: the POWHEG method*, *JHEP* **11** (2007) 070, [arXiv:0709.2092].

[83] H.-L. Lai, M. Guzzi, J. Huston, Z. Li, P. M. Nadolsky, J. Pumplin, and C. P. Yuan, *New parton distributions for collider physics*, *Phys. Rev.* **D82** (2010) 074024, [arXiv:1007.2241].

[84] S. Frixione and B. R. Webber, *Matching NLO QCD computations and parton shower simulations*, *JHEP* **06** (2002) 029, [hep-ph/0204244].

[85] **GEANT4** Collaboration, S. Agostinelli et al., *GEANT4: A Simulation toolkit*, *Nucl. Instrum. Meth.* **A506** (2003) 250–303.

[86] **CMS** Collaboration, F. Beaudette, *The CMS Particle Flow Algorithm*, arXiv:1401.8155.

[87] **CMS Collaboration** Collaboration, *Particle-Flow Event Reconstruction in CMS and Performance for Jets, Taus, and MET*, *CMS-PAS-PFT-09-001* (Apr, 2009).

[88] **CMS** Collaboration, S. Chatrchyan et al., *Description and performance of track and primary-vertex reconstruction with the CMS tracker*, *JINST* **9** (2014), no. 10 P10009, [arXiv:1405.6569].

[89] R. Fruhwirth, *Application of Kalman filtering to track and vertex fitting*, *Nucl.Instrum.Meth.* **A262** (1987) 444–450.

[90] "New world record - first pp collisions at 8 TeV — CMS Experiment." http://cms.web.cern.ch/news/new-world-record-first-pp-collisions-8-tev

[91] Kenneth Rose, *Deterministic annealing for clustering, compression, classification, regression, and related optimization problems*, *Proceedings of the IEEE* **86** (1998), no. 11 2210–2239.

[92] R. Fruhwirth and Waltenberger, Wolfgang and Vanlaer, Pascal, *Adaptive Vertex Fitting*, .

[93] "The CMS Collaboration, "Slice of the CMS detector"." http://cms-project-cmsinfo.web.cern.ch/cms-project-cmsinfo/Resources/Website/Media/Videos/Animations/files/CMS_Slice.gi

[94] " Stand-Alone Muon Reconstruction ." "https://twiki.cern.ch/twiki/bin/view/CMSPublic/SWGuideStandAloneMuonReco"

[95] **CMS Collaboration** Collaboration, *Electron reconstruction and identification at sqrt(s) = 7 TeV*, *CMS-PAS-EGM-10-004* (2010), no. CMS-PAS-EGM-10-004.

[96] W. Adam, and R. Fruhwirth, and A. Strandlie, and T. Todorov, *Reconstruction of electrons with the Gaussian-sum filter in the CMS tracker at the LHC*, *Journal of Physics G: Nuclear and Particle Physics* **31** (2005), no. 9 N9.

[97] **CMS** Collaboration, *Commissioning of the Particle-flow Event Reconstruction with the first LHC collisions recorded in the CMS detector*, .

[98] S. Baffioni, C. Charlot, F. Ferri, D. Futyan, P. Meridiani, et al., *Electron reconstruction in CMS*, *Eur.Phys.J.* **C49** (2007) 1099–1116.

[99] G. P. Salam and G. Soyez, *A Practical Seedless Infrared-Safe Cone jet algorithm*, *JHEP* **0705** (2007) 086, [arXiv:0704.0292].

[100] M. Cacciari, G. P. Salam, and G. Soyez, *The Anti-k(t) jet clustering algorithm*, *JHEP* **0804** (2008) 063, [arXiv:0802.1189].

[101] CMS Collaboration, *Determination of jet energy calibration and transverse momentum resolution in CMS*, *Journal of Instrumentation* **6** (2011) 11002, [1107.4277].

[102] A. B. Galtieri, F. Margaroli, and I. Volobouev, *Precision measurements of the top quark mass from the Tevatron in the pre-LHC era*, *Rept. Prog. Phys.* **75** (2012) 056201, [arXiv:1109.2163].

[103] **CMS Collaboration** Collaboration, *Performance of b tagging at $\sqrt{s}$=8 TeV in multijet, $t\bar{t}$ and boosted topology events*, .

[104] CMS Collaboration, *MET performance in 8 TeV data*, .

[105] "Met regression in high pile-up environment." https://twiki.cern.ch/twiki/bin/viewauth/CMS/MVAMet#Documentation Accessed: 2015-07-13.

[106] **CMS** Collaboration, Top Physics Analysis Group, *Top PAG reference selection.*, *https://twiki.cern.ch/twiki/bin/viewauth/CMS/TWikiTopRefEventSel.* **[Unpublished. Online]** (2015).

[107] "Standard model cross sections for cms at 8 tev." https://twiki.cern.ch/twiki/bin/view/CMS/StandardModelCrossSectionsat8TeV Accessed: 2015-07-30.

[108] **CMS** Collaboration, S. Chatrchyan et al., *Measurement of the $t\bar{t}$ production cross section and the top quark mass in the dilepton channel in pp collisions at $\sqrt{s} = 7$ TeV*, *JHEP* **07** (2011) 049, [arXiv:1105.5661].

[109] JSON File. /afs/cern.ch/cms/CAF/certification/Collisions12/8TeV/929Reprocessing/Cert_190456-208686_8TeV_22Jan2013ReReco_930Collisions12_JSON.txt

[110] Asin Cruz, Ivan, *Measurement of Top-Quark-Pair Differential Cross Sections in Proton-Proton Collisions at $\sqrt{s}$ = 8TeV with the CMS Experiment*, Ph.D. thesis, Universitaet Hamburg (2014).

[111] HCAL Noise Library . https://twiki.cern.ch/twiki/bin/viewauth/CMS/HcalNoiseInfoLibrary

[112] **CMS** Collaboration, C. Collaboration, *Absolute Calibration of the Luminosity Measurement at CMS: Winter 2012 Update*, .

[113] "Estimating systematic errors due to pileup modeling." https://twiki.cern.ch/twiki/bin/viewauth/CMS/PileupSystematicErrors Accessed: 2015-07-28.

[114] "Tag and probe." https://twiki.cern.ch/twiki/bin/view/CMSPublic/TagAndProbe Accessed: 2015-07-30.

[115] "Pf based isolation for 2015+ data." https://twiki.cern.ch/twiki/bin/view/CMS/EgammaPFBasedIsolationRun2#Delta_Beta_corrections Accessed: 2016-01-22.

[116] **CMS** Collaboration, S. Chatrchyan et al., *Performance of CMS muon reconstruction in pp collision events at* $\sqrt{s} = 7$ *TeV*, *JINST* **7** (2012) P10002, [arXiv:1206.4071].

[117] Sonnenschein, Lars, *Analytical solution of* $t\bar{t}$ *dilepton equations*, *Phys. Rev. D* **73** (Mar, 2006) 054015.

[118] Sonnenschein, Lars, *Erratum: Analytical solution of* $t\bar{t}$ *dilepton equations [Phys. Rev. D* ***73*** *, 054015 (2006)]*, *Phys. Rev. D* **78** (Oct, 2008) 079902.

[119] **CMS** Collaboration, S. Chatrchyan et al., *Measurement of differential top-quark pair production cross sections in pp colisions at* $\sqrt{s} = 7$ *TeV*, *Eur. Phys. J.* **C73** (2013), no. 3 2339, [arXiv:1211.2220].

[120] "Top-12-028 measurement of the differential top-quark pair production cross section in the dilepton channel at 8 tev." https://twiki.cern.ch/twiki/bin/view/CMSPublic/PhysicsResultsTOP12028

[121] S. Schmitt, *TUnfold: an algorithm for correcting migration effects in high energy physics*, *JINST* **7** (2012) T10003, [arXiv:1205.6201].

[122] Tikhonov, A. N., *Solution of incorrectly formulated problems and the regularization method*, *Soviet Math. Dokl.* **4** (1963) 1035–1038.

[123] P. C. Hansen, *The L-Curve and its Use in the Numerical Treatment of Inverse Problems*, in *in Computational Inverse Problems in Electrocardiology, ed. P. Johnston, Advances in Computational Bioengineering*, pp. 119–142, WIT Press, 2000.

[124] V Blobel, *Data Unfolding*, *Terra Scale statistics school Hamburg* (2010).

[125] Glen Cowan, *Statistical Data Analysis*. Clarendon (Oxford), Oxford (1998 (ISBN: 0-19-850156-0 or 0-19-850155-2 in paperback)).

[126] **CMS Collaboration** Collaboration, *CMS Luminosity Based on Pixel Cluster Counting - Summer 2013 Update*, *CMS-PAS-LUM-13-001* (2013).

[127] **CMS Collaboration** Collaboration, C. Diez Pardos and J. Kieseler., *Dilepton trigger and lepton identification effiencies for the top quark pair production cross section measurements at 8 TeV in the dilepton decay channel*, *CMS AN-2012/389* (2013).

[128] **CMS Collaboration** Collaboration, *Jet Energy Corrections determination at 7 TeV*, *CMS-PAS-JME-10-010* (2010).

[129] "Jet energy resolution." https://twiki.cern.ch/twiki/bin/viewauth/CMS/JetResolution Accessed: 2015-08-03.

[130] **ATLAS, CDF, CMS, D0** Collaboration, *First combination of Tevatron and LHC measurements of the top-quark mass*, arXiv:1403.4427.

[131] A. Ferroglia, B. D. Pecjak, and L. L. Yang, *Top-quark pair production at high invariant mass: an NNLO soft plus virtual approximation*, *JHEP* **09** (2013) 032, [arXiv:1306.1537].

[132] H. T. Li, C. S. Li, D. Y. Shao, L. L. Yang, and H. X. Zhu, *Top quark pair production at small transverse momentum in hadronic collisions*, *Phys. Rev.* **D88** (2013) 074004, [arXiv:1307.2464].

[133] L. Sonnenschein, *Algebraic approach to solve $t\bar{t}$ dilepton equations*, *Phys.Rev.* **D72** (2005) 095020, [hep-ph/0510100].

Acknowledgements

I would like to express my gratitude to the people, who were accompanying and supporting me throughout my way to completing this thesis.

First of all I would like to thank Olaf Behnke for his guidance through all the aspects of this analysis. It was a great pleasure to work with you and to learn from your experience. You were always supporting me in every situation.

I would also like to thank Christian Sander for the fruitful discussions on the analysis. Your ideas and suggestions were always helpful and wise.

I would also like to thank the DESY Top Group for the support in many aspects. For the cooperation and helpful discussions and suggestions, I would like to thank Maria Aldaya, Andreas Meyer, Carmen Diez Pardos, Ivan Asin, Johannes Hauk, Oleksandr Zenaiev, Ganna Dolinska, Nazar Bartosik, Jasone Garay, Mykola Savitskyi and Till Arnd.

My gratitude also goes to Stefan Schmitt, who always took his time to explain me the details of the TUnfold and to guide me whenever I had difficulties or problems.

As a part of my PhD project, I was working on the CMS pixel detector upgrade with Daniel Pitzl. I would like to thank Daniel for his support and sharing his knowledge. You made the work in the lab and on the test beam exciting, your enthusiasm was always encouraging.

In the context of the work on the pixel detector upgrade, I would also like to thank Simon Spannagel who was always there to help me with many aspects of the work I was doing.

Finally, a special acknowledgement goes to my family for the support and understanding.